






Universitat Autònoma de Barcelona

**ADVERTIMENT.** L'accés als continguts d'aquesta tesi queda condicionat a l'acceptació de les condicions d'ús establertes per la següent llicència Creative Commons:  [http://cat.creativecommons.org/?page\\_id=184](http://cat.creativecommons.org/?page_id=184)

**ADVERTENCIA.** El acceso a los contenidos de esta tesis queda condicionado a la aceptación de las condiciones de uso establecidas por la siguiente licencia Creative Commons:  <http://es.creativecommons.org/blog/licencias/>

**WARNING.** The access to the contents of this doctoral thesis it is limited to the acceptance of the use conditions set by the following Creative Commons license:  <https://creativecommons.org/licenses/?lang=en>



Universitat Autònoma  
de Barcelona

**Silica-supported Multicomponent Materials  
for Environmental Remediation  
Biomedical and Energy Applications**

**Gubakhanim Shahnazarova**

**Directors:**

Dr. Albert Serra

Dra. Maria Jose Esplandiu

Dr. Borja Sepulveda

**Tutor:**

Eva Pellicer

Universitat Autònoma de Barcelona

Department of Physics

Doctoral Program in Materials Science

Barcelona, January 2023



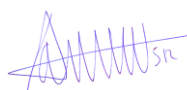
The present work entitled 'Silica-supported multicomponent materials for environmental remediation, biomedical and energy applications' presented by Gubakhanim Shahnazarova to obtain the degree of Doctor in Materials Science by Universitat Autònoma de Barcelona, was performed at the Magnetic Nanostructures Group at the Catalan Institute of Nanotechnology and Nanoscience (ICN2), under the supervision of Albert Serra, Maria Jose Esplandiú, and Borja Sepulveda.

The present thesis was also performed under the doctoral studies 'PhD in Materials Science' at the Physics Department, Sciences Faculty, Universitat Autònoma de Barcelona, under the tutorship of Dr Eva Pellicer.



Gubakhanim Shahnazarova

(Author)



Dr. Albert Serra  
(Director)



Dr. Maria Jose Esplandiú  
(Director)



Dr. Borja Sepulveda  
(Director)



Eva Pellicer  
(Tutor)



# PREFACE

## I. Acknowledgements

First of all, I would like to thank my supervisors Dr. Albert Serra, Dra. Maria Jose and Dr. Borja Sepulveda and tutor Dra. Eva Pellicer for their support, guidance and patience during these years.

A million thanks are given to Maria Jose for her wonderful personality, forbearance and always having a smiley face no matter what happens. A special thanks go to Borja Sepulveda. Thank you for your continuous encouragement and solid support during my study. I really admire your positive attitude, great passion for your work and for giving me push.

I am very grateful to Albert Serra for his sincere suggestions for work, for answering my questions and for helping me out during these years. Also, I would like to thank Prof. Josep Nogues.

I owe a deep sense of gratitude to Jordi Fraxedas for his great help in XPS characterization.

All friends are greatly acknowledged. Special thanks go to Nour Al Hoda. I think this PhD would be less fun without the days we spent together. I will miss your letters, funny suggestions and furious days. No matter good or bad, I will always remember them with a big smile on my face. I would like to thank Jessica also, for her friendliness and the days we spent together. I am grateful for everything you did for me. Many thanks to Flippos, for always helping me with global issues, for his humour and for answering my questions whenever and wherever he is. I am grateful to Aritz for his help and for trying his best to solve any problem. Thanks to all, for your help. I will cherish these memorable days with you.

I would like to thank Alex for his wonderful personality. Thanks to Yue, Li, Javi and Pau for the time we spent together.

I also thank all the technicians (Raul, Marcos, Javier, Jessica, Francisco) in ICN2 for training me to use all the equipment that was needed during this thesis.

Very special gratitude goes to my husband Tural. Thank you for your care, unconditional love and strong support during all my good and bad times. Especially, making my thesis writing process easier.

Last but not least I would like to express my deepest gratitude to my dearest parents, my sister, my brother and my parents-in-law. Thank you for your love and constant encouragement all the time.

*Gubakhanim Shahmazarova*



## II. Resumen

La combinación de múltiples materiales con diferentes propiedades físicas y químicas en soportes nanoestructurados permite la integración de múltiples funcionalidades con potenciales efectos sinérgicos. Además, el ensamblaje de los materiales multicomponente en un soporte puede solventar los problemas que presentan los materiales "libres", incluida la mala solubilidad y su estabilidad fisicoquímica limitada.

Las partículas de sílice mesoporosas con morfología de poros controlable y biocompatibilidad pueden convertirse en excelentes soportes para catalizadores, proporcionando un área superficial muy alta, accesibilidad a los reactivos y reducen la aglomeración. En este contexto, esta Tesis Doctoral se ha centrado en el desarrollo de sistemas multicomponentes multifuncionales catalíticos y fotocatalíticos sobre nanoestructuras de sílice mesoporosas o de poro grande siguiendo diferentes rutas de fabricación.

En la primera parte de la tesis, se fabricaron nanoreactores galvánicos multifuncionales de Fe/Au mediante una técnica de dos pasos que consistió en el autoensamblaje coloidal de partículas de sílice de poro grande y deposición física de metales por vapor para generar semicapas bimetálicas de Fe/Au. La capa de Au sobre la superficie de Fe mejoró significativamente la actividad catalítica de los nanoreactores debido a su diferencia de potencial electroquímico con respecto al Fe. Como resultado, las capas de Fe y Au actuaron como ánodo y cátodo, respectivamente. Este sistema galvánico promovió la oxidación y liberación eficiente de Fe a  $\text{Fe}^{2+}$  y la transferencia de los electrones a la capa de Au para la generación simultánea de  $\text{H}_2\text{O}_2$  in situ, proporcionando así los ingredientes principales para desencadenar la reacción de Fenton en agua a pH 7. El  $\text{Fe}^{2+}$  liberado catalizó la descomposición del  $\text{H}_2\text{O}_2$  produciendo radicales hidroxilos altamente reactivos a pH neutro sin necesidad de aditivos externos o aporte de energía. La producción de  $\text{H}_2\text{O}_2$  in situ se detectó empleando una reacción enzimática de alta sensibilidad, que mostró una concentración de  $\text{H}_2\text{O}_2$  36 veces mayor en el nanoreactor galvánico de Fe/Au en comparación con los nanoreactores de Fe. La alta reactividad se demostró mediante la degradación eficiente de los contaminantes orgánicos azul de metileno y tetraciclina con una dosis mínima de catalizadores. Los nanoreactores de Fe/Au mostraron una constante cinética notablemente más alta (5 veces), así como mayores eficiencias de degradación y mineralización en comparación con nanoreactores de Fe. Hasta



donde se sabe, los reactores galvánicos de Fe/Au han demostrado reacciones de Fenton sin precedentes a pH 7 en comparación con otros sistemas basados en Fe, sin la necesidad de agregar  $\text{H}_2\text{O}_2$  externamente y mostrando una de las constantes cinéticas normalizadas más altas. Combinados con sus propiedades fototérmicas y ferromagnéticas, estos nanoreactores galvánicos podrían tener aplicaciones atractivas en terapias locales basadas en ROS.

En la segunda parte de la tesis, se desarrollaron nanoreactores 2D  $\text{MoS}_2/\text{Cu}$  fotocatalíticamente activos sobre partículas de sílice mesoporosas mediante la combinación de síntesis hidrotérmal y deposición física de vapor. El  $\text{MoS}_2$  obtenido consta de dos fases semiconductoras, el prismático trigonal 2H y la octaédrica distorsionada 1T'. En la fase semiconductor 2H, el orbital d se divide en tres bandas y presenta una banda prohibida ancha de 1,9 eV. Por lo tanto, la fase 2H muestra una menor capacidad de transferencia de carga. Sin embargo, en la fase 1T', el orbital d está parcialmente lleno y posee una banda prohibida muy pequeña, lo que facilita una mayor capacidad de transferencia de carga. A su vez la fase 1T' obtenida exhibió mayor densidad de defectos, los cuales constituyen sitios activos para los procesos redox interfaciales. Por otro lado, la deposición de una capa fina de Cu, que rápidamente se oxida a  $\text{Cu}_2\text{O}$ , permitió generar una heterounión con el  $\text{MoS}_2$  facilitando una mayor separación de los portadores de carga fotogenerados, además de contribuir con una mayor absorción de luz, que de por sí ya es muy buena en el  $\text{MoS}_2$ . Todos estos atributos hacen que los nanoreactores de  $\text{MoS}_2/\text{Cu}$  presenten una actuación fotocatalítica eficiente con luz blanca e incluso con luz infrarroja cercana. La actividad fotocatalítica fue comprobada mediante la degradación de Tetraciclina (antibiótico) y Anatoxina-A (biotoxina), como contaminantes orgánicos modelo. Los nanoreactores fotocatalíticos mostraron una excelente actividad fotocatalítica bajo luz blanca a pH 6 y pH 8. El rendimiento catalítico de los nanoreactores se probó mientras estaban inmovilizados en un sustrato de silicio sin causar ninguna contaminación secundaria y con una gran robustez, mostrando una degradación mínima después de 10 ciclos catalíticos. Además, los nanoreactores iluminados por luz infrarroja cercana en la primera ventana biológica (660 nm) pudieron matar células cancerosas de manera eficiente *in vitro* a pesar de la gran separación entre los nanoreactores y las células (100  $\mu\text{m}$ ). Estos resultados, combinados con la baja citotoxicidad, demuestran el alto potencial de los nanoreactores  $\text{MoS}_2/\text{Cu}$  para aplicaciones medioambientales o de salud.

La última parte recoge los resultados preliminares de nanorreactores termocatalíticos de Ni/Pt ricos en Ni para la conversión de ácido levulínico en  $\gamma$ -Valerolactona mediante hidrogenación por transferencia catalítica utilizando ácido fórmico como donante de hidrógeno. Estos reactores se fabricaron sobre nanopartículas de sílice porosa autoensambladas, mediante evaporación por haz de electrones y tratamiento térmico a 500 °C en atmósfera de hidrógeno y argón para aumentar el rendimiento catalítico. Este tratamiento térmico permitió la aleación de los metales y una distribución óptima de Pt en la capa de Ni para mejorar la actividad catalítica. Las propiedades de eficiencia fototérmica de los nanorreactores de Ni/Pt soportados los convierten en candidatos prometedores para aplicaciones foto-termo-catalíticas.

En resumen, esta tesis ha demostrado la versatilidad de los nanomateriales multicomponentes con soporte catalítico o fotocatalítico, que pueden abrir el camino a aplicaciones prometedoras en áreas que incluyen la remediación ambiental, los tratamientos biomédicos basados en ROS o la conversión de energía con la capacidad potencial de explotar aún más sus propiedades magnetoplásmonicas.

### III. Abstract

The combination of multiple materials with different physical and chemical properties into nanostructured supports enables the integration of multiple functionalities with potential synergistic effects. Moreover, the assembly of the multicomponent materials on support can overcome problems exhibited by 'free' materials including poor solubility and limited physicochemical stability.

Mesoporous silica particles with controllable pore morphology, high surface area, pore volume, and appealing biocompatibility can become excellent catalyst supports, providing very high surface area, accessibility to the reactants, and decreasing their agglomeration. In this context, this PhD Thesis has been focused on the development of catalytically and photocatalytically active multifunctional multicomponent systems on mesoporous or large pore silica nanostructures following different fabrication routes.

In the first part of the Thesis, multifunctional Fe/Au galvanic nanoreactors were fabricated by a two-step technique of colloidal self-assembly of large pore silica particles and physical vapor deposition to construct Fe/Au bimetallic semi-shells. The Au layer on the Fe surface significantly improved the catalytic activity of the nanoreactors due to their electrochemical potential difference. As a result, the Fe and Au layers acted as anode and cathode, respectively. This galvanic system promoted the efficient oxidation and release of Fe to Fe<sup>2+</sup> and the transfer of electrons to the Au layer for the simultaneous onsite generation of H<sub>2</sub>O<sub>2</sub>, thereby providing the main ingredients to trigger the Fenton reaction in water at pH 7. The released Fe<sup>2+</sup> catalyzed the decomposition of the produced H<sub>2</sub>O<sub>2</sub> into highly reactive hydroxyl radicals without the need for external additives or energy input at neutral pH. The onsite H<sub>2</sub>O<sub>2</sub> production was detected by employing a highly sensitive enzymatic reaction, showing a 36-fold higher H<sub>2</sub>O<sub>2</sub> concentration in the galvanic Fe/Au nanoreactor compared to Fe nanoreactors. The high reactivity was demonstrated by the efficient degradation of the organic pollutants Methylene Blue and Tetracycline with a minimal dosage of catalysts. The Fe/Au nanoreactors showed remarkably higher kinetic constant (5-fold), as well as higher degradation and mineralization efficiencies compared to the Fe counterpart. To our knowledge, the galvanic Fe/Au reactors exhibited unprecedented Fenton reactions in Fe-based systems at pH 7 without the need for externally added H<sub>2</sub>O<sub>2</sub>, showing one of the highest normalized kinetic constants. Combined with their photothermal and ferromagnetic properties,

These galvanic nanoreactors could have appealing applications in ROS-based local therapies.

In the second part of the thesis, photocatalytically active 2D MoS<sub>2</sub>/Cu nanoreactors on mesoporous silica particles were developed by combining hydrothermal synthesis and physical vapor deposition. The obtained MoS<sub>2</sub> consists of two semiconducting phases, the trigonal prismatic 2H and distorted octahedral 1T' phase. In the semiconducting 2H phase, the d orbital splits into three bands and is separated by an energy gap. Therefore, the 2H phase shows a lower charge transfer capability with a band gap of 1.9 eV. However, in the 1T' phase, the d orbital is partially filled and possesses a very small bandgap which facilitates higher charge transfer capability. In turn, the 1T' phase exhibited a higher density of defects, which constitute active sites for interfacial redox processes. On the other hand, the deposition of a thin layer of Cu, which quickly oxidizes to Cu<sub>2</sub>O, allowed the generation of a heterojunction with MoS<sub>2</sub>, facilitating a larger separation of the photogenerated charge carriers, as well as contributing to a greater absorption of light, which is already very good in MoS<sub>2</sub>. All these attributes in MoS<sub>2</sub>/Cu nanoreactors enable efficient photo-catalytic actuation with white and even near-infrared light. The photocatalytic activity was proven by the degradation of Tetracycline (antibiotic) and Anatoxin-A (biotoxin), as model organic pollutants. The photocatalytic nanoreactors possessed excellent photocatalytic activity under white light at pH 6 and pH 8. Notably, the catalytic performance of the nanoreactors was tested while immobilized on a silicon substrate without causing any secondary pollution, and with high robustness, showing minimal degradation after 10 catalytic cycles. Moreover, the nanoreactors illuminated by near-infrared light in the first biological window (660 nm) could efficiently kill cancer cells in vitro despite the large separation from the nanoreactors to the cells (100 μm). These results, combined with the low cytotoxicity, demonstrate the high potential of the supported MoS<sub>2</sub>/Cu nanoreactors for environmental or health applications.

The last part gathers the preliminary results of Ni-rich Ni/Pt thermocatalytic nanoreactors for the conversion of Levulinic acid into  $\gamma$ -Valerolactone via catalytic transfer hydrogenation using formic acid as a hydrogen donor. These reactors were fabricated on self-assembled large porous silica nanoparticles, by electron beam evaporation and thermal treatment at 500 °C under a hydrogen and argon atmosphere to increase the catalytic performance. This thermal treatment enabled the Ni/Pt alloying and an optimum distribution of Pt in the Ni

layer to improve the catalytic activity. The photothermal efficiency properties of the supported Ni/Pt nanoreactors make them promising candidates for photo-thermo-catalytic applications.

In summary, this thesis has shown the versatility of the catalytic, or photocatalytic-supported multicomponent nanomaterials, which can open the path to promising applications in areas including environmental remediation, ROS-based biomedical treatments or energy conversion with the added capability to further exploit their magnetoplasmonic properties.

## IV. Table of Contents

PREFACE .....	5
I. Acknowledgements .....	5
II. Resumen .....	7
III. Abstract .....	10
IV. Table of Contents .....	13
V. Motivation.....	16
VI. Aims and Objectives.....	17
VII. Outline.....	18
VIII. References .....	19
IX. List of Abbreviations .....	20
1. INTRODUCTION.....	21
1.1 The Impact of Nanotechnology and Physicochemical Properties.....	22
1.1.1 Surface area, surface energy, and chemical reactivity .....	22
1.1.2 Optoelectronic properties .....	25
1.1.3 Magnetic properties of nanoparticles.....	30
1.2 Multifunctional Nanomaterials .....	35
1.2.1 Mesoporous silica particles as catalyst template and support .....	35
1.2.2 The synergy of noble metal and magnetic nanostructures: catalysis and chemical reactivity.....	36
1.2.3 Heterostructured nanocatalysts as galvanic cells.....	39
1.2.4 Heterostructured nanocatalysts and their synergy by thermal effects .....	40
1.3 2D transition metal dichalcogenides .....	42
1.3.1 TMD structure.....	42
1.3.2 Synthesis of TMD .....	44
1.3.3 Optoelectronic properties .....	45
1.3.4 Chemical properties .....	48
1.4 References.....	49
2. Chemical and photocatalysis for water remediation .....	61
2.1 The global picture of chemical pollution.....	62
2.1.1 Advanced oxidation processes .....	63
2.2 Non-photochemical advanced oxidation processes .....	65
2.2.1 Fenton reaction .....	66
2.2.2 Zero-valent iron and zero-valent metals.....	68
2.3 Nanophotocatalytic advanced oxidation processes.....	72

---

2.3.1	TMDs as nanophotocatalysts .....	74
2.4	Catalytic Transfer Hydrogenation .....	75
2.5	Catalysts for biomedical applications.....	77
2.6	References.....	81
3.	Synthesis of mesoporous and large porous silica nanoparticles.....	91
3.1	Introduction .....	92
3.2	Results and discussion .....	95
3.2.1	Fabrication of the mesoporous silica nanoparticles (MSN).....	95
3.2.2	Large pore silica nanoparticles (LPSN).....	98
3.2.3	Post-processing of the porous silica nanoparticles.....	102
3.2.4	X-Ray diffraction and colloidal analysis.....	103
3.2.5	Optical properties of silica particles.....	104
3.3	Conclusions.....	105
3.4	Materials and Methods.....	105
3.5	References.....	107
4.	Fe/Au galvanic nanoreactors triggering Fenton reaction without additives in water at neutral pH.....	111
4.1	Introduction .....	112
4.2	Results .....	114
4.2.1	Fabrication of the galvanic nanoreactors .....	114
4.2.2	Galvanic reaction pathway.....	115
4.2.3	Catalytic activity.....	117
4.3	Discussion .....	120
4.4	Conclusions.....	125
4.5	Materials and methods.....	126
4.5.1	Synthesis of large pore silica nanoparticles.....	126
4.5.2	Fabrication of Fe/Au and Fe nanoreactors.....	126
4.5.3	Characterization of the nanoreactors.....	127
4.5.4	Detection of the produced H <sub>2</sub> O <sub>2</sub> .....	127
4.5.5	Catalytic activity tests .....	127
4.5.6	Scavenger experiments.....	128
4.6	References.....	128
5.	2D MoS <sub>2</sub> /Cu photocatalytic nanoreactors on 3D mesoporous silica support for environmental remediation and biomedical applications.....	135

---

5.1	Introduction .....	136
5.2	Results and discussions .....	137
5.2.1	Fabrication .....	137
5.2.2	Structural characterization of 2D MoS <sub>2</sub> /Cu nanoreactors on mesoporous SiO <sub>2</sub> supports .....	138
5.2.3	Photocatalytic degradation of organic pollutants.....	144
5.3	Conclusions.....	151
5.4	Materials and methods.....	151
5.4.1	Studies on the degradation of pollutants .....	151
5.4.2	Studies of cancer cell apoptosis .....	152
5.4.3	Studies of XPS.....	152
5.5	References.....	152
6.	Ni/Pt nanoreactors on porous silica nanostructures as thermocatalysts .....	158
6.1	Introduction .....	159
6.2	Materials and methods.....	160
6.2.1	The fabrication of Ni/Pt alloy nanoreactors .....	160
6.2.2	The experimental conditions.....	161
6.3	Results .....	162
6.4	Discussion .....	163
6.5	Conclusion.....	165
6.6	References.....	165
7.	Conclusion.....	170
7.1	Future perspectives.....	172
	Appendix A: Supporting Information (Chapter 4) .....	173
	Appendix B: Magnetic properties .....	175



## V. Motivation

Nanostructured multicomponent materials can exhibit unique features such as high surface area, high density of active sites, flexibility, and tunable magnetic and optoelectronic properties due to the combination of different materials with distinctive physical and chemical properties. These unique characteristics make them remarkable candidates for various applications in environmental remediation and biomedical applications. The catalytically active multicomponent materials could be obtained by combining several different metals and semiconductors. This combination can yield synergistic reactivity, i.e., the catalytic performance exceeds their single counterpart. In addition, the efficiency of the multicomponent materials could be further increased by nanostructured supports. The support material may not contribute to the reaction process, but it can increase the reactivity by giving controlled access to the reactants near the supported catalyst<sup>1</sup>. Moreover, the support can help to improve the stability and activity of the multicomponent materials thanks to their high surface area. This is very important when expensive metals, such as gold, silver, platinum, ruthenium, palladium, etc., are used as catalysts<sup>2</sup>. The supports can also give the catalysts their geometrical shape, texture, mechanical resistance, and even certain activity, particularly for bifunctional catalysts<sup>3</sup>. Therefore, the physicochemical properties of the surfaces affect the performance of the supported catalysts. Keeping these requirements in mind, various oxides and carbon compounds have been used as support catalytic materials. Among all of them, meso or nanoporous silica ( $\text{SiO}_2$ ) acts as excellent catalyst support due to its outstanding chemical and physical properties, where the shape, size and density of pores have an important effect on the activity and stability of supported catalysts. This has been shown in metal nanoparticles supported on porous silica-based supports, which exhibited higher catalytic activity arising from the higher accessibility of the active sites. The chemical inertness and high stability of the porous silica templates make these materials ideal catalyst supports. Therefore, in this thesis, the main attention has been focused on the development of multimaterial catalytic and photocatalytic nanoreactors on nanostructured porous silica supports with the aim of achieving novel and enhanced reactivities for biomedical, wastewater treatment and biomass conversion applications.

## **VI. Aims and Objectives.**

Multifunctional nanomaterials are receiving considerable attention due to their exceptional properties and advantages over traditional materials. Their appealing physical and chemical behavior emerges from the synergistic properties of the different materials and nanoscale sizes. The main aim of this thesis has been the development of catalytically or photo-catalytically active multifunctional materials on mesoporous silica supports. In particular, this Thesis, have been focused on three different catalytic systems on nanoporous silica supports:

1. Novel synergistic Fe/Au nanoreactors driven by their galvanic properties and high surface area drastically enhance their reactivity to generate Fenton reactions at pH7 without external additives, thus having potential for ROS-based therapies.
2. Innovative multifunctional 2D MoS<sub>2</sub>/Cu photocatalysts, on 3D porous silica nanostructures, which can be activated with visible and near-infrared light, with potential application in environmental remediation and cancer therapy.
3. Ni/Pt thermocatalyst alloy with enhanced activity for biomass conversion via hydrothermal treatment.

## VII. Outline

The thesis is divided into seven chapters which are summarized below.

1. The first chapter provides a broad overview of the physical and chemical properties of nanomaterials including magnetic, optoelectronic and surface properties. It also emphasizes the emerging superior catalytic performance of different nanomaterial combinations.
2. The second chapter discusses the applications of multi-component materials in various fields, such as environmental remediation, biomedical therapies, or sustainable catalytic processes. It covers various advanced oxidation processes including zero-valent iron, heterogeneous (photo)catalysts, etc. In addition, it presents information about catalytic transfer hydrogenation and chemodynamic cancer therapies.
3. In the third chapter the synthesis of tunable mesoporous silica particles is explored by changing the reaction conditions. It also describes the post-processing steps of the silica particles to obtain the desirable catalyst supports.
4. In the fourth chapter Fe/Au galvanic nanoreactors on the large pore silica nanoparticles are developed via the combination of colloidal self-assembly and electron beam deposition. The Au layer favors the charge transfer and the onsite production of hydrogen peroxide, while the zero valent Fe layer continuously degrades the hydrogen peroxide and generates the active species, which are demonstrated by the efficient degradation of organic pollutants.
5. The fifth chapter exhibits the fabrication of 2D MoS<sub>2</sub>-Cu nanoreactors on 3D mesoporous silica support with applications in environmental remediation and cancer therapy. The MoS<sub>2</sub>-Cu nanoreactors exhibit excellent photocatalytic activity under white light and degrade Tetracycline and Anatoxin-A due to their hybrid crystallographic structure and consequent electronic properties. Furthermore, in vitro assay with cancer cells demonstrates excellent antitumor activity.
6. The sixth chapter includes the preliminary results related to the conversion of levulinic acid to  $\gamma$ -valerolactone using Ni/Pt thermocatalytic treatment nanoreactors. The nanoreactor fabrication process involves chemical vapor deposition and thermal treatment to obtain the Ni/Pt alloy on the nanoporous silica support.

7. Finally, the seventh chapter presents the summary of the conclusions obtained from this thesis and the future perspectives.
8. Appendix A contains supplementary information about the Fe/Au nanoreactors. Appendix B contains additional information about magnetic properties of nanomaterials.

## VIII. References

1. Van Deelen TW, Hernández Mejía C, de Jong KP. Control of metal-support interactions in heterogeneous catalysts to enhance activity and selectivity. *Nat Catal.* 2019;2(11):955-970. doi:10.1038/s41929-019-0364-x
2. Gutiérrez LF, Hamoudi S, Belkacemi K. *Synthesis of Gold Catalysts Supported on Mesoporous Silica Materials: Recent Developments*. Vol 1.; 2011. doi:10.3390/catal1010097
3. Khodakov AY, Bechara R, Griboval-Constant A. Fischer-Tropsch synthesis over silica supported cobalt catalysts: Mesoporous structure versus cobalt surface density. *Appl Catal A Gen.* 2003;254(2):273-288. doi:10.1016/S0926-860X(03)00489-7

## IX. List of Abbreviations

<b>NP</b>	<b>Nanoparticle</b>
<b>SPR</b>	Surface Plasmon Resonances
<b>TMD</b>	Two Dimensional Materials
<b>MSN</b>	Mesoporous Silica nanoparticles
<b>LPSN</b>	Large Porous Silica Nanoparticles
<b>CTAB</b>	Cetyltrimethylammonium Bromide
<b>TEOS</b>	Tetraethyl orthosilicate
<b>TMB</b>	1-3-5 trimethylbenzene
<b>CVD</b>	Chemical Vapor Deposition
<b>AOPs</b>	Advanced Oxidation Processes
<b>ROS</b>	Reactive Oxygen Species
<b>ZVI</b>	Zero-Valent Iron
<b>CTH</b>	Catalytic Transfer Hydrogenation
<b>CTD</b>	Chemodynamic Therapy
<b>DMF</b>	Dimethylformamide
<b>EtOH</b>	Ethanol
<b>TC</b>	Tetracycline
<b>MB</b>	Methylene Blue
<b>NIR</b>	Near-infrared
<b>PLL</b>	Poly-L-lysine
<b>MCM-41</b>	Matter No 41
<b>SBA</b>	University of California at Santa Barbara
<b>DMHA</b>	N, N-dimethylhexadecylamine
<b>TA</b>	Tannic Acid
<b>RIE</b>	Reactive Ion Etching
<b>SEM</b>	Scanning Electron Microscopy
<b>TEM</b>	Transmission Electron Microscopy
<b>XRD</b>	X-Ray Diffraction
<b>E-beam</b>	Electron beam
<b>PL</b>	Photoluminescence
<b>DLS</b>	Dynamic Light Scattering
<b>XPS</b>	X-ray Photoelectron Spectroscopy

# 1. INTRODUCTION

This thesis deals with the synergistic combination of mesoporous silica nanostructures and different electrochemically, photocatalytically or catalytically active nanomaterials (i.e., metals and semiconductors) with promising applications in environmental remediation, biomedicine and energy. These hybrid nanomaterials take advantage of the amazing physical and chemical properties that emerge with miniaturization, which in turn make these nanomaterials powerful multifunctional tools. Therefore, the first part of this introductory section will address fundamental aspects of the changes in physical-chemical properties with size, describing benefits that can be exploited for the applications. Although some of these characteristics have not been fully exploited in this thesis, they are still listed since they contribute to giving future perspectives to the present work. Then an introduction to the nanomaterials used in this thesis will be provided, emphasizing the synergy in properties that can be achieved when they are combined.

Then and under the perspective of highly relevant global problems such as water remediation, new cancer treatment therapies, or green energy use, the state of the art of nanomaterials and (photo)catalytic processes will be covered, stressing mainly the generation of advanced oxidative pathways or the generation of value-added chemicals. This framework will serve as the basis to motivate and establish this thesis's objectives, which will focus on the design of multifunctional nanoreactors and novel strategies that could contribute to solving problems of great social interest.

## 1.1 The Impact of Nanotechnology and Physicochemical Properties.

Nanotechnology is based on nanosized materials. A nanoparticle (NP) is a fundamental component of nanotechnology. NPs with extraordinary properties can be composed of metals, metal/nonmetal oxides, metal (di)chalcogenide, polymers, metal-organic materials, or carbon-based materials (carbon dots, fullerene, carbon nanotubes, graphene). Unlike bulk materials, NPs represent highly tuneable systems for adjusting chemical and physical properties and thus boosting processes in a fast, controllable, and efficient way for a wide range of applications, from information technology, medicine, transportation, energy, and food safety to environmental remediation, among many others<sup>1</sup>. On one hand, the high surface-volume ratio of these nanosized materials makes the surface effects, especially surface energy, play a leading role in enhancing reactivity, adsorption, and catalytic properties.

On the other hand, miniaturization with the consequent quantum effects enables new optical, electronic, and magnetic properties that can unveil new applications or improve efficiency in the already existing ones. For example, metallic NPs can be used as ultrasensitive optical sensors of (bio)chemical analytes through the generation of resonance surface plasmon resulting from the interaction of electromagnetic radiation with the electron density of nanoparticles<sup>2</sup>.

Furthermore, semiconductor nanomaterials can be used as electronic or photoluminescent sensors of high intensity and stability, with emission wavelengths or conductivities depending on the size of the particle due to changes in the band gap with confinement<sup>3</sup>. Magnetic nanomaterials can also increase their magnetization and be more reversible to applying magnetic fields with confinement, which can affect contaminant removal processes<sup>4</sup>.

### 1.1.1 Surface area, surface energy, and chemical reactivity

Nanoscale materials have a far larger surface area-to-volume ratio than bulk materials. The high surface/volume ratio under miniaturization can be rationalized by subdividing/breaking down a bulk parent material into nanoclusters while keeping the volume of the parent material constant (Figure 1-1a). An amazing increase in the collective surface area of the nanomaterials (that is, the additive contribution in surface area of all the clusters) is achieved, which explains the high specific surface area (total surface area of a material per unit of mass or volume) of the nanomaterials.

The increase of surface-to-volume ratio can be also easily illustrated with one particle under shrinking its size. In the case of spheroidal nanoparticles, the ratio between the particle surface ( $A_{\text{sphere}} = 4 \pi r^2$ ) and the volume ( $V_{\text{sphere}} = \frac{4}{3} \pi r^3$ ) equals to  $3/r_{\text{sphere}}$ , indicating how the surface atom proportion increases with respect to the one at the bulk as the particle size decreases (Figure 1-1b). As a consequence, all the surface-dependent processes become more important.

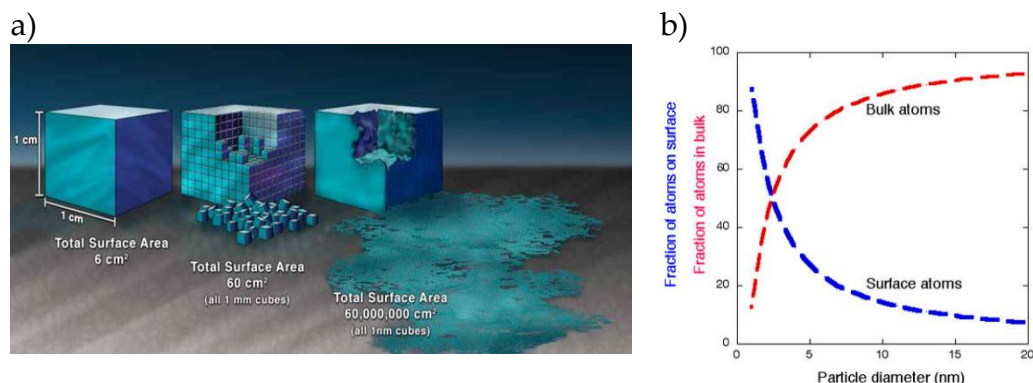


**Figure 1-1.** Illustrations portraying the increase of surface-volume ratio under material shrinking a) Increase of the collective surface area by subdividing a cube in small nanocubes and b) the increase of surface atom fraction with respect to the volume one under miniaturization<sup>5</sup>.

The significant difference between the surface and interior atoms gives nanomaterials outstanding physical and chemical properties<sup>6</sup>. For instance, the surface area plays a significant role in chemical kinetics. Increasing the surface area, makes the nanomaterials to be more exposed to the surrounding environment, which can greatly speed up chemical reactions of these materials<sup>7</sup>. The surface area of the NPs can be further increased by creating rough or porous surfaces<sup>8</sup>. That can boost the surface reactivity, increase dissolution rates, and alter biocompatibility and toxicity, favouring their use in a wide range of applications, including energy storage devices, catalysts support, and sensor arrays<sup>9</sup>.

A key quantity related to chemical reactivity is the surface energy that comes up as a consequence of the break of interactions of the surface atoms as compared to the bulk ones<sup>10</sup>. The latter ones are highly coordinated among them and consequently are more stable. Atoms at the surface are under-coordinated, and because breaking bonds costs energy, surface atoms always have higher energy than atoms in the bulk. Thus, surface energy can be defined as the excess energy at the surface of a material compared to the bulk<sup>11</sup>. This parameter is consequently proportional to the density of the so-called surface dangling bonds present in the under-coordinated atoms (also called unsatisfied or unsaturated bonds). These surface bonds result from having unfilled outer orbital shells of the atoms and often bear a partial electric charge. This energy is called surface energy and can be expressed as<sup>12</sup>:



$$\gamma = \frac{1}{2} N_b \epsilon \rho_a \quad 1.1$$

Where  $\rho_a$  surface atomic density,  $N_b$  is a number of unsatisfied bonds and  $\epsilon$  is bond strength. A higher density of dangling bonds is found at corrugation sites (corners, kinks, edges, vacancy/void defects) (Figure 1-2a). These unsatisfied bonds not only determine the surface energy of the materials, but also the local electron density, chemical reactivity, adsorption and catalytic activity<sup>13</sup>. Material size reduction enhances the density of corrugation sites which are prone to interact with the outside environment to reduce their energy, thus intensifying their instability and chemical reactivity. Figure 1-2b, c illustrate typical processes that can be enhanced with miniaturization such as different adsorption processes or different chemical reactions<sup>10</sup>. The figure also indicates active sites for these processes (corners, kinks, edges, etc.) whose density is increased with the size decrease, shape, or crystal faceting. As a consequence of these surface effects, for example bulk noble metals such as Au and Pt which are chemically inert and resistant to oxidation, become chemically active and more prone to oxidation in the form of nanoparticles<sup>14</sup>. Additionally, decreasing the particle size changes the thermodynamic properties of nanoparticles. Melting and evaporation temperatures are drastically reduced with NP size decrease<sup>15,16</sup>. These changes in the thermodynamic properties are related to the surface energy.

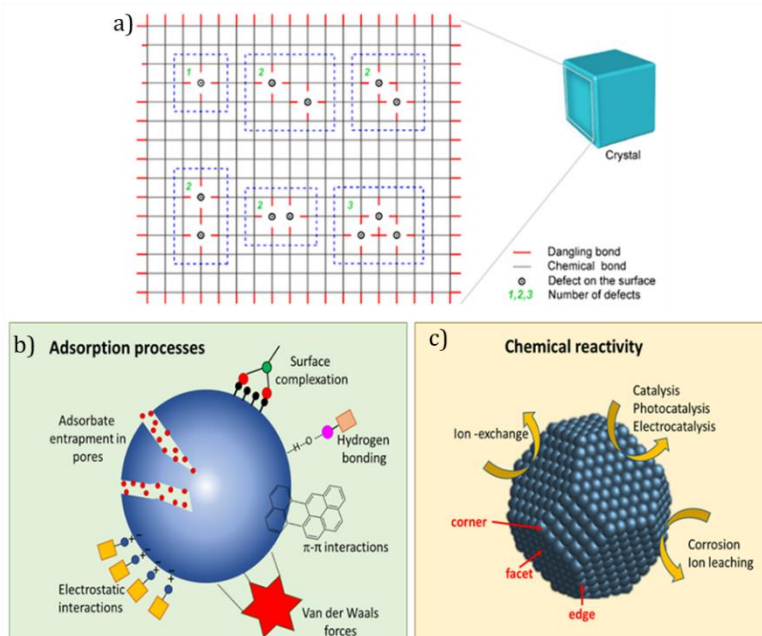


**Figure 1-2.** Schematic representation of dangling bonds on a NPs surface<sup>10</sup>. b)-c) Different processes that can be enhanced with size decrease: adsorption and chemical reactivity. Figure c also indicates sites of higher activity or reactivity at which a higher density of dangling bonds is found.

### 1.1.2 Optoelectronic properties

The interaction of light with structured materials can vary considerably depending on the size of the nanostructure. Different responses can take place when NPs are irradiated with light<sup>17</sup>: i) light absorption, ii) light scattering, iii) reemission of the absorbed light (fluorescence), iv) enhancement of the local electromagnetic field of the incoming light, thereby enhancing spectroscopic signals from molecules at the NP surface v) charge generation and transfer, vi) resonance energy transfer to an adjacent material, and vii) heating. The optical properties of NPs can be manipulated by changing the size, shape, surface charge, and surface area for different applications<sup>18</sup>. The outstanding optical properties of NPs have gained diversified applications in the fields of sensors, lasers, photochemistry, photocatalysts and biomedicine.

In general, quantum effects affecting material band structures and the emergence of surface plasmon resonances (SPR) are the most important factors for the determining optical and electronic properties of NPs<sup>19</sup>. SPR is an optical phenomenon induced when light hits the metal films or NPs<sup>20,21</sup>.

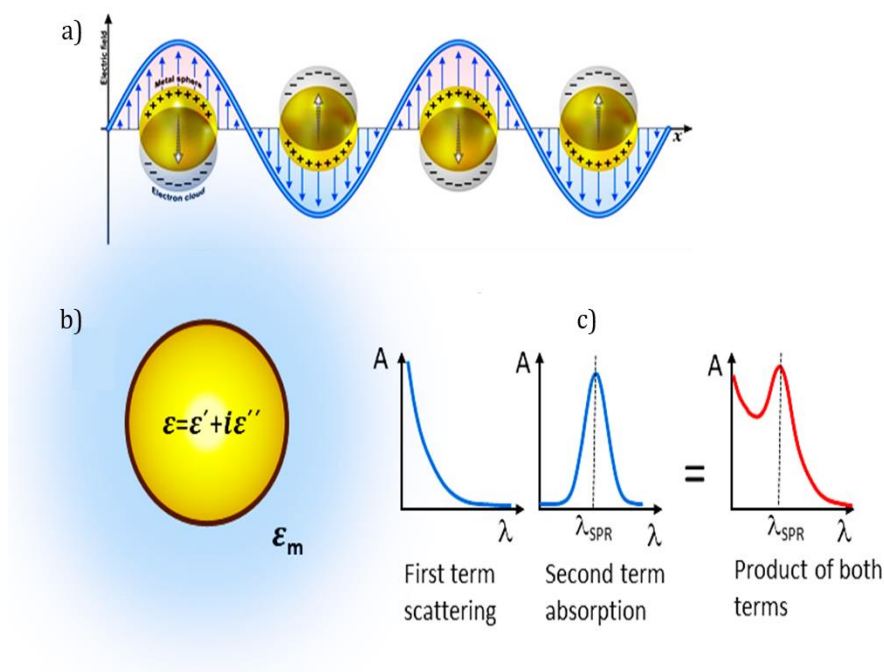


**Figure 1-3.** a) Schematic illustration of SPR of gold NPs<sup>22</sup>, b) Schematics showing the different dielectric constants involved in the Mie equation<sup>12</sup>, c) Schemes of the absorbance profile according to the Mie equation, the scattering term represented by the first term, the resonance plasmon mode absorption represented by the second term. The product of both terms is the spectrum observed experimentally.

In brief, when photons interact with the surface electrons, the oscillating electromagnetic field of the light induces the coherent and collective oscillation of conduction band free electrons<sup>23</sup>. During this process the particles build up

regions of negative charge, leaving a positive charge on the opposite side and thus creating a dipole oscillating at a certain frequency (Figure 1-3a). The collective oscillation of the electrons in the nanoparticles is called plasmon. The natural frequency at which the electrons can oscillate in a certain particle is called plasmon resonance frequency. When the frequency of the incoming electromagnetic wave matches the natural resonance frequency of the electrons a huge enhancement of the electromagnetic field is produced at the metal nanoparticles, and the nanoparticles strongly absorb/scatter light. Such extremely effective light absorption/scattering at the resonance frequency explains the color of the metal nanoparticles, which makes them easily detectable even at extremely low concentrations. The plasmon resonance frequency depends on the size of the particles which makes metallic colloidal dispersions adopt different tone colors depending on the size. Apart from the nanoparticle's nature and size, the resonance frequency also depends on particle shape and the surrounding environment. For instance, nanoparticles in oblate or nanorods shapes will have two different plasmon frequencies depending on the axis the electrons are oscillating along: the longitudinal oscillation mode and the orthogonal oscillation mode.

Moreover, surface plasmon absorption can be channelled into heat production, which is especially useful when natural resonance frequencies of the plasmons hit the near-infrared wavelength region.

Mie's theory describes the relationship between the physical parameters that determine the plasmon resonance frequency of spherical particle<sup>24</sup>. According to Mie's theory, absorbance  $A$  is expressed as the product of two terms:

$$A = \frac{\varepsilon^{3/2} R^3}{\lambda} \frac{\varepsilon''}{2(\varepsilon' + 2\varepsilon_m)^2 + \varepsilon''^2} \quad 1.2$$

The first term represents the scattering which depends on the dielectric constant of the medium ( $\varepsilon_m$ ), on the particle radius and on the inverse wavelength of the incoming radiation. The second term represents the absorption due to the plasmon resonance which depends on the real ( $\varepsilon'$ ) and imaginary part ( $\varepsilon''$ ) of the dielectric constant of the metal particles and on the dielectric constant of the medium ( $\varepsilon_m$ ). The real part of the dielectric constant is related to the refractive index and with the ability of the material to slow down light. The imaginary part of the dielectric constant is related to the damping losses, which come from the absorption of the light traveling through the material. The denominator of the second term would approach zero if  $\varepsilon'$  approaches the value of  $-2\varepsilon_m$ . At that condition, as the denominator approaches zero, the second term would increase dramatically, generating the condition of resonance which is represented by a strong absorption peak (Figure 1-3b c).

SPR favours the application of NP in medical diagnostics<sup>25</sup> and therapeutics<sup>26</sup>, chemical<sup>27</sup> and biochemical sensors<sup>28</sup>, substrates for enhanced spectroscopy<sup>29</sup>, for promoting photocatalysis processes, etc. Additionally, the electromagnetic fields propagating in the form of surface plasmons are not diffraction-limited, which allows for designing small-scale, fast optical devices<sup>30</sup>. More insights into these SPR-mediated applications will be explained in more detail in the coming sections.

The other factor that affects the optical/electronic properties of NPs is the quantum confinement effect (QC). Such phenomenon can be easily illustrated with semiconducting materials. In bulk or large-size semiconducting materials, the electronic states bunch up into a continuum valence band and a conduction band separated by a band-gap<sup>31</sup>.

Figure 1-4 shows the build-up of the bands starting from single atoms with their corresponding atomic orbitals. As the number of interacting atoms is increased to form molecules or larger molecular aggregates, their contributing orbitals are split into bonding and anti-bonding molecular orbitals. As the number of atoms in the semiconducting cluster increases, the discrete molecular orbitals evolve into continuous energy bands as observed in bulk semiconducting materials. The confinement effect is conceived in the reverse way, going from bulk material to particles or clusters of decreasing size, and is featured by an increase of the bandgap and the discretization of energy levels at the band edges<sup>32</sup>. Nanoparticles under the confinement effects are called quantum dots and exhibit an intermediate state between molecules and bulk materials.

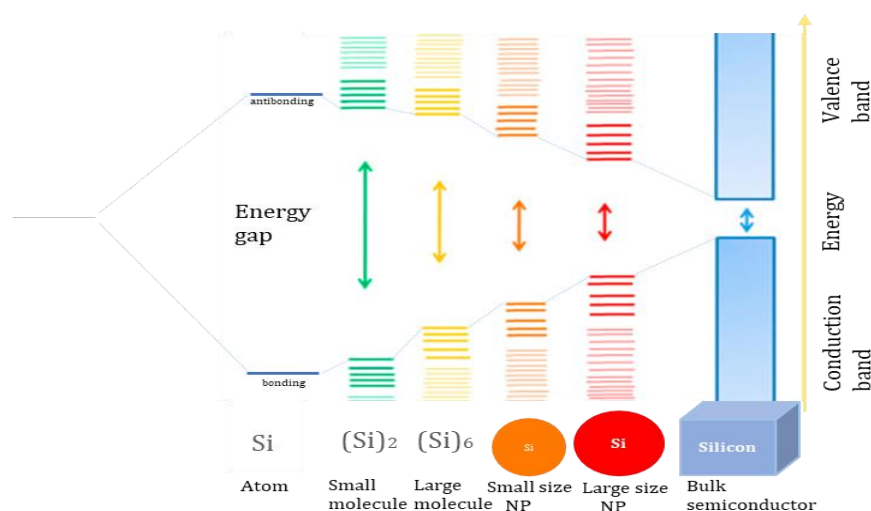


**Figure 1-4.** Confinement effect from a macroscopic semiconductor material to isolated atoms of the material. The band gap energy and the energy discretization increase as the material is miniaturized.

A more physical way to describe the quantum confinement effect is by looking at the electron-hole pair that is generated when exciting electrons from the valence band to the conduction band. Due to the Coulomb interactions, the excited electron is still bound to the hole in the valence band forming a pair called exciton<sup>33</sup>. The exciton occupies a certain space that is described by the exciton Bohr radius ( $a_0$ ),

$$a_0 = \frac{h^2 \epsilon}{e^2} + \left( \frac{1}{m_e^*} + \frac{1}{m_h^*} \right) \quad 1.3$$

Which depends on the effective masses of the electron and the hole, which, in turn, depends on the nature of the material. When the semiconductor is significantly larger than the  $a_0$ , the exciton can freely move through the semiconductor. When the size of the semiconductor is about the same as that of  $a_0$ , the exciton will no longer be able to freely move through the nanomaterial and therefore will be spatially confined. When the nanoparticle size decreases at values smaller than  $a_0$ , the exciton will not only become confined but will also increase in energy, similar to the typical case of quantum physics of a particle in a box, increasing its energy as the 'box' decreases in size<sup>34</sup>. The size-dependent bandgap of a confined semiconducting nanoparticle is then described by the Brus Equation,

$$E_0 = E_{gap} \frac{h^2}{8R^2} \left( \frac{1}{m_e^*} + \frac{1}{m_h^*} \right) \quad 1.4$$

where  $E_0$  is the energy gap of a semiconducting nanoparticle,  $E_{gap}$  is the bulk band gap, and  $R$  is the radius of the particle.

Therefore, the confinement effect has consequences on the electronic and optical properties. For electric conductivity, electrons need to be able to move around in a material. As mentioned before, the excitons can move quite freely in bulk semiconductors but as soon as the material is confined the exciton mobility is decreased, the band-gap energy increases and the energy states start to be discretized, lowering their density at the band edges. All these factors make these nanomaterials less conductive<sup>35</sup>.

Concerning the optical properties, the excitation of electrons to the conduction band produces radiative relaxation through photoluminescence, being this process size-tunable provided by the band-gap energy changes with particle size. There are many examples of semiconductor nanoparticles under quantum confinement converting UV light absorbance into fluorescence with narrow emission bands in the visible to near-infrared region depending on their size, with smaller nanoparticles emitting more in the blue range and bigger particles more in the red one<sup>36</sup>.

Figure 1-5 shows the blue shift in the fluorescence emission as the semiconductor nanoparticle decreases in size.

Their highly tunable optical properties based on their size have led to a variety of research and commercial applications including bioimaging, solar cells, lasers, light emitting diodes, etc.

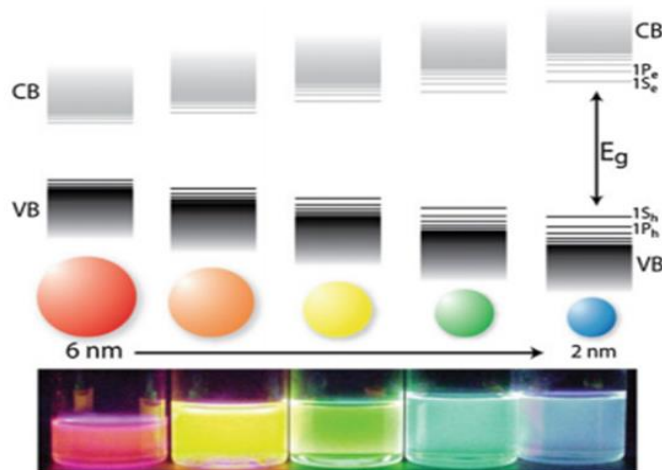


**Figure 1-5.** Effect of decreasing the size of semiconductor nanoparticles on the optical properties<sup>35</sup>. The color change of the nanoparticles is observed as their size decreases together with the increase in the gap and the increase of energy discretization.

Quantum confinement has been also observed in 2D materials, being graphene one of the most studied systems<sup>37</sup>. Graphene which is a semimetal can be transformed into a semiconductor with a finite and size-tunable energy gap by confining the 2D layer into graphene nanoribbons or graphene dots. These nanostructures have shown strong changes in their electrical properties and also in the optical ones featuring size-dependent fluorescence in the visible range. In relation to other 2D materials organized in layers such as the transition metal dichalcogenides, layer-dependent changes in the band gap have been observed. This strongly affects the optoelectronic properties of these materials. For instance, in the case of MoS<sub>2</sub>, an increase in photoluminescence has been observed when decreasing the number of MoS<sub>2</sub> layers which has been attributed to the increase and transformation from indirect to band gap<sup>1</sup> due to confinement effects<sup>38–40</sup>. Thus, for single-layer MoS<sub>2</sub> the direct band gap transition of electrons is favored enhancing the photoluminescence.

<sup>1</sup> Direct bandgap: the electron promoted from valence band to the conduction band will only change its potential (energy) but not the momentum (k vector). In indirect bandgap: the electron promoted from valence band to the conduction band will change its potential (energy) and momentum.

### 1.1.3 Magnetic properties of nanoparticles

Magnetism in materials arises from two types of electron motion in atoms: the precession of the electrons around their axes (spin magnetic moment) and the motion of electrons around the nucleus (orbital magnetic moment)<sup>41</sup>. Strong magnetic effects can be found in materials with d or f orbital shells with unpaired electrons. The magnetic properties of the materials can be classified into five main types depending on their response to applied magnetic fields: diamagnetic, paramagnetic, ferromagnetic, and antiferromagnetic (See Appendix B for more details concerning the distinctive characteristics of these materials).

The magnetic properties not only depend on the material's nature but also on the size, shape, and surface effects (e.g. surface anisotropy in crystal structure/composition, dangling bonds, oxidation, etc.), with the role of surface effects becoming more important as the particle size decreases<sup>42</sup>. Magnetism as a size-dependent property holds huge benefits in many biological and technological applications, including magnetic data storage, medical diagnostics, biosensors, therapeutics, and catalysis<sup>43</sup>. Magnetic nanoparticles have already drawn special attention in biomedicine because of their biocompatibility, low toxicity, and manipulation capabilities<sup>44</sup>.

To better describe the magnetic size-dependent properties of nanomaterials let's focus on ferromagnetic materials as model systems. Examples of ferromagnetic materials are Fe, Ni, or Co. These materials possess unpaired electrons which form special neighbourhoods termed domains as illustrated in Figure 1-6a. The reason for the existence of magnetic domains is energy-related: the higher the number of domains, the lower internal energy of the material (See Appendix B for more details). Each domain contains atoms whose magnetic moments are parallel producing a net magnetic moment of the domain that points in some direction. The magnetic moments of the different domains are randomly oriented with respect to each other giving a zero net magnetic moment of the material in absence of a magnetic field. When the ferromagnetic material is placed in a magnetic field, the magnetic moments of the domains will increasingly align along the direction of the applied magnetic field forming a large net magnetic moment.

To exemplify the impact of size on the magnetic response, it is insightful to compare the complete magnetization curve of bulk ferromagnetic material undergoing miniaturization when applying a magnetic field not only in one direction but also in the opposite one.

Figure 1-6b, shows the different stages of macroscopic bulk ferromagnetic material starting with its demagnetized state (stage 1). At this point, magnetic multi-domains are randomly oriented resulting in a zero net magnetic moment in absence of a magnetic field. Upon an increase of the magnetic field in one direction, the domain whose magnetization is closest to the field direction starts

to grow at the expense of the other domains (Figure 1-6c). The growth occurs by domain-wall motion.

Further increase in magnetization can only occur by rotating the magnetic dipoles from the easy axis of magnetization into the direction of the applied field (Figure 1-6c).<sup>2</sup> Thus, each domain will increasingly align with the applied field up to reaching saturation ( $M_s$ ) (stage 2). Upon a decrease of the applied field to zero the magnetic domains are unable to revert to a completely random orientation. That would lead to a remanent magnetization ( $M_r$ ) (stage 3). To cancel out such remanent magnetization. It is necessary to apply a magnetic field in the opposite direction, named coercive field ( $H_c$ ) (stage 4). By increasing the applied field in the opposite direction, the magnetic domains will increasingly align with the applied field to reach again saturation but in the other sense (stage 5). This process leads to a hysteresis loop in the magnetization behaviour which is greatly affected by sample purity and quality. For example, a sample with many defects or impurities will require a large field to magnetize it but will retain much of its magnetization when the field is removed.

As can be seen, one of the features that characterize the magnetization loop in magnetic materials is coercivity, which is a parameter strongly dependent on size and therefore will be analyzed in more detail. compiles the trend in the changes of magnetic properties as a function of particle miniaturization, emphasizing the changes in the magnetization loop and the coercivity evolution<sup>45</sup>. As the particle size decreases, the coercivity increases to a maximum at a critical particle diameter size and then decreases to zero with increasing miniaturization. Consequently, the magnetization loop has the typical shape shown in Figure 1-7 for large ferromagnetic particles, but as the particle shrinks, the loop becomes squarer as it reaches the critical size corresponding to the maximum coercivity and it finally loses the hysteresis behavior at very small particle sizes.

---

<sup>2</sup> As already described in Appendix B, magnetic materials exhibit magnetocrystalline anisotropy which refers to the crystal's property to be more easily magnetized in some directions in comparison to others.

For a crystal, the axis that is easiest to magnetize is known as the easy axis, and the axis that is most difficult to magnetize is known as the hard axis



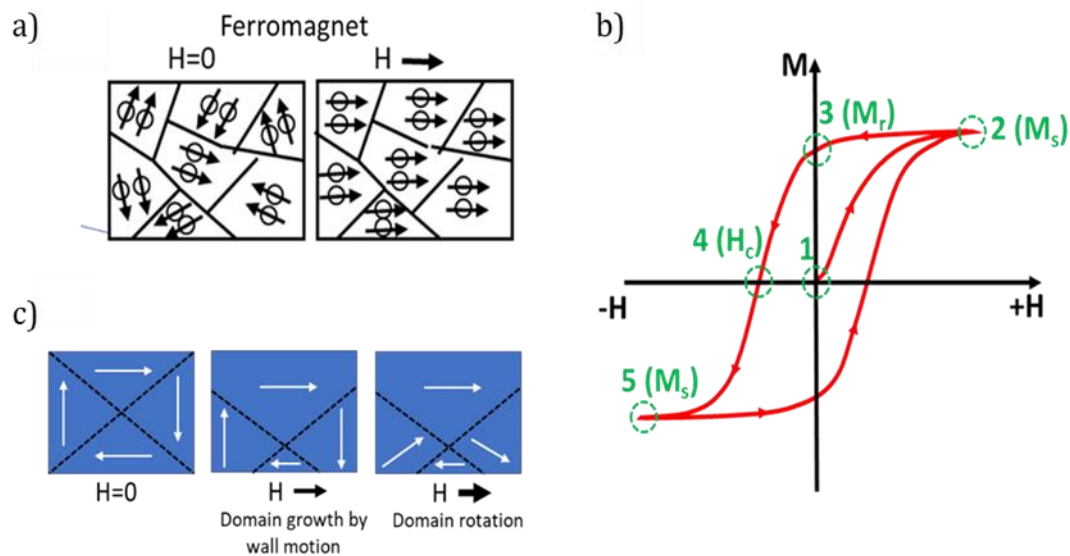


**Figure 1-6.** a) Schematic representation of magnetic dipole alignment for a multidomain ferromagnet in the absence and presence of an applied magnetic field  $H$ . b) Magnetization loop for a ferromagnet starting from the demagnetized state. c) Domain changes under an increasing applied magnetic field: domain growth by wall motion and by domain rotation.

When the size of the magnetic material decreases below such critical size, the nanoparticles start exhibiting single domains. At this point, the cost of energy to create a domain wall is greater than supporting the magnetic potential energy of a single-domain state (magnetostatic energy)<sup>46</sup>. The critical diameter ( $D_c$ ) can be estimated from the equation

$$D_c \approx \frac{36\sqrt{AK}}{\mu_0 M_s^2} \quad 1.5$$

Where  $A$  is the exchange constant,  $K$  is the magnetocrystalline anisotropy that measures the energy per unit volume required to flip magnetization direction,  $\mu_0$  is the vacuum permeability, and  $M_s$  is the saturated magnetization. For most magnetic materials  $D_c$  varies from tens to hundreds of nanometres. Nevertheless, if the effective anisotropy  $K$ , is significantly large, the single domain size can be close to the micrometer range. Thus, the configuration of the magnetization inside a single domain particle strongly depends on magnetic anisotropy. When the particle size is about the critical size, the magnetic dipole of the single domain normally lies along an easy direction in absence of a magnetic field. When applying an external magnetic field in the opposite direction, the particle is unable to respond by domain-wall motion in their dipole alignment, and instead, the magnetic dipole must rotate through the hard direction (not the preferred direction) to the new easy direction. The anisotropy forces which hold the

magnetization in an easy direction are strong, and lead to a strong enhancement in coercivity and hence to a squarer hysteresis loop.

Below  $D_c$ , the coercivity value decreases with decreasing particle size due to a decrease in magnetic anisotropy energy<sup>47</sup>. The simple magnetization reversal energy becomes equal to the energy at room temperature (e.g., typical ferromagnets with critical diameter below 30 nm). The thermal fluctuations at room temperature are strong enough to spontaneously demagnetize previously saturated magnetic nanoparticles, thus exhibiting reversible magnetization behavior with zero coercivity and no hysteresis. These nanoparticles become superparamagnetic: they show magnetism in the presence of an external magnet but revert quickly to a non-magnetic state in the absence of a magnetic field.

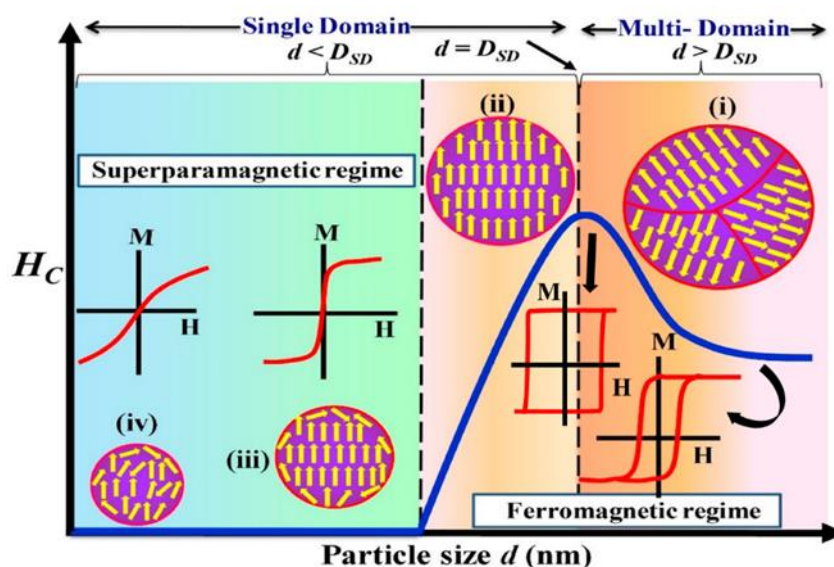


**Figure 1-7.** Variation of coercivity ( $H_c$ ) (blue solid line) and magnetization curves with particle size  $d$ . (i) With a decrease in the size of ferromagnetic particles, the  $H_c$  initially increases and then attains a maximum value at the critical single domain size ( $D_c$ ) due to domain rotation. (ii) Further, in the single domain regime ( $d < D_c$ ), the  $H_c$  decreases as the particle size decreases and (iii) becomes zero at the superparamagnetic regime due to the thermal agitation. (iv) Finally, in ultra-small regimes, due to high-spin disorder of elemental spins, the nanoparticles exhibit a linear relationship between the magnetization and the applied magnetic field. Figure readapted from<sup>47,48</sup>.

Thus, superparamagnetic particles behave like paramagnets but with the particularity of exhibiting high magnetic susceptibility<sup>3</sup> in a certain range of particle sizes (being comparable or even larger than the one of the bulk materials). Only at ultra-small paramagnetic nanoparticles the magnetic

<sup>3</sup> The magnetic susceptibility ( $\chi=M/H$ ) is defined as the ratio of the intensity of magnetization to the intensity(force) of the magnetizing field

susceptibility can reach smaller values than the bulk material. Thus, particle sizes around or above the critical size exhibit strong remanence in absence of a magnetic field upon previous magnetization. One consequence of such magnetic behaviour is the promotion of particle aggregation in absence or after removal of a magnetic field. Although the development of permanent magnets is very useful for many applications, it is a disadvantage for instance in bio-applications. In biomedical environments, magnetic nanomaterials with high magnetic susceptibility, with fast and reversible response to applied magnetic fields and without magnetic memory in absence of an external magnetic field are pursued<sup>49</sup>. This ensures a safe removal from the body as there is no risk of unwanted aggregation of the nanoparticles. Under this context, superparamagnetic nanomaterials exhibiting zero remanence and no hysteresis loop have become promising candidates. Applied magnetic fields have been used to produce different forces and torques on magnetic nanoparticles to induce particle translation, rotation and energy dissipation which are harnessed for theranostics purposes. Therapies using magnetic nanomaterials as drug or gene carriers/release or for cancer cell annihilation by hyperthermia (based on the concept that nanoparticles can heat locally the environment when external alternating magnetic fields are applied) are being actively researched. Disease diagnosis using magnetic nanoparticles in biosensors or for immunoassays or as improved contrast agents for magnetic resonance imaging (MRI) are also areas of intense activity<sup>50</sup>. Moreover, that is a topic not only very appealing for bioapplications but also for environmental remediation tasks for magnetic trapping/transport and thermal degradation of contaminants.

Although superparamagnetic nanoparticles exhibit very interesting attributes, the production of these nanoparticles with high magnetization susceptibility and with high magnetic actuation capabilities at moderate magnetic fields is difficult to achieve<sup>51-53</sup>.

More recently, another kind of nanostructures (which can exhibit larger sizes than their superparamagnetic counterparts) are offering new opportunities to overcome the limitations of superparamagnetic nanoparticles<sup>54</sup>. Examples of nanostructures with vortex configurations are 2D confined structures such as discs or nanodomes or nanorings. In a vortex configuration, the magnetic moments are curled in the plane of the structure, organized in closed circles to minimize the magnetostatic energy<sup>55</sup>. Only at the center, at the core of the vortex, the magnetic moments get out of the plane and point perpendicularly (See Annex 2 Figure 3A). These structures have shown high saturation magnetization and magnetic remanence and coercivity close to zero, and hence avoiding nanoparticle agglomeration in absence of a magnetic field (Annex 2). Such attributes have been also exploited for efficient magnetic guidance or magnetic stirring/rotation<sup>56,57</sup>.

## 1.2 Multifunctional Nanomaterials

This thesis pursues the combination of noble metal, magnetic, semiconductor, and dielectric nanomaterials with different physical and chemical properties to promote property synergies for multifunctional purposes. Accordingly, the state of the art and potentialities of these nanomaterials alone or combined will be briefly summarized.

### 1.2.1 Mesoporous silica particles as catalyst template and support

The discovery of mesoporous silica particles has brought enormous economic and environmental benefits to various industries. Mesoporous silica has been extensively investigated since features unique properties, such as low toxicity, good biocompatibility, high surface area (as high as 1000 m<sup>2</sup>/g), high adsorption capacity, chemical, thermal and mechanical stability, ease of surface modification with various organic functional groups, and cost-effectiveness. Furthermore, silica particles with different morphologies, such as hollow spheres, hexagonal, cubic, and worm-like NPs, with tuneable pore size, shape and distribution and dimensions from nm to cm can be synthesized by controlling the reaction conditions<sup>58</sup>. All these attributes make silica particles one of the essential NPs in biomedical, environmental, catalysis and energy. Because of their unique properties, such as low toxicity with good biocompatibility, ease of surface modification, stability, and cost-effectiveness, silica NPs have been extensively investigated and are used in a wide range of applications such as environmental, biomedical, energy, and catalysis and energy industries<sup>59,60</sup>.

Catalysts are essential to current chemical, pharmaceutical, and petroleum industries<sup>61</sup>. Recently, scientists have made considerable efforts to develop highly reactive and efficient catalysts. Nevertheless, achieving highly stable, cost-competitive catalysts remain a challenge. The most active catalysts contain small NPs. However, their high activity could be lost over time because of their aggregation. Therefore, some templates are needed to improve the performance and stability of the catalysts. Due to their intriguing structural or textural properties, Mesoporous Silica Nanoparticles (MSN) are an appealing material for use as high surface area catalyst supports in various heterogeneous catalytic reactions.

Colloidal mesoporous silica particles with embedded nanocatalysts are highly beneficial in catalytic applications because they ensure better mass transfer properties and uniform distribution of metal or metal oxide nanocatalysts in solution. Moreover, MSN boost the catalytic activity of the supported material because of the easy accessibility to the active sites. The shape and pore size contribute to the activity and stability of the catalysts. All these remarkable physical and chemical properties make MSN an ideal catalyst support (Figure 1-8).

Let's briefly describe some examples of MSN as catalyst support. Taking advantage of the surface chemistry, such as the surface area of the mesoporous silica Gabaldon *et al.* fabricated Au nanoparticles on the silica pores, and demonstrated the increased stability and high reactivity of Au particles<sup>62</sup>. The particles showed high stability even after three times CO oxidation. The same principle was used by Yin *et al.* who fabricated Pt NPs onto the MSN, to increase the stability of Pt NPs<sup>63</sup>. Wu *et al.* carried out size-controlled synthesis of Pt particles on MSN. The results showed that the MSN supporting Pt NPs exhibited much better (100%) CO oxidation than that of single Pt NPs because of the high stability and reactivity<sup>64</sup>. Furthermore, Yan *et al.* described a facile, environmental route for efficient self-assembly of Ag NPs on the surface of 2D MSN with fast reduction of 4-nitrophenol in 40s<sup>65</sup>.

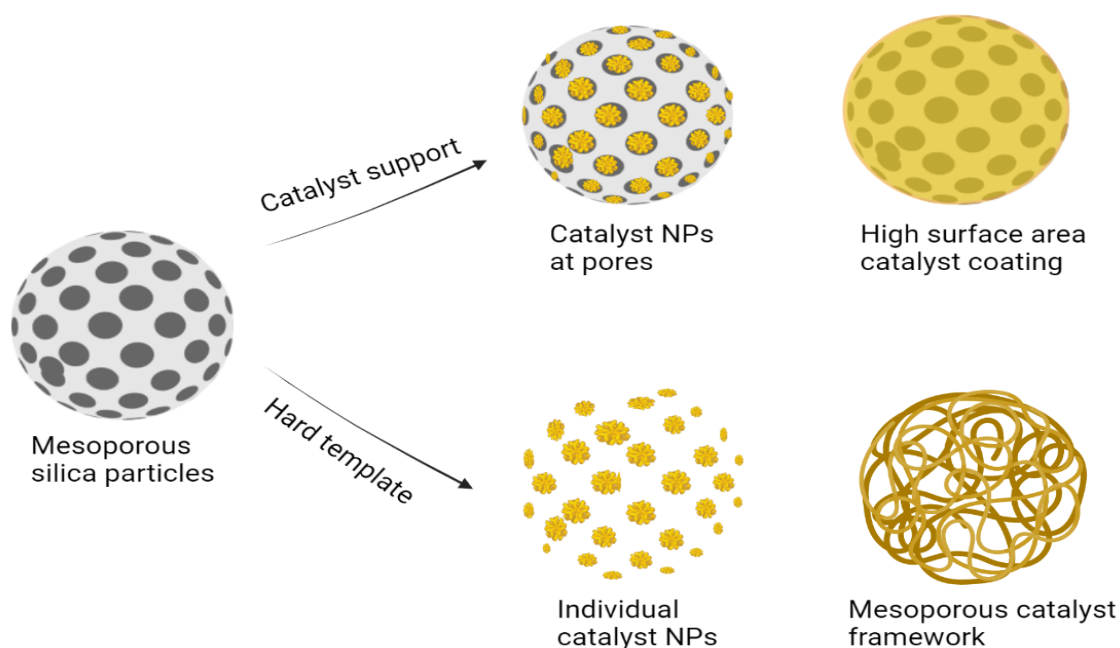


**Figure 1-8.** Schematics depicting the functions of mesoporous silica as catalytic support or as sacrificial hard template for the synthesis of individual catalyst nanoparticles or mesoporous catalyst frameworks.

Apart from the catalyst support material, MSN have also drawn huge attention as a hard template or hard sacrificial material. In this case, the pores of MSN could be filled with desired reactants and at the end the MSN template would be removed by using different etching techniques<sup>66,67</sup>.

## 1.2.2 The synergy of noble metal and magnetic nanostructures: catalysis and chemical reactivity

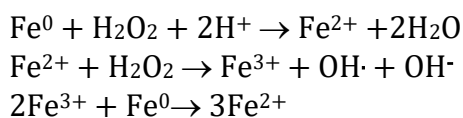
### 1.2.2.1 Monometallic nanocatalysts

Over the past decades, noble metal nanoparticles (Au, Ag, Pd, Pt, Ru, Ir *etc.*) have received increased attention as a result of their distinctive physiochemical

properties and prospective uses in a wide range of fields such as biomedicine<sup>68</sup>, sensing<sup>69</sup>, photothermal therapy<sup>70</sup> and particularly catalysis<sup>71</sup>. Although many parameters affect the catalytic properties of noble metals, their surface electronic structure is the key descriptor of catalytic performance. Good catalysts exhibit either an optimum degree of d-band vacancy to donate or accept electrons from other molecules or low ionization potential to donate charge in case of having complete d orbitals (e.g., Ag). Through fine-tuning of the surface charge density and charge transfer, the catalysts promote the adsorption and intramolecular bond breaking of reactants and the new bond formation among reactants. For good catalytic performance, an optimum bond strength with the reactants should be achieved: not too weak in order to activate the reactants, and not too strong so as to desorb the products.

Platinum and Palladium are standard catalysts in many reactions especially in dehydrogenation/hydrogenation reactions or selective oxidation of organic molecules with incremental catalytic power under nanosized conditions. Gold was earlier considered to be chemically inert and regarded as a poor catalyst<sup>72</sup>. However, under nanosized conditions, it has become a highly active catalyst for many reactions (e.g. CO oxidation, selective oxidation of alcohols and polyols, glucose, etc.). Ni and Fe metals with their two 4s outermost electrons and unsaturated 3d electron shells also possess catalytic performance apart from their special magnetic properties. For instance, iron-based catalysts are attracting much attention recently as potential greener alternatives to noble metals, as well as due to their non-toxic nature and easy recyclability.

Very interesting iron-based catalysts are the zero-valent iron nanoparticles (nZVI) which have been widely used in Fenton-like catalytical processes by promoting the iron ions release in acidic solution to initiate the Fenton reaction in the presence of H<sub>2</sub>O<sub>2</sub>:



Thereafter, the generated ferric cations (Fe<sup>3+</sup>) react with ZVI to yield a continuous supply of ferrous ions for a sustained Fenton-like reaction. However, the application of bare nZVI in a catalytic system such as in this case or in another system is challenging due to the poor chemical stability of metallic iron. nZVI surface is easily passivated in the air or in the aqueous environment impairing its catalytical performance over time. That is indeed the main drawback for catalytic applications<sup>73,74</sup>.

Metallic nickel is chemically more stable than Fe. It is an interesting cost-effective alternative catalyst that is known due to its capability to break C-C- bonds and catalyze hydrogenation reactions. For instance, Ni has been used in the chemical

conversion of the biomass-derived compound “levulinic acid” into  $\gamma$ -valerolactone, a valuable chemical used as a clean additive for automotive fuels, mediating dehydration and hydrogenation processes<sup>75</sup>. Nickel has also become a key catalyst in the methane steam/dry reforming technology to convert  $\text{CH}_4$  into  $\text{H}_2$ . Nevertheless, one of its major drawbacks lies in its lack of selectivity, linked to side reactions of hydrogenolysis and over-hydrogenation.

### 1.2.2.2 Multimetallic nanocatalysts

One of the strategies to overcome the limitations of the monometallic catalysts such as low catalytic activity, lack of chemical stability or selectivity is combining different catalysts (e.g., different noble metals or combinations of noble metals/non-noble metals). In general, a monolayer or sub-monolayer amount of noble metal on a less noble metal is already enough for enhanced performance. These bimetallic catalysts often show electronic and chemical properties that are quite superior to those of their parent metals offering the opportunity to obtain new catalysts with highly improved performance. That can be mainly attributed to i) ensemble effects, that is, a finite number of surface atoms in a particular geometric orientation that are required for promoting a catalytic process, and ii) changes in electronic structure resulting from hetero-nuclear metal–metal bond formation<sup>87</sup> (known as ligand effect). This latter could involve charge transfer between the metals or orbital rehybridization of one or both metallic components. Let's illustrate those effects with Pd–Au bimetallic catalysts which often display enhanced catalytic activities and selectivity compared with Pd-alone. The ensemble effect arises from the dilution of the more catalytic active Pd by the less active Au. With increasing surface Au coverage, contiguous Pd ensembles disappear and isolated Pd ensembles are formed. In some reactions, this effect is responsible for increasing reaction rates via the formation of highly active surface sites, e.g., isolated Pd pairs. The disappearance of contiguous Pd ensembles also switches offside reactions, explaining the selectivity increase of certain reactions, for example, the direct  $\text{H}_2\text{O}_2$  production instead of water formation from oxygen/hydrogen sources<sup>76</sup>. On the other hand, the ligand effects cause the d band of Pd to be more filled by a direct charge transfer between Pd and Au (Au gains s, p electrons and loses d electrons whereas Pd loses s, p electrons but gains d electrons). For Pd, gaining d electrons shifts the d band center away from the Fermi level, which leads to weaker interaction between adsorbates and surface Pd atoms. Moreover, the Pd–Au alloying perturbs the lattice constant of Pd, adopting values closer to the Au one. That makes the Pd–Pd bond length increase causing the Fermi level within the Pd d band to rise. This also enhances the atomic-like character of Pd atoms and correspondingly, weakens binding toward reactants. In summary, Au weakens the binding strength of Pd towards reactants and products by perturbing its d band via charge transfer and bond length arguments. This does not mean that Au weakens the catalytic activity of Pd. In contrast, higher activity, selectivity, and non-poisoning of Pd are frequently

found within Pd-Au alloys compared to pure Pd. Similar effects have been observed with Pd/Ag for the direct synthesis of  $\text{H}_2\text{O}_2$ <sup>77</sup>.

Apart from the already mentioned excellent attributes of bimetallic catalysts, the reduction of catalyst costs is another important issue behind bimetallic catalysts. Introducing magnetic metal in noble metal catalysts can significantly reduce the cost while exhibiting very good activity, stability and selectivity. For instance, one of the fields which has profited from these benefits is the field of direct alcohol oxidation fuel cells. The use of noble metals such as Pt and Pd is mandatory to increase the kinetics of methanol/ethanol oxidation and the activity for oxygen reduction. However, many studies in the last decade have shown that the use of shelled or alloyed Pt catalysts with magnetic metals such as mesoporous nanostructures of CoPt, CoNiPt and NiPt (with a very low load of Pt) exhibit excellent electrocatalytic activity, low catalyst poisoning, and high corrosion stability/durability<sup>78-81</sup>.

In the same line, new mesoporous Ni-rich Ni-Pt nanostructures have been used as very promising heterogeneous catalysts for the hydrogenation of levulinic acid to  $\gamma$ -valerolactone using formic acid as the sole hydrogen source and with minimal nickel leaching into the reaction mixture as compared to those with higher nickel contents<sup>82</sup>.

### 1.2.3 Heterostructured nanocatalysts as galvanic cells

Many multicomponent nanocatalysts exhibit intermetallic galvanic reactions that accelerate electron transfer processes, which can be exploited for many applications. The process of internal electrolysis starts when two materials, having different electrochemical potentials, are brought into contact forming a pair of nanoelectrodes, with one of them playing the role of cathode and the other of anode (Figure 1-9).

Such processes are the basis behind the self-propulsion in bimetallic nanomotors in presence of a chemical fuel. Spontaneous galvanic reactions are produced on the metallic segments in presence of a chemical fuel in which one of the metals induces oxidation reactions and the other reduction reactions. The process induces intermetallic electron transfer and ionic currents in the fluid, triggering electrokinetic processes which make the object move<sup>83</sup>.

Galvanic cell reactions are also behind the important strategies to control corrosion processes, being one of them the cathodic protection. In this technique the metal to be protected acts as cathode and is faced to a sacrificial metal which is easily corroded acting as anode. As a consequence, the sacrificial metal corrodes instead of the protected metal<sup>84-86</sup>.

Recently different studies have shown that multicomponent nanocatalysts can feature such galvanic cell effects to highly promote the catalytic performance of such heterostructured systems, being the catalytic activation of Fenton-like



reactions one of such examples. Under this context, many heterostructures or alloy systems based on zero valent iron such as FeCu, FeNi, FeC, FePC, FeZnC, FeCuBP, Fe<sub>2</sub>B, FeBC, etc., can be used to build up galvanic cells in which the Fe acts as anode donating electrons to the other component and thus promoting the Fe<sup>2+</sup> ion release as one of the ingredients in Fenton-like reactions<sup>87–97</sup>. The higher the electrochemical potential difference between the anode/cathode of such galvanic cells is, the higher the driving force for Fe<sup>2+</sup> leaching is. Alternatively, similar iron/metal systems (FePd, FeNi, FeSn, FeCu, FeC) take advantage of the other material counterpart acting as cathode (electron acceptor) to efficiently promote interfacial reduction processes such as hydrogen production, oxygen reduction, heavy metal reduction, etc<sup>98–103</sup>.

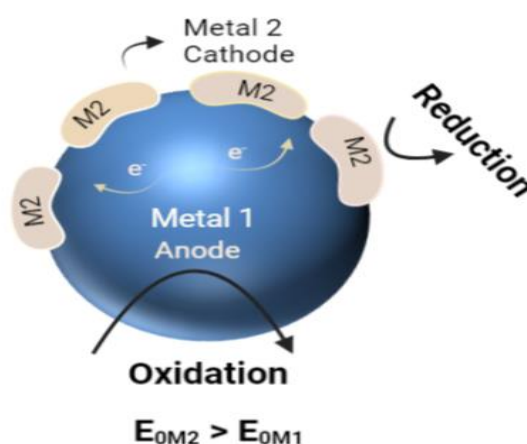


**Figure 1-9.** Scheme of a galvanic cell in a heterostructure particle in which the electron transfer is triggered between M1 (acting as anode) and M2 (as cathode), due to the difference of electrochemical potentials.

#### 1.2.4 Heterostructured nanocatalysts and their synergy by thermal effects

The combination of different metals not only improves the effectiveness as catalysts<sup>104</sup>, but also brings some additional properties which broaden the application fields. Combining magnetic and noble metals can substantially improve the magneto-optical activity and support propagating surface plasmon modes<sup>105,106</sup>.

As previously discussed, noble metal nanoparticles scatter and absorb light very efficiently due to the resonant oscillation of their free electrons in the presence of light. The plasmon resonance can either radiate light, a process with significant applications in the optical and imaging fields, or be quickly transformed into heat, enabling new applications in a variety of fields<sup>107</sup>.

Accordingly, metallic nanoparticles with large absorption coefficients such as Au are suitable for many photothermal processes such as photothermal catalysis, photothermal therapy, drug release, photoacoustic imaging, photothermal

contrast imaging, photothermal-induced resonance imaging, photothermal polymerization, plasmonic patterning, etc. In the particular case of catalysis, the possibility of speeding up chemical reactions by gold-mediated photothermal processes is a very appealing synergistic effect that can be even enhanced by tuning the composition of the metal nanoparticle. In this line, it has been recently shown that metal nanoparticle alloys such as Au-Fe ones have superior absorption cross section to the pure Au counterparts<sup>56</sup>. The augmented plasmon absorption in iron-doped Au nanoalloys has been mainly observed in the red and near-infrared (NIR) frequencies, which actually is the working window for most photothermal applications. Such synergetic effect is due to the modification of the band structure of gold after doping with iron, with a consequent increase of the lossy part of the optical constant<sup>108</sup>. These results suggest that the band structure of noble metals can be engineered by doping with the appropriate combination of transition metals to obtain the optimized plasmonic properties, opening a promising field.

The combination of magnetic nanostructures with noble metals facilitates the manipulation of their magnetic properties to also confer synergistic properties or multi-functionality. For instance, plasmonic effects of the heterostructures for inducing local heating can be coupled with magnetic strategies for temperature detection and thermometry. The integrated concept of magnetoplasmonic is based on the detection of tiny viscosity variations around magnetoplasmonic nanostructures (e.g., Co/Au, Fe/Au) when they are optically heated. The local thermometry is achieved by optically tracking the viscosity-dependent rotation dynamics of the nanostructures activated by a weak external alternating magnetic field<sup>109</sup>.

Moreover, as mentioned previously, magnetic hyperthermia can also be achieved with magnetic nanostructures and can be harnessed to thermally enhance the chemical catalytic performance of the hetero nanostructures. When a magnetic field is applied, energy is given to the particles which will force the magnetic moments of the nanoparticles to align along the field direction away from the easy axis. When the field is removed, the nanoparticles relax, aligning along the easy axis. The gained energy by the applied magnetic field can be lost as heat during relaxation. If an alternating magnetic field is applied, the magnetic moment aligning and relaxation processes will continue, and thus heat will be generated as long as the alternating field is applied<sup>110</sup>.

Enhanced catalytic activity can be also accomplished on the nanostructures by applying magnetic fields to induce nanoparticle stirring, favouring effective mass transfer and fast mixing of reagents for promoting chemical reactions<sup>111</sup>.

As can be seen, the combination of multicomponent chemical nanoreactors with magnetoplasmonic properties opens up a world of possibilities for property synergy and multifunctionality that can be exploited in a wide variety of

applications. Moreover, we must not forget that if these structures are supported on mesoporous platforms such as silica, as described before, many of the effects can be magnified, increasing the added value of these multicomponent nanostructures.

### 1.3 2D transition metal dichalcogenides

In this thesis some unique attributes of 2 transition metal dichalcogenides (TMDs) will be exploited in combination with mesoporous silica and metal structures for photocatalyst development. Therefore, in this section the state of the art and prospects of these materials will be briefly summarized.

Two-dimensional materials have gained a great attention since the breakthrough of graphene. Examples of such materials are the transition metal dichalcogenides (TMDs). In contrast to graphene that possess a set of defined properties, TMDs exhibit versatility in properties depending on the metal and chalcogen atoms forming the TMD material. Figure 1-10 shows a periodic table highlighting in various colors different groups of transitions metal atoms and in orange the chalcogen atoms. With the wide set of different metal and chalcogen atoms that form a TMD, coupled with the 3 possible atomic configurations, yield a tremendous amount of  $MX_2$  combinations all with their unique properties. TMDs have a potential broad impact in various applications such as nanoelectronics and semiconductor industry, quantum computing, (photo)catalysis, water filtration, (bio)sensing, energy storage, solar cells, light emission diodes, piezoelectric, etc<sup>112–114</sup>.

**Periodic Table of the Elements**

M: Transition metal  
X: Chalcogen  
}  $MX_2$

1 1A H Hydrogen 1.008	2 2A He Helium 4.003																	13 3A B Boron 10.811	14 4A C Carbon 12.011	15 5A N Nitrogen 14.007	16 6A O Oxygen 15.999	17 7A F Fluorine 18.998	18 8A Ne Neon 20.180																		
3 Li Lithium 6.941	4 Be Beryllium 9.012																	5 Al Aluminum 26.982	6 Si Silicon 28.086	7 P Phosphorus 30.974	8 S Sulfur 32.06	9 Cl Chlorine 35.453	10 Ar Argon 39.948																		
11 Na Sodium 22.990	12 Mg Magnesium 24.305	13 Al Aluminum 26.982	14 Si Silicon 28.086	15 P Phosphorus 30.974	16 S Sulfur 32.06	17 Cl Chlorine 35.453	18 Ar Argon 39.948																	19 K Potassium 39.098	20 Ca Calcium 40.078	21 Sc Scandium 44.956	22 Ti Titanium 47.88	23 V Vanadium 50.942	24 Cr Chromium 51.996	25 Mn Manganese 54.938	26 Fe Iron 55.845	27 Co Cobalt 58.933	28 Ni Nickel 58.693	29 Cu Copper 63.546	30 Zn Zinc 65.38	31 Ga Gallium 69.723	32 Ge Germanium 72.631	33 As Arsenic 74.922	34 Se Selenium 78.96	35 Br Bromine 79.904	36 Kr Krypton 83.796
37 Rb Rubidium 85.468	38 Sr Strontium 87.62	39 Y Yttrium 88.906	40 Zr Zirconium 91.224	41 Nb Niobium 92.906	42 Mo Molybdenum 95.94	43 Tc Technetium 98.906	44 Ru Ruthenium 101.07	45 Rh Rhodium 102.906	46 Pd Palladium 106.42	47 Ag Silver 107.868	48 Cd Cadmium 112.414	49 In Indium 114.818	50 Sn Tin 118.710	51 Sb Antimony 121.760	52 Te Tellurium 127.6	53 I Iodine 126.905	54 Xe Xenon 131.29																								
55 Cs Cesium 132.905	56 Ba Barium 137.327	57-71 Lanthanide Series La Ce Pr Nd Pm Sm Eu Gd Tb Dy Ho Er Tm Yb Lu	72 Hf Hafnium 178.49	73 Ta Tantalum 180.948	74 W Tungsten 183.84	75 Re Rhenium 186.207	76 Os Osmium 190.23	77 Ir Iridium 192.222	78 Pt Platinum 195.084	79 Au Gold 196.967	80 Hg Mercury 200.592	81 Tl Thallium 204.383	82 Pb Lead 207.2	83 Bi Bismuth 208.980	84 Po Polonium 209	85 At Astatine 210	86 Rn Radon 222																								
87 Fr Francium 223	88 Ra Radium 226	89-103 Actinide Series Ac Th Pa U Np Pu Am Cm Bk Cf Es Fm Md No Lr	104 Rf Rutherfordium 261	105 Db Dubnium 262	106 Sg Seaborgium 263	107 Bh Bohrium 264	108 Hs Hassium 265	109 Mt Meitnerium 266	110 Ds Darmstadtium 271	111 Rg Roentgenium 272	112 Cn Copernicium 285	113 Nh Nihonium 286	114 Fl Flerovium 289	115 Mc Moscovium 288	116 Lv Livermorium 293	117 Ts Tennessine 294	118 Og Oganesson 294																								

**Figure 1-10.** Highlighted elements represent layered transition-metal dichalcogenides.

#### 1.3.1 TMD structure

TMDs share the chemical formula  $MX_2$ , where M is a transition metal atom (Mo, W, etc) and X is a chalcogenide atom (Se, S, Te). TMDs are van der Waals layered materials (Figure 1-11a). Each TMD monolayer consists of an intercalated metal atomic plane between two chalcogenide atomic planes (the planes of M are attached to the other two planes of X through covalent bonds). These three planes

make up the TMD monolayer, thus the thickness of each monolayer is only 3 atoms. Bulk and multilayered  $\text{MX}_2$  are constructed by monolayer units that vertically stack via Van der Waals forces.

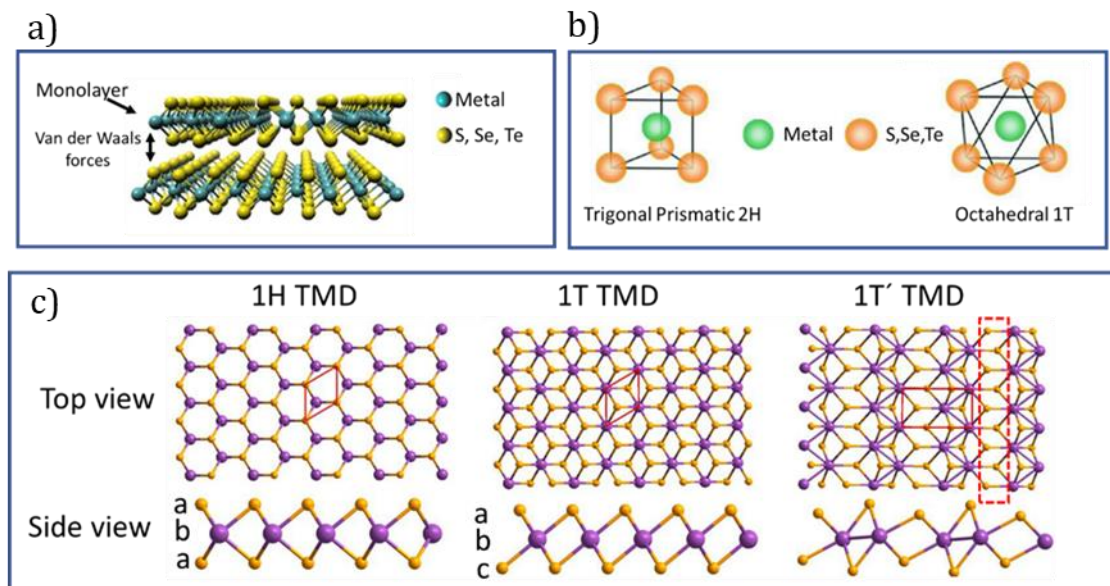
TMDs display different polymorphic phases.  $\text{MX}_2$  monolayer generally involves two basic phases, the trigonal prismatic phase (1 H-TMDs if monolayer or 2H-TMD if multilayer) and the octahedral phase (1T phase) (Figure 1-11b). There is also a distorted trigonal phase, 1 T'. Bulk molybdenum sulfide exists as 1T, 2H, or 3R polymorphs<sup>4</sup>.

Figure 1-11c shows a top side, and perspective view of the different structures in a TMD monolayer. These structural phases can also be viewed in terms of different stacking orders of the three atomic planes (chalcogen–metal–chalcogen) forming the individual layers of these materials. The 2H or 1H phase have a trigonal prismatic coordination pattern, corresponding to an ABA stacking in which chalcogen atoms in different atomic planes occupy the same position A and are located on top<sup>94</sup>. The 1 T has an octahedral pattern in which the top layer of chalcogen atoms have shifted with respect to the bottom, exposing all the chalcogen atoms (Figure 1-11c). This configuration results in an ABC stacking order. The 1T' phase is a distorted 1T phase. Starting from the 1T phase, if one strains the unit cell on either side, one would isolate a line of chalcogen atoms<sup>115</sup>. The isolated chalcogen has been highlighted in the figure (dashed red square).

Depending on the particular combination of the transition metal and the chalcogen (S, Se) elements the thermodynamically stable phase is either the 2H or 1T phase. The theoretical calculations based on density functional theory (DFT) show that the 1H phase is the ground-state phase of all monolayer  $\text{MX}_2$  except for  $\text{WTe}_2$ , in which the 1T' phase possesses the lowest energy<sup>117</sup>.

---

<sup>4</sup> Here, the letters are labeled as trigonal (T), hexagonal (H) and rhombohedral (R), and the numbers indicate the number of layers in the unit cell. The 3R polytype is similar to the 2H, in that it involves trigonal prismatic coordination of the transition metal. However, it differs in its stacking pattern.



**Figure 1-11.** a) Illustrations showing the structure of two monolayers of TMD, b) the trigonal prismatic and octahedral unit cells c) the top and side view of different structural phases of a monolayer of TMD<sup>116</sup>.

In the case of multilayer and bulk samples, TMDs are also defined by the configuration of the individual layers and by possible distortions that lower the periodicity. The distortions can induce the formation of metal-metal bonds.

### 1.3.2 Synthesis of TMD

There are different routes for the synthesis of TMDs, the so-called top-down and bottom-up approaches (Figure 1-12). Mechanical or chemical exfoliation from bulk TMDs are the typical top-down techniques. Chemical vapor deposition (CVD) or hydrothermal processes represent the bottom-up approaches.

In top-down approach natural crystals (2H-TMDs) are exfoliated into thin layers by mechanical cleavage or by liquid exfoliation (Figure 1-12b). Mechanical exfoliation can be performed in a similar way as in the case of graphene using tapes or polymers such polydimethylsiloxane (PDMS). Liquid exfoliation can be performed under sonication with organic solvents (e.g., ethanol, N-methylpyrrolidone) or in water assisted by ion intercalation (e.g., Li ions) or surfactants. 1T-TMD phases are generally achieved when using ion-intercalation liquid processing<sup>119–121</sup>.

In a typical CVD process, metal and chalcogen precursors react/or decompose in the gas phase at relatively high temperature and the TMD product is then deposited as mono- or few-layer film on the exposed substrate (Figure 1-12a). Typical precursors for MoS<sub>2</sub> are MoO<sub>3</sub> and sulfur powder under sublimation. The CVD process generates the typical 1H or 2H-TMD phase. With this technique ultrathin TMDs materials with high crystal quality, scalable size, tunable thickness, and excellent electronic properties can be achieved<sup>122,123</sup>.

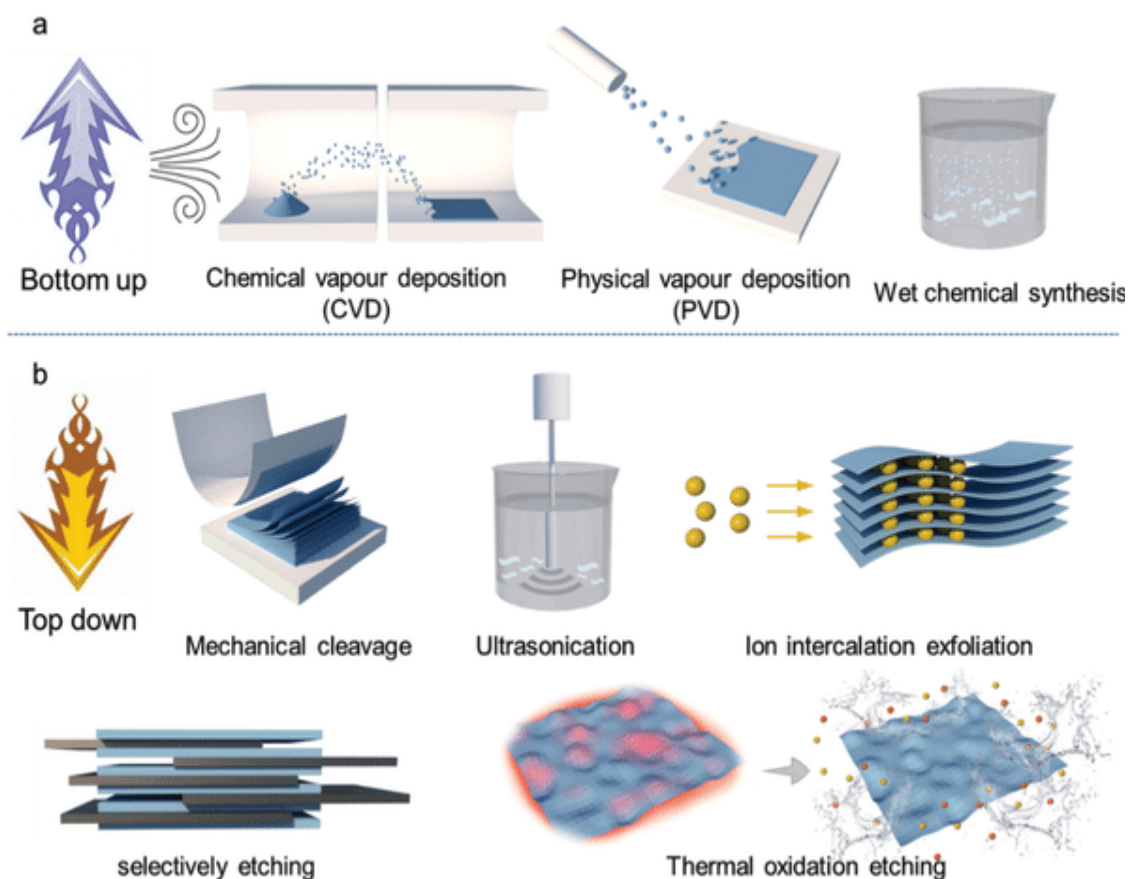


**Figure 1-12.** Bottom-up a) and Top-down b) approaches for TMD synthesis<sup>118</sup>.

Hydrothermal is a widely used technique for the synthesis of TMDs. It consists in the chemical reduction of the Metal precursors (e.g. Mo(VI)) with the chalcogen compounds (e.g.  $S^{2-}$  used as sulfur source and reductant) in an aqueous medium at high pressure and temperature using a suitable sealed vessel. Hydrothermal syntheses produce highly active, defect rich, high surface area TMDs, and easily synthesized as hierarchical structures on a range of supports in a one-pot reaction. This process has been widely used for  $MoS_2$  synthesis, but its final structure is under debate. Although many studies have concluded that the structure is the metallic 1T  $MoS_2$  phase, recent studies have revealed inconsistencies and misinterpretations in previous TMD characterization work. Such study has argued that the hydrothermal product is a variant of 1T  $MoS_2$  with ion intercalation and Mo in a lower oxidation state ( $Cat^+Mo^{(III)}S_2$ )<sup>124</sup>.

### 1.3.3 Optoelectronic properties

The diversity of chemical compositions and structural phases of TMDs result in a broad range of properties<sup>125</sup>. The combination of the d-electron configuration is one of the predominant factors in determining TMD electronic properties. The filling of d orbitals in the transition metal dictates the electronic structure of the TMDs. Apart from the d electron count in the transition metal, the structural

coordination of the transition metal and the chalcogen within the TMD also determines their electronic property. In 2H-phase TMDs, the non-bonding d orbitals of the transition metal split into 3 degenerate states  $d_{z^2}$  ( $a_1$ ),  $d_{x^2-y^2, xy}$  ( $e$ ) and  $d_{xz, yz}$  ( $e'$ ). Conversely, 1T-phase TMDs form degenerate  $d_{z^2, x^2-y^2}$  ( $e_g$ ) and  $d_{xz, yz, xy}$  ( $t_{2g}$ ) orbitals. Completely filled orbitals results in semiconducting conductivity whereas partially occupied orbitals are metallic.

In this discussion, we will focus on the TMDs formed by groups VI of the transition metals, such as Mo and W combined with S, Se, and Te (Figure 1-13a), in their thermodynamically stable 2H phase, bulk  $\text{MoS}_2$ ,  $\text{MoSe}_2$ ,  $\text{WS}_2$  and  $\text{WSe}_2$  are semiconductors whereas  $\text{WTe}_2$  with a  $1T'$  thermodynamically stable phase exhibits a semi-metallic behavior. Figure 1-13b shows the evolution of the band structure of 2H- $\text{MoS}_2$  as calculated from first principles upon reducing its thickness from bulk to monolayer. The positions of valence and conduction band edges with decreasing thickness, resulting in an increase in the bandgaps (2D quantum confinement). Figure 1-13c shows the changes in bandgaps from bulk to monolayer for different  $\text{MX}_2$  materials in their more stable configuration. This highlights one of the relevant attributes of these materials: the bandgap tunability with the number of stacked layers. Additionally, the energy values are located in the visible range, which is very appealing for environmental applications. Moreover, the Figure 1-13b also shows the crossover from an indirect gap in multilayer  $\text{MoS}_2$  (or bulk materials) to direct bandgap results when the lowest energy level at the conduction band and the highest energy level in the valence band are not aligned. In the case of a monolayer  $\text{MoS}_2$ , the levels are aligned providing a direct bandgap. The difference between a direct and indirect bandgap is better highlighted in Figure 1-13d.

For a direct bandgap, when an electron and hole pair (exciton) align they can recombine and emit a photon ( $h\nu$ ) with an energy equal to gape energy. For an indirect bandgap, a phonon must be first emitted to align the electron and hole pair in k-space, then this is followed by the recombination and emission of a photon. The probability of a phonon followed by a photon is very low, therefore by changing the layer number we are not only tuning the bandgap but also modulating the light emission. Because of the indirect bandgap, the bulk  $\text{MoS}_2$  displays a negligible photoluminescence signal whereas the monolayer  $\text{MoS}_2$  exhibits a powerful photoluminescence signal with pronounced emissions at 670 and 627nm<sup>126-128</sup>.

TMDs can exhibit polymorphic phase transitions at near-ambient conditions by applying external stimuli<sup>131</sup>, which is an additional attribute for tuning the optoelectronic properties of the materials. Theoretical calculations have predicted that the energy difference between the 2H and  $1T'$  phases is not so large and decreases in the order of  $\text{MS}_2 \rightarrow \text{MSe}_2 \rightarrow \text{MTe}_2$  ( $M$ =metal). Therefore, different approaches have been addressed to induce phase conversion and thus tailor the electronic properties of the materials. For instance, the transition of  $\text{MoS}_2$  from the 2H phase to the 1T or  $1T'$  phase has been achieved through the intercalation

of alkali metals by charge transfer from the  $s$  orbitals of alkali metals to the  $d$  orbitals of the transition-metal atoms. The increase in  $d$ -orbital filling causes the stability of the 1T or 1T' phase to be higher than that of the 2H phase beyond a certain doping threshold.

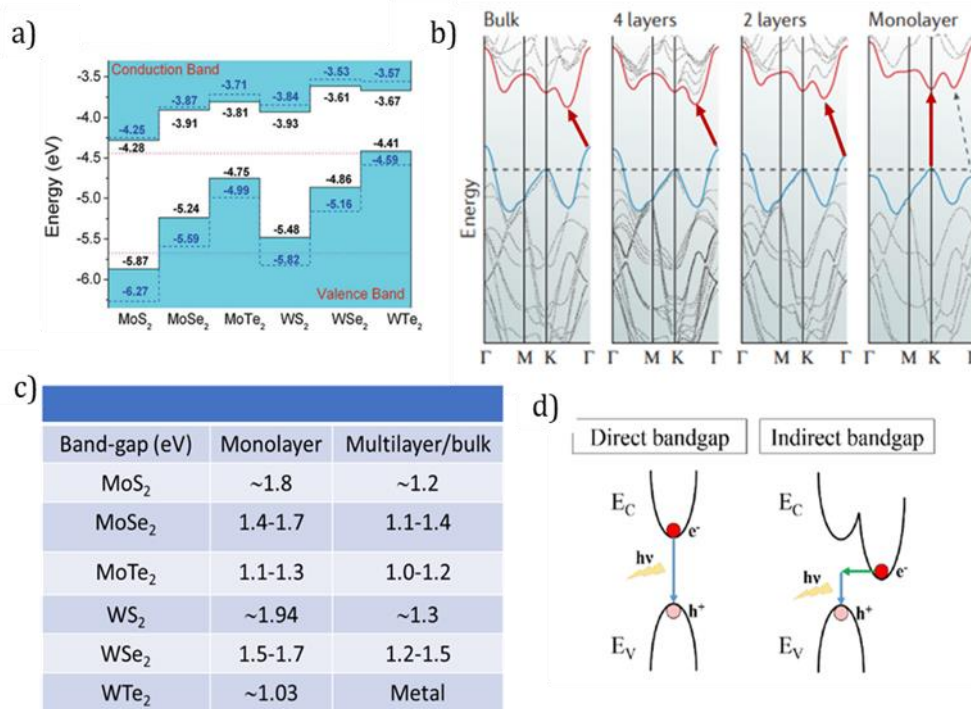


**Figure 1-13.** a) Calculated band alignment for transition metal dichalcogenide monolayers. Solid lines and dashed lines are obtained by different simulation approaches; b) Calculated band structures of bulk, quadlayer, bilayer and monolayer MoS<sub>2</sub>. The solid arrows indicate the electronic transitions through indirect (bulk, quadlayer and bilayer MoS<sub>2</sub>) and direct band-gap transition (monolayer MoS<sub>2</sub>); c) table with band-gap values for monolayer and multilayer/bulk MoS<sub>2</sub>; a d) Scheme of a direct and indirect band-gap transition

129,130.

This approach has been used for electronic device fabrication by patterning metallic (1T or T') and semiconducting (2H) regions on a monolayer MoS<sub>2</sub> by area-selective phase transformation. Compared to MoS<sub>2</sub>, the 2H and 1T' phases of MoTe<sub>2</sub> have a smaller energy difference, enabling a wider range of external stimuli to induce the 2H- to-1T' phase transition such as temperature, tensile strain, laser irradiation, electrostatic doping and electric fields.

The optoelectronic properties of TMDs can be also tuned by introducing point defects to the lattice. The main point defects are metal/chalcogen vacancies and interstitials. For example, patterned p-n homojunctions can be produced on TMDs by inducing defects with charged particle beam irradiation, chemical or electrostatic doping<sup>108</sup>. The formation of this homojunction through 2D defect



patterning facilitates the formation of 2D diodes within a TMD single flake. Additionally, TMDs could also be used for next generation of ultrathin, low power, flexible and high-performance electronic devices. In the context of nanoelectronics, the TMDs with an intrinsic band gap typically in the range 1–2 eV overcome the key shortcomings of graphene for electronic applications and make them ideal for use in transistors. But also, TMDs hold promise for flexible optoelectronic devices<sup>132</sup>. For example, three single-layer TMDs MoSe<sub>2</sub>, WS<sub>2</sub>, and MoS<sub>2</sub>, can absorb up to 5-10% incident sunlight in a thickness of less than 1 nm within the power conversion efficiency of up to 1%, which is higher than the best existing ultrathin solar cells. Enhanced optoelectronic characteristics can be accomplished by heterogeneous scaffold architectures with other 2D materials such as graphene<sup>133</sup>.

Finally, the absence of crystallographic symmetry, together with 2D quantum confinement and strong spin–orbit coupling, lead to many unique properties in layered TMDs, including optical harmonic generation, spin-valley coupling, magnetoelectricity, and piezoelectricity.

### 1.3.4 Chemical properties

TMDs exhibit a high surface area which, together with their semiconducting and metallic character, are relevant ingredients to be exploited as photo and electrocatalysts<sup>108</sup>. In fact, these materials have been used in many catalytic processes, including hydrogen evolution reaction, water splitting, CO<sub>2</sub> reduction, reactive oxygen species generation for contaminant degradation, among others. Furthermore, these layered materials exhibit chemical anisotropy. Theoretical calculations and experimental results have revealed that the basal plane of TMDs is more catalytically inert, while the surface edges are highly active for adsorption, catalysis, or chemical reactions. Therefore, increasing the density of active sites is an important task for their catalytic performance. In fact, efforts have already been invested to grow stacked layers with vertical alignment with respect to the base support and thus expose the highest density of edges to the environment. Alternatively, reactive sites can also be activated in basal plane through nanoengineering by introducing chalcogenide vacancies, active metal ions, charge doping, or dopants.

Not only the density of active sites is important for an enhanced catalytic performance but also the chemical nature of these active sites. As an example, TMDs have been shown to be very good electrocatalysts for hydrogen evolution reaction. The Gibbs free energy for hydrogen adsorption on the active sites plays a key role in the catalytic efficiency and depends on the nature of the TMD atoms at the edge (metal-edge or chalcogen edge)<sup>108</sup>. For instance in the series MoSe<sub>2</sub>, WS<sub>2</sub>, MoS<sub>2</sub> and WSe<sub>2</sub>, it has been demonstrated that MoSe<sub>2</sub> is the best-performing electrocatalyst, exhibiting appropriate hydrogen adsorption energy at both the

Mo-edge and the Se-edge, which allows to catalyze efficiently the hydrogen evolution reaction.

## 1.4 References

1. Gordon AT, Lutz GE, Boninger ML, Cooper RA. Introduction to nanotechnology: Potential applications in physical medicine and rehabilitation. *Am J Phys Med Rehabil.* 2007;86(3):225-241. doi:10.1097/PHM.0b013e318031ee1a
2. Wang DS, Fan SK. Microfluidic surface plasmon resonance sensors: From principles to point-of-care applications. *Sensors (Switzerland).* 2016;16(8). doi:10.3390/s16081175
3. Dey C, Molla AR, Karmakar B. *Semiconductor Glass Nanocomposites: Preparation, Properties, and Applications.* Elsevier Inc.; 2016. doi:10.1016/B978-0-323-39309-6.00012-2
4. Shukla S, Khan R, Daverey A. Synthesis and characterization of magnetic nanoparticles, and their applications in wastewater treatment: A review. *Environ Technol Innov.* 2021;24:101924. doi:10.1016/j.eti.2021.101924
5. Su EP, Justin DF, Pratt CR, et al. Effects of titanium nanotubes on the osseointegration, cell differentiation, mineralisation and antibacterial properties of orthopaedic implant surfaces. *Bone Jt J.* 2018;100B(1):9-16. doi:10.1302/0301-620X.100B1.BJJ-2017-0551.R1
6. Asha AB, Narain R. *Nanomaterials Properties.* Elsevier Inc.; 2020. doi:10.1016/B978-0-12-816806-6.00015-7
7. Shaji A, Zachariah AK. *Surface Area Analysis of Nanomaterials.* Vol 3. Elsevier Inc.; 2017. doi:10.1016/B978-0-323-46139-9.00009-8
8. Characteristics S, Account NO, The T, Filtration S, Tool AS. = P – M J. 2021;(2011):2020-2022.
9. Royston E, Ghosh A, Kofinas P, Harris MT, Culver JN. Self-assembly of virus-structured high surface area nanomaterials and their application as battery electrodes. *Langmuir.* 2008;24(3):906-912. doi:10.1021/la7016424
10. Xu L, Liang HW, Yang Y, Yu SH. Stability and Reactivity: Positive and Negative Aspects for Nanoparticle Processing. *Chem Rev.* 2018;118(7):3209-3250. doi:10.1021/acs.chemrev.7b00208
11. Malhotra BD, Ali MA. *Nanomaterials in Biosensors.*; 2018. doi:10.1016/b978-0-323-44923-6.00001-7
12. Patil SP, Burungale V V. *Physical and Chemical Properties of Nanomaterials.* Elsevier Inc.; 2020. doi:10.1016/b978-0-12-820016-2.00002-1

13. Roduner E. Size matters: Why nanomaterials are different. *Chem Soc Rev.* 2006;35(7):583-592. doi:10.1039/b502142c
14. Ivanova OS, Zamborini FP. Electrochemical size discrimination of gold nanoparticles attached to glass/indium-tin-oxide electrodes by oxidation in bromide-containing electrolyte. *Anal Chem.* 2010;82(13):5844-5850. doi:10.1021/ac101021q
15. Nanda KK, Kruis FE, Fissan H. Evaporation of Free PbS Nanoparticles: Evidence of the Kelvin Effect. *Phys Rev Lett.* 2002;89(25):1-4. doi:10.1103/PhysRevLett.89.256103
16. Koppes JP, Muza AR, Stach EA, Handwerker CH. Comment on "size-dependent melting properties of small tin particles: Nanocalorimetric measurements." *Phys Rev Lett.* 2010;104(18):99-102. doi:10.1103/PhysRevLett.104.189601
17. Buzea C, Pacheco I. *Nanomaterials and Their Classification.* Vol 62.; 2017. doi:10.1007/978-81-322-3655-9\_1
18. Bharmoria P, Ventura SPM. *Optical Applications of Nanomaterials.* Vol 118. Springer Singapore; 2019. doi:10.1007/978-981-13-9833-9\_1
19. Bernardi M, Ataca C, Palummo M, Grossman JC. Optical and Electronic Properties of Two-Dimensional Layered Materials. *Nanophotonics.* 2017;6(2):479-493. doi:10.1515/nanoph-2015-0030
20. Barakat NAM, Woo K Do, Kanjwal MA, Choi KE, Khil MS, Kim HY. Surface plasmon resonances, optical properties, and electrical conductivity thermal hysteresis of silver nanofibers produced by the electrospinning technique. *Langmuir.* 2008;24(20):11982-11987. doi:10.1021/la802084h
21. Bohren CF. Absorption and scattering of light by small particles. *Absorpt Scatt Light by small Part.* Published online 1983. doi:10.1088/0031-9112/35/3/025
22. Guglielmelli A, Pierini F, Tabiryan N, Umeton C, Bunning TJ, De Sio L. Thermoplasmonics with Gold Nanoparticles: A New Weapon in Modern Optics and Biomedicine. *Adv Photonics Res.* 2021;2(8):2000198. doi:10.1002/adpr.202000198
23. Zhu X, Gao T. *Spectrometry.* Elsevier Inc.; 2018. doi:10.1016/B978-0-12-815053-5.00010-6
24. Acharya R. Interaction of waves with medium. *Satell Signal Propagation, Impair Mitig.* Published online 2017:57-86. doi:10.1016/b978-0-12-809732-8.00003-x
25. Hirsch LR, Stafford RJ, Bankson JA, et al. Nanoshell-mediated near-

- infrared thermal therapy of tumors under magnetic resonance guidance. *Proc Natl Acad Sci U S A*. 2003;100(23):13549-13554. doi:10.1073/pnas.2232479100
26. El-Sayed IH, Huang X, El-Sayed MA. Surface plasmon resonance scattering and absorption of anti-EGFR antibody conjugated gold nanoparticles in cancer diagnostics: Applications in oral cancer. *Nano Lett*. 2005;5(5):829-834. doi:10.1021/nl050074e
  27. Mcfarland AD, Duyne RP Van. NI034372S. Published online 2009:1-6. papers2://publication/uuid/90A93501-00B6-4878-821F-E3FB6D547018
  28. Cognet L, Tardin C, Boyer D, Choquett D, Tamarat P, Lounis B. Single metallic nanoparticle imaging for protein detection in cells. *Proc Natl Acad Sci U S A*. 2003;100(20):11350-11355. doi:10.1073/pnas.1534635100
  29. Jiang J, Bosnick K, Maillard M, Brus L. Single molecule Raman spectroscopy at the junctions of large Ag nanocrystals. *J Phys Chem B*. 2003;107(37):9964-9972. doi:10.1021/jp034632u
  30. Brongersma ML, Zia R, Schuller JA. Plasmonics - The missing link between nanoelectronics and microphotonics. *Appl Phys A Mater Sci Process*. 2007;89(2):221-223. doi:10.1007/s00339-007-4151-1
  31. Neikov OD, Yefimov NA. *Nanopowders*. 2nd ed. Elsevier Ltd.; 2019. doi:10.1016/b978-0-08-100543-9.00009-9
  32. Padilla JL, Gamiz F, Godoy A. A simple approach to quantum confinement in tunneling field-effect transistors. *IEEE Electron Device Lett*. 2012;33(10):1342-1344. doi:10.1109/LED.2012.2207876
  33. Slavin S, McEwan K, Haddleton DM. *Cobalt-Catalyzed Chain Transfer Polymerization: A Review*. Vol 3. Elsevier B.V.; 2012. doi:10.1016/B978-0-444-53349-4.00068-6
  34. Harry ST, Adekanmbi M. Confinement Energy of Quantum Dots and the Brus Equation. *Int J Res -GRANTHAALAYAH*. 2020;8(11):318-323. doi:10.29121/granthaalayah.v8.i11.2020.2451
  35. Rabouw FT, de Mello Donega C. Excited-State Dynamics in Colloidal Semiconductor Nanocrystals. *Top Curr Chem*. 2016;374(5):1-30. doi:10.1007/s41061-016-0060-0
  36. Zhao P, Xu Q, Tao J, et al. Near infrared quantum dots in biomedical applications: current status and future perspective. *Wiley Interdiscip Rev Nanomedicine Nanobiotechnology*. 2018;10(3):1-16. doi:10.1002/wnan.1483
  37. Dean CR, Young AF, Cadden-Zimansky P, et al. Multicomponent fractional quantum Hall effect in  $\hat{A}$  graphene. *Nat Phys*. 2011;7(9):693-696.

- doi:10.1038/nphys2007
38. Splendiani A, Sun L, Zhang Y, et al. Emerging photoluminescence in monolayer MoS<sub>2</sub>. *Nano Lett.* 2010;10(4):1271-1275. doi:10.1021/nl903868w
  39. Wang Y, Ou JZ, Balendhran S, et al. Electrochemical control of photoluminescence in two-dimensional MoS<sub>2</sub> nanoflakes. *ACS Nano.* 2013;7(11):10083-10093. doi:10.1021/nn4041987
  40. Scheuschner N, Ochedowski O, Kaulitz AM, Gillen R, Schleberger M, Maultzsch J. Photoluminescence of freestanding single- and few-layer MoS<sub>2</sub>. *Phys Rev B - Condens Matter Mater Phys.* 2014;89(12):2-7. doi:10.1103/PhysRevB.89.125406
  41. Hu W, Wilson RJ, Koh A, et al. High-moment antiferromagnetic nanoparticles with tunable magnetic properties. *Adv Mater.* 2008;20(8):1479-1483. doi:10.1002/adma.200703077
  42. Lu AH, Salabas EL, Schüth F. Magnetic nanoparticles: Synthesis, protection, functionalization, and application. *Angew Chemie - Int Ed.* 2007;46(8):1222-1244. doi:10.1002/anie.200602866
  43. Ali A, Zafar H, Zia M, et al. Synthesis, characterization, applications, and challenges of iron oxide nanoparticles. *Nanotechnol Sci Appl.* 2016;9:49-67. doi:10.2147/NSA.S99986
  44. Vasilakaki M, Trohidou KN, Nogués J. Enhanced magnetic properties in antiferromagnetic-core/ferrimagnetic-shell nanoparticles. *Sci Rep.* 2015;5. doi:10.1038/srep09609
  45. Hedayatnasab Z, Abnisa F, Daud WMAW. Review on magnetic nanoparticles for magnetic nanofluid hyperthermia application. *Mater Des.* 2017;123:174-196. doi:10.1016/j.matdes.2017.03.036
  46. Hu M, Butt HJ, Landfester K, Bannwarth MB, Wooh S, Thérien-Aubin H. Shaping the Assembly of Superparamagnetic Nanoparticles. *ACS Nano.* 2019;13(3):3015-3022. doi:10.1021/acsnano.8b07783
  47. Mohapatra J, Xing M, Liu JP. Inductive thermal effect of ferrite magnetic nanoparticles. *Materials (Basel).* 2019;12(19):26-29. doi:10.3390/ma12193208
  48. Lisjak D, Mertelj A. Anisotropic magnetic nanoparticles: A review of their properties, syntheses and potential applications. *Prog Mater Sci.* 2018;95:286-328. doi:10.1016/j.pmatsci.2018.03.003
  49. Mittal A, Roy I, Gandhi S. Magnetic Nanoparticles: An Overview for Biomedical Applications. *Magnetochemistry.* 2022;8(9). doi:10.3390/magnetochemistry8090107

50. Peddis D, Cannas C, Piccaluga G, Agostinelli E, Fiorani D. Spin-glass-like freezing and enhanced magnetization in ultra-small CoFe<sub>2</sub>O<sub>4</sub> nanoparticles. *Nanotechnology*. 2010;21(12). doi:10.1088/0957-4484/21/12/125705
51. Guslienko KY, Novosad V, Otani Y, Shima H, Fukamichi K. Magnetization reversal due to vortex nucleation, displacement, and annihilation in submicron ferromagnetic dot arrays. *Phys Rev B - Condens Matter Mater Phys*. 2002;65(2):244141-2441410. doi:10.1103/PhysRevB.65.024414
52. Guslienko KY, Novosad V, Otani Y, Shima H, Fukamichi K. Field evolution of magnetic vortex state in ferromagnetic disks. *Appl Phys Lett*. 2001;78(24):3848-3850. doi:10.1063/1.1377850
53. Goiriena-Goikoetxea M, García-Arribas A, Rouco M, Svalov A V., Barandiaran JM. High-yield fabrication of 60 nm Permalloy nanodiscs in well-defined magnetic vortex state for biomedical applications. *Nanotechnology*. 2016;27(17):0. doi:10.1088/0957-4484/27/17/175302
54. Gajbhiye NS, Sharma S, Nigam AK, Ningthoujam RS. Tuning of single to multi-domain behavior for monodispersed ferromagnetic cobalt nanoparticles. *Chem Phys Lett*. 2008;466(4-6):181-185. doi:10.1016/j.cplett.2008.10.065
55. Issa B, Obaidat IM, Albiss BA, Haik Y. Magnetic nanoparticles: Surface effects and properties related to biomedicine applications. *Int J Mol Sci*. 2013;14(11):21266-21305. doi:10.3390/ijms141121266
56. Li Z, Aranda-Ramos A, Güell-Grau P, et al. Magnetically amplified photothermal therapies and multimodal imaging with magneto-plasmonic nanodomains. *Appl Mater Today*. 2018;12:430-440. doi:10.1016/j.apmt.2018.07.008
57. Li Z, Lopez-Ortega A, Aranda-Ramos A, et al. Simultaneous Local Heating/Thermometry Based on Plasmonic Magnetochromic Nanoheaters. *Small*. 2018;14(24):1-10. doi:10.1002/smll.201800868
58. Shinde PS, Suryawanshi PS, Patil KK, et al. A brief overview of recent progress in porous silica as catalyst supports. *J Compos Sci*. 2021;5(3):1-17. doi:10.3390/jcs5030075
59. Wu SH, Lin HP. Synthesis of mesoporous silica nanoparticles. *Chem Soc Rev*. 2013;42(9):3862-3875. doi:10.1039/c3cs35405a
60. Stevens WJJ, Lebeau K, Mertens M, Van Tendeloo G, Cool P, Vansant EF. Investigation of the morphology of the mesoporous SBA-16 and SBA-15 materials. *J Phys Chem B*. 2006;110(18):9183-9187. doi:10.1021/jp0548725

61. Singh B, Na J, Konarova M, et al. Functional mesoporous silica nanomaterials for catalysis and environmental applications. *Bull Chem Soc Jpn.* 2020;93(12):1459-1496. doi:10.1246/BCSJ.20200136
62. Gabaldon JP, Bore M, Datye AK. Mesoporous silica supports for improved thermal stability in supported Au catalysts. *Top Catal.* 2007;44(1-2):253-262. doi:10.1007/s11244-007-0298-4
63. Yin Y, Yang ZF, Wen ZH, et al. Modification of as Synthesized SBA-15 with Pt nanoparticles: Nanoconfinement Effects Give a Boost for Hydrogen Storage at Room Temperature. *Sci Rep.* 2017;7(1):1-10. doi:10.1038/s41598-017-04346-9
64. Wu HC, Chen TC, Lai NC, et al. Synthesis of sub-nanosized Pt particles on mesoporous SBA-15 material and its application to the CO oxidation reaction. *Nanoscale.* 2015;7(40):16848-16859. doi:10.1039/c5nr04943a
65. Yan Z, Fu L, Zuo X, Yang H. Green assembly of stable and uniform silver nanoparticles on 2D silica nanosheets for catalytic reduction of 4-nitrophenol. *Appl Catal B Environ.* 2018;226(December 2017):23-30. doi:10.1016/j.apcatb.2017.12.040
66. Tian B, Liu X, Yang H, et al. General Synthesis of Ordered Crystallized Metal Oxide Nanoarrays Replicated by Microwave-Digested Mesoporous Silica. *Adv Mater.* 2003;15(16):1370-1374. doi:10.1002/adma.200305211
67. Sun X, Shi Y, Zhang P, et al. Container effect in nanocasting synthesis of mesoporous metal oxides. *J Am Chem Soc.* 2011;133(37):14542-14545. doi:10.1021/ja2060512
68. Jain PK, Huang X, El-Sayed IH, El-Sayed MA. Noble metals on the nanoscale: Optical and photothermal properties and some applications in imaging, sensing, biology, and medicine. *Acc Chem Res.* 2008;41(12):1578-1586. doi:10.1021/ar7002804
69. Xu Y, Chen L, Wang X, Yao W, Zhang Q. Recent advances in noble metal based composite nanocatalysts: Colloidal synthesis, properties, and catalytic applications. *Nanoscale.* 2015;7(24):10559-10583. doi:10.1039/c5nr02216a
70. Dreaden EC, Alkilany AM, Huang X, Murphy CJ, El-Sayed MA. The golden age: Gold nanoparticles for biomedicine. *Chem Soc Rev.* 2012;41(7):2740-2779. doi:10.1039/c1cs15237h
71. Blondeau D, Roy L, Dumont S, Godin G, Martineau I. Physicians' and pharmacists' attitudes toward the use of sedation at the end of life: Influence of prognosis and type of suffering. *J Palliat Care.* 2005;21(4):238-245. doi:10.1177/082585970502100402

72. Tahir MB, Nawaz T, Nabi G, Sagir M, Khan MI, Malik N. Role of nanophotocatalysts for the treatment of hazardous organic and inorganic pollutants in wastewater. *Int J Environ Anal Chem.* 2022;102(2):491-515. doi:10.1080/03067319.2020.1723570
73. Nogueira RFP, Oliveira MC, Paterlini WC. Simple and fast spectrophotometric determination of H<sub>2</sub>O<sub>2</sub> in photo-Fenton reactions using metavanadate. *Talanta.* 2005;66(1):86-91. doi:10.1016/j.talanta.2004.10.001
74. Zhang J, Huang B, Shao Q, Huang X. Highly Active, Selective, and Stable Direct H<sub>2</sub>O<sub>2</sub> Generation by Monodisperse Pd-Ag Nanoalloy. *ACS Appl Mater Interfaces.* 2018;10(25):21291-21296. doi:10.1021/acsami.8b03756
75. Dutta S, Yu IKM, Tsang DCW, et al. Green synthesis of gamma-valerolactone (GVL) through hydrogenation of biomass-derived levulinic acid using non-noble metal catalysts: A critical review. *Chem Eng J.* 2019;372:992-1006. doi:10.1016/j.cej.2019.04.199
76. Gao F, Goodman DW. Pd–Au bimetallic catalysts: Understanding alloy effects from planar models and (supported) nanoparticles. *Chem Soc Rev.* 2012;41(24):8009-8020. doi:10.1039/c2cs35160a
77. Zhu W, Chen S. Recent Progress of Single-atom Catalysts in the Electrocatalytic Reduction of Oxygen to Hydrogen Peroxide. *Electroanalysis.* 2020;32(12):2591-2602. doi:10.1002/elan.202060334
78. Serrà A, Gómez E, Vallés E. Novel electrodeposition media to synthesize CoNi-Pt Core@Shell stable mesoporous nanorods with very high active surface for methanol electro-oxidation. *Electrochim Acta.* 2015;174:630-639. doi:10.1016/j.electacta.2015.06.069
79. Serrà A, Gómez E, Montiel M, Vallés E. Effective new method for synthesizing Pt and CoPt<sub>3</sub> mesoporous nanorods. New catalysts for ethanol electro-oxidation in alkaline medium. *RSC Adv.* 2016;6(53):47931-47939. doi:10.1039/c6ra06407h
80. Serrà A, Gómez E, Golosovsky I V., Nogués J, Vallés E. Effective ionic-liquid microemulsion based electrodeposition of mesoporous Co-Pt films for methanol oxidation catalysis in alkaline media. *J Mater Chem A.* 2016;4(20):7805-7814. doi:10.1039/c6ta02035f
81. Serrà A, Montiel M, Gómez E, Vallés E. Electrochemical synthesis of mesoporous CoPt nanowires for methanol oxidation. *Nanomaterials.* 2014;4(2):189-202. doi:10.3390/nano4020189
82. Serrà A, Artal R, Philippe L, Gómez E. Electrodeposited Ni-Rich Ni-Pt Mesoporous Nanowires for Selective and Efficient Formic Acid-Assisted



- Hydrogenation of Levulinic Acid to  $\gamma$ -Valerolactone. *Langmuir*. 2021;37(15):4666-4677. doi:10.1021/acs.langmuir.1c00461
83. Esplandiu MJ, Zhang K, Fraxedas J, Sepulveda B, Reguera D. Unraveling the Operational Mechanisms of Chemically Propelled Motors with Micropumps. *Acc Chem Res*. 2018;51(9):1921-1930. doi:10.1021/acs.accounts.8b00241
84. Ding R, Li W, Wang X, et al. A brief review of corrosion protective films and coatings based on graphene and graphene oxide. *J Alloys Compd*. 2018;764:1039-1055. doi:10.1016/j.jallcom.2018.06.133
85. Ashworth V. Principles of cathodic protection. *Shreir's Corros*. 2010;2:2747-2762. doi:10.1016/B978-044452787-5.00152-9
86. Paul D. DC Stray Current in Rail Transit Systems and Cathodic Protection [History]. *IEEE Ind Appl Mag*. 2016;22(1):8-13. doi:10.1109/MIAS.2015.2481754
87. Wang Q, Ma Y, Xing S. Comparative study of Cu-based bimetallic oxides for Fenton-like degradation of organic pollutants. *Chemosphere*. 2018;203:450-456. doi:10.1016/j.chemosphere.2018.04.013
88. Shen H, Sun P, Meng X, Wang J, Liu H, Xu L. Nanoscale Fe<sub>0</sub>/Cu<sub>0</sub> bimetallic catalysts for Fenton-like oxidation of the mixture of nuclear-grade cationic and anionic exchange resins. *Chemosphere*. 2021;269(xxxx):128763. doi:10.1016/j.chemosphere.2020.128763
89. Li H, Yuan Z, Xing Y, et al. Acetone fractionation: A simple and efficient method to improve the performance of lignin for dye pollutant removal. *RSC Adv*. 2019;9(61):35895-35903. doi:10.1039/c9ra07017f
90. Liu Y, Chen Z, Yang X, et al. A facile synthesis of high entropy alloy nanoparticle-activated carbon nanocomposites for synergetic degradation of methylene blue. *RSC Adv*. 2021;11(40):24636-24646. doi:10.1039/d1ra03661k
91. Zhang S, Wang D, Zhou L, Zhang X, Fan P, Quan X. Intensified internal electrolysis for degradation of methylene blue as model compound induced by a novel hybrid material: Multi-walled carbon nanotubes immobilized on zero-valent iron plates (Fe<sub>0</sub>-CNTs). *Chem Eng J*. 2013;217:99-107. doi:10.1016/j.cej.2012.11.103
92. Plasqui G, Kester ADM, Westerterp KR. Seasonal variation in sleeping metabolic rate, thyroid activity, and leptin. *Am J Physiol - Endocrinol Metab*. 2003;285(2 48-2):338-343. doi:10.1152/ajpendo.00488.2002
93. Wei B, Li X, Sun H, Song K, Wang L. Improved degradation capability of

- Fe81B10C9 amorphous ribbon with the nanoscale layer rich of small atoms (B, C). *J Non Cryst Solids*. 2021;564(April):120838. doi:10.1016/j.jnoncrysol.2021.120838
94. Li X, Yang S, Dzakpasu M, et al. Galvanic corrosion of zero-valent iron to intensify Fe<sup>2+</sup> generation for peroxydisulfate activation. *Chem Eng J*. 2021;417:128023. doi:10.1016/j.cej.2020.128023
  95. Liang SX, Zhang Q, Jia Z, Zhang W, Wang W, Zhang LC. Tailoring surface morphology of heterostructured iron-based Fenton catalyst for highly improved catalytic activity. *J Colloid Interface Sci*. 2021;581:860-873. doi:10.1016/j.jcis.2020.07.138
  96. Xie Y, Xie S, Yang H, Deng Y, Qian H, Zeng X. A dramatically improved degradation efficiency of azo dyes by zero valent iron powders decorated with in-situ grown nanoscale Fe<sub>2</sub>B. *J Alloys Compd*. 2020;842:155818. doi:10.1016/j.jallcom.2020.155818
  97. Ju Y, Liu X, Liu R, et al. Environmental application of millimeter-scale sponge iron (s-Fe<sup>0</sup>) particles (II): The effect of surface copper. *J Hazard Mater*. 2015;287(Ii):325-334. doi:10.1016/j.jhazmat.2015.01.019
  98. Bayat M, Nasernejad B, Falamaki C. Preparation and characterization of nano-galvanic bimetallic Fe/Sn nanoparticles deposited on talc and its enhanced performance in Cr(VI) removal. *Sci Rep*. 2021;11(1):1-17. doi:10.1038/s41598-021-87106-0
  99. Fu P, Lin X, Chen Z. Porous Fe<sup>0</sup>/C ceramsites for removal of aqueous Pb(II) ions: Equilibrium, long-term performance and mechanism studies. *RSC Adv*. 2018;8(45):25445-25455. doi:10.1039/c8ra05164j
  100. Lai B, Zhang Y, Chen Z, Yang P, Zhou Y, Wang J. Removal of p-nitrophenol (PNP) in aqueous solution by the micron-scale iron-copper (Fe/Cu) bimetallic particles. *Appl Catal B Environ*. 2014;144:816-830. doi:10.1016/j.apcatb.2013.08.020
  101. Yang W, Logan BE. Engineering a membrane based air cathode for microbial fuel cells: Via hot pressing and using multi-catalyst layer stacking. *Environ Sci Water Res Technol*. 2016;2(5):858-863. doi:10.1039/c6ew00098c
  102. Ren Y, Zhou J, Lai B, Tang W, Zeng Y. Fe<sup>0</sup> and Fe<sup>0</sup> fully covered with Cu<sup>0</sup> (Fe<sup>0</sup> + Fe/Cu) in a fixed bed reactor for nitrate removal. *RSC Adv*. 2016;6(110):108229-108239. doi:10.1039/c6ra24014c
  103. Wei X, Zhu N, Huang J, et al. Rapid and efficient reduction of chromate by novel Pd/Fe@biomass derived from *Enterococcus faecalis*. *Environ Res*. 2022;204(PA):112005. doi:10.1016/j.envres.2021.112005

104. Corma A, Garci H. Supported gold nanoparticles as catalysts for organic reactions. *Chem Soc Rev.* 2008;37(9):2096-2126. doi:10.1039/b707314n
105. Lohse SE, Murphy CJ. The quest for shape control: A history of gold nanorod synthesis. *Chem Mater.* 2013;25(8):1250-1261. doi:10.1021/cm303708p
106. Estevez MC, Alvarez M, Lechuga LM. Integrated optical devices for lab-on-a-chip biosensing applications. *Laser Photonics Rev.* 2012;6(4):463-487. doi:10.1002/lpor.201100025
107. Kidambi S, Li J, Dai JH, Bruening ML. Catalytic Pd nanoparticles embedded in polyelectrolyte multilayers. *Abstr Pap Am Chem S.* 2004;227(Part 2):201-PMSE.
108. Amendola V, Saija R, Maragò OM, Iatì MA. Superior plasmon absorption in iron-doped gold nanoparticles. *Nanoscale.* 2015;7(19):8782-8792. doi:10.1039/c5nr00823a
109. Li Z, Lopez-Ortega A, Aranda-Ramos A, et al. Simultaneous Local Heating/Thermometry Based on Plasmonic Magnetochromic Nanoheaters. *Small.* 2018;14(24):1-10. doi:10.1002/smll.201800868
110. Obaidat IM, Narayanaswamy V, Alaabed S, Sambasivam S, Muralee Gopi CVV. Principles of magnetic hyperthermia: A focus on using multifunctional hybrid magnetic nanoparticles. *Magnetochemistry.* 2019;5(4). doi:10.3390/magnetochemistry5040067
111. Chong WH, Chin LK, Tan RLS, Wang H, Liu AQ, Chen H. Stirring in suspension: Nanometer-sized magnetic stir bars. *Angew Chemie - Int Ed.* 2013;52(33):8570-8573. doi:10.1002/anie.201303249
112. Sun S, Murray CB, Weller D, Folks L, Moser A. Monodisperse FePt nanoparticles and ferromagnetic FePt nanocrystal superlattices. *Science (80- ).* 2000;287(5460):1989-1992. doi:10.1126/science.287.5460.1989
113. Salem AK, Searson PC, Leong KW. Multifunctional nanorods for gene delivery. *Nat Mater.* 2003;2(10):668-671. doi:10.1038/nmat974
114. Pullen AE, Zeltner S, Olk RM, Hoyer E, Abboud KA, Reynolds JR. Electrically Conducting Materials Based on  $\mu$ -Tetrathiooxalato-Bridged Bimetallic Ni(II) Anionic Complexes. *Inorg Chem.* 1997;36(19):4163-4171. doi:10.1021/ic9701219
115. Zhang C, Kc S, Nie Y, et al. Charge Mediated Reversible Metal-Insulator Transition in Monolayer MoTe<sub>2</sub> and W<sub>x</sub>Mo<sub>1-x</sub>Te<sub>2</sub> Alloy. *ACS Nano.* 2016;10(8):7370-7375. doi:10.1021/acsnano.6b00148
116. Lv R, Robinson JA, Schaak RE, et al. Transition metal dichalcogenides and

- beyond: Synthesis, properties, and applications of single- and few-layer nanosheets. *Acc Chem Res.* 2015;48(1):56-64. doi:10.1021/ar5002846
117. Duerloo KAN, Li Y, Reed EJ. Structural phase transitions in two-dimensional Mo-and W-dichalcogenide monolayers. *Nat Commun.* 2014;5(May). doi:10.1038/ncomms5214
  118. Ou M, Wang X, Yu L, et al. The Emergence and Evolution of Borophene. *Adv Sci.* 2021;8(12):1-29. doi:10.1002/advs.202001801
  119. Das S, Bera MK, Tong S, et al. A Self-Limiting Electro-Ablation Technique for the Top-Down Synthesis of Large-Area Monolayer Flakes of 2D Materials. *Sci Rep.* 2016;6(December 2015):1-9. doi:10.1038/srep28195
  120. Yang R, Mei L, Zhang Q, et al. High-yield production of mono- or few-layer transition metal dichalcogenide nanosheets by an electrochemical lithium ion intercalation-based exfoliation method. *Nat Protoc.* 2022;17(2):358-377. doi:10.1038/s41596-021-00643-w
  121. Zhang L, Chen C, Zhou J, et al. Solid Phase Exfoliation for Producing Dispersible Transition Metal Dichalcogenides Nanosheets. *Adv Funct Mater.* 2020;30(45):1-8. doi:10.1002/adfm.202004139
  122. Shen PC, Lin Y, Wang H, et al. CVD Technology for 2-D Materials. *IEEE Trans Electron Devices.* 2018;65(10):4040-4052. doi:10.1109/TED.2018.2866390
  123. Zhang J, Wang F, Shenoy VB, Tang M, Lou J. Towards controlled synthesis of 2D crystals by chemical vapor deposition (CVD). *Mater Today.* 2020;40(xx):132-139. doi:10.1016/j.mattod.2020.06.012
  124. Zhang X, Ma G, Wang J. Hydrothermal synthesis of two-dimensional MoS<sub>2</sub> and its applications. *Tungsten.* 2019;1(1):59-79. doi:10.1007/s42864-019-00014-9
  125. Han SA, Bhatia R, Kim SW. Synthesis, properties and potential applications of two-dimensional transition metal dichalcogenides. *Nano Converg.* 2015;2(1). doi:10.1186/s40580-015-0048-4
  126. Li H, Lu G, Yin Z, et al. Optical identification of single- and few-layer MoS<sub>2</sub> sheets. *Small.* 2012;8(5):682-686. doi:10.1002/smll.201101958
  127. Zhang W, Chuu CP, Huang JK, et al. Ultrahigh-Gain Photodetectors Based on Atomically Thin Graphene-MoS<sub>2</sub> Heterostructures. *Sci Rep.* 2015;4:1-8. doi:10.1038/srep03826
  128. Zeng H, Dai J, Yao W, Xiao D, Cui X. Valley polarization in MoS<sub>2</sub> monolayers by optical pumping. *Nat Nanotechnol.* 2012;7(8):490-493. doi:10.1038/nnano.2012.95

129. Manzeli S, Ovchinnikov D, Pasquier D, Yazyev O V., Kis A. 2D transition metal dichalcogenides. *Nat Rev Mater.* 2017;2. doi:10.1038/natrevmats.2017.33
130. Pulkin A, Yazyev O V. Spin- and valley-polarized transport across line defects in monolayer MoS<sub>2</sub>. *Phys Rev B.* 2016;93(4):1-5. doi:10.1103/PhysRevB.93.041419
131. Li W, Qian X, Li J. Phase transitions in 2D materials. *Nat Rev Mater.* 2021;6(9):829-846. doi:10.1038/s41578-021-00304-0
132. Temnov V V., Armelles G, Woggon U, et al. Active magneto-plasmonics in hybrid metal-ferromagnet structures. *Nat Photonics.* 2010;4(2):107-111. doi:10.1038/nphoton.2009.265
133. Choi JR, Oh SJ, Ju H, Cheon J. Massive fabrication of free-standing one-dimensional Co/Pt nanostructures and modulation of ferromagnetism via a programmable barcode layer effect. *Nano Lett.* 2005;5(11):2179-2183. doi:10.1021/nl051190k

## **2. Chemical and photocatalysis for water remediation**

The multi-component particles developed in this thesis can be useful tools for different application fields, such as environmental remediation, novel medical therapies, or sustainable catalytic processes involving the in-situ production of valuable chemicals. Therefore, in this section, a brief summary of the state of the art of these applications will be compiled.

## 2.1 The global picture of chemical pollution.

Remediation of polluted environments is one of the biggest challenges faced by the global community to provide sustainable living conditions. Increased industrialization, urbanization and agricultural activities with the rampant use of pesticides have led to unprecedented mining of natural resources and improper disposal of harmful industrial by-products, all of which directly and severely impact soil, water and air degradation (Figure 2-1). The precious water resource is suffering not only the ravages of pollution, but there is also a growing problem of scarcity, promoted by climate change and the depletion of natural water reservoirs. It is estimated that at least 1 out of 4 people will be affected by water shortages by 2050, threatening one of the fundamental rights of humanity. Therefore, the exploration of sustainable strategies to guarantee clean and affordable water has become a global and urgent focus in research programs and political actions which should be fulfilled.

The nature and origin of water pollutants are diverse. Contaminants can be frequently detected in treated wastewater, surface and groundwater, and drinking water and can be of organic, inorganic, or biological origin. Typical inorganic contaminants are heavy metals, fluorides and nitrates. Organic pollutants have their origin in agricultural activity (fertilizers, pesticides, and herbicides), livestock activity or from the inadequate disposal of by-products of the chemical industry (plasticizers, oils, lubricants, oily residues, volatile aromatic hydrocarbons, chlorinated byproducts, etc.)<sup>1</sup>. In addition to the above compounds, there is a growing presence of so-called "emerging organic pollutants" such as pharmaceuticals or species found in household or personal care products. Many of these compounds belong to the so-called Persistent Organic Pollutants (POPs), which are expensive to treat and can also travel long distances, bioaccumulate in human tissues and aquatic and terrestrial animals, as well as biomagnify through the food chain, seriously affecting our entire ecosystem<sup>2</sup>. Finally, climate change and biological organisms (bacteria, viruses, etc.) comprise the other big family of contaminants, causing many infectious diseases transmitted through water. Moreover, the increased use of antibiotics and bactericides has resulted in the development of multi-resistant bacteria that are difficult to be inactivated. In this scenario, the exponential growth of these microorganisms represents a threat to global health<sup>3</sup>.

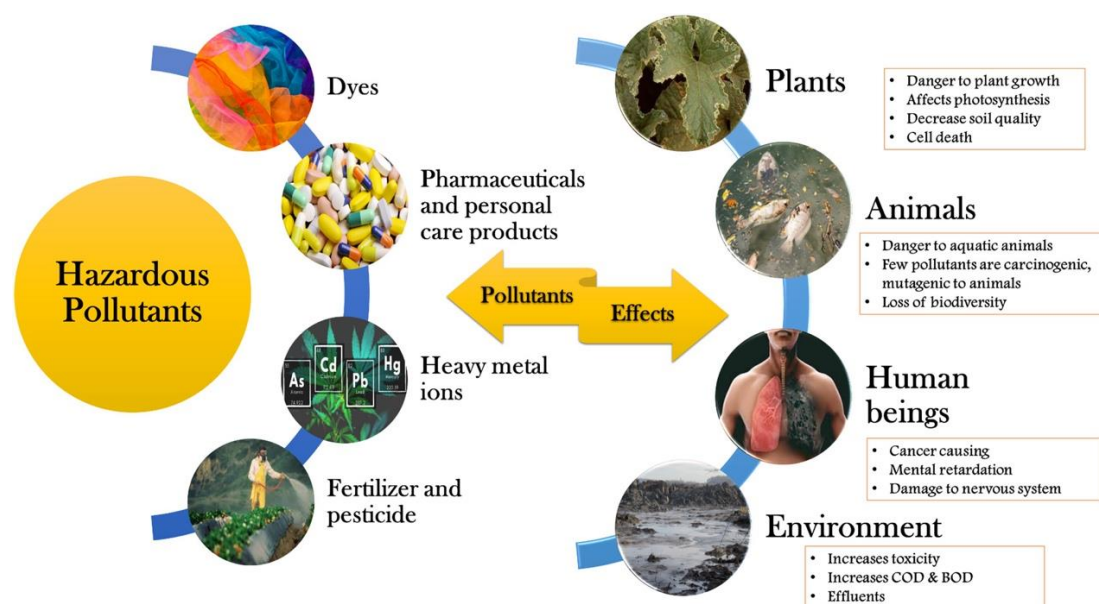


**Figure 2-1.** Hazardous contaminants and their effects on the environment<sup>4</sup>.

### 2.1.1 Advanced oxidation processes

As mentioned, the presence of chemical pollutants in both industrial and municipal wastewater is one of the major concerns nowadays. The majority of these contaminants, both synthetic organic chemicals and naturally occurring substances, enter the aquatic medium in a variety of ways and depending on their water solubility, can be transported and distributed throughout the water cycle<sup>5</sup>.

Several technologies remove and degrade toxic pollutants from water and wastewater, such as pollutant coagulation, sedimentation, adsorption, membrane process, chemical oxidation process or biological treatments<sup>6</sup>. However, these processes can yield incomplete removal, require high consumption of chemical reagents, involve high cost and time-consuming treatments, and can generate toxic secondary pollutants. In addition, Effective and more sustainable alternatives for water treatment technologies are required to improve water treatments, especially for the so-called Persistent Organic Pollutants (POPs)<sup>7</sup>.

Over the decades, many research efforts devoted to developing a new, eco-friendly, and more promising technique called Advanced oxidation processes (AOPs).

AOPs are the aqueous phase oxidation methods that rely on the intermediation of highly reactive species such as hydroxyl radicals ( $\cdot\text{OH}$ ), which lead to the destruction of target pollutant<sup>8</sup>. Unlike conventional methods, AOPs can be applied for the treatment of several types of wastewaters in most cases with total mineralization efficiency. Mineralization refers the complete conversion of pollutants into  $\text{CO}_2$ ,  $\text{H}_2\text{O}$ , and other inorganic ions.



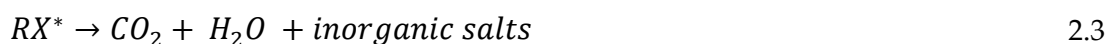
Reactive oxygen species are atoms or molecules that contain an unpaired electron around the atomic shells making them highly unstable and reactive (e.g. superoxide ( $\cdot\text{O}_2^-$ ), hydroperoxyl ( $\text{HO}_2\cdot$ ), hydroxyl ( $\cdot\text{OH}$ ))<sup>9</sup>. Although in the degradation process there are other species involved, the hydroxyl radicals are the strongest oxidants after fluorine that are responsible for the degradation of the contaminants.

Having a high standard potential of 2.8 V versus normal hydrogen electrode (NHE) in acidic media and 1.55 V versus NHE in basic media,  $\cdot\text{OH}$  can oxidize almost every highly toxic organic compound to  $\text{CO}_2$  and inorganic ions (Table 2-1)<sup>10</sup>.

**Table 2-1.** Oxidation potential of some oxidants<sup>6</sup>.

Species	Oxidation potential (V)
Fluorine	3.03
Hydroxyl Radical	2.80
Atomic Oxygen	2.42
Ozone	2.07
Hydrogen Peroxide	1.78
Perhydroxyl Radical	1.70
Permanganate	1.68
Hypobromous Acid	1.59
Chlorine Dioxide	1.57
Hypochlorous Acid	1.49
Hypoiodous Acid	1.45
Chlorine	1.36
Bromine	1.09
Iodine	0.54

Hydrogen abstraction is one of the mechanisms for oxidation of organic molecules by hydroxyl radical (2.1). As a result, this reaction generates organic radicals, which by the addition of molecular oxygen yield peroxy radicals (2.2). Last, these intermediates trigger thermal (chain) oxidative degradation reactions, yielding carbon dioxide, water and inorganic salts, a process called mineralization (2.3).



The reaction scheme shows that the rate and efficiency of the oxidative degradation processes, which are primarily based on the production and the reactivity of radical intermediates, depend on the energy needed in order to homolyse a given chemical bond, and to a large extent on the concentration of dissolved molecular oxygen<sup>9</sup>.

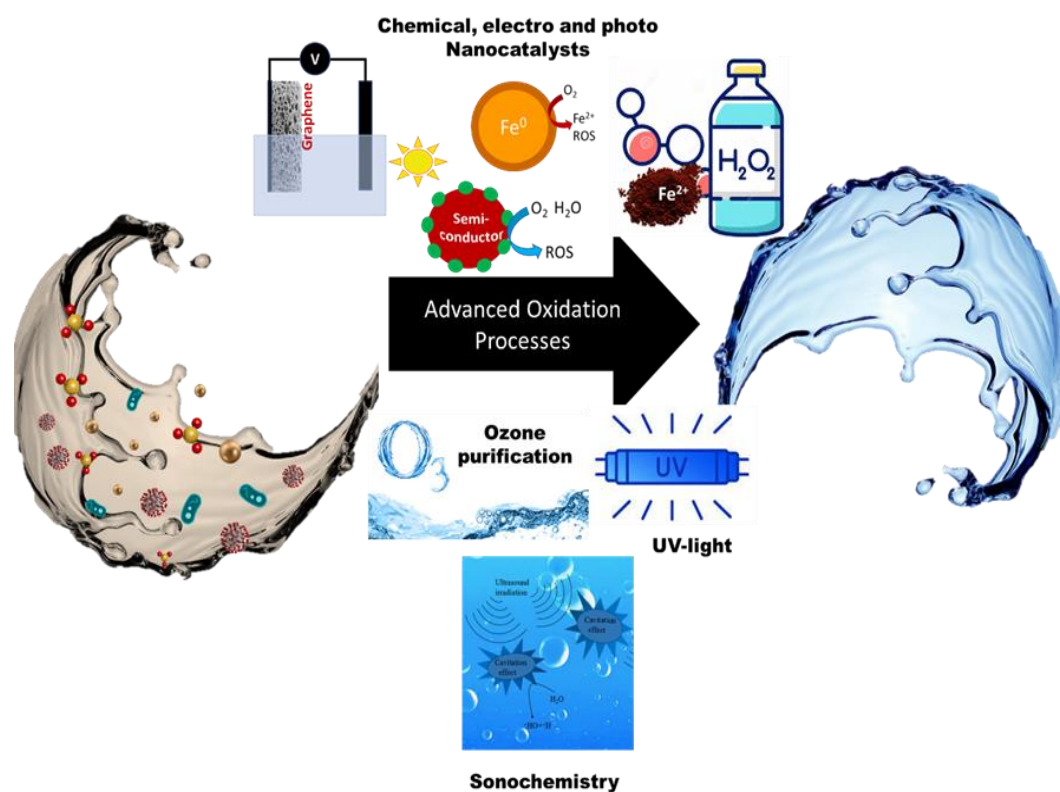


**Figure 2-2.** Different advanced oxidation processes.

AOPs are divided into two main groups: nonphotochemical and photochemical<sup>11,12</sup>. Non-photochemical AOPs include: sono-chemical cavitation, Fenton and Fenton-like processes, ozonation at high pH, ozone/hydrogen peroxide, wet air oxidation, catalytic–electrochemical processes, etc. Photochemical oxidation processes include homogenous processes such as vacuum UV photolysis, UV/H<sub>2</sub>O<sub>2</sub>, UV/O<sub>3</sub>, UV/ O<sub>3</sub>/ H<sub>2</sub>O<sub>2</sub>, photo-Fenton, etc, and heterogeneous photocatalysis processes (Figure 2-2)<sup>13</sup>.

## 2.2 Nonphotochemical advanced oxidation processes

The diverse nature of water contaminants has led to the development of a wide variety of treatment systems, which can be applied individually or in a combined way. Chemical degradation causes crucial changes in the chemical structure of pollutants, being able to degrade them even at low concentrations.

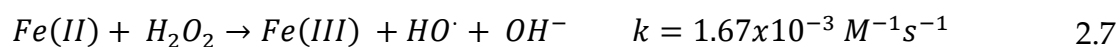
Sonochemical processes entail using ultrasound (US), which refers to sound waves with frequencies ranging from 20 kHz to 500 MHz<sup>14</sup>. In a sonochemical process, ultrasound waves perpetrate through an aqueous solution, generating

cavitation bubbles. Thus, highly reactive radicals ( $\cdot\text{OH}$ ) are formed, moving through the liquid/gas interface, turn into hydroperoxyl ( $\text{HO}_2$ ) radicals. In case of a high concentration, hydroperoxyl radicals recombine with each other and form  $\text{H}_2\text{O}_2$  destroying organic contaminants. However, the application of sonolysis is limited because of high energy consumption, which prevents its use in high volumes<sup>15-17</sup>.

On the contrary, ozonation is extremely powerful with short reaction times, allowing the treatment of a huge number of wastewaters. The process relies on ozone, which is unstable in water and decomposes spontaneously through a complex mechanism involving the production of hydroxyl free radicals. As a result, both ozone and radicals contribute to the degradation of pollutants. Similarly, ozonation also requires high operating costs primarily associated with ozone generation. However, combining ozone technology and ultraviolet (UV) radiation can significantly decrease energy consumption. Additionally, the UV photons can activate ozone molecules resulting in the formation of hydroxyl radicals<sup>12,18,19</sup>.

### 2.2.1 Fenton reaction

Fenton and related reactions are one of the most used AOPs in the treatment of wastewater. The typical Fenton process is a homogeneous catalytic process based on the reaction between iron and hydrogen peroxide, resulting in the formation of reactive oxygen species (ROS)<sup>20</sup>. The mixture of  $\text{H}_2\text{O}_2$  and  $\text{Fe}^{2+}$  is called a Fenton reagent. In 1894 Fenton reported that ferrous salts ( $\text{Fe}^{2+}$ ) could activate  $\text{H}_2\text{O}_2$  to degrade tartaric acid<sup>21</sup>. Essentially, the Fenton reaction starts with the formation of ROS, such as hydroxyl radicals, with a high-rate constant. Firstly,  $\text{Fe}^{2+}$  oxidizes  $\text{Fe}^{3+}$  in the presence of hydrogen peroxide ( $\text{H}_2\text{O}_2$ ) (2.4). Next  $\text{Fe}^{3+}$  reacts with hydrogen peroxide (2.5) and forms  $\text{Fe}^{2+}$  which then decomposes  $\text{H}_2\text{O}_2$  and generates hydroxyl and superoxide radicals (2.7). Most Fenton-based AOPs use iron as a catalyst, and their success depends on efficient redox cycling of iron between the oxidation states II and III (Figure 2-3)<sup>22</sup>.



The Fenton reaction can be carried out at room temperature and atmospheric pressure. Additionally, the reagents are cost-effective, easy to handle, readily available and environmentally friendly<sup>23</sup>. However, the Fenton reaction such has some drawbacks, which include the high  $\text{H}_2\text{O}_2$  concentration, the acidic reaction conditions and the high amount of ferrous iron salts needed, which must be separated from the treated effluent (generally by precipitation) leading to considerable loads of iron-containing sludge that require further management.

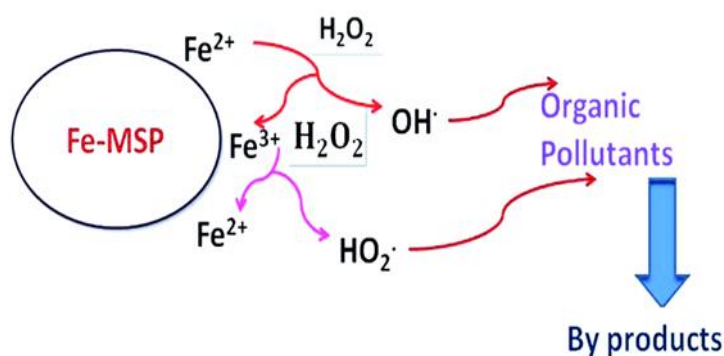


**Figure 2-3.** Schematic illustration of Fenton reaction<sup>24</sup>.

As mentioned, Fenton reaction strongly depends on the reaction pH. The optimum pH for the Fenton reaction is 3 in most systems<sup>25,26</sup>. The activity of the reaction at higher pH decreases due to the presence of relatively inactive iron oxyhydroxides, and the formation of ferric hydroxide precipitates<sup>27,28</sup>. Thus, less ROS is generated due to the presence of fewer iron ions. At high pHs, the oxidation potential of hydroxyl radicals also decreases<sup>29</sup>. Furthermore, the auto-decomposition rate of  $\text{H}_2\text{O}_2$  is accelerated<sup>30</sup>. At very low pH, the rate of contaminant removal diminishes with the formation of iron complex species  $[\text{Fe}(\text{H}_2\text{O})_6]^{2+}$ , which reacts with  $\text{H}_2\text{O}_2$  extremely slowly compared to  $\text{Fe}^{2+}$  or  $\text{Fe}^{3+}$ . Moreover, at low pH,  $\text{H}^+$  acts as a hydroxyl radical scavenger, forming oxonium ions  $\text{H}_3\text{O}_2^+$  that cause hydrogen peroxide to become electrophilic, reducing its reactivity with iron.

Generally, increasing the concentration of ferrous ions increases the rate of the Fenton reaction. However, the excess amount of ferrous ions also increases the formation of iron salts in the process, which leads to iron poisoning<sup>31</sup>.

The overall efficiency of the Fenton process also depends on the concentration of  $\text{H}_2\text{O}_2$ . Increasing the  $\text{H}_2\text{O}_2$  concentration increases the contaminant degradation significantly. However, the excess amount of  $\text{H}_2\text{O}_2$  scavenges generated hydroxyl radicals<sup>32</sup>. Thus, the optimum concentration should be selected during the Fenton process.

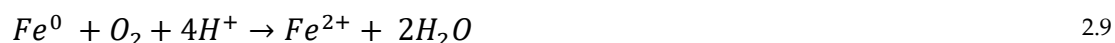
### 2.2.2 Zero-valent iron and zero-valent metals

Zero-valent metals (such as Fe, Cu, Ag, Ni) are both reducing agents and heterogeneous catalysts for triggering oxidative pathways through Fenton like reactions with the consequent generation of hydroxyl radicals. Among them, zero-valent iron (ZVI) which is non-toxic, abundant, inexpensive and with strong reduction ability, is an ideal candidate. ZVI can easily participate in reduction reactions in Fenton processes providing a large amount of  $Fe^{2+}$  and thus, avoiding the use of extra Fe salts and the formation of Fe sludge<sup>33</sup>.

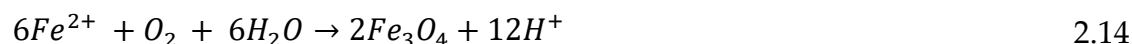
ZVI systems have found relevant applications in remediation of groundwater and wastewater contaminated with various organic and inorganic pollutants. Although granular ZVI has been widely used for such purposes, zero-valent iron nanoparticles have become a more effective version due to their increased specific surface area and chemical reactivity<sup>34</sup>.

ZVI chemistry for contaminant removal/degradation involves complex pathways such as dissolution, adsorption, redox reaction, and etc, which are very dependent on the reaction conditions<sup>35</sup>. The basic reaction of ZVI with water is a redox process consisting in the anodic dissolution of Fe with the consequent cathodic release of hydrogen gas ( 2.8). Under more aerobic conditions, ZVI promotes the oxygen reduction either to water or  $H_2O_2$  ( 2.9 and 2.10) with the concomitant  $Fe^{2+}$  ions release.  $Fe^{2+}$  ions are very sensitive to  $O_2$  and can be oxidized to  $Fe^{3+}$  ( 2.11). The redox processes consume protons with time, making the environment more basic. The changes in pH together with the presence of oxygen can promote the formation of Fe(II) and Fe(III) hydroxides and oxides, forming a passivating layer on iron which can grow over time (2.12-2.14). The oxide layer can be discontinuous at the beginning, but the aging process of oxyhydroxides is usually accompanied by dehydration and conversion to a less porous structure<sup>36</sup>. Additionally, such oxide/hydroxide layer also depends on the size of the ZVI, being more defective and disordered on nanosized ZVI systems as compared to macro/micro sized ZVI systems<sup>37</sup>. Importantly, the passive layer on the surface of pristine ZVI particles acts as a barrier for reagents and products with the consequent drop in the corrosion rate.

Basic condition



Hydroxide/oxide iron shell formation.



Fenton-like reaction.



In fact, such corrosion processes are the key ingredients for contaminant removal, and even the undesirable oxygen-rich passivation layer also has a role to play on that<sup>36</sup>. Figure 2-4 shows different scenarios that can yield to contaminant degradation: reductive degradation, oxidative degradation, (co)precipitation and adsorption (Figure 2-4a, b, c, d). On one hand, some contaminants (e.g., heavy metal compounds, nitrates, dyes, polychlorinated biphenyls, chlorinated pesticides, etc.) can be reductively degraded by: i) the direct reducing power of zero valent iron, ii) in a more indirect way through H<sub>2</sub> or activated hydrogen atoms (H<sup>\*</sup>) adsorbed at the iron surface, or iii) the reducing power of Fe<sup>2+</sup><sup>38</sup>. The direct reduction by ZVI involves the transfer of electrons between ZVI and the oxidizing species (O<sub>2</sub>, H<sup>+</sup>, and contaminants that can accept electrons). This process, due to the interfacial nature of the electron transfer reactions, typically involves a series of steps, including the mass transport of the oxidizing species from the bulk solution to the ZVI surface, the reaction between ZVI and the oxidizing species, as well as the mass transport of products away from the ZVI surface to the bulk solution. Therefore, the direct reduction of the contaminant at the ZVI surface will depend on the structure of the oxide film that grows with time (composition, porosity, thickness) and the nature of the contaminant (chemical nature, size, diffusivity, affinity to the oxide film). Oxide defects such as pits or pinholes can favour the direct electron transfer process.

Although the iron oxide layer limits redox pathways over time, some positive aspects from this layer can be rescued to be used in decontamination processes. For instance, the outer layer provides active sites for chemisorption and electrostatic interactions that help the adsorption, precipitation or co-precipitation of contaminants, a strategy widely used in heavy metal removal<sup>39</sup>.

On the other hand, the corrosion products of Fe<sup>2+</sup> and H<sub>2</sub>O<sub>2</sub> are the key ingredients to produce hydroxyl radicals ·OH (2.15-2.17) and trigger the oxidative pathway for degradation of organic contaminants towards their mineralization<sup>40</sup>. One of the expected advantages of these Fenton-like reactions is that the external supply of H<sub>2</sub>O<sub>2</sub> could not be required. In fact, some water

pollutants such as surfactants, herbicides, phenols, etc., have been degraded with the in-situ produced  $\text{H}_2\text{O}_2$ <sup>36</sup>.

As can be seen, the ZVI system offers different possible routes for water remediation. However, more actions are needed to improve the reductive degradation pathway and especially the Fenton-oxidative pathway, focusing on minimizing the effects of the passivation layer and increasing the ZVI redox activity over time. For instance, ZVI activation procedures have been implemented to degrade the oxide layer such as acidic washing, ultrasound or  $\text{H}_2$  pretreatments<sup>41,42</sup>. Other strategies have been focused on accelerating ZVI corrosion by coupling ZVI with another metal<sup>43,44</sup>. For instance Fe is oxidized more slowly when is in contact with a more active metal (e.g., Zn, Al, Mg) and faster when is in contact with a less active metal (e.g., Cu, Pd, Ag) due to the formation of galvanic cells, in which one of the metals act as anode and the other as cathode<sup>45</sup>. As already mentioned in this introductory part (section or page...), when iron is coupled with a more noble material (in the role of cathode), the  $\text{Fe}^{2+}$  release can be enhanced depending on the electrochemical potential difference between both materials. The electrons donated by Fe can be transferred to the noble metal to promote efficiently different reduction processes<sup>46</sup>.

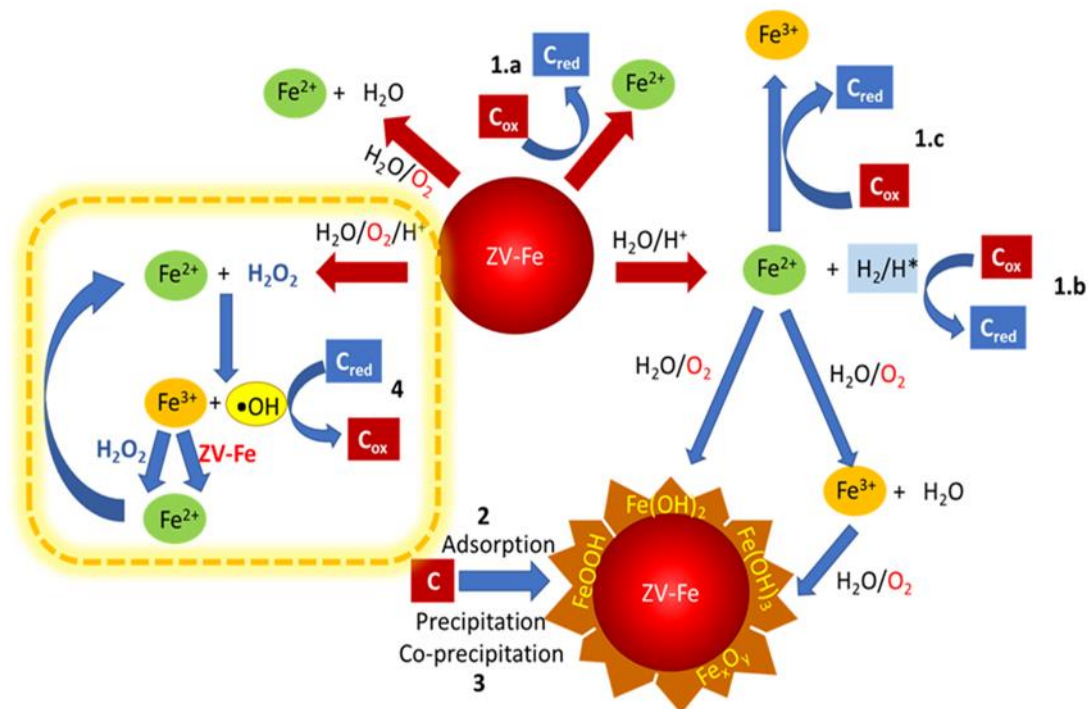


**Figure 2-4.** Different contaminant removal pathways: 1a-c) Reductive degradation, 2) contaminant adsorption, 3) precipitation and co-precipitation, 4) oxidative degradation.

In the case of more anaerobic conditions, the more noble metal can become the reducing agent, promoting the hydrogen production, the direct reduction of contaminants (heavy metal ions/organic compounds) or the indirect reduction of contaminants by activated hydrogen atoms adsorbed on its surface. For instance, the use of Cu/ZVI has significantly improved the generation of activated atomic hydrogen adsorbed on the surface and increased the oxidation of ZVI, which has been exploited for the efficient nitrate reduction or degradation of nitrophenol, polybrominated diphenyl ethers or rhodamine B<sup>47-49</sup>. Moreover, including Cu showed high processing efficiency in a wide range of pHs. A Cu/ZVI system has been also used to degrade the pollutant Trichloroethylene (TCE), displaying better removal (95%) than the ZVI system (25%) at various pH ranges (pH=3-6)<sup>50</sup>. Other examples include the ultrafast and complete reduction of chromates over a wide range of pHs using Pd/ZVI particles and the efficient reduction of arsenates with a ZVI/C system<sup>51-53</sup>.

Under more oxic conditions, it is expected that the reduction of O<sub>2</sub> to H<sub>2</sub>O<sub>2</sub> is facilitated in the more noble metal, accelerating the Fenton process. At the same time, the reducing power of the noble metal can also enhance the reconversion of Fe<sup>3+</sup> to Fe<sup>2+</sup> (2.17) to efficiently sustain the Fenton cycle, while minimizing Fe(OH)<sub>3</sub> hydroxides, which are forming part of the passivation layer. In addition, the acceleration of Fenton-type reactions reduces the formation of some undesirable by-products during remediation, thus achieving a more complete degradation of contaminants<sup>54</sup>. Although there are many studies in the literature of ZVI bimetallic catalysts combined with the external supply of H<sub>2</sub>O<sub>2</sub> (spoiling one of the benefits of ZVI systems), more studies are coming up only relying on the ROS production from the in-situ generation of H<sub>2</sub>O<sub>2</sub> with the improved galvanic cell configuration. That is the case for the ZVI/Carbon system in which H<sub>2</sub>O<sub>2</sub> production and the cycle rate of Fe<sup>2+</sup>/Fe<sup>3+</sup> were significantly increased leading to a fast and complete removal of dyes (e.g., RhB, Methylene blue or Azo orange dyes<sup>55-57</sup>).

Even though there are several papers reporting on the performance of bimetallic ZVI catalysts for water remediation, many aspects still need better characterization, to establish more unequivocally the chemical pathway for pollutant degradation. In some cases, it is not clear enough whether the ·OH radical is actively generated through Fenton/Fenton-type reactions in the ZVI bimetallic catalyst or the process follows more a reductive pathway. For example, a recent article using a ZVI/Cu system under oxic conditions demonstrated that the generation of activated hydrogen atoms enhanced by the generated galvanic cells were the responsible ones for inducing a reductive degradation of a dye, in addition to the adsorption pathway<sup>53</sup>.

This type of study only shows that a deeper research and characterization of the key parameters or ingredients determining the different pollutant removal



pathways are needed to avoid misconceptions and misinterpretations and thus to better establish prospects and challenges. In this respect, part of this thesis will address the use of nZVI in combination with noble metals to elucidate perspectives on their ROS generation performance.

### 2.3 Nanophotocatalytic advanced oxidation processes

Photocatalysis is based on the interaction of photons with molecules or semiconductors. It is an effective, fast, and economical approach for cleaning the toxic ions from industrial wastewater. Similarly, to the chemical catalysts, photocatalysts can be homogeneous or heterogeneous. The homogeneous photocatalysis consists of an assembly of soluble molecular catalysts including a light-absorbing system (photosensitizer) and catalytic sites for oxidation/reduction processes, all in the same phase as the reactants. Heterogeneous photocatalysts are based on the reactions taken place through solid semiconductors. When a semiconductor material is irradiated by light, it absorbs photons with energies higher or equal to its band gap energy,  $E_{bg}$ . As a result, the electron-hole pair is generated due to the excitation of the electrons from the valence band (VB) to the conduction band (CB)<sup>58</sup>. The electrons and holes can migrate to the semiconductor surface for inducing interfacial reduction and oxidation reactions, respectively, thus triggering different contaminant degradation pathways (Figure 2-5a). Nevertheless, these redox pathways also compete with the undesired electron-hole recombination process which must be minimized. The photogenerated electrons and holes must fulfil the minimum thermodynamic energies to allow such surface redox reactions. The bottom of the conduction band must be located at a more negative potential than the redox level of the species undergoing reduction, whereas the top of the valence band must be located at a more positive potential than the redox level of the species undergoing oxidation<sup>59,60</sup>.

Some semiconductors exhibit an appropriate band gap and energy levels for inducing redox reactions with  $H_2O$  and  $O_2$  to produce reactive oxygen species (ROS). In water decontamination processes, both electron–holes and ROS (i.e., peroxides, superoxide, hydroxyl radicals, singlet oxygen, and alpha-oxygen) are responsible either for the degradation and mineralization (that is, the total oxidation of an organic compound, which results in the formation of  $CO_2$  and inorganic salts) of persistent organic compounds or for killing microorganisms<sup>61-63</sup>.

Some of the advantages of heterogeneous photocatalysts are: (i) the potential use of solar energy, (ii) the non-selective degradation of contaminants (even with different physical phases) without generating toxic secondary pollutants, (iii) the short reaction time, mild reaction conditions and less chemical input, and (iv) the quick recovery of the photocatalyst at the end of the process<sup>64,65</sup>.

Recently, researchers have put much effort into improving the efficiency of photocatalysts. One of the strategies is the use of nanomaterials or nanostructured semiconductors which allow: (i) increasing the effective surface area, favouring the adsorption of contaminants prior to the photodegradation reaction; (ii) facilitating and increasing light absorption; (iii) continuous tuning of the position of the CB/VB of the semiconductor as well as the energy of the band gap with the semiconductor dimensions, thus enabling the use of visible light and better adjustment of the redox potential of the bands with respect to the energy level of the species to be degraded; (iv) improving the efficiency of charge carrier transport, which reduces the charge recombination that occurs in most semiconductors; and (v) designing complex structures that can significantly increase pollutant and light-catalyst interaction. All these features have promoted the development of different nanophotocatalysts based on metal oxides (e.g.,  $\text{TiO}_2$ ,  $\text{ZnO}$ ,  $\text{Cu}_2\text{O}$ ,  $\text{CuO}$  etc.), metal sulfides (e.g.,  $\text{CdS}$ ,  $\text{CuS}$ ,  $\text{ZnS}$  etc.), complex oxides (e.g.,  $\text{Bi}_2\text{WO}_6$ ), carbon nitrides, metal-organic structures, dendrimers, and polymeric nanocomposites, among other materials<sup>66,67</sup>.

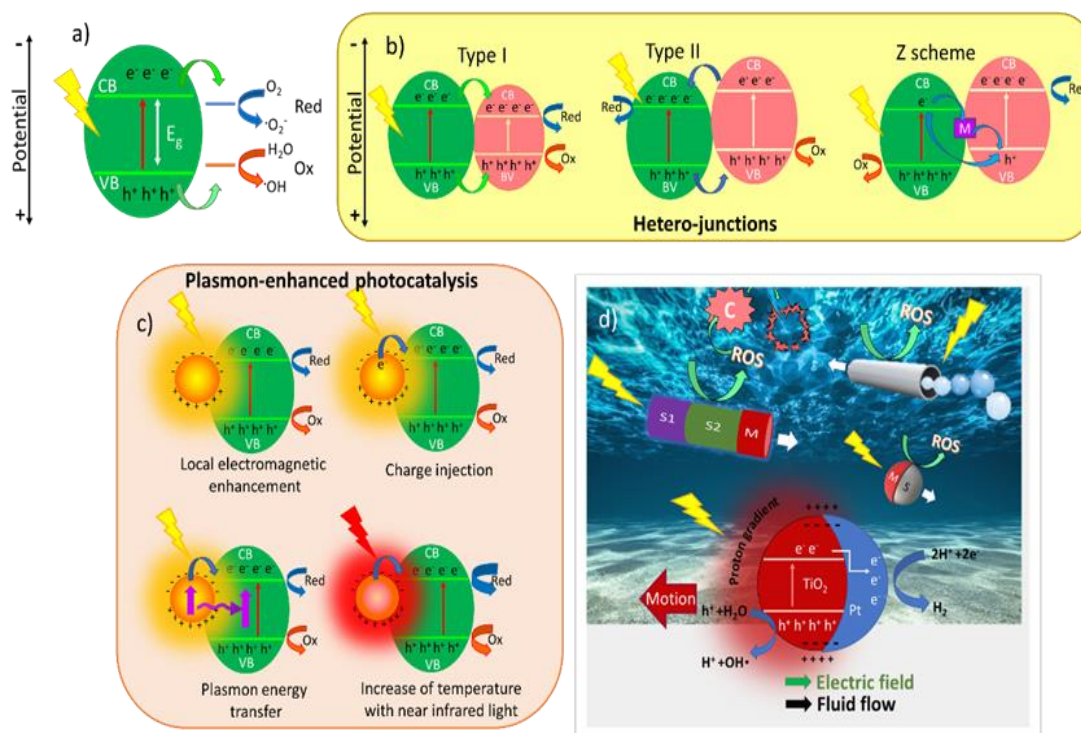


**Figure 2-5.** a) Photoactivation process in a semiconductor. b-d) Strategies to improve photocatalysis by b) using semiconductor heterostructures to separate charges and better adjust the oxidizing and reducing power, c) incorporating plasmonic nanoparticles, d) designing photocatalysts with locomotion capabilities.

A greater synergy in the photocatalytic performance can be achieved by combining the semiconducting nanomaterials with other semiconductor nanomaterials or metals. By coupling nano-photocatalysts with other

semiconductors through heterojunctions charge transfer, charge separation and better band alignment with respect to the redox potential of the species in solution can be tailored (Figure 2-5b). Coupling metal nanostructures with photocatalysts can also minimize electron-hole recombination since metals can act as electron acceptors or as charge mediators between semiconductor heterojunctions. Moreover, the plasmonic effects of metals can contribute to maximize the photocatalysis efficiency through: (i) the injection of hot electrons into the semiconductor's CB, (ii) the increase in photo-absorption via the local amplification of the electromagnetic field with plasmons, (iii) the enhancement of resonance energy transfer to the semiconductor, or (iv) the increase in the photoreaction speed by plasmonic heating (Figure 2-5c)<sup>68,69</sup>. In addition, the diffusion of ROS and the interaction with pollutants can be enhanced by designing micro/nano-photocatalytic platforms with motility capabilities (e.g., nanomotors, nanorobots, and nano-swimmers). These motors can be self-propelled by either chemical reactions, the photoreaction itself (Figure 2-5d) or external magnetic fields, thereby allowing more efficient photodegradation and photomineralization "on the fly"<sup>70</sup>.

### 2.3.1 TMDs as nanophotocatalysts

With the discovery of graphene, related 2D materials have come out with very promising optoelectronic properties. Under this context, semiconductors based on transition metal dichalcogenides (TMDs) such as MoS<sub>2</sub>, WS<sub>2</sub>, MoSe<sub>2</sub>, WSe<sub>2</sub> are showing great potential in the field of photocatalysis<sup>6,71,11</sup>. Some of the special attributes are: (i) low band bandgap for efficient solar energy conversion, (ii) fast and large photon absorption under low photon-flux density due to their large surface area; (iii) tunability of their optoelectronic properties with the number of stacked layers; (iv) very good physicochemical characteristics for creating heterojunctions to facilitate charge transfer; (v) high capability of surface tailoring to exploit edges effects to increase catalytic effects<sup>72,73</sup>; (vi) suitable energy band structure with respect to the redox potentials for hydrogen evolution or water oxidation<sup>73</sup>, (vii) versatility to tune layer stack growth in different orientations and exploit layer edges as highly catalytic activity. All these features make these materials very versatile and tuneable for visible light-responsive photocatalysts or as co-catalysts to enhance photocatalytic activities. Moreover, and as previously discussed, these materials feature different structural phases with different optoelectronic properties that can be also harnessed.

The performance of TMD based photocatalysts can be even increased by coupling the semiconductors with noble metals<sup>74,61,75,76</sup>. At the same time, noble metals can be used to adjust the surface charge density of the photocatalyst and better tune the reagent adsorption process involved in the photocatalysis and thus increase its efficiency or product selectivity in the reaction.

Moreover, the coupling of TMDs with magnetic elements also increases the attributes of the photocatalysts conferring them the possibility of recovery and recycling when used as micro/nanoparticles. Additionally, the magnetic properties can be even exploited to induce hyperthermia or magnetic stirring for increasing (photo)reactants reactivity, mass diffusion and mixing.

Given the appealing physicochemical attributes of TMDs and the synergies that can be accomplished in combination with other nanomaterials, part of these will delve into the photocatalytic aspects of these nanomaterials.

## 2.4 Catalytic Transfer Hydrogenation

The high demand on fossil fuels is destroying the environment by increasing atmospheric pollution, enhancing the greenhouse effect, and depleting the ozone layer. Switching to renewable energy sources can significantly decrease the anthropogenic carbon footprint on a global scale.

Biomass is a clean, renewable, and underused energy source. In particular, lignocellulosic biomasses have enormous potential to meet future demand for bio-based chemicals and materials, reducing our reliance on petroleum resources<sup>77</sup>. Biofuels such as biodiesel and bioethanol, biochemicals, glucose and levulinic acid (LA), and biomaterials such as biodegradable polymers can be produced from biomass. Hydrodeoxygenation (HDO) is essential in converting biomass-derived feedstocks into fuels and valuable chemicals<sup>78</sup>. It is a chemical process that can easily break the bond between C-C or C-H by simultaneously adding H<sub>2</sub>. Conventional processes suffer from several limitations, especially in managing hydrogen gas. The first step starts with reducing the oxygen content, which requires organic solvents to prevent thermal decomposition of biomass. Because of the poor solubility of H<sub>2</sub> in most solvents, high-pressure molecular hydrogen is needed. However, using molecular hydrogen brings its own challenges, such as purchase, transport, safety issues, and hefty storage infrastructure. Therefore, a greener alternative is needed to overcome all of the drawbacks of the conventional method<sup>79,80</sup>.

Catalytic transfer hydrogenation (CTH) is a highly attractive, environmentally friendly, and cost-effective way to valorize renewable compounds. Unlike conventional methods, the hydrogen supply to the system is provided by organic molecules. CTH offers an eco-friendly way of using organic molecules as hydrogen donors in the presence of metal catalysts (Figure 2-6a). Furthermore, it eliminates safety hazards regarding handling hydrogen gas. Additionally, the high-solubility and lower hydrogenating of hydrogen donors in the liquid phase allow highly selective and targeted hydrogenation<sup>77,78</sup>.

Alcohols, formic acid, and formates are reductive organic molecules that can be used as hydrogen sources in biomass conversion. In some cases, after CTH, additional separation and recovery units are needed to recycle the unconverted

hydrogen donor from the reaction mixture. The recycled hydrogen donor can also be reused for other steps of biomass upgrading. For instance, recycled alcohol can produce aldehydes and ketones through carbon chain growth reactions<sup>81</sup>. Besides the hydrogen donor, CTH also requires the catalyst to efficiently activate, cleave, and rearrange the H-H and C-H bonds of hydrogen donor.

Generally, metal and noble metal catalysts are used for the CTH process. They can either be on a high surface area support or unsupported. The support material, it can be inert, e.g., activated carbon<sup>83-85</sup> or can have the acid and base sites of  $\text{Al}_2\text{O}_3$ <sup>86</sup>, zeolites<sup>87,88</sup>, etc. Apart from catalyst support, porous metals such as Ni-Pt, Cu, etc., can increase the surface area. In general, the CTH process starts with the activation of the hydrogen donors by the metal catalysts (Figure 2-6b). Then, the substrate reacts with the catalysts to form the final product.

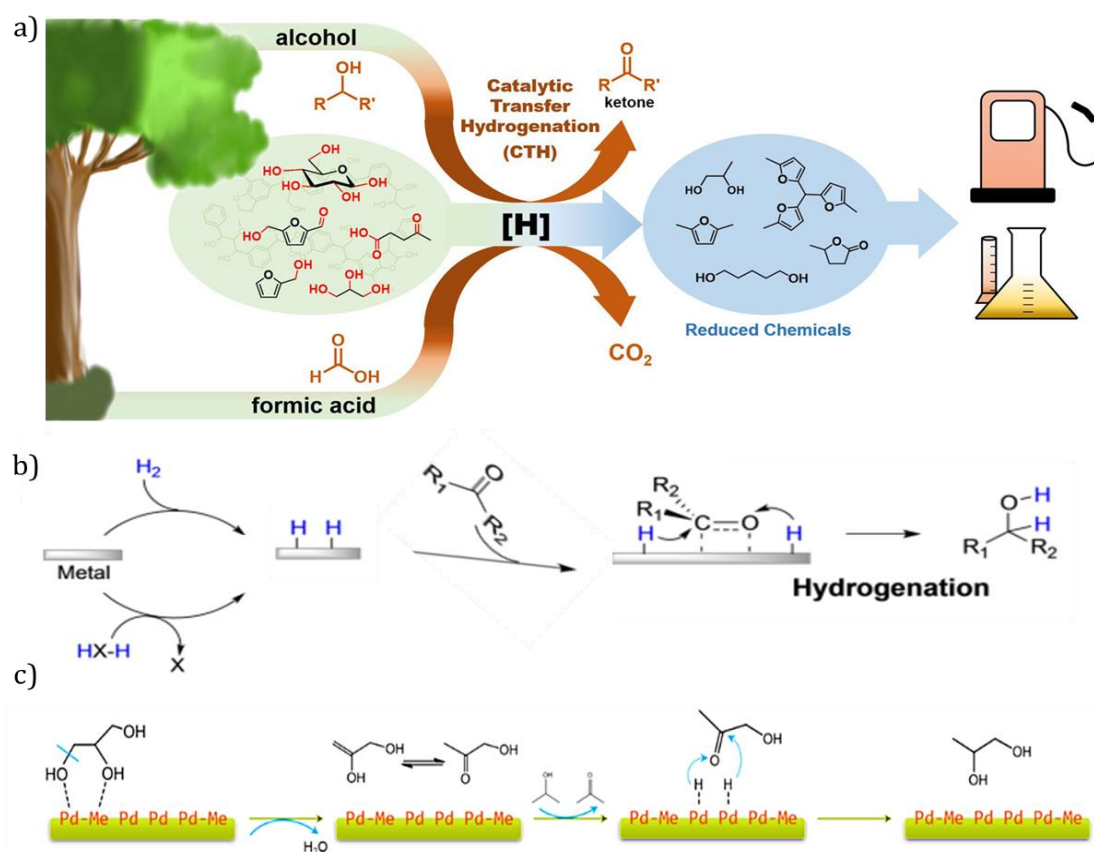


**Figure 2-6.** a) Catalytic transfer hydrogenation of various constituents of lignocellulose<sup>15</sup>, b) reaction mechanism of CTH, c) mechanism of CTH over Pd/ $\text{Fe}_3\text{O}_4$  catalyst<sup>82</sup>.

Alcohols are one of the most commonly used cost-effective and sustainable hydrogen donors in CTH processes, overcoming the drawbacks of hydrogen gas. For instance, 2-pentanol and 2-butanol has been used as hydrogen donors for

efficient CTH of biomass derived furfural to methyl furan using Ru/RuO<sub>2</sub>/C catalyst<sup>89</sup>. Propanol has been used for the selective and high yield conversion of glycerol (one by-product of biodiesel fuel) to 1,2-propanediol (PDO) (a crucial polymer precursor) using Pd/Fe<sub>2</sub>O<sub>3</sub> catalysts (Figure 2-6c)<sup>82</sup>. By using ethanol as solvent and hydrogen donor, it was possible to convert cinnamaldehyde to cinnamyl alcohol with 97.8% yield. However, in some cases, using alcohol can trigger some side reactions, including self-esterification which is the major drawback of alcohol assisted CTH processes.

Formic acid (FA) is one of the most promising materials for CTH. It can be obtained from lignocellulosic biomass or reduction of CO<sub>2</sub>. Having the highest reversible volumetric hydrogen storage, it can be used for miscellaneous catalytic transformations. Taking advantage of the properties of formic acid, it can be used for high-purity hydrogen production or CHT. For example, FA can significantly improve the conversion of furfuryl to methyl furfural with 79.2% yield versus 2-propanol (5%)<sup>86</sup>

Another study was carried out by Serra and co-workers. FA was used as a hydrogen donor for CTH process, to reduce levulinic acid (LA) to  $\gamma$ -valerolactone (GVL) in the presence of Ni-rich Ni-Pt catalysts and formic acid (FA) as a hydrogen source. The prepared catalysts exhibited complete transformation (99%) to GVL<sup>90</sup>.

This latter work gives rise to highlight the importance of CTH processes with levulinic acid. This compound has been recognized as one of the “top 10” most promising platform molecules derived from biomass. Many value-added chemicals can be synthesized directly from levulinic acid. Among these products, GVL has received widespread attention due to its excellent physical and chemical properties. It can be used as a solvent, flavouring agent, food ingredient, pharmaceutical intermediate, fuel additives, etc. Given the technological importance of these compounds together with the search for green, sustainable and energy-efficient synthetic approaches, part of this thesis will also address the selective transformation of levulinic acid into  $\gamma$ -valerolactone via a CTH process using the synergy novel multifunctional mesoporous nanocatalysts.

## 2.5 Catalysts for biomedical applications

Cancer is a leading cause of death worldwide. It is a dynamic disease with extreme heterogeneity, and inherent genomic instability and despite extensive research and significant efforts for developing personalized gene-targeted therapies, it is still an alarming condition with a poor prognosis and high mortality.

Conventional cancer therapies, include chemotherapy, surgery, and radiotherapy. Each of them however has its disadvantages and limitations. For instance, chemotherapy drugs show low efficacy due to difficulties to achieve

lethal drug concentration inside solid tumors, as a result of a fast clearance of the drugs. Moreover, tumor heterogeneity contributes to develop resistance to chemotherapy, as the bulk tumour might include a diverse collection of cells carrying distinct molecular signatures with differential levels of sensitivity to the treatment. Furthermore, chemotherapy lacks selectivity, affecting not only the tumor cells but also causing damage to normal cells causing side effects in different organs<sup>91</sup>. Likewise, radiotherapy suffers from a similar lack of specificity and is also an expensive, complex and invasive method that can cause multiple side effects<sup>92</sup>.

Promising gene-targeted and immuno-therapies directed at molecular mutations are emerging but have many challenges ahead<sup>78</sup>. Although cancer is an (acquired) genetic disorder, the abnormalities are polygenic. Moreover, there is substantial genetic heterogeneity not only between tumors in different individuals, but also between tumors at different sites within the same patient. A combination of target-specific agents might be required to effectively eliminate these cells, which makes a very complex task finding the appropriate treatment for each patient. Therefore, gene- and immunotherapies need to be customized to be effective, thus losing the universal character of a general therapy that would allow to kill tumor cells of different types.

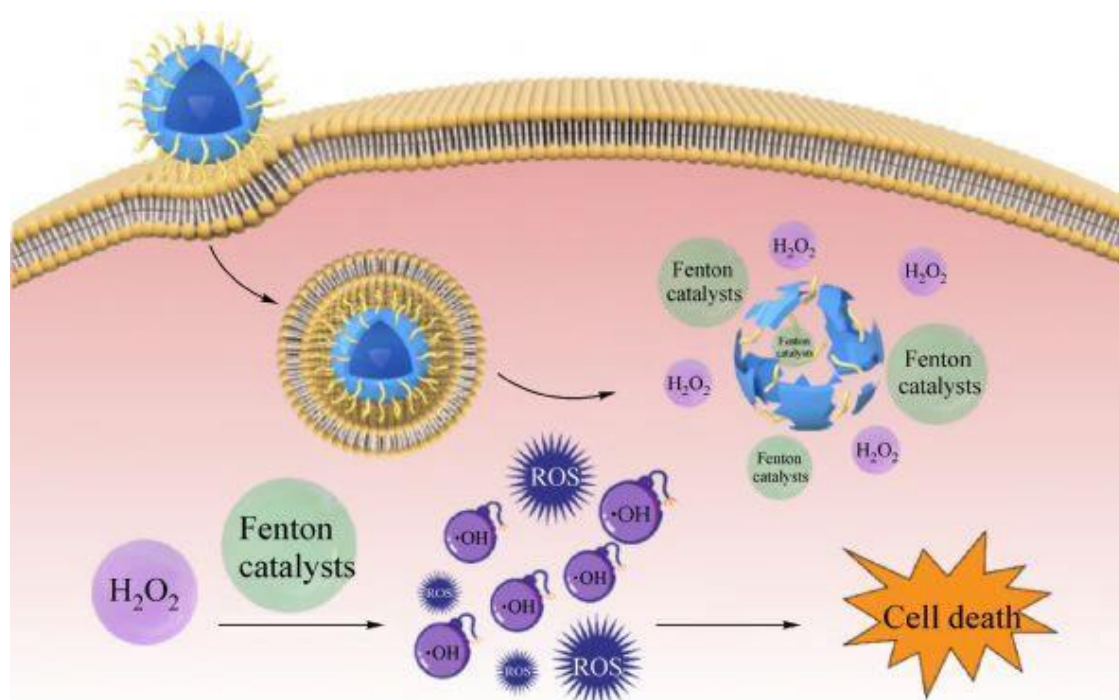


**Figure 2-7.** Schematic of OH mediated cancer therapy<sup>68</sup>.

With the emergence of nanotechnology, nanotherapies appear as innovative cancer treatments with spatially and temporally controlled cancer drug delivery. While these nanotherapies based on drug loaded nanoparticles overcome some of the side effects of chemotherapy and radiotherapy, they also exhibit important

hurdles related to their passive delivery and low drug accumulation at the targeted tumoral regions.

Thus, there is a great need to develop new general and cost-effective therapeutic methods independent of the tumor type, heterogeneity, and state and also with an enhanced delivery to the tumoral region. Under this context, hyperthermia therapies to kill cancer cells by local heating of the tumoral regions are quite promising. Typical nanomaterials for hyperthermia are magnetic nanostructures exhibiting high specific absorption rates in presence of alternating magnetic fields or gold nanostructures with strong plasmon absorption in the near infrared (NIR) light in the so-called optical therapeutic window<sup>5</sup>.

Another interesting therapeutic pathway is the one based on the in-situ cancer cell modulation of reactive oxygen species (Figure 2-7). Most of the intracellularly generated ROS come from mitochondria, and the other main sources are endoplasmic reticulum, peroxisomes, microsomes, etc. Under normal physiological conditions, the endogenous ROS level is regulated by a series of antioxidant enzymes, keeping it in a dynamic equilibrium. ROS with a moderate level plays multiple roles in the body, especially in cellular signal transduction, immune regulation, redox homeostasis, or in the proper function of cardiovascular system. However, if the ROS concentration is above a normal concentration, it may interfere with the normal cell signaling or cause oxidative stress to damage the cells. In cells, the main targets of ROS are nucleic acids, proteins, lipids and sugars. Intracellular oxidative stress has been proved to induce cancer, aging, inflammation, diabetes and neurodegeneration. On the other hand, due to their highly toxic nature, ROS can be applied to kill pathogens or cancer cells, in which a further increase in ROS concentration over the threshold could directly activate the apoptosis death pathway of tumor cells. With recent advances in ROS-relevant nanomaterials, some ROS-mediated therapeutic modalities have started to emerge to treat infectious diseases and cancers. In fact, chemodynamic therapy (CDT) is an antitumor therapy based on Fenton and Fenton-like reactions which holds promise to destroy tumor cells by the endogenous generation of reactive oxygen species (ROS) in the tumor microenvironment (TME) characterized by relatively elevated levels of H<sub>2</sub>O<sub>2</sub> and slightly acidic pH<sup>93</sup>. The CTD strategy is based on three steps: 1) ROS-inducer nanomaterials accumulate in the tumour cells due to enhanced permeability and retention effects<sup>6</sup>, 2) H<sub>2</sub>O<sub>2</sub> excessively accumulates in tumour cell, and 3)

---

<sup>5</sup> This therapeutic window stems from the fact that human skin tissues only weakly absorb light with wavelengths between 650 and 900 nm (optical window). Therefore, NIR light can optically penetrate biological tissues and excite the nanoparticles to generate localized heating.

<sup>6</sup> Enhanced Permeability and Retention effects (EPR) are related to the trend of species accumulation liposomes, nanoparticles, and macromolecular drugs) in tumor tissue much more than they do in normal tissues due to an abnormal leaky vasculature in the tumoral region. Nevertheless, the effectiveness of the EPR effect has become controversial in recent years.



excessive ROS generation in the tumour due to Fenton and Fenton-like reactions<sup>93</sup>.

Many efforts are being carried out to improve the CDT efficacy with nanocatalysts. Most of them have been focused on the use of iron oxide, copper and manganese-based nanoparticles<sup>93</sup>. The common hurdle is the insufficient endogenous H<sub>2</sub>O<sub>2</sub>, which undoubtedly reduces the ability to generate ROS to a certain extent<sup>94</sup>. Then each material exhibits different cons and pros. For instance, iron-based nanomaterials also show low catalytic activity mainly due to low reconversion rates of Fe<sup>3+</sup> to Fe<sup>2+</sup> to sustain the Fenton reaction and pH conditions not low enough for an optimized performance<sup>95</sup>. Cu based nanoparticles have better performance for ROS generation. The Cu<sup>2+</sup> to Cu<sup>+</sup> reconversion for Fenton like reactions is faster than in the case of iron ions. Moreover Cu<sup>2+</sup> can also react with glutathione (GSH, an antioxidant peptide whose levels are elevated in tumor cells) to produce Cu<sup>+</sup> which even enhanced the ion conversion in the catalytic process<sup>96</sup>. However, copper ions exhibit in general more toxicity effects on the body than iron ions<sup>97</sup>. Manganese based nanoparticles have the advantage to exhibit effective catalytic activity in a wide pH range, and has the best catalytic activity at pH 5. Similar to Cu<sup>2+</sup>, MnO<sub>2</sub> can also consume GSH and produce Mn<sup>2+</sup> with higher catalytic efficiency<sup>162</sup>. Manganese can also activate pathways to enhance immune surveillance and immune clearance of tumor cells<sup>98</sup>.

To alleviate the relevant shortcoming of endogenous H<sub>2</sub>O<sub>2</sub> different strategies have been carried out. For instance, the synthesis of copper-based nanoparticles with H<sub>2</sub>O<sub>2</sub> loading<sup>161</sup>, the coupling of based nanoparticles with selenium, which activate the enzyme superoxide dismutase to promote H<sub>2</sub>O<sub>2</sub> increase, or the enzymatic modification of these metal-based nanoparticles with oxidases. For instance, the modification of Fe, Cu or Mn particles with glucose oxidase can locally increase the H<sub>2</sub>O<sub>2</sub> production and at the same time consume glucose, a nutrient for cancer cells<sup>93</sup>. In this way different antitumor pathways are triggered: the Fenton/Fenton-like reactions and cancer cell starvation as a synergetic cancer cell therapy.

As can be seen, there are different strategies to increase the performance of ROS-producer nanomaterials and the prospects are becoming increasingly promising with the emergence of new nanomaterials, that can even use light as an additional tool for increasing ROS activity. Moreover, the strategy of integrating different multifunctional nanomaterials increases this encouraging panorama. For instance, different therapeutic routes can be carried out with a functional nanomaterial (e.g., ROS + immunotherapy, ROS + hyperthermia<sup>99</sup>, etc.) or can improve the therapy delivery by integrating magnetic nanostructures for an external control of the transport and accumulation of the therapeutic vectors at the targeted regions.

Moreover, biosensing and imaging are crucial methods for the early detection of diseases, especially cancer<sup>100</sup>. Semiconductor, noble and magnetic nanoparticles, have been widely used in biosensing and imaging because of their high size-dependent and remarkable optical/magnetic properties (e.g. CdSe-ZnO, Au-Ag NPs, FeO<sub>x</sub>, etc)<sup>100</sup>. For instance,  $\gamma$ -Fe<sub>2</sub>O<sub>3</sub> and Fe<sub>3</sub>O<sub>4</sub> MNPs have been widely used in the area of Magnetic Resonance Imaging as T2 negative contrast agent<sup>40</sup> and Au nanoparticles as optical contrast imaging agents in cancer diagnosis and therapy under NIR light activation<sup>101</sup>. Therefore, the integration of nanomaterials with opto/magnetic properties is very relevant for the development of theranostics agents.

All this discussion makes evident that multicomponent nanostructures are becoming powerful synergistic therapeutical or theranostics agents, allowing to tackle pathological problems from different angles. In this thesis preliminary results of hybrid functional materials for an enhanced ROS therapeutic route will be introduced.

## 2.6 References

1. Rathi BS, Kumar PS, Vo DVN. Critical review on hazardous pollutants in water environment: Occurrence, monitoring, fate, removal technologies and risk assessment. *Sci Total Environ.* 2021;797:149134. doi:10.1016/j.scitotenv.2021.149134
2. Alharbi OML, Basheer AA, Khattab RA, Ali I. *Health and Environmental Effects of Persistent Organic Pollutants*. Vol 263. Elsevier B.V; 2018. doi:10.1016/j.molliq.2018.05.029
3. KC Jones, Voogt P De. Attribute Learning for Image / Video Understanding. *Persistent Org Pollut state Sci.* 1999;100(1):209-221.
4. Wu CY. Nanoparticles and the environment. *J Air Waste Manag Assoc.* 2005;55(6):708-746. doi:10.1080/10473289.2005.10464656
5. Dewil R, Mantzavinos D, Poulios I, Rodrigo MA. New perspectives for Advanced Oxidation Processes. *J Environ Manage.* 2017;195:93-99. doi:10.1016/j.jenvman.2017.04.010
6. Crini G, Lichtfouse E. Advantages and disadvantages of techniques used for wastewater treatment. *Environ Chem Lett.* 2020;17(1):145-155. doi:10.1007/s10311-018-0785-9
7. Oturan MA, Aaron JJ. Advanced Oxidation Processes in Water/Wastewater Treatment: Principles and Applications. A Review. *Crit Rev Environ Sci Technol.* 2014;44(23):2577-2641. doi:10.1080/10643389.2013.829765

8. Dewil R, Mantzavinos D, Poulios I, Rodrigo MA. New perspectives for Advanced Oxidation Processes. *J Environ Manage.* 2017;195:93-99. doi:10.1016/j.jenvman.2017.04.010
9. Legrini O, Oliveros E, Braun AM. Photochemical Processes for Water Treatment. *Chem Rev.* 1993;93(2):671-698. doi:10.1021/cr00018a003
10. Klavarioti M, Mantzavinos D, Kassinos D. Removal of residual pharmaceuticals from aqueous systems by advanced oxidation processes. *Environ Int.* 2009;35(2):402-417. doi:10.1016/j.envint.2008.07.009
11. Sharma M, Mohapatra PK, Bahadur D. Improved photocatalytic degradation of organic dye using Ag<sub>3</sub>PO<sub>4</sub>/MoS<sub>2</sub> nanocomposite. *Front Mater Sci.* 2017;11(4):366-374. doi:10.1007/s11706-017-0404-x
12. Ikehata K, El-Din MG, Snyder SA. Ozonation and advanced oxidation treatment of emerging organic pollutants in water and wastewater. *Ozone Sci Eng.* 2008;30(1):21-26. doi:10.1080/01919510701728970
13. Kausley SB, Desai KS, Shrivastava S, Shah PR, Patil BR, Pandit AB. Mineralization of alkyd resin wastewater: Feasibility of different advanced oxidation processes. *J Environ Chem Eng.* 2018;6(3):3690-3701. doi:10.1016/j.jece.2017.04.001
14. Anandan S, Kumar Ponnusamy V, Ashokkumar M. A review on hybrid techniques for the degradation of organic pollutants in aqueous environment. *Ultrason Sonochem.* 2020;67:105130. doi:10.1016/j.ultsonch.2020.105130
15. Goel M, Hongqiang H, Mujumdar AS, Ray MB. Sonochemical decomposition of volatile and non-volatile organic compounds - A comparative study. *Water Res.* 2004;38(19):4247-4261. doi:10.1016/j.watres.2004.08.008
16. Antoniadis A, Poulios I, Nikolakaki E, Mantzavinos D. Sonochemical disinfection of municipal wastewater. *J Hazard Mater.* 2007;146(3):492-495. doi:10.1016/j.jhazmat.2007.04.065
17. Lim M, Son Y, Khim J. Frequency effects on the sonochemical degradation of chlorinated compounds. *Ultrason Sonochem.* 2011;18(1):460-465. doi:10.1016/j.ultsonch.2010.07.021
18. Acero JL, Von Gunten U. Characterization of oxidation processes: Ozonation and the AOP O<sub>3</sub>/H<sub>2</sub>O<sub>2</sub>. *J Am Water Work Assoc.* 2001;93(10):90-100. doi:10.1002/j.1551-8833.2001.tb09311.x
19. Rosenfeldt EJ, Linden KG, Canonica S, von Gunten U. Comparison of the efficiency of {radical dot}OH radical formation during ozonation and the

- advanced oxidation processes O<sub>3</sub>/H<sub>2</sub>O<sub>2</sub> and UV/H<sub>2</sub>O<sub>2</sub>. *Water Res.* 2006;40(20):3695-3704. doi:10.1016/j.watres.2006.09.008
20. Jain B, Singh AK, Kim H, Lichtfouse E, Sharma VK. Treatment of organic pollutants by homogeneous and heterogeneous Fenton reaction processes. *Environ Chem Lett.* 2018;16(3):947-967. doi:10.1007/s10311-018-0738-3
  21. Babuponnusami A, Muthukumar K. A review on Fenton and improvements to the Fenton process for wastewater treatment. *J Environ Chem Eng.* 2014;2(1):557-572. doi:10.1016/j.jece.2013.10.011
  22. Pan B, Pignatello JJ, Yang Z, Shan C. The Fenton reaction in water assisted by picolinic acid: Accelerated Iron Cycling and Co-generation of a Selective Fe-Based Oxidant. *Environ Sci Technol.* 2021;55(12):8299-8308. doi:10.1021/acs.est.1c00230
  23. Pignatello JJ, Oliveros E, MacKay A. Advanced oxidation processes for organic contaminant destruction based on the fenton reaction and related chemistry. *Crit Rev Environ Sci Technol.* 2006;36(1):1-84. doi:10.1080/10643380500326564
  24. Rezaei F, Vione D. Effect of pH on zero valent iron performance in heterogeneous Fenton and Fenton-like processes: A review. *Molecules.* 2018;23(12). doi:10.3390/molecules23123127
  25. Rivas FJ, Beltrán FJ, Frades J, Buxeda P. Oxidation of p-hydroxybenzoic acid by Fenton's reagent. *Water Res.* 2001;35(2):387-396. doi:10.1016/S0043-1354(00)00285-2
  26. Eisenhauer HR. Oxidation of phenolic wastes. *Water Pollut Control Fed.* 1964;36(9):1116-1128.
  27. Ma YS, Huang ST, Lin JG. Degradation of 4-nitrophenol using the Fenton process. *Water Sci Technol.* 2000;42(3-4):155-160. doi:10.2166/wst.2000.0373
  28. Babuponnusami A, Muthukumar K. Degradation of Phenol in Aqueous Solution by Fenton, Sono-Fenton and Sono-photo-Fenton Methods. *Clean - Soil, Air, Water.* 2011;39(2):142-147. doi:10.1002/clen.201000072
  29. Bossmann SH, Oliveros E, Göb S, et al. New evidence against hydroxyl radicals as reactive intermediates in the thermal and photochemically enhanced fenton reactions. *J Phys Chem A.* 1998;102(28):5542-5550. doi:10.1021/jp980129j
  30. Szpyrkowicz L, Juzzolino C, Kaul SN. A comparative study on oxidation of disperse dyes by electrochemical process, ozone, hypochlorite and fenton reagent. *Water Res.* 2001;35(9):2129-2136. doi:10.1016/S0043-1354(00)00487-5

31. Lin SH, Lin CM, Leu HG. Operating characteristics and kinetic studies of surfactant wastewater treatment by fenton oxidation. *Water Res.* 1999;33(7):1735-1741. doi:10.1016/S0043-1354(98)00403-5
32. Ito K, Jian W, Nishijima W, Baes AU, Shoto E, Okada M. Comparison of ozonation and AOPs combined with biodegradation for removal of THM precursors in treated sewage effluents. *Water Sci Technol.* 1998;38(7 pt 6):179-186. doi:10.1016/S0273-1223(98)00620-9
33. Chen W, Chen Q, Ma Y, Leng X, Bai S Di, Deng L. Formal Co(0), Fe(0), and Mn(0) complexes with NHC and styrene ligation. *Chinese Chem Lett.* 2020;31(5):1342-1344. doi:10.1016/j.ccllet.2019.11.019
34. Bhanvase BA, Sonawane SH, Pawade VB, Pandit AB. *Handbook of Nanomaterials for Wastewater Treatment: Fundamentals and Scale up Issues.* Elsevier; 2021.
35. Yan Q, Zhang J, Xing M. Cocatalytic Fenton Reaction for Pollutant Control. *Cell Reports Phys Sci.* 2020;1(8):100149. doi:10.1016/j.xcrp.2020.100149
36. Guglielmelli A, Pierini F, Tabiryan N, Umeton C, Bunning TJ, De Sio L. Thermoplasmonics with Gold Nanoparticles: A New Weapon in Modern Optics and Biomedicine. *Adv Photonics Res.* 2021;2(8):2000198. doi:10.1002/adpr.202000198
37. Wu Y, Yao H, Khan S, Hu S, Wang L. Characteristics and Mechanisms of Kaolinite-Supported Zero-Valent Iron/H<sub>2</sub>O<sub>2</sub> System for Nitrobenzene Degradation. *Clean - Soil, Air, Water.* 2017;45(3). doi:10.1002/clen.201600826
38. Nanda KK, Kruis FE, Fissan H. Evaporation of Free PbS Nanoparticles: Evidence of the Kelvin Effect. *Phys Rev Lett.* 2002;89(25):1-4. doi:10.1103/PhysRevLett.89.256103
39. Temnov V V., Armelles G, Woggon U, et al. Active magneto-plasmonics in hybrid metal-ferromagnet structures. *Nat Photonics.* 2010;4(2):107-111. doi:10.1038/nphoton.2009.265
40. Selvan ST, Yang Tan TT, Kee Yi D, Jana NR. Functional and multifunctional nanoparticles for bioimaging and biosensing. *Langmuir.* 2010;26(14):11631-11641. doi:10.1021/la903512m
41. Ribas D, Černík M, Benito JA, Filip J, Marti V. *Activation Process of Air Stable Nanoscale Zero-Valent Iron Particles.* Vol 320.; 2017. doi:10.1016/j.cej.2017.03.056
42. Stefaniuk M, Oleszczuk P, Ok YS. Review on nano zerovalent iron (nZVI): From synthesis to environmental applications. *Chem Eng J.* 2016;287:618-632. doi:10.1016/j.cej.2015.11.046

43. Li Y, Zhao HP, Zhu L. Remediation of soil contaminated with organic compounds by nanoscale zero-valent iron: A review. *Sci Total Environ.* 2021;760:143413. doi:10.1016/j.scitotenv.2020.143413
44. Zhang Y fei, Zhang C hui, Xu J hui, et al. Strategies to enhance the reactivity of zero-valent iron for environmental remediation: A review. *J Environ Manage.* 2022;317:115381.
45. Li XQ, Elliott DW, Zhang WX. Zero-valent iron nanoparticles for abatement of environmental pollutants: Materials and engineering aspects. *Crit Rev Solid State Mater Sci.* 2006;31(4):111-122. doi:10.1080/10408430601057611
46. Yi Q, Liu W, Tan J, Yang B, Xing M, Zhang J. Mo<sup>0</sup> and Mo<sup>4+</sup> bimetallic reactive sites accelerating Fe<sup>2+</sup>/Fe<sup>3+</sup> cycling for the activation of peroxymonosulfate with significantly improved remediation of aromatic pollutants. *Chemosphere.* 2020;244:125539. doi:10.1016/j.chemosphere.2019.125539
47. Ren Y, Zhou J, Lai B, Tang W, Zeng Y. Fe<sup>0</sup> and Fe<sup>0</sup> fully covered with Cu<sup>0</sup> (Fe<sup>0</sup>+ Fe/Cu) in a fixed bed reactor for nitrate removal. *RSC Adv.* 2016;6(110):108229-108239.
48. Lai B, Zhang Y, Chen Z, Yang P, Zhou Y, Wang J. Removal of p-nitrophenol (PNP) in aqueous solution by the micron-scale iron-copper (Fe/Cu) bimetallic particles. *Appl Catal B Environ.* 2014;144:816-830. doi:10.1016/j.apcatb.2013.08.020
49. Ju Y, Liu X, Liu R, et al. Environmental application of millimeter-scale sponge iron (s-Fe<sup>0</sup>) particles (II): The effect of surface copper. *J Hazard Mater.* 2015;287(Ii):325-334. doi:10.1016/j.jhazmat.2015.01.019
50. Choi K, Lee W. Enhanced degradation of trichloroethylene in nano-scale zero-valent iron Fenton system with Cu(II). *J Hazard Mater.* 2012;211-212:146-153. doi:10.1016/j.jhazmat.2011.10.056
51. Dou X, Li R, Zhao B, Liang W. Arsenate removal from water by zero-valent iron/activated carbon galvanic couples. *J Hazard Mater.* 2010;182(1-3):108-114. doi:10.1016/j.jhazmat.2010.06.004
52. Ji X, Ge L, Liu C, et al. Capturing functional two-dimensional nanosheets from sandwich-structure vermiculite for cancer theranostics. *Nat Commun.* 2021;12(1):1-18. doi:10.1038/s41467-021-21436-5
53. Yamaguchi R, Kurosu S, Suzuki M. Hydroxyl radical generation by zero-valent iron/Cu (ZVI/Cu) bimetallic catalyst in wastewater treatment: Heterogeneous Fenton/Fenton-like reactions by Fenton reagents formed in-situ under oxic conditions. *Chem Eng J.* 2018;334:1537-1549.

- doi:10.1016/j.cej.2017.10.154
54. Huang Q, Cao M, Ai Z, Zhang L. Reactive oxygen species dependent degradation pathway of 4-chlorophenol with Fe@Fe<sub>2</sub>O<sub>3</sub> core-shell nanowires. *Appl Catal B Environ.* 2015;162:319-326. doi:10.1016/j.apcatb.2014.06.046
  55. Zhang W, Chuu CP, Huang JK, et al. Ultrahigh-Gain Photodetectors Based on Atomically Thin Graphene-MoS<sub>2</sub> Heterostructures. *Sci Rep.* 2015;4:1-8. doi:10.1038/srep03826
  56. Wei X, Zhu N, Huang J, et al. Rapid and efficient reduction of chromate by novel Pd/Fe@biomass derived from *Enterococcus faecalis*. *Environ Res.* 2022;204(PA):112005. doi:10.1016/j.envres.2021.112005
  57. Bergendahl JA, Thies TP. Fenton's oxidation of MTBE with zero-valent iron. *Water Res.* 2004;38(2):327-334. doi:10.1016/j.watres.2003.10.003
  58. Hisatomi T, Kubota J, Domen K. Recent advances in semiconductors for photocatalytic and photoelectrochemical water splitting. *Chem Soc Rev.* 2014;43(22):7520-7535. doi:10.1039/c3cs60378d
  59. Okuyama K. Sintering. *Powder Technol Fundam Part Powder Beds, Part Gener.* Published online 2006:213-218. doi:10.5940/jcrsj.31.82
  60. Manzano M, Vallet-Regí M. Mesoporous Silica Nanoparticles for Drug Delivery. *Adv Funct Mater.* 2020;30(2):3-5. doi:10.1002/adfm.201902634
  61. Zhang N, Han C, Fu X, Xu Y jun. Function-Oriented Engineering of Metal-Based Nanohybrids for Photoredox Catalysis : Exerting Plasmonic Effect and Beyond. *CHEMPR.* 2018;4(8):1832-1861. doi:10.1016/j.chempr.2018.05.005
  62. Mittal A, Roy I, Gandhi S. Magnetic Nanoparticles: An Overview for Biomedical Applications. *Magnetochemistry.* 2022;8(9). doi:10.3390/magnetochemistry8090107
  63. Commentary G. Semiconductor Photocatalysis @ Past, Present, and Future Outlook. Published online 2012.
  64. Singh B, Na J, Konarova M, et al. Functional mesoporous silica nanomaterials for catalysis and environmental applications. *Bull Chem Soc Jpn.* 2020;93(12):1459-1496. doi:10.1246/BCSJ.20200136
  65. Qu Y, Duan X. Progress, challenge and perspective of heterogeneous photocatalysts. *Chem Soc Rev.* 2013;42(7):2568-2580. doi:10.1039/c2cs35355e
  66. Xu L, Liang HW, Yang Y, Yu SH. Stability and Reactivity: Positive and Negative Aspects for Nanoparticle Processing. *Chem Rev.* 2018;118(7):3209-

3250. doi:10.1021/acs.chemrev.7b00208
67. Lv R, Robinson JA, Schaak RE, et al. Transition metal dichalcogenides and beyond: Synthesis, properties, and applications of single- and few-layer nanosheets. *Acc Chem Res.* 2015;48(1):56-64. doi:10.1021/ar5002846
  68. Liu T, Li L, Teng X, et al. Single and repeated dose toxicity of mesoporous hollow silica nanoparticles in intravenously exposed mice. *Biomaterials.* 2011;32(6):1657-1668. doi:10.1016/j.biomaterials.2010.10.035
  69. Liu D, Xue C. Plasmonic Coupling Architectures for Enhanced Photocatalysis. *Adv Mater.* 2021;33(46):1-22. doi:10.1002/adma.202005738
  70. Patil SP, Burungale V V. *Physical and Chemical Properties of Nanomaterials.* Elsevier Inc.; 2020. doi:10.1016/b978-0-12-820016-2.00002-1
  71. Yuan Y, Guo R tang, Hong L fei, Ji X yin, Li Z sheng, Lin Z dong. Colloids and Surfaces A: Physicochemical and Engineering Aspects Recent advances and perspectives of MoS<sub>2</sub>-based materials for photocatalytic dyes degradation: A review. *Colloids Surfaces A Physicochem Eng Asp.* 2021;611(November 2020):125836. doi:10.1016/j.colsurfa.2020.125836
  72. Kong D, Wang H, Cha JJ, et al. Synthesis of MoS<sub>2</sub> and MoSe<sub>2</sub> Films with Vertically Aligned Layers. Published online 2013.
  73. Islam A, Church J, Han C, Chung H suk, Ji E, Hun J. Noble metal-coated MoS<sub>2</sub> nanofilms with vertically-aligned 2D layers for visible light-driven photocatalytic degradation of emerging water contaminants. *Sci Rep.* 2017;(July):1-10. doi:10.1038/s41598-017-14816-9
  74. Zhang Y, He S, Guo W, et al. Surface-Plasmon-Driven Hot Electron Photochemistry. *Chem Rev.* Published online 2018. doi:10.1021/acs.chemrev.7b00430
  75. Wu N. Plasmonic metal–semiconductor photocatalysts and photoelectrochemical cells: a review. *Nanoscale.* 2018;10(6):2679-2696. doi:10.1039/C7NR08487K
  76. Djurišić AB, He Y, Ng AMC. Visible-light photocatalysts: Prospects and challenges. *APL Mater.* 2020;8(3):030903. doi:10.1063/1.5140497
  77. Johnstone RAW, Wilby AH, Entwistle ID. Heterogeneous Catalytic Transfer Hydrogenation and Its Relation to Other Methods for Reduction of Organic Compounds. *Chem Rev.* 1985;85(2):129-170. doi:10.1021/cr00066a003
  78. Brieger G, Nestrick TJ. Catalytic transfer hydrogenation. *Chem Rev.* 1974;74(5):567-580. doi:10.1021/cr60291a003



79. Yin Y, Yang ZF, Wen ZH, et al. Modification of as Synthesized SBA-15 with Pt nanoparticles: Nanoconfinement Effects Give a Boost for Hydrogen Storage at Room Temperature. *Sci Rep.* 2017;7(1):1-10. doi:10.1038/s41598-017-04346-9
80. Jin W, Pastor-Pérez L, Yu J, Odriozola JA, Gu S, Reina TR. Cost-effective routes for catalytic biomass upgrading. *Curr Opin Green Sustain Chem.* 2020;23:1-9. doi:10.1016/j.cogsc.2019.12.008
81. Chheda JN, Dumesic JA. An overview of dehydration, aldol-condensation and hydrogenation processes for production of liquid alkanes from biomass-derived carbohydrates. *Catal Today.* 2007;123(1-4):59-70. doi:10.1016/j.cattod.2006.12.006
82. Musolino MG, Scarpino LA, Mauriello F, Pietropaolo R. Selective transfer hydrogenolysis of glycerol promoted by palladium catalysts in absence of hydrogen. *Green Chem.* 2009;11(10):1511-1513. doi:10.1039/b915745j
83. Etacheri V, Di Valentin C, Schneider J, Bahnemann D, Pillai SC. Visible-light activation of TiO<sub>2</sub> photocatalysts: Advances in theory and experiments. *J Photochem Photobiol C Photochem Rev.* 2015;25:1-29. doi:10.1016/j.jphotochemrev.2015.08.003
84. Sawadjoon S, Lundstedt A, Samec JSM. Pd-catalyzed transfer hydrogenolysis of primary, secondary, and tertiary benzylic alcohols by formic acid: A mechanistic study. *ACS Catal.* 2013;3(4):635-642. doi:10.1021/cs300785r
85. Jae J, Zheng W, Lobo RF, Vlachos DG. Production of dimethylfuran from hydroxymethylfurfural through catalytic transfer hydrogenation with ruthenium supported on carbon. *ChemSusChem.* 2013;6(7):1158-1162. doi:10.1002/cssc.201300288
86. Wang H, Liu B, Liu F, et al. Transfer Hydrogenation of Cinnamaldehyde Catalyzed by Al<sub>2</sub>O<sub>3</sub> Using Ethanol as a Solvent and Hydrogen Donor. *ACS Sustain Chem Eng.* 2020;8(22):8195-8205. doi:10.1021/acssuschemeng.0c00942
87. Subramanian T, Pitchumani K. Selective Reduction of Nitroarenes by using Zeolite-Supported Copper Nanoparticles with 2-Propanol as a Sustainable Reducing Agent. *ChemCatChem.* 2012;4(12):1917-1921. doi:10.1002/cctc.201200443
88. Pellet RJ. Hydrogen transfer catalysis by platinum on zeolites. *J Catal.* 1998;177(1):40-52. doi:10.1006/jcat.1998.2031
89. Panagiotopoulou P, Martin N, Vlachos DG. Effect of hydrogen donor on liquid phase catalytic transfer hydrogenation of furfural over a Ru/RuO<sub>2</sub>/C

- catalyst. *J Mol Catal A Chem.* 2014;392:223-228. doi:10.1016/j.molcata.2014.05.016
90. Serrà A, Artal R, Philippe L, Gómez E. Electrodeposited Ni-Rich Ni-Pt Mesoporous Nanowires for Selective and Efficient Formic Acid-Assisted Hydrogenation of Levulinic Acid to  $\gamma$ -Valerolactone. *Langmuir.* 2021;37(15):4666-4677. doi:10.1021/acs.langmuir.1c00461
  91. Mu L, Wang M, Jiang F, et al. Boosting Photo-Fenton reactions by amidoxime chelated ferrous iron (Fe(III)) catalyst for highly efficient pollutant control. *Appl Catal B Environ.* 2021;298(April):120574. doi:10.1016/j.apcatb.2021.120574
  92. Gu J, Huang K, Zhu X, et al. Sub-150nm mesoporous silica nanoparticles with tunable pore sizes and well-ordered mesostructure for protein encapsulation. *J Colloid Interface Sci.* 2013;407:236-242. doi:10.1016/j.jcis.2013.06.028
  93. Cao W, Jin M, Yang K, et al. Fenton/Fenton-like metal-based nanomaterials combine with oxidase for synergistic tumor therapy. *J Nanobiotechnology.* 2021;19(1):1-35. doi:10.1186/s12951-021-01074-1
  94. Goldstein S, Meyerstein D, Czapski G. The Fenton reagents. *Free Radic Biol Med.* 1993;15(4):435-445. doi:10.1016/0891-5849(93)90043-T
  95. Zhang C, Bu W, Ni D, et al. Synthesis of iron nanometallic glasses and their application in cancer therapy by a localized fenton reaction. *Angew Chemie - Int Ed.* 2016;55(6):2101-2106. doi:10.1002/anie.201510031
  96. Lin L Sen, Huang T, Song J, et al. Synthesis of Copper Peroxide Nanodots for H<sub>2</sub>O<sub>2</sub> Self-Supplying Chemodynamic Therapy. *J Am Chem Soc.* Published online 2019. doi:10.1021/jacs.9b03457
  97. Chudal L, Pandey NK, Phan J, et al. Copper-Cysteamine Nanoparticles as a Heterogeneous Fenton-Like Catalyst for Highly Selective Cancer Treatment. *ACS Appl Bio Mater.* 2020;3(3):1804-1814. doi:10.1021/acsabm.0c00098
  98. Ou J, Tian H, Wu J, et al. MnO<sub>2</sub>-Based Nanomotors with Active Fenton-like Mn<sup>2+</sup>-Delivery for Enhanced Chemodynamic Therapy. *ACS Appl Mater Interfaces.* 2021;13(32):38050-38060. doi:10.1021/acsami.1c08926
  99. Shi Q, Yu T, Wu R, Liu J. Metal-Support Interactions of Single-Atom Catalysts for Biomedical Applications. *ACS Appl Mater Interfaces.* 2021;13(51):60815-60836. doi:10.1021/acsami.1c18797
  100. Rosi NL, Mirkin CA. Nanostructures in biodiagnostics. *Chem Rev.* 2005;105(4):1547-1562. doi:10.1021/cr030067f

- 
101. Tran VT, Kim J, Tufa LT, Oh S, Kwon J, Lee J. Magnetoplasmonic Nanomaterials for Biosensing/Imaging and in Vitro/in Vivo Biocompatibility. *Anal Chem.* 2018;90(1):225-239. doi:10.1021/acs.analchem.7b04255

### **3. Synthesis of mesoporous and large porous silica nanoparticles**

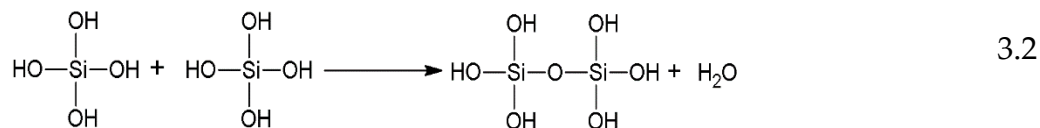
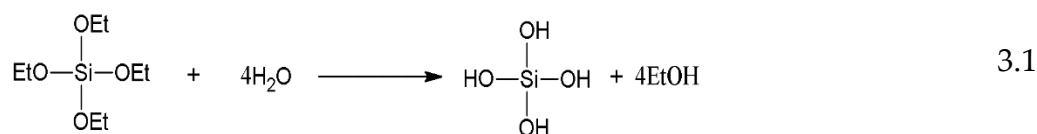
Porous materials, especially mesoporous silica particles are of great interest in scientific research because of their unique surface and structural properties. The synthesis of silica particles with different dimensions and pore sizes has developed rapidly due to their emerging application areas. In the following chapter, the synthesis of mesoporous and large pore silica particles will be described. The precursor concentration enables the formation of mesoporous silica particles with desired particle size and colloidal stability. Moreover, the pore-expanding agent and the catalyst allow tuning pore size.

### 3.1 Introduction

Mesoporous silica nanoparticles (MSN) with high surface area, large pore volume and chemical stability offer an excellent platform to host various chemicals or molecules, thereby being widely used in different application areas, including catalysis, biomedicine, energy storage, environmental remediation and many multidisciplinary fields<sup>1</sup>. The first monodispersed silica particles were synthesized by *Stöber et. al.*<sup>2</sup>. However, the insufficient surface area and absence of pores limited the application of these pioneer particles. Therefore, enormous efforts have been dedicated to synthesize mesoporous silica particles with tuneable pore and particle sizes, surface functionalities and morphologies<sup>3-5</sup>. The first series of mesoporous materials with a pore size of 2-50 nm were synthesized by Mobil's researchers in 1992, and were initially referred to as the Mobil Composition of Matter No 41 (MCM-41). Then SBA-15 nanostructures (University of California at Santa Barbara) with large pores of 4.6-30 nm were developed by *Stucky et. al.* and opened the path to use them in the different research fields mentioned above<sup>6-8</sup>.

The unique properties of MSN including, good biocompatibility, low toxicity, facile surface modification and stability make them outstanding nanocarriers in various application fields. For instance, having a well-defined large pore and surface area makes MSN appealing adsorbents of heavy metal ions<sup>9</sup>. Additionally, the tuneable pore size allows loading a large amount of bioactive therapeutic molecules that have proven high potential for targeted drug delivery in biomedical applications<sup>10</sup>. The high encapsulation ability of the cargo molecules inside the pore channels prevents the leakage of therapeutic agents and protects them from enzymatic degradation<sup>11-13</sup>. Furthermore, the silanol groups on the surface of the MSN can be easily modified for grafting or anchoring different organic functional groups either via covalent bonding or electrostatic interactions, thus providing a high versatility for the controlled release of the cargo materials<sup>14</sup>.

Numerous research articles have been published recently related to the synthesis of MSN or large pore silica nanoparticles (LPSN) with tailored properties. By using the simple sol-gel method, scientists have been able to synthesize silica particles with diverse morphology and pore size including zero-dimensional (0-D) MSN, one-dimensional (1D) mesoporous silica nanorods, nanowires, two-dimensional (2-D) nanofilms and three-dimensional (3-D) powders<sup>15-17</sup>. The sol-gel process in oxides is based on the formation of an oxide network through



hydrolysis/condensation reactions of a molecular precursor in a liquid. The process involves the conversion of monomers into a colloidal solution (sol) that acts as a precursor to an integrated network (or gel) of discrete particles. In the hydrolysis reaction, alkoxy groups ( $\text{OC}_2\text{H}_5$ ) of tetraethoxysilane (TEOS) ( $\text{Si}(\text{OC}_2\text{H}_5)_4$ ) were substituted by hydroxyl groups (OH) under basic condition(3.1)<sup>18,19</sup>. The hydrolysis of TEOS is then followed by the condensation process in which two silanol groups form the siloxane groups.

In each subsequent hydrolysis and condensation step, the negatively charged transition state becomes more stable with the increased electron-withdrawing capabilities of  $-\text{OH}$  and  $-\text{OSi}$  compared to  $-\text{EtO}$ <sup>20</sup>. As a result, the increased stability of the transition state escalates the reaction rate, and each subsequent step occurs faster as the hydrolysis and condensation proceeds<sup>21</sup>.

In general, mesoporous silica particles are fabricated using surfactants as templates for defining the pores. Cetyltrimethylammonium bromide (CTAB) is a widely used surfactant for the synthesis of MSN, but the different surfactants can significantly alter the properties and morphologies of the MSN. Depending on the assembly of the surfactant micelles, the pores will be either hexagonal, cubic or lamellar (Figure 3-1). For example, Poly-l-lysine (PLL) was used for the synthesis of the hexagonal structured MCM-41<sup>22</sup> (Figure 3-1a), whereas changing the surfactant to triblock polymer ( $(\text{EO}_{20}\text{PO}_{70}\text{EO}_{20})$ -butanol) and GPTMS2 (glycidoxypropyltrimethoxysilane) led to the cubic (Figure 3-1b) and lamella-like (Figure 3-1c) arrangement in the MCM-48, MCM-50 materials, respectively<sup>23,24</sup>.

Recently, Teng et. al. developed a new method for the synthesis of hollow spherical silica NPs by using different organic molecules<sup>26</sup>. Castro and co-workers reported a facile method to develop MSN with different morphologies by changing the water surfactant ratio<sup>27</sup>.

In the case of the synthesis of large pore silica nanoparticles, LPSN, there are generally two pathways: (i) post-synthetic treatment using different silica etching chemicals, and (ii) use of swelling agents during the silica synthesis. Large pore hollow silica particles were developed by Yang et al. via post-synthetic treatment method<sup>28</sup>. They used NaOH to gently etch the silica particles and obtained LPSN with irregular pores whose size was around 10 nm. In the second pathway, amphiphilic copolymers, surfactants with long

hydrophobic chains, alcohols, acids or amines have been used as a template or pore expanding agent. For instance, a combination of *N,N*-dimethylhexadecylamine (DMHA) with octadecyltrimethylammonium bromide (OTAB) has been employed to produce MSN with a pore diameter of 4.6 nm<sup>28</sup>.

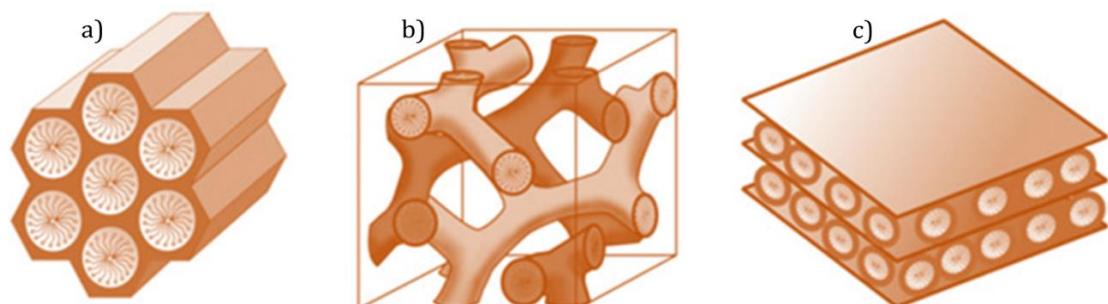


**Figure 3-1.** Structures of mesoporous materials a) MCM-41 (hexagonal), b) MCM-48 (cubic), c) MCM-50 (lamellar)<sup>25</sup>.

Tannic acid (TA) can also significantly improve the pore diameter (6-13 nm)<sup>29</sup>. However, a further increase is limited. Most of the reported LPSNs possess small particle sizes, around 50-100 nm, with a pore diameter ca. 15 nm. Therefore, cost-effective synthesis methods are needed for the fabrication of LPSN with larger pores and particle sizes.

In this Chapter, the sol-gel process was applied to synthesize monodisperse silica particles with controllable pore diameter, either mesoporous or large pore, and particle size. The synthesized silica templated by cetyltrimethylammonium bromide (CTAB) exhibited the mesopore structure. The reaction temperature and concentration of the precursor played an important role in the modification of the particle diameter from 100 nm up to 700 nm. On the other hand, the pore size was controlled by tuning the amount of pore-expanding agent. After the synthesis, the particles were cleaned from the excess of surfactant by ammonium nitrate. Then the silica beads were colloidally self-assembled on the silicon wafer and cleaned with oxygen plasma to remove any possible surfactant residues, therefore being ready for the next fabrication steps that have been carried out in this thesis.

## 3.2 Results and discussion

### 3.2.1 Fabrication of the mesoporous silica nanoparticles (MSN).

The synthesis of MSN started with the formation of surfactant (CTAB) micelles in water by increasing the solution temperature (Figure 3-2). The micelle formation and amount of H<sub>2</sub>O strongly affected the surface area and porosity of the MSN. The addition of alcohol, especially ethanol, lead to the formation of high-quality, clear and uniform micelles with spherical morphology. Moreover, ammonia (NH<sub>3</sub> 35 %) was used as a weak catalyst to tune the hydroxyl concentration in the reaction system. Ammonia is alkalescent ( $K_b = 1.8 \times 10^{-5}$ ) and partially decomposes to control hydroxyl concentration in solution. With the increase of the ammonia amount, hydroxyl concentration was raised and a larger number of hydroxyl groups substituted alkoxy groups of TEOS<sup>30</sup>. Hence, the hydrolysis and condensation of TEOS was accelerated around the CTAB micelles.

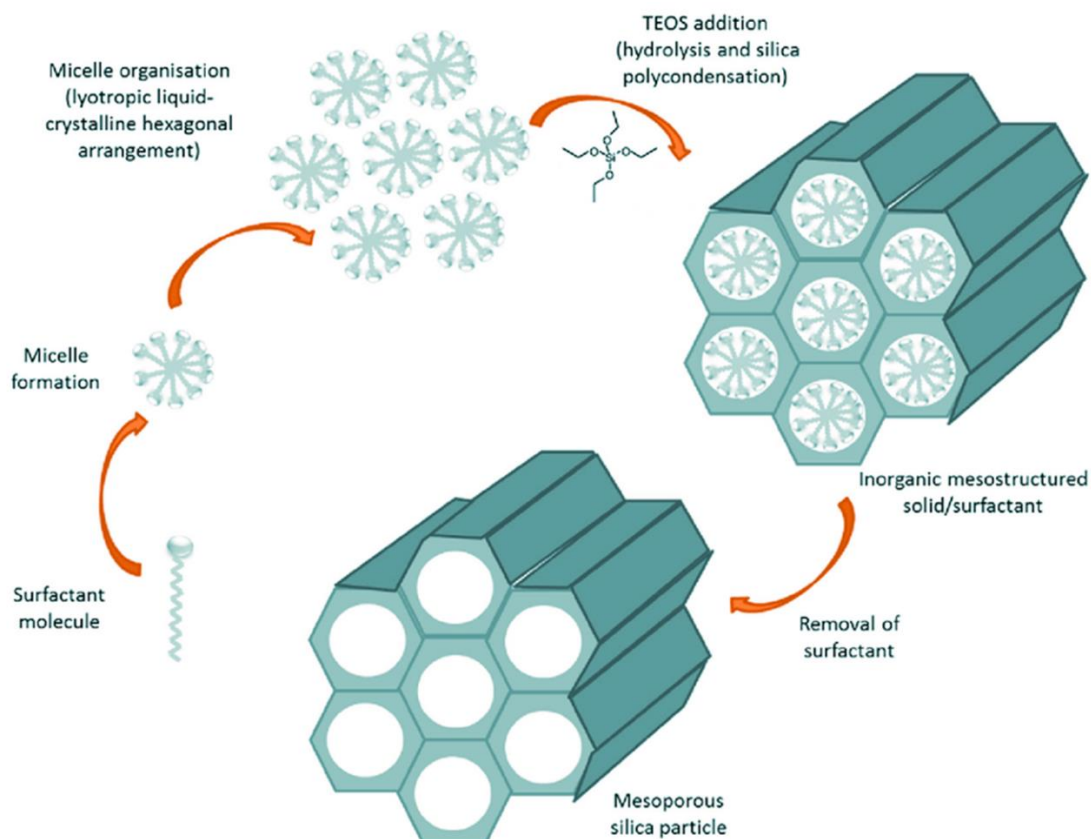


**Figure 3-2.** The synthesis strategy of MSN via a surfactant-templated route<sup>31</sup>.

#### 3.2.1.1 The effect of the amount of TEOS on mesoporous silica particles

In the case of MSN, we selected the amount of TEOS as the main factor to control the particle size. According to our experience, the TEOS addition rate and the surfactant concentration showed negligible effect on the MSN particle morphology and size. Moreover, we observed that increasing the reaction time



had no significant effect on the particle size. As TEOS is the source of the monomers that forms the mesoporous silica network, when the amount of TEOS is increased, both the hydrolysis and condensation rates speed up.

**Table 2.** Average particle size under different reaction conditions.

Name of the sample	Experimental conditions						Results	
	CTAB (g)	EtOH (mL)	H <sub>2</sub> O (mL)	NH <sub>3</sub> ( $\mu$ L)	TEOS (mL)	TEOS addition temperature ( $^{\circ}$ C)	Average pore size (nm)	Average particle size (nm)
MSN-1	1.02	120	340	100	1	80	2.5	168
MSN-2	1.02	120	340	100	1.5	80	2.5	240
MSN-3	1.02	120	340	100	2.5	80	2.5	357
MSN-4	1.02	120	340	100	4	80	2.5	540
MSN-5	1.02	120	340	100	4.5	80	2.5	706
MSN-6	1.02	120	340	100	1	35	-	No particles
MSN-7	1.02	120	340	100	2.5	35	-	No particles

The detailed synthesis conditions of MSNs are represented in *Table 2*. The morphology of the monodispersed MSN was characterized by High-Resolution Scanning Electron Microscopy (HRSEM). As can be seen from the SEM images, the size of MSN could be easily tuned by varying the amount of TEOS systematically from 1 to 5 mL. The morphology of all synthesized MSN was spherical with uniform size. By increasing the TEOS concentration, the size of the samples was raised from 168 nm (MSN-1) up to 706 nm (MSN-5). The particle size of all samples was determined by using ImageJ software on SEM micrographs and corresponding histograms were generated revealing average particle sizes of 168 nm, 240 nm, 347 nm, 540 nm, 706 and 706 nm for TEOS quantities equal to 1 mL, 1.5 mL, 2.5 mL, 4 mL, 5 mL respectively (Figure 3-3a, b, c, d, e). Additionally, we conducted two experiments by adding TEOS at 35 $^{\circ}$ C, which showed no particle formation. This could be explained because of extremely slow TEOS hydrolysis and condensation rates at low temperature, thereby taking days for particles formation.

The STEM analysis showed (Figure 3-3a-f) that although the size of MSN increased with TEOS concentration, the pore size remained stable at around 2.5 nm.

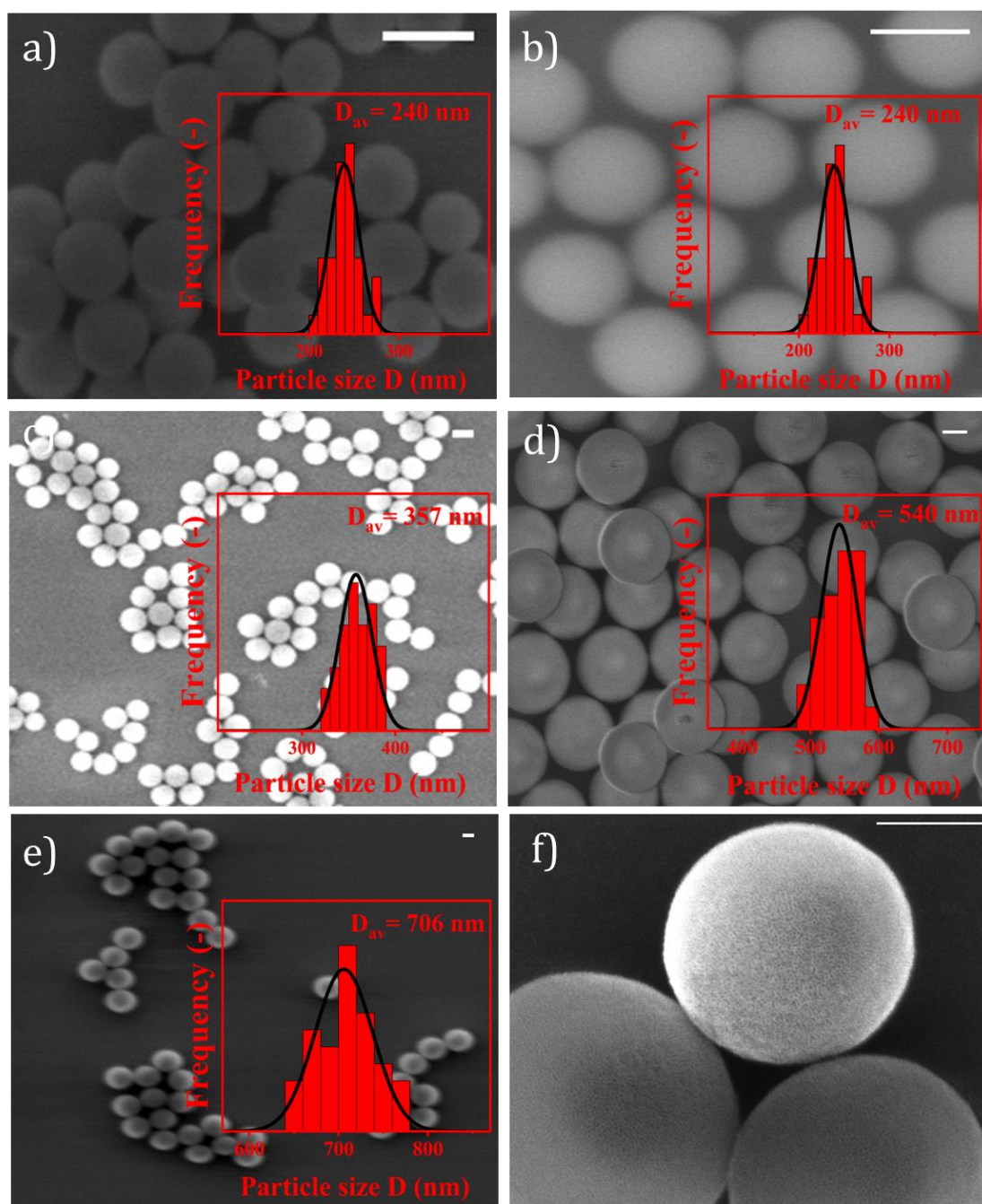


**Figure 3-3.** SEM images of MSN prepared by sol-gel method at various TEOS concentration a) MSN-1 b) MSN-2 c) MSN-3 d) MSN-4 e) MSN-5 f) STEM image of MSN-2. Scale bars 200 nm (a, b,d), 300 nm (c, e) and 100 nm (f).

### 3.2.2 Large pore silica nanoparticles (LPSN)

Three main factors were followed to control the pore size in the LPSN: i) the amount of  $\text{NH}_3$ , ii) the amount of TEOS, iii) the amount of pore-expanding agent. In this case TMB, triethanolamine (TEA) and dimethylhexylamine (DMHA) were used as expanding agents. The reaction conditions for the synthesis of LPSN are shown in Table 3.

In the synthesis process  $\text{NH}_3$  was used as a basic catalyst in order to speed up the rate of silica condensation process. The pore and particle size of LPSN depend on the rate of TEOS hydrolysis and condensation. Therefore, different amounts of ammonia can have a significant effect on the pore and particle size of the LPSN (Figure 3-4). We observed that using a small amount of ammonia (100  $\mu\text{L}$ ) alongside TMB has no effect on the pore size of silica particles. In order to obtain the NPs with desired pore size the amount of ammonia also needs to be increased. High amount of ammonia increases the formation rate of micelles and TEOS hydrolysis and decrease the reaction time up to 2 h. This could be explained due to the pH of the reaction system. The hydrolysis of TEOS is quite slow in the reaction system, because this reaction occurs at the liquid-liquid (TEOS/water) interface. Namely, silicate species have a restricted supply due to the limited surface area of the TEOS/water interface. On the other hand, as the reaction proceeds, the condensation process becomes faster, which is caused by the decrease of pH in water phase due to the presence of ammonia.

The pore size in the MCM-41 materials can be controlled by the hydrophobic alkyl chain length of the surfactants or with the aid of auxiliary organic compounds (*i.e.*, trimethylbenzene) as spacers and fillers<sup>32</sup>. When the auxiliary organic species are added to the reaction gel, they are solubilized inside the hydrophobic regions of the micelles, causing an increase in micelle diameter which leads to an increase in the pore size of the final product<sup>33</sup>. When triethanolamine (TEA) was used as swelling agent, no expansion of the pore size of the LPSN-1 (2.2 nm) was observed by the addition of 3 mL of  $\text{NH}_3$ . In the case of DMHA as swelling agent, a significant increase in the pore size (8 nm in LPSN-2) was obtained by the addition of 4 mL DMHA. Nevertheless, the pore size stayed unchanged with the further increase of the amount of DMHA.

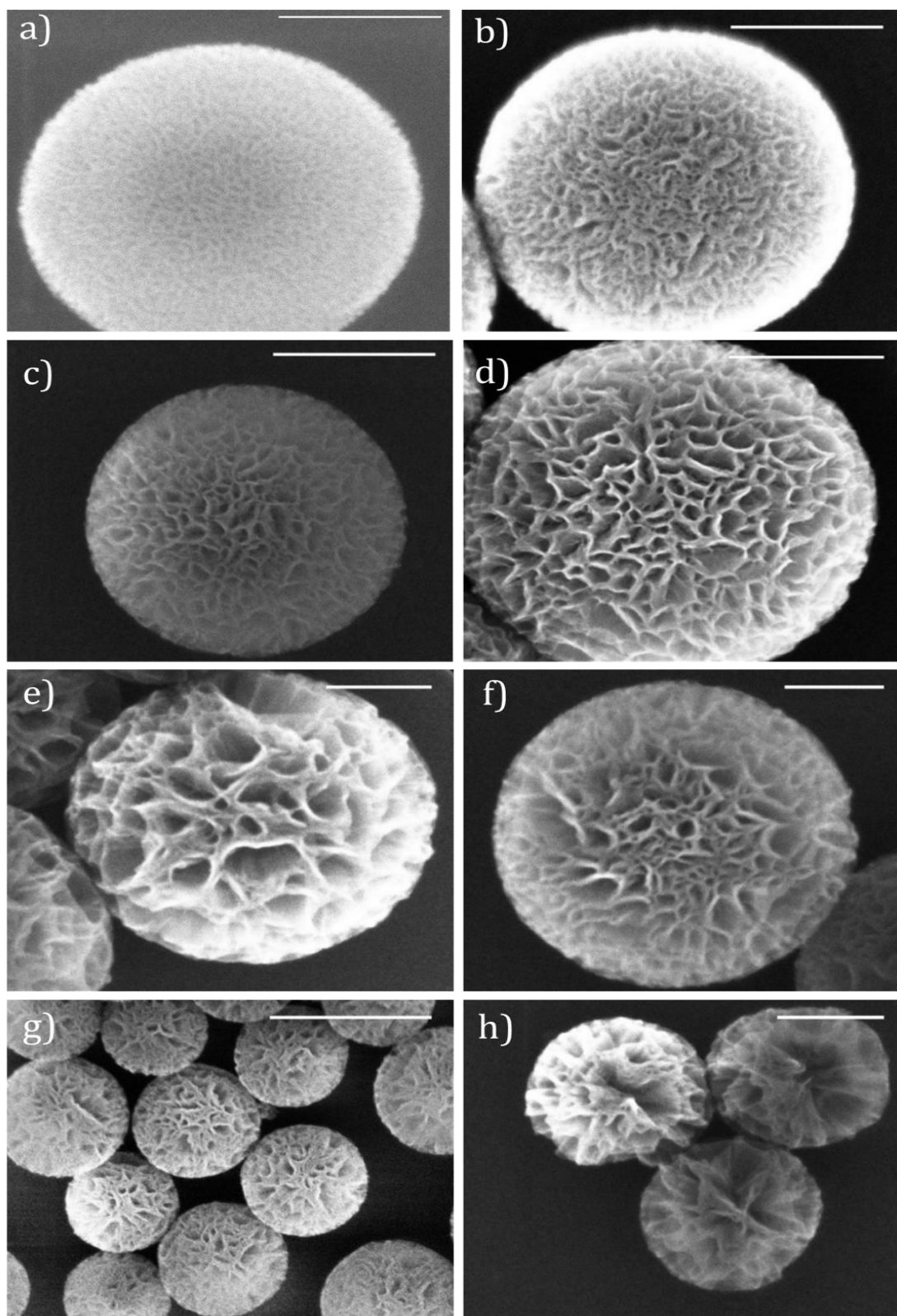


**Figure 3-4.** SEM images of LPSNs synthesized by simple sol/gel method by using TMB as pore expanding agent. a) LPSN-1 b) LPSN-2 c) LPSN-3 d) LPSN-4 e) LPSN-5 f) LPSN-6 g) LPSN-7 h) LPSN-8. Scale bars 200 nm (a, b, c, f, g), 100 nm (e, h)

In contrast, Mesitylene (TMB) could significantly enlarge the pores size of the LPSN from 10 nm up to 58 nm (LPSN-3; LPSN-8) by tuning the reaction conditions. Unlike the other swelling agents, TMB showed better selectivity and tunability of the pore expansion in the LPSN. By tuning the amount of TMB, LPSN with different pore sizes could be synthesized without addition of any other polymer, such as Pluronic (F123 and F127).

Compared to MSN, the LPSN samples showed disordered pore structure with wide pore distributions from 2 nm up to 58 nm (Figure 3-4d), which could be related with the low boiling point of ammonia (-33 °C), leading to the fast evaporation from the reaction mixture, resulting the decrease of reaction pH. The decrease of reaction pH in the reaction mixture affected the degree of pore ordering, resulting in the formation of the disordered pore distribution<sup>34</sup>. Additionally, the particle size could be tuned by increasing the amount of TEOS. TMB allowed the formation of different pore sizes without significantly decreasing the particle diameter which could be maintained by tuning the amount of TEOS.

Therefore, by controlling both the amount of TMB and TEOS, silica NPs with both tailored pore and particle sizes could be synthesized. However, higher amount of TMB and ammonia (amount of TMB > 8 mL, NH<sub>3</sub>=5 mL) prevented further increase of the particle size (LPSN-8) due to the high pH value of the reaction mixture.

**Table 3.** Experimental conditions of LPSN with different pore sizes.

Name of the sample	Experimental conditions								Results	
	CTAB (g)	EtOH (mL)	H <sub>2</sub> O (mL)	NH <sub>3</sub> (mL)	TEOS (mL)	Mesitylene (mL) (TMB)	Triethanolamine (TEA) (mL)	Dimethylhexylamine (DMHA) (mL)	Average pore size (nm)	Average particle size (nm)
LPSN-1	1.02	120	340	3	1	-	3	-	2.2 nm	125 nm
LPSN-2	1.02	120	340	3	1.5	-	-	4	8 nm	255 nm
LPSN-3	1.02	120	340	3	3	2	-	-	44 nm	400 nm
LPSN-4	1.02	120	340	2	2	1.5	-	-	28 nm	140 nm
LPSN-5	1.02	120	340	2	3	4	-	-	49nm	345 nm
LPSN-6	1.02	120	340	3	3	1.5	-	-	14 nm	580 nm
LPSN-7	1.02	120	340	1.5	1.5	1	-	-	35 nm	230 nm
LPSN-8	1.02	120	340	5	5	8	-	-	58 nm	170 nm

### 3.2.3 Post-processing of the porous silica nanoparticles

Once the porous, MSN or LPSN, nanoparticles are synthesized, the complete removal of the surfactants is necessary for the pursued applications in this Thesis. The typical methods of the surfactant removal are calcination or acid extraction. Calcination is one of the most common methods for removal of organic residues from the pores of silica. In this method, the dried silica particles are heated up to 550 °C (4-24 h) in the presence of carrier gas (nitrogen, oxygen, air) to remove the organic residues<sup>35-37</sup>. However, prolonged, continuous heating of silica particles results in complete removal of silanol groups thereby preventing the complete dispersion of NPs in solution and promoting the formation of aggregates. Moreover, the high temperature also leads to structural shrinkage and pore deformation, and the burned surfactants can leave carbon deposits blocking the pores. To avoid these problems, in this synthesis we used a combination of solvent extraction and oxygen plasma to completely clean silica particles without damaging the particle morphology and to keep the silanol groups in the silica network. For the solvent extraction, particles were dissolved in ammonium nitrate (60 mg) solution in ethanol (200 ml) for 1 h at 80 °C followed by washing with ethanol three times by repeated centrifuging<sup>38</sup>. Since silica has high stability in alcohols, the already washed particles were resuspended in ethanol for long term storage.

In the applications related to this thesis, the porous particles are self-assembled on silicon wafers to continue the fabrication processes (Figure 3-5). This step enabled an additional cleaning and activation by oxygen plasma. The MSNs were deposited on silicon substrates by a colloidal self-assembly based on the previous formation of monolayer silica particles on the air/water surface on the immersed silicon wafer, thus leading to the formation of a hexagonal close-packed array. Then the water was drained to deposit the self-assembled monolayer on the silicon wafer. Once the wafer was fully dried, then the substrate with MSN was subjected to oxygen plasma (400 W, 60 sccm, 4 min) which was performed while introducing oxygen to the plasma system. The oxygen plasma allowed the fast and complete removal of residual contaminants without damaging the particle and pore morphology of the assembled MSN.

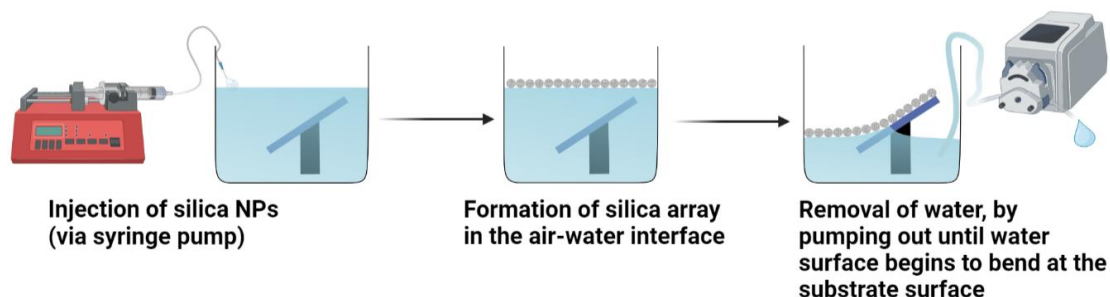


**Figure 3-5.** Schematic of colloidal self-assembly.

To tailor the size of NPs, the obtained silica array was etched using Reactive ion etching (RIE) (Figure 3-6a). RIE is a process that removes materials chemically from substrates using ion bombardment. RIE was performed using  $\text{CHF}_3$  gas for 45 seconds. Once the process finished, the substrate was cleaned with  $\text{O}_2$  plasma for 3 min to completely remove excess fluor (F) from the pores (Figure 3-6b, c).

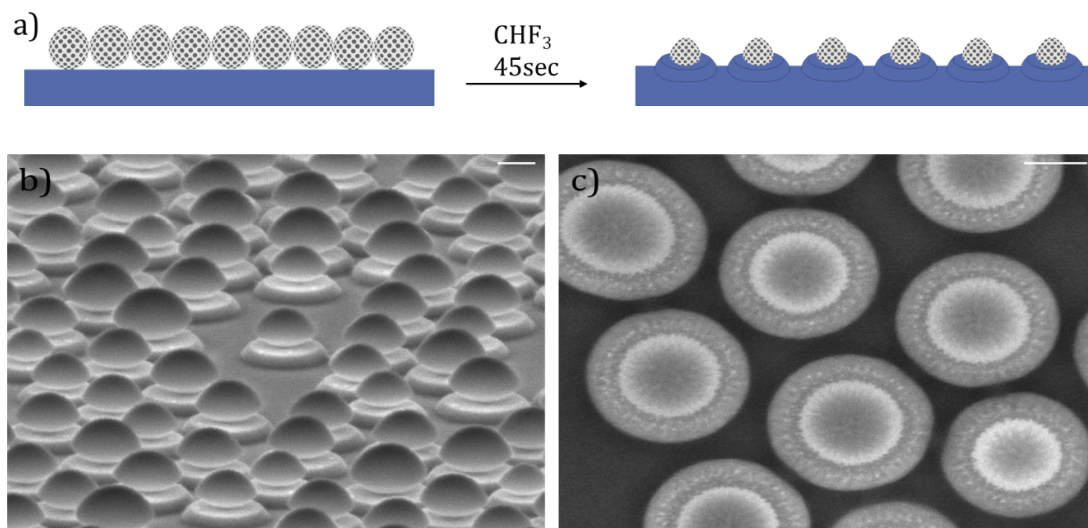


**Figure 3-6.** a) Schematic of reactive ion etching of silica NPs, b) the etched silica NPs c) top view of etched silica NPs. Scale bar 100 nm.

### 3.2.4 X-Ray diffraction and colloidal analysis

To assess the crystallographic structure and colloidal stability, the MSN-3 sample was analyzed by Dynamic Light Scattering (DLS) and X-ray Diffraction (XRD). The MSN-3 particles were dispersed in water and the particle size distribution of the suspension was evaluated by DLS. The analysis exhibited a monodisperse size distribution (PDI=0.07) with an average size of  $335 \pm 5$  nm, which confirms the high stability of the as-synthesized MSN-3 sample (Figure 3-7a).

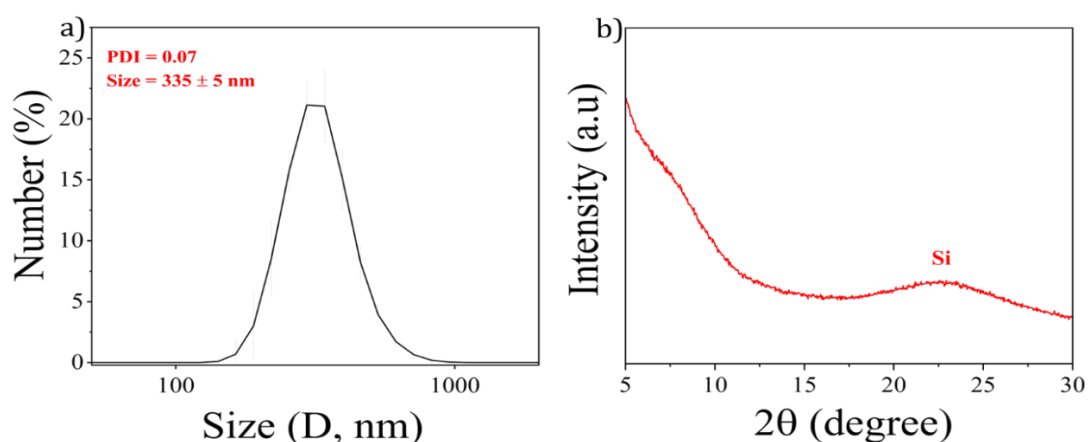


**Figure 3-7.** a) Dynamic light scattering (DLS) spectrum, and b) XRD spectra of MSN-3 sample.



An amorphous peak of MSN-3 sample between  $20^\circ$  and  $30^\circ$  was observed in the X-ray diffraction confirming the amorphous silica network in the NPs and the absence of crystalline phases (Figure 3-7b).

### 3.2.5 Optical properties of silica particles.

The photoluminescence (PL) spectroscopy was used to characterize the optical emission properties of MSN. Figure 3-8a, b exhibits the PL spectra of MSN-2 sample. For the PL analysis the sample was prepared by assembling MSN on the silicon wafer. The PL spectra were collected with the excitation beam from a laser at 405 nm continuously shining a sample.

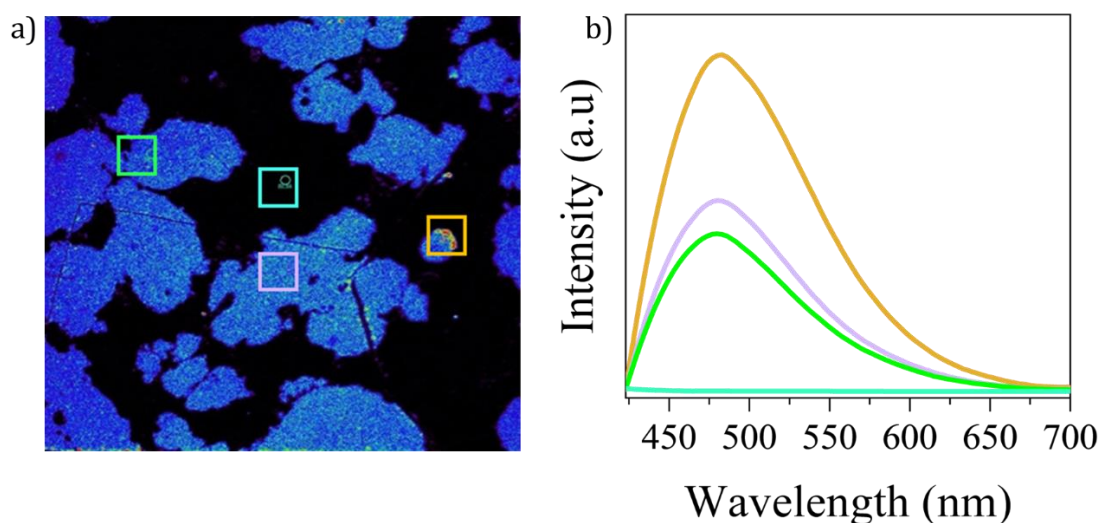


**Figure 3-8.** a) MSN-2 sample used for PL spectra b) PL spectra of MSN-2 sample.

The PL spectra were taken from four different spots of the MSN-2 sample with the excitation wavelength 405 nm at room temperature. To confirm the impact of substrate on the PL emission, firstly, the PL spectrum of silicon substrate was taken (Figure 3-8a). As can be seen from the spectra, the substrate has no effect on the PL emission. However, when the spectra were taken on the silica particles, the PL spectra showed one broad PL emission band in the wavelength range from 400 to 800 nm. In the regions of high concentration of particles the PL emission significantly increased (Figure 3-8b).

This very interesting photoluminescence in amorphous porous silica nanoparticles can be due to the existence of diverse defects (vacancies and impurities) which play the role of emission centers<sup>39</sup>. Indeed, the defects can create different electronic states that can cause optical transitions as absorption and luminescence with lower energies than the fundamental absorption edge of the silica material, approximately 9 eV, from the valence to the conduction band. These optical properties can be extremely interesting in the bioimaging field.

### 3.3 Conclusions

In this Chapter, silica particles with different particle (MSN) and pore sizes were synthesized by a simple sol-gel method. The main advantage of this method is its reproducibility with the controlled pore and particle size. A series of monodispersed MSN with controlled particle size were developed by controlling the amount of TEOS which is the main factor for the particle growth. Additionally, the MSNPs showed high stability and uniformity according to the DLS results. In addition to particle size, the pore size also could be adjusted from 2.5 nm to 58 nm by controlling the amount of swelling agent (TMB). We found out that, the pore size of NPs mainly depends on the amount of pore expanding agent alongside ammonia catalyst ( $\text{NH}_3$ ). Given their uniform and adjustable pore and particle size, both MSN and LPSN are expected to be useful in many industrial applications, especially in bio-applications including drug delivery, and in environmental remediation as catalyst support material or adsorbent for the organic pollutants.

### 3.4 Materials and Methods

The MSNs were synthesized with a simple sol-gel method using the silicon precursor TEOS and CTAB as a surfactant template. The schematic of the synthesis pathway of the MSNs is shown in Figure 3-9. The experimental procedure started by dissolving the surfactant CTAB (1.02 g) in distilled water (340 mL) in an Erlenmeyer flask (500 mL). Next, the CTAB-water solution was sonicated until the solution color became transparent and the flask was transferred to an oil bath. Except for the TEOS, the rest of the reactants were added while vigorously stirring and maintaining the reaction temperature between 30-35 °C. During the synthesis the flask was kept closed to prevent the solution evaporation. When the solution temperature reached 30 °C, ethanol (120 mL; absolute 99 %), was added to the CTAB solution. Upon the addition of ethanol, the solution color became cloudy and recovered its transparency by further stirring. Then,  $\text{NH}_3$  (100  $\mu\text{L}$  35 %) was added to the CTAB solution, and the temperature was set to 80 °C for 2 h. Finally, when the solution temperature was 80 °C, 1 mL of TEOS was added dropwise while stirring, and the mixture was maintained at constant 80 °C for 2 h. After 10 min, the solution color turned white due to the light scattering generated by the synthesized silica particles. After the 2 h, the particles were recovered by centrifugation (5 min; 10000 rpm; 26 °C) and washed with ethanol three times.

The synthesis of the LPSN also followed the same procedure except for the addition of Mesitylene (also called trimethylbenzene (TMB)) as pore-expanding agent, and the increase of the ammonia amount for rising the TEOS hydrolysis rate. Apart from TMB, Dimethylhexylamine (DMHA) and Triethylamine (TEA) were also tested as pore-expanding agents. However, TMB was finally selected as the main swelling agent due to its better performance such as allowing the

synthesis of monodisperse silica particles with desired pores and particle size without decreasing the size further. In Addition, the reaction time is fast compared with DMHA and TEA.

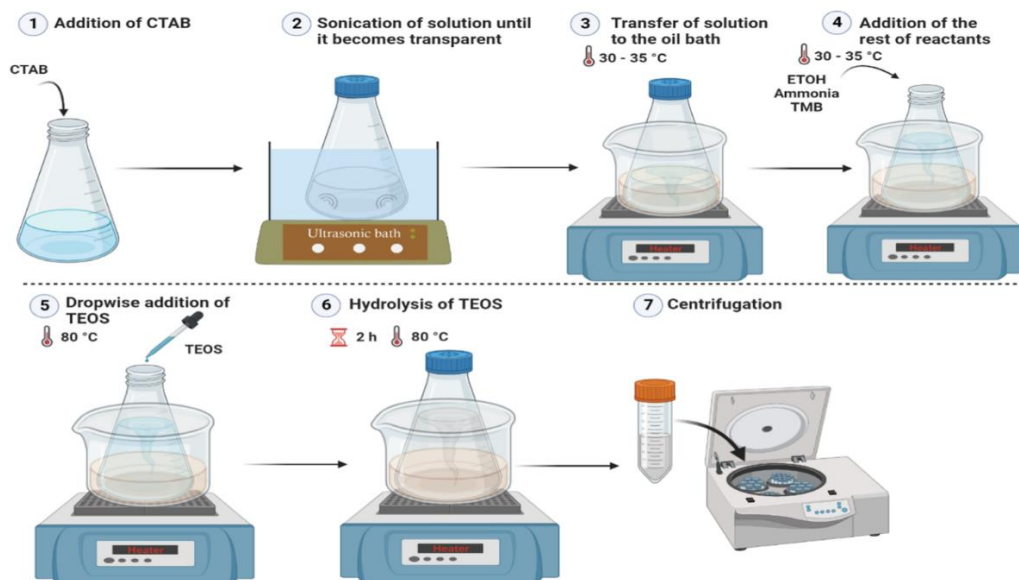


**Figure 3-9.** Schematics of synthesis pathways of mesoporous silica particles (MSN).

### 3.5 References

1. Pal N, Lee JH, Cho EB. Recent trends in morphology-controlled synthesis and application of mesoporous silica nanoparticles. *Nanomaterials*. 2020;10(11):1-38. doi:10.3390/nano10112122
2. Wang X, Zhang Y, Luo W, et al. Synthesis of Ordered Mesoporous Silica with Tunable Morphologies and Pore Sizes via a Nonpolar Solvent-Assisted Stöber Method. *Chem Mater*. 2016;28(7):2356-2362. doi:10.1021/acs.chemmater.6b00499
3. Wang J, Tsung CK, Hayward RC, Wu Y, Stucky GD. Single-crystal mesoporous silica ribbons. *Angew Chemie - Int Ed*. 2004;44(2):332-336. doi:10.1002/anie.200461296
4. Chao MC, Wang DS, Lin HP, Mou CY. Control of single crystal morphology of SBA-1 mesoporous silica. *J Mater Chem*. 2003;13(12):2853-2854. doi:10.1039/b313028m
5. Zhao D, Feng J, Huo Q, et al. Triblock copolymer syntheses of mesoporous silica with periodic 50 to 300 angstrom pores. *Science (80- )*. 1998;279(5350):548-552. doi:10.1126/science.279.5350.548
6. Zhao D, Yang P, Melosh N, Feng J, Chmelka BF, Stucky GD. Continuous mesoporous silica films with highly ordered large pore structures. *Adv Mater*. 1998;10(16):1380-1385. doi:10.1002/(SICI)1521-4095(199811)10:16<1380::AID-ADMA1380>3.0.CO;2-8
7. Kresge CT, Leonowicz ME, Roth WJ, Vartuli JC, Becht JS. Ordered mesoporous molecular sieves synthesized by a liquid-crystal template mechanism. 1992;359(October):710-712.
8. Vartuli JC, Schmitt KD, Kresge CT, et al. Effect of Surfactant/Silica Molar Ratios on the Formation of Mesoporous Molecular Sieves: Inorganic Mimicry of Surfactant Liquid-Crystal Phases and Mechanistic Implications. *Chem Mater*. 1994;6(12):2317-2326. doi:10.1021/cm00048a018
9. Yuan Q, Li N, Chi Y, et al. Effect of large pore size of multifunctional mesoporous microsphere on removal of heavy metal ions. *J Hazard Mater*. 2013;254-255(1):157-165. doi:10.1016/j.jhazmat.2013.03.035
10. Knežević N, Durand JO. Large pore mesoporous silica nanomaterials for application in delivery of biomolecules. *Nanoscale*. 2015;7(6):2199-2209. doi:10.1039/c4nr06114d
11. Hoang Thi TT, Cao V Du, Nguyen TNQ, Hoang DT, Ngo VC, Nguyen DH. Functionalized mesoporous silica nanoparticles and biomedical applications. *Mater Sci Eng C*. 2019;99(January):631-656.

- doi:10.1016/j.msec.2019.01.129
12. Wang Y, Zhao Q, Han N, et al. Mesoporous silica nanoparticles in drug delivery and biomedical applications. *Nanomedicine Nanotechnology, Biol Med.* 2015;11(2):313-327. doi:10.1016/j.nano.2014.09.014
  13. Li Z, Barnes JC, Bosoy A, Stoddart JF, Zink JJ. Mesoporous silica nanoparticles in biomedical applications. *Chem Soc Rev.* 2012;41(7):2590-2605. doi:10.1039/c1cs15246g
  14. Peng S, Huang B, Lin Y, Pei G, Zhang L. Effect of Surface Functionalization and Pore Structure Type on the Release Performance of Mesoporous Silica Nanoparticles. *Microporous Mesoporous Mater.* 2022;336(March):111862. doi:10.1016/j.micromeso.2022.111862
  15. Shen D, Yang J, Li X, et al. Biphasic stratification approach to three-dimensional dendritic biodegradable mesoporous silica nanospheres. *Nano Lett.* 2014;14(2):923-932. doi:10.1021/nl404316v
  16. Zhao D, Sun J, Li Q, Stucky GD. Morphological control of highly ordered mesoporous silica SBA-15. *Chem Mater.* 2000;12(2):275-279. doi:10.1021/cm9911363
  17. Yang Y, Bernardi S, Song H, et al. Anion Assisted Synthesis of Large Pore Hollow Dendritic Mesoporous Organosilica Nanoparticles: Understanding the Composition Gradient. *Chem Mater.* 2016;28(3):704-707. doi:10.1021/acs.chemmater.5b03963
  18. Sosa V, Leonart ME, Li Z. START PAGE COUNT – MAX 10 PAGES Magneto-plasmonic nanostructures as nanobatteries / sensors for locally controlled. 2018;606(2012):1-10.
  19. Acero JL, Von Gunten U. Characterization of oxidation processes: Ozonation and the AOP O<sub>3</sub>/H<sub>2</sub>O<sub>2</sub>. *J Am Water Work Assoc.* 2001;93(10):90-100. doi:10.1002/j.1551-8833.2001.tb09311.x
  20. Okuyama K. Sintering. *Powder Technol Fundam Part Powder Beds, Part Gener.* Published online 2006:213-218. doi:10.5940/jcrsj.31.82
  21. Lee K, Look JL, Harris MT, McCormick A V. Assessing extreme models of the Stober synthesis using transients under a range of initial composition. *J Colloid Interface Sci.* 1997;194(1):78-88. doi:10.1006/jcis.1997.5089
  22. Tran VT, Kim J, Tufa LT, Oh S, Kwon J, Lee J. Magnetoplasmonic Nanomaterials for Biosensing/Imaging and in Vitro/in Vivo Biocompatibility. *Anal Chem.* 2018;90(1):225-239. doi:10.1021/acs.analchem.7b04255
  23. Sreeharsha N, Philip M, Krishna SS, et al. Multifunctional Mesoporous Silica Nanoparticles for Oral Drug Delivery. *Coatings.* 2022;12(3).

- doi:10.3390/coatings12030358
24. Kholafazad Kordasht H, Pazhuhi M, Pashazadeh-Panahi P, Hasanzadeh M, shadjou N. Multifunctional aptasensors based on mesoporous silica nanoparticles as an efficient platform for bioanalytical applications: Recent advances. *TrAC - Trends Anal Chem.* 2020;124:115778. doi:10.1016/j.trac.2019.115778
  25. Hollamby MJ, Borisova D, Brown P, Eastoe J, Grillo I. Growth of Mesoporous Silica Nanoparticles Monitored by Time-Resolved Small-Angle Neutron Scattering. Published online 2012:4425-4433. doi:10.1021/la203097x
  26. Liu T, Li L, Teng X, et al. Single and repeated dose toxicity of mesoporous hollow silica nanoparticles in intravenously exposed mice. *Biomaterials.* 2011;32(6):1657-1668. doi:10.1016/j.biomaterials.2010.10.035
  27. Vazquez NI, Gonzalez Z, Ferrari B, Castro Y. Synthesis of mesoporous silica nanoparticles by sol-gel as nanocontainer for future drug delivery applications. *Bol la Soc Esp Ceram y Vidr.* 2017;56(3):139-145. doi:10.1016/j.bsecv.2017.03.002
  28. Meng Q, Xiang S, Zhang K, et al. A facile two-step etching method to fabricate porous hollow silica particles. *J Colloid Interface Sci.* 2012;384(1):22-28. doi:10.1016/j.jcis.2012.06.043
  29. Gao Z, Zharov I. Large pore mesoporous silica nanoparticles by templating with a nonsurfactant molecule, tannic acid. *Chem Mater.* 2014;26(6):2030-2037. doi:10.1021/cm4039945
  30. Zeng H, Dai J, Yao W, Xiao D, Cui X. Valley polarization in MoS<sub>2</sub> monolayers by optical pumping. *Nat Nanotechnol.* 2012;7(8):490-493. doi:10.1038/nnano.2012.95
  31. Nanda KK, Kruis FE, Fissan H. Evaporation of Free PbS Nanoparticles: Evidence of the Kelvin Effect. *Phys Rev Lett.* 2002;89(25):1-4. doi:10.1103/PhysRevLett.89.256103
  32. Alothman ZA. A review: Fundamental aspects of silicate mesoporous materials. *Materials (Basel).* 2012;5(12):2874-2902. doi:10.3390/ma5122874
  33. Moon DS, Lee JK. Tunable synthesis of hierarchical mesoporous silica nanoparticles with radial wrinkle structure. *Langmuir.* 2012;28(33):12341-12347. doi:10.1021/la302145j
  34. Wang L, Bahnemann DW, Bian L, Dong G, Zhao J, Wang C. Two-Dimensional Layered Zinc Silicate Nanosheets with Excellent Photocatalytic Performance for Organic Pollutant Degradation and CO<sub>2</sub>

- Conversion. *Angew Chemie - Int Ed.* 2019;58(24):8103-8108. doi:10.1002/anie.201903027
35. Trewyn BG, Giri S, Slowing II, Lin VSY. Mesoporous silica nanoparticle based controlled release, drug delivery, and biosensor systems. *Chem Commun.* 2007;(31):3236-3245. doi:10.1039/b701744h
  36. Knežević N, Durand JO. Large pore mesoporous silica nanomaterials for application in delivery of biomolecules. *Nanoscale.* 2015;7(6):2199-2209. doi:10.1039/c4nr06114d
  37. Kleitz F, Schmidt W, Schüth F. Evolution of mesoporous materials during the calcination process: Structural and chemical behavior. *Microporous Mesoporous Mater.* 2001;44-45:95-109. doi:10.1016/S1387-1811(01)00173-1
  38. Ghauch A, Tuqan A. Catalytic degradation of chlorothalonil in water using bimetallic iron-based systems. *Chemosphere.* 2008;73(5):751-759. doi:10.1016/j.chemosphere.2008.06.035
  39. Gupta J, Bahadur D. Defect-Mediated Reactive Oxygen Species Generation in Mg-Substituted ZnO Nanoparticles: Efficient Nanomaterials for Bacterial Inhibition and Cancer Therapy. *ACS Omega.* 2018;3(3):2956-2965. doi:10.1021/acsomega.7b01953

#### **4. Fe/Au galvanic nanoreactors triggering Fenton reaction without additives in water at neutral pH.**

The efficient generation of reactive oxygen species (ROS) via the Fenton reaction has received significant attention for environmental and biomedical applications. This reaction can be triggered by zero-valent metal nanoparticles by converting externally added  $\text{H}_2\text{O}_2$  into hydroxyl radicals ( $\cdot\text{OH}$ ) in acidic media. To avoid the need for any external additive or energy supply, the development of self-sustained catalytic systems enabling continuous onsite production of  $\text{H}_2\text{O}_2$  at a neutral pH is particularly important. In this Chapter, novel Fe/Au galvanic nanoreactors are fabricated by the physical vapor deposition of a metallic Fe/Au bilayer on arrays of nanoporous silica nanostructures. These nanoreactors enable the direct production of  $\text{H}_2\text{O}_2$  and efficiently release  $\text{Fe}^{2+}$  as soon as they are immersed in water at a neutral pH, thereby triggering the Fenton reaction by exploiting the large electrochemical potential difference between the Fe and Au layers. The galvanic nanoreactors simultaneously promote the  $\text{Fe}^{2+}/\text{Fe}^{3+}$  circulation and minimize side reactions that passivate the iron surface, which enhances their reactivity.



## 4.1 Introduction

Reactive oxygen species (ROS) are highly reactive free radicals with a wide range of applications, from the removal of toxic organic pollutants to the selective destruction of cancer cells<sup>1-5</sup>. A widely extended mechanism to efficiently generate ROS is through the Fenton reaction, which uses H<sub>2</sub>O<sub>2</sub> as a precursor generating the highly oxidant hydroxyl radical ( $\cdot\text{OH}$ ). This process can be catalyzed by transition metal cations such as iron, copper, aluminum, or silver. The interest in the Fenton reaction has increased with the development of highly reactive zero-valent metal nanoparticles, which can efficiently generate metal cations through their corrosion in water media, as a result of the electron transfer between the metals and O<sub>2</sub><sup>6</sup>. Examples of such zero-valent nanoparticles are silver, copper, aluminum, and iron nanoparticles<sup>7-9</sup>, the latter being the most widely studied due to their low cost, low toxicity, abundance, and reducing activity<sup>9-12</sup>.

The zero-valent iron nanoparticles (nZVI) are highly reactive reagents that can trigger different reaction pathways, such as redox, adsorption, or precipitation, depending on the reaction conditions<sup>13</sup>. Despite the merits of nZVI in Fenton reactions and other reaction pathways, they also exhibit important limitations. For instance, nZVI can easily aggregate in solution due to magnetic and electrostatic interactions, which can decrease their reaction performance<sup>14</sup>. Different support materials, such as silica or metal-organic frameworks, can be used to overcome such limitations and increase their stability and reactivity<sup>15,16</sup>. Another drawback is their short lifetime due to the surface passivation of the nZVI over time caused by the formation of oxyhydroxides or oxides that hinder the electron transfer from the Fe<sup>0</sup> core to the surface. Such a problem is intensified at higher pH, thus limiting the activity of the Fe nanoparticles to a narrow acidic pH range<sup>17-19</sup>. The surface passivation can restrict the applications of nZVI in environmental remediation when the redox process is the main decontamination pathway. However, the passivated iron nanoparticles can also be exploited for pollutant adsorption and co(precipitation) through chemisorption and electrostatic interactions<sup>20</sup>.

On the other hand, to simplify the Fenton reaction with zero-valent nanoparticles, new strategies to minimize the need for external additives (e.g., H<sub>2</sub>O<sub>2</sub>) or energy supplies (e.g., UV light, ultrasounds) are needed, thereby avoiding the increase in complexity and costs. The capability to produce H<sub>2</sub>O<sub>2</sub>

*in-situ* is therefore very relevant for activating Fenton or Fenton-like processes and generating reactive oxygen species with higher oxidizing power<sup>21</sup>. However, the majority of the Fenton nZVI systems have relied on the external supply of H<sub>2</sub>O<sub>2</sub> to achieve proper ROS generation, which reflects the difficulties in tuning the reactivity of the nZVI/O<sub>2</sub> system due to the many dependent reaction parameters (e.g., nZVI particle size, pH, O<sub>2</sub> dosage dissolved in water, growing passivation layer over time). Different strategies have been proposed to improve the nZVI systems, such as introducing other metals or components into the nZVIs to create intermetallic galvanic cells that enhance iron reactivity. The galvanic effect is induced when two metals, with different electrochemical potentials, are brought into contact, forming a pair of electrodes, with one of them acting as a cathode and the other as an anode<sup>22-25</sup>. The galvanic effect has been used for a variety of purposes, including cathodic protection<sup>26-30</sup>, which involves using a sacrificial metal as the anode to protect a more valuable metal as the cathode. However, the galvanic effect could also be applied to boost the reactivity of the anodes for the efficient generation of reactive oxygen species. There are some examples in the literature of ZVI-based systems that use the galvanic effect to trigger reductive decomposition or Fenton oxidation of analytes, such as Fe-based metallic glasses, high entropy alloys, and bi-component systems. Fe-based metallic glass catalysts (e.g., FeB, FeBC, FeBP, FeSiB, FePC, FeSiBCu, FeNbSiB) are characterized for exhibiting a high density of reactive sites due to the formation of local nanosized galvanic cells between different Fe-rich and Fe-poor atomic clusters, which promotes the rapid degradation of dyes<sup>31-39</sup>. On the other hand, Fe-based high entropy alloys are typically made by mixing Fe with roughly equal amounts of multiple metallic elements, such as Cu, Co, Cr, Ni, Mn, etc. The resulting materials, which have highly disordered atomic structures, have been mainly exploited for dye decomposition through reductive pathways<sup>40</sup>. Finally, bi-component systems integrating Fe with Co, Ni, Cu, Pt, Pd, or carbon have also been studied for the reductive trapping of heavy ions or the reductive degradation of organic contaminants<sup>41-45</sup>. However, very few studies have demonstrated the Fenton-like pathway for analyte decomposition. Moreover, in most of these systems, external addition of H<sub>2</sub>O<sub>2</sub> was required, as the *in-situ* generation of H<sub>2</sub>O<sub>2</sub> was insufficient to stimulate the generation of •OH radicals. The very few cases that have been able to produce *in-situ* sufficient H<sub>2</sub>O<sub>2</sub> for activating the ROS production were under acidic medium conditions (pH~3) or using very large catalyst dosages<sup>46-48</sup>.

Here, a novel Fe/Au galvanic nanoreactor system with an enhanced reactivity obtained by merging the large electrochemical potential difference between the constituent metals and the high surface area of the nanoreactor. This catalytic system is fabricated by depositing a Fe/Au bilayer on an array of self-assembled porous silica nanoparticles. The Fe/Au nanoreactors enable efficient simultaneous Fe<sup>2+</sup> release and H<sub>2</sub>O<sub>2</sub> generation to effectively trigger the

production of reactive oxygen species via the Fenton reaction without the need for any external chemical additive or energy source. Moreover, in contrast to previous Fe-based systems, we also show that the Fe/Au nanoreactors are highly efficient at neutral pH, requiring very low amounts of catalyst, as demonstrated by the rapid degradation and mineralization of relevant organic pollutants, like the dye methylene blue and the antibiotic tetracycline.

## 4.2 Results

### 4.2.1 Fabrication of the galvanic nanoreactors

The Fe/Au galvanic nanoreactors consist of arrays of self-assembled large pore nanoporous silica nanoparticles (diameter 200-250 nm, pore size 35 nm) on which Fe (60 nm) and Au (20 nm) layers are deposited by electron beam evaporation, forming a bimetallic semi-shell (Figure 4-1a). The highly hydrophilic nanoporous silica nanoparticles act as a high surface area support, conferring high reactivity to the bimetallic coverage and allowing direct contact of water with both metals. To assess the reaction mechanisms of the galvanic Fe/Au nanoreactors, similar structures of zero-valent Fe (60 nm thick) were also studied. The ROS generation tests were conducted with the nanoreactors attached to silicon substrates to enable monitoring the fast reaction, which was triggered as soon as the samples were immersed in water. The nanoreactor immobilization also provided a quick and simple approach for the recovery of the catalyst. The morphology of the Fe/Au nanoreactors can be observed in Figure 4-1b and c, showing the obtained metallic Fe and Au semi-shell layers on the porous silica nanoparticles. Importantly, this fabrication method enables assembling the Fe and Au layers without any interlayer passivation, as the deposition is done under high vacuum conditions.

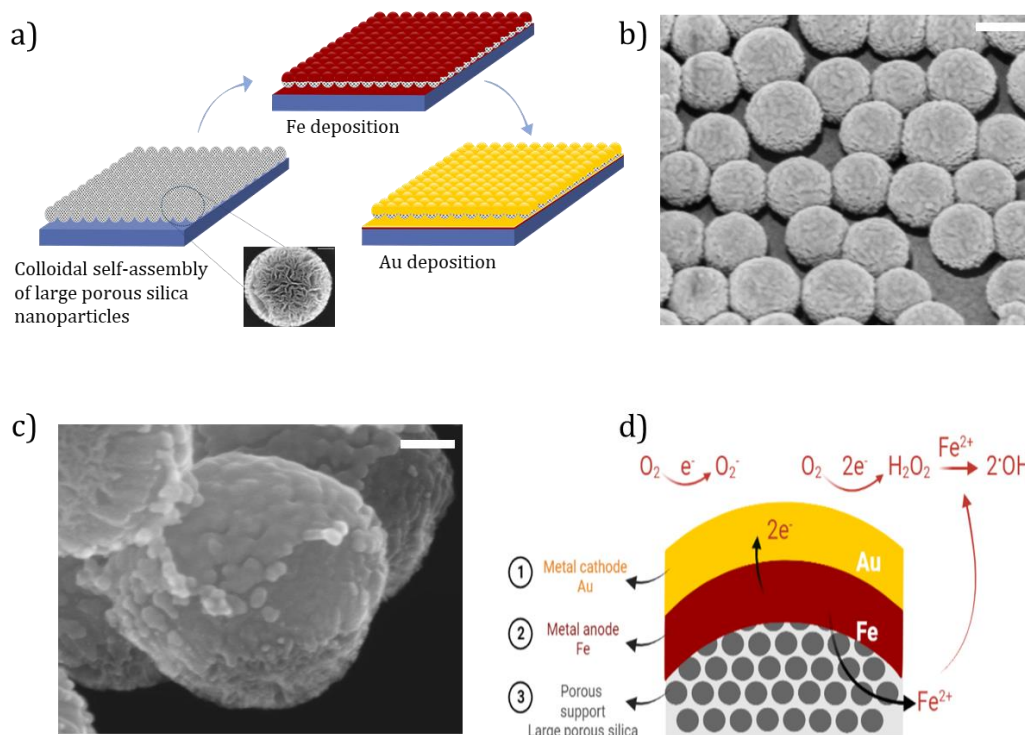


**Figure 4-1.** a) Schematic of the Fe/Au galvanic nanoreactors fabrication process, starting with the self-assembly of the large pore silica particles on a silicon substrate and the subsequent evaporation of Fe and Au layers on top. The inset shows a scanning electron microscopy (SEM) image of one porous silica particle (50 nm). b) SEM image of the self-assembled nanoreactors (scale bar 200 nm). c) SEM image of Fe/Au nanoreactors (scale bar 50 nm). d) Schematic depicting the galvanic Fe/Au reaction mechanism, showing the main reactions pathway.

#### 4.2.2 Galvanic reaction pathway.

The proposed galvanic reaction pathway for the generation of reactive oxygen species is shown in Figure 4-1d. In the Fe/Au nanoreactors the Fe layer acts as an anode and the Au layer as a cathode due to the electrochemical potential difference between the Fe ( $E^0(\text{Fe}^{2+}/\text{Fe}^0) = -0.44 \text{ V}$ ) and Au ( $E^0(\text{Au}^+/\text{Au}^0) = +1.83 \text{ V}$ ) layers. The galvanic reaction starts with the oxidation of Fe to  $\text{Fe}^{2+}$  at the anode, transferring the released electrons to the Au layer by the voltage difference. Then, due to their high solubility in water, the  $\text{Fe}^{2+}$  cations are released to the solution through the pores of the silica support. Therefore, in this galvanic system, the Au capping layer increases the corrosion of the Fe surface and accelerates the electron transfer rate. Once the electrons are transferred to the Au layer, there are two possible reaction pathways. The transferred electrons to the Au layer can reduce oxygen to superoxide radical and, taking several steps, to  $\text{H}_2\text{O}_2$ . Alternatively, both electrons could move to the cathode to directly produce  $\text{H}_2\text{O}_2$  from the available  $\text{O}_2$  in water. Finally, the released  $\text{Fe}^{2+}$  cations decompose the produced  $\text{H}_2\text{O}_2$  to generate the hydroxyl radicals, thus triggering the Fenton cycle.

To validate this reaction pathway, the main ingredients needed to trigger the Fenton reaction were first identified, by monitoring the  $\text{H}_2\text{O}_2$  production and the release of iron cations during the spontaneous reaction of the nanoreactors in water at pH 7. The detection of the produced  $\text{H}_2\text{O}_2$  is complex due to its short lifetime, as it undergoes a fast reaction with the iron cations. Moreover, most conventional techniques have high detection limits (about mg/L) or require very acidic medium conditions<sup>46,49,50</sup>. To overcome these challenges, we adapted a procedure for detecting  $\text{H}_2\text{O}_2$  that has been used in biological samples<sup>51</sup>, which relies on an enzymatic reaction to generate a fluorescent probe of the  $\text{H}_2\text{O}_2$ , whose emission intensity is proportional to the  $\text{H}_2\text{O}_2$  concentration. Briefly, the  $\text{H}_2\text{O}_2$  was detected with the Amplex<sup>TM</sup> Red reagent (10-acetyl-3,7-dihydroxyphenoxazine), which is an extremely sensitive peroxidase substrate in the presence of the enzyme horseradish peroxidase (HRP), to produce highly fluorescent resorufin (more details are given in the Materials and Methods section). As an additional advantage, this approach enables collecting the fluorescence signals at the nanoreactor interface using confocal fluorescence microscopy.

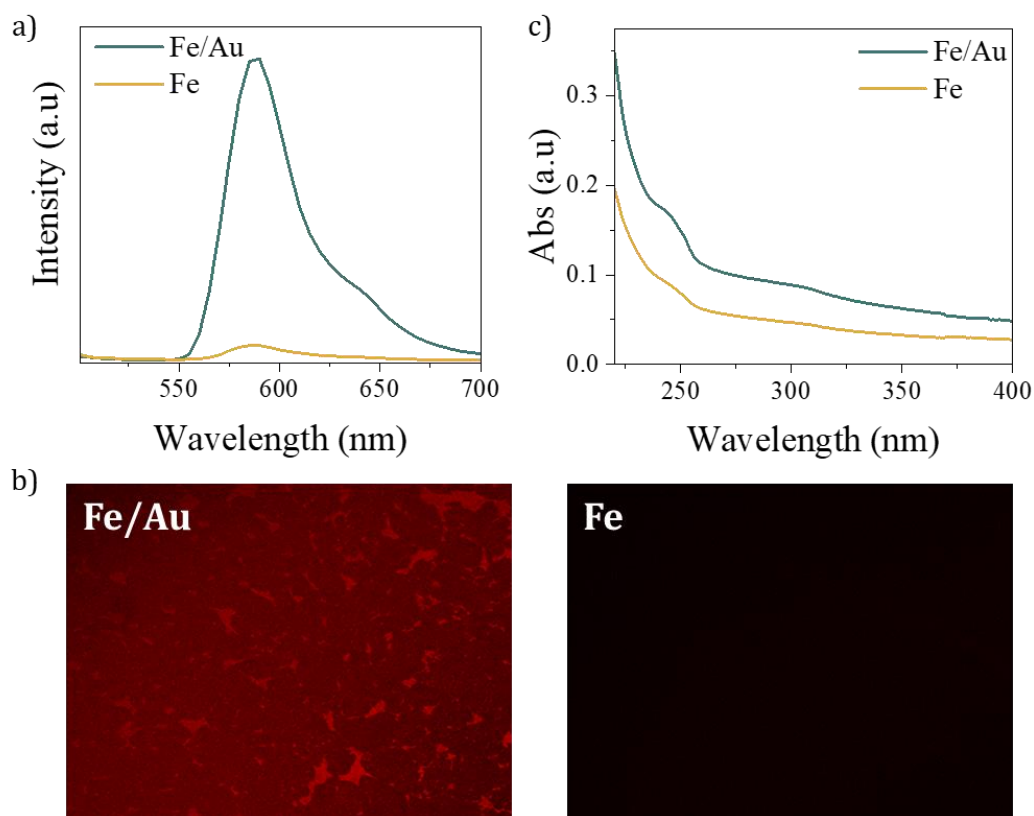


**Figure 4-2.** a) Fluorescence emission of resorufin for the Fe/Au and Fe nanoreactors excited at 488 nm. b) Fluorescence images of the Fe/Au and the Fe nanoreactors surfaces, respectively. c) UV absorbance of the reaction fluid for the Fe/Au and the Fe nanoreactors after 90 min of reaction (for the detection of Fe ions).

Figure 4-2a shows the intensity of the fluorescence emission spectra of resorufin for the galvanic Fe/Au reactors compared to the Fe system. The high intensity of the resorufin fluorescence signal confirmed the enhanced *in-situ* production of H<sub>2</sub>O<sub>2</sub> in the Fe/Au galvanic cell, whereas it was minimal for the Fe reactors. The H<sub>2</sub>O<sub>2</sub> concentration was determined through an H<sub>2</sub>O<sub>2</sub> calibration curve. After the first ten minutes of reaction the H<sub>2</sub>O<sub>2</sub> concentration was remarkably higher (36-fold) in the Fe/Au nanoreactors (1.8 μM) compared to the Fe reactors (0.05 μM). In addition, the confocal images of Figure 4-2b confirm the drastically enhanced fluorescence intensity mapping for the Fe/Au nanoreactors. On the other hand, the release of Fe cations in water was evaluated by UV spectroscopy, by detecting their absorption in the UV below 300 nm<sup>52</sup>, after immersing the Fe/Au and Fe systems in water for 90 min. Interestingly, as illustrated in Figure 4-2c, the amount of released Fe ions by the Fe/Au nanoreactors was significantly higher than the Fe counterpart after 90 min in water, despite the substantially lower iron surface in direct contact with water. The enhanced release of Fe<sup>2+</sup> ions was a direct result of the galvanic effect. The release of iron cations was further confirmed and quantified by ICP-mass spectroscopy, showing concentrations of 19.4 and 5.1 ppb for the Fe/Au and Fe nanoreactors, respectively.

Consequently, these results indicate that the Fe/Au galvanic system can effectively produce the fundamental ingredients (H<sub>2</sub>O<sub>2</sub> and Fe<sup>2+</sup> ions) to trigger the Fenton catalytic pathway with high efficiency in water at neutral pH without any external additive<sup>53</sup>.

### 4.2.3 Catalytic activity

To demonstrate the additive-free Fenton reaction in water at neutral pH, the catalytic activity of the Fe/Au and Fe nanoreactors was evaluated for the degradation and mineralization of two typical non-biodegradable environmental pollutants<sup>54,55</sup>: methylene blue (MB) and tetracycline (TC). Importantly, the catalytic tests were conducted using very low concentrations of Fe/Au and Fe nanoreactors of 14.8 μg/mL and 14 μg/mL, respectively. The degradation of the MB (10 ppm, 3.2 mg/L) was first analyzed by the decrease of its UV-VIS spectra (absorbance peak centered at 664 nm) during 90 min reaction time. As shown in Figure 4-3a and 3b, the MB removal was extremely fast for the Fe/Au nanoreactors, with an almost complete degradation in the first 15 min, compared to the substantially lower kinetics of the Fe nanoreactors. This clearly indicates the enhanced reactivity conferred by the galvanic cell formed between the Fe and Au layers. The degradation efficiencies of MB after 90 min were 94.0 % and 86.3 % for Fe/Au and Fe nanoreactors, respectively (Figure 4-3c).

Next, the MB mineralization ability of Fe/Au and Fe nanoreactors was quantified by measuring the total organic content (TOC) (Figure 4-1c), showing efficiencies of 86.1 % and 81.1 % for the Fe/Au and Fe nanoreactors, respectively, further confirming the efficient ROS generation by the galvanic effect.

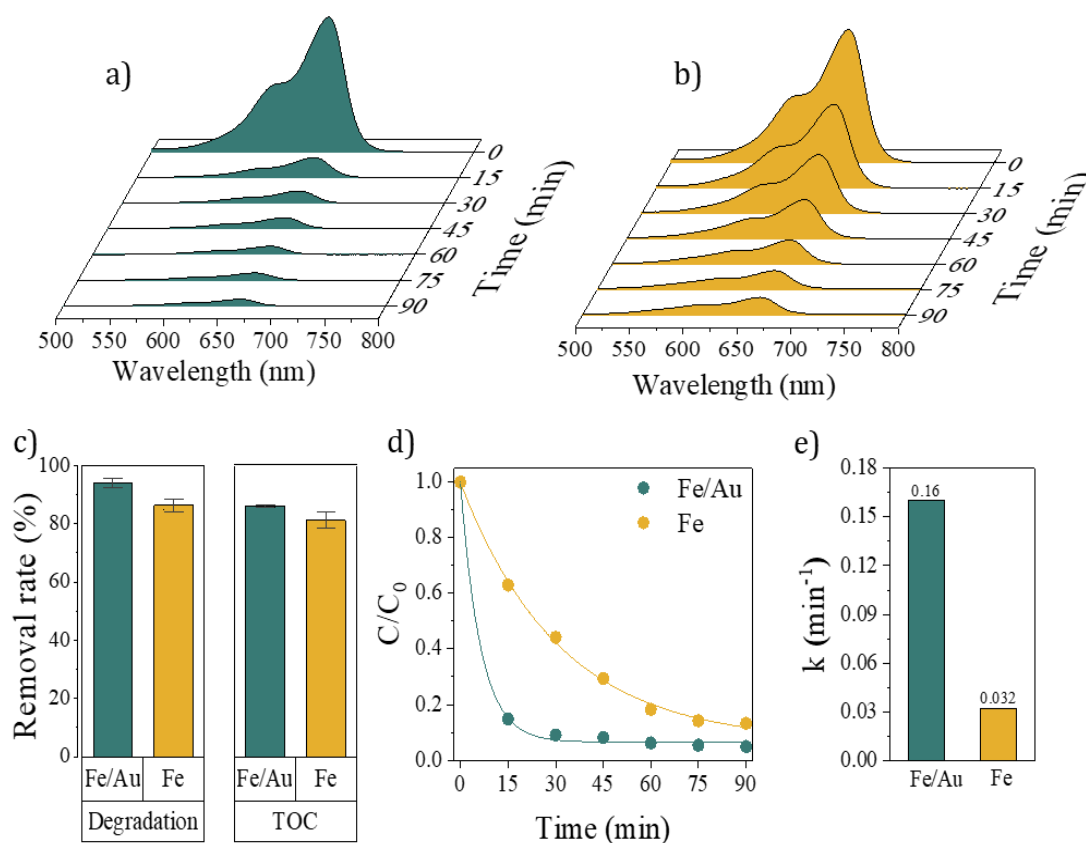


**Figure 4-3.** Catalytic degradation of MB in the presence of a) Fe/Au and b) Fe nanoreactors. c) Degradation and TOC removal rates after 90 min of reaction. d) Comparison of kinetic fitting of MB decay through pseudo-first order-nonlinear kinetics ( $R^2_{\text{Fe/Au}} = 0.998$ ,  $R^2_{\text{Fe}} = 0.997$ ) and e) the corresponding reaction rate ( $k$ ).

The kinetics of the MB removal process (Figure 4-3d) exhibited a pseudo first-order kinetics for both Fe/Au and Fe nanoreactor, following the equation  $C_t = C_0 e^{-kt}$ , where  $C_t$  represents the contaminant concentration at time  $t$ ,  $C_0$  the initial concentration, and  $k$  the first-order kinetic reaction rate constant. The  $k$  values of the Fe/Au and Fe systems were  $0.16 \text{ min}^{-1}$  and  $0.032 \text{ min}^{-1}$ , respectively (Figure 4-3e). Therefore, the Fe/Au nanoreactor had a 5-fold higher reaction rate compared the bare Fe case.

Considering the fast MB degradation by the Fe/Au nanoreactors, we analyzed the degradation and mineralization after only 15 min of reaction (Figure 4-1a). In this case, the difference between the galvanic Fe/Au reactor and the Fe reactor was remarkably higher. After just 15 min, the Fe/Au nanoreactors achieved 74.8 % degradation versus 32.6 % by the Fe nanoreactors. A similar trend was observed in the mineralization rate, reaching 64.4 % and 19.7 % for the Fe/Au and Fe systems, respectively.

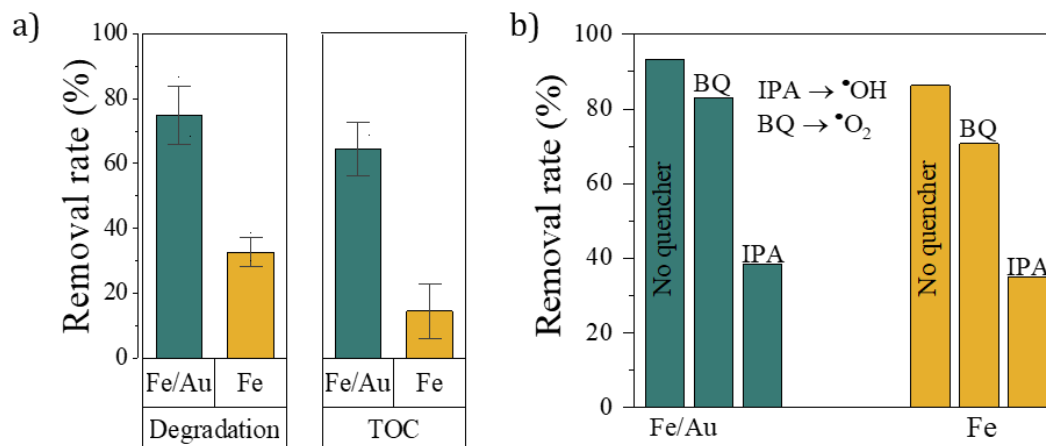


**Figure 4-4.** a) Degradation efficiency and TOC removal rates of MB after 15 min of reaction. b) MB degradation rate in the presence of the ROS quenchers benzoquinone (BQ) and isopropanol (IPA) for the Fe/Au and Fe nanoreactors after 90 min of reaction.

To further confirm the Fenton reaction pathway and the generated ROS species, radical quenching experiments were performed. To this end, isopropanol and benzoquinone were used as quenchers of the hydroxyl ( $\bullet\text{OH}$ ) and superoxide ( $\bullet\text{O}_2^-$ ) radicals, respectively. As shown in Figure 4-4b, when isopropanol was added to the reaction solution, the MB degradation rate declined distinctly to 38.3 % and 35.0 % for the Fe/Au and Fe systems, respectively. However, the degree of degradation of the MB decreased only slightly to 83.17 % and 70.8 % for Fe/Au and Fe nanoreactors, respectively, after adding a benzoquinone superoxide scavenger. Thus, these results again corroborated that the main reactive species for the MB removal were hydroxyl radicals, with superoxide radicals playing a secondary role, as expected from the Fenton pathway.



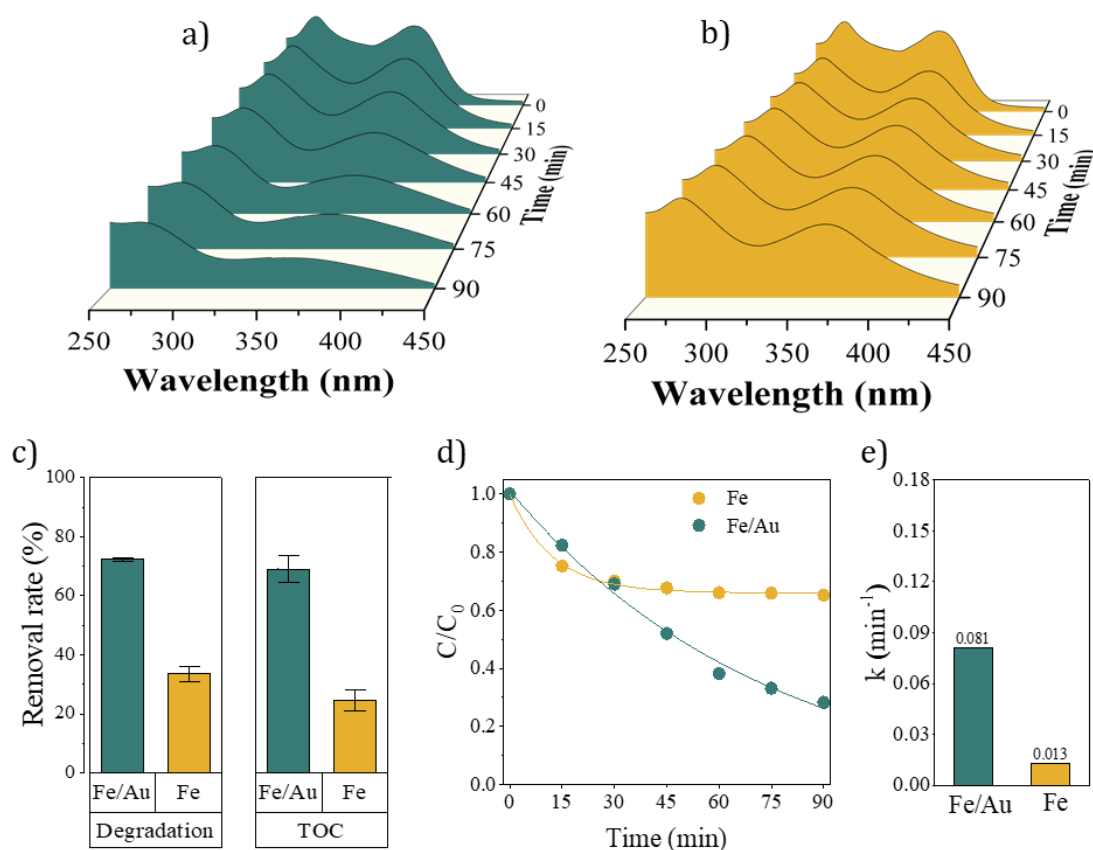


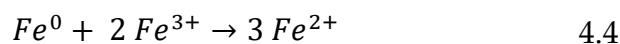
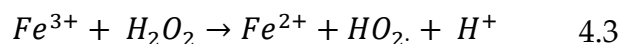
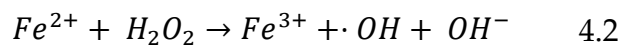
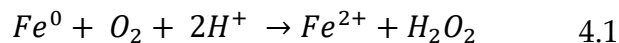
**Figure 4-5.** TC degradation in the presence of the a) Fe/Au and b) Fe nanoreactors. c) Degradation and TOC removal rates. d) Comparison of kinetic fitting of TC decay through pseudo-first order-nonlinear kinetics ( $R^2_{Fe/Au} = 0.996$ ,  $R^2_{Fe} = 0.992$ ) and e) the corresponding reaction rates ( $k$ ).

The high reactivity of the Fe/Au galvanic nanoreactors was also proven by the degradation analysis of the pollutant tetracycline (40 ppm, 17.7 mg/L), again at neutral pH and without the addition of H<sub>2</sub>O<sub>2</sub>. The absorbance spectra of TC significantly decreased (72.3 %) in the presence of the Fe/Au reactors (Figure 4-5a). In contrast, the Fe nanoreactors showed a poor performance towards TC degradation, with only 33.6 % of removal (Figure 4-5b, c). These results were correlated with mineralization efficiencies of 69.4 % and 29.4 % for Fe/Au and Fe nanoreactors, respectively (Figure 4-5d). In addition, the kinetic constants were estimated to be 0.081 min<sup>-1</sup> and 0.013 min<sup>-1</sup> for Fe/Au and Fe nanoreactors, respectively (Figure 4-5e), thereby demonstrating once more the high reactivity of the galvanic reactors.

### 4.3 Discussion

The comparative degradation studies of MB and TC clearly indicate the enhanced performance of Fe/Au with respect to Fe catalytic nanoreactors, which is ascribed to the galvanic cell formation in the bimetallic system. The potential difference between both metals is the driving force to accelerate iron oxidation and the transfer of the released electrons to the Au region for the efficient reduction of

oxygen to hydrogen peroxide. The *in-situ* generation of iron cations and H<sub>2</sub>O<sub>2</sub>, as proved by UV-visible absorption, mass spectrometry, and confocal fluorescence microscopy, are the basic ingredients for triggering the generation of •OH and Fe<sup>2+</sup> as outlined in the chemical equations below.



Therefore, the hydroxyl radicals, which were identified by quenching analysis, play a key role in degrading the organic pollutants. However, an efficient regeneration of Fe<sup>3+</sup> to Fe<sup>2+</sup> is also key to sustaining the redox catalytical loop and the efficacy of the degradation process. In absence of Au, the Fe<sup>3+</sup> reduction is mainly accomplished with the released electrons at the Fe<sup>0</sup> interface. However, it is known that the iron cations, and particularly Fe<sup>3+</sup>, can easily hydrolyze water and form iron hydroxides or react with oxygen to form oxides, which passivate the metallic iron over time, thus hindering the electron transfer and mass transport of reagents and products. The presence of Au on the zero-valent iron and the efficacy of the high-driving force galvanic cell to channel electrons into the Au region make Au an additional source of electrons for Fe<sup>3+</sup> regeneration (4.5), leading to an enhancement in the reconversion rate of Fe<sup>2+</sup>/Fe<sup>3+</sup>. The increased cycle rate of the iron cations helps to efficiently sustain the Fenton cycle while minimizing the side reactions of iron hydroxides/oxides formation at the nanoreactor surface. The acceleration of Fenton-type reactions also leads to more complete degradation of the organic compounds, with fewer by-products being produced, as proved by the mineralization TOC analysis.

Another benefit of using the Fe/Au galvanic system is that it allows the operation of the reaction at more neutral pH values. Generally, Fe-based catalysts show their optimum activity at acidic pH (~3). Increasing the pH significantly decreases the activity of the Fe-based systems due to the formation of the hydroxide/oxide passivating layers, which occurs more quickly at higher pH. In contrast, the Fe/Au nanoreactors can operate at a more neutral pH while maintaining their high catalytic activity. This effect could be ascribed to the accelerated Fenton reaction process and the fast iron cation reconversion through the high reducing power of Au. This allows the ROS-mediated degradation reaction to be the dominant pathway, minimizing the occurrence of competing side reactions.

To contextualize the performance of the catalytic Fe/Au nanoreactors with respect to other Fenton galvanic cells reported in the literature has been included. The table collects various parameters of different studies addressing the degradation of MB and TC (such as catalyst dosage, external H<sub>2</sub>O<sub>2</sub> supply, pollutant concentration, degradation efficiency, and reaction rate constants). The normalized rate constants ( $k_{\text{norm}}$ ) with respect to catalyst dosage have also been indicated for easier comparison. The cells in the table that are colored blue indicate the use of external hydrogen peroxide, acidic pH conditions, or large amounts of catalyst (>0.05g/L). The cells highlighted in yellow indicate normalized rate constants above 5. The table also includes the reaction conditions and results obtained using the Fe/Au and Fe nanoreactors of the current work.

While MB has been extensively studied using other galvanic systems, there have been very few studies on the degradation of TC using Fenton galvanic cells. Most of the studies on TC involve the removal of antibiotics, primarily through adsorption. Therefore, we have also included studies on derivatives of TC, such as oxytetracycline (OT) and chlortetracycline (CTC).

As previously mentioned, many studies on MB degradation have been conducted using metallic glasses as catalysts forming galvanic cells. In all the cases an external supply of H<sub>2</sub>O<sub>2</sub> was required, in addition to very acidic conditions (pH~3) in most of them, and high catalyst dosage. One of these studies stands out due to its very high normalized rate constant of 18, which was achieved through a complex pretreatment of the catalyst involving high annealing temperatures and ball milling, in addition to the use of external hydrogen peroxide or the adjustment of the operating pH to 3. With respect to TC degradation, most of the studies were performed under more acidic conditions and using large dosage of catalysts.

Under this comparative context, the galvanic reactors reported in this work exhibit a very relevant improved degradation performance for MB and TC under conditions at which the other reported systems are ineffective. These results emphasize the benefits of the use of zero-valent iron, in terms of its capability to produce enough *in-situ* H<sub>2</sub>O<sub>2</sub> to trigger Fenton reactions. This has been achieved by forming a galvanic cell with a high driving force and a large surface area that allows operating at neutral pH and with a very low amount of catalysts, as reflected in the high normalized rate constant obtained.

Notably, the Fe/Au galvanic nanoreactors can be easily detached from the substrate by ultrasonication and dispersed in a liquid. Thus, they have the potential for their use in therapeutic applications, particularly in cancer treatment, due to their ability to generate high levels of ROS. Typically, in Fenton-based cancer treatments, high concentrations of nanoparticles are required to reach high ROS levels in order to be toxic to cancer cells<sup>56</sup>. Additionally, Fenton-based therapies often fail to treat tumors with only the endogenous hydrogen

peroxide concentration<sup>57</sup>. In contrast, Fe/Au nanoreactors, which rely on efficient self-supplying H<sub>2</sub>O<sub>2</sub>, could potentially offer high therapeutic efficiency at very low particle concentrations (~10 µg/mL) to produce sufficient local ROS concentrations to kill cancer cells. Additionally, the magnetic character of the iron layer allows for a straightforward magnetic targeting of the tumors<sup>58,59</sup>.

**Table 4.** Comparison of reported studies with Fenton galvanic cells for degradation of MB and TC together with the results of this work.

<b>Methylene Blue (MB) removal</b>							
<b>Catalyst</b>	<b>Catalyst dosage</b>	<b>[MB]</b>	<b>H<sub>2</sub>O<sub>2</sub> supply</b>	<b>pH</b>	<b>D.E.</b>	<b>k (min<sup>-1</sup>)</b>	<b>k<sub>norm</sub> (min<sup>-1</sup>g<sup>-1</sup>)</b>
Fe/Au*	0.015 g/L	3.2 mg/L	No	7	94.6%	0.16	10.6
Fe*	0.014 g/L	3.2 mg/L	No	7	86.3%	0.032	2.3
Fe/CNTs plates <sup>46</sup>	-	20 mg/L	No	3	-	0.085 2	-
Fe/C <sup>60</sup>	1.25 g/L	-	57 mM	3	100%	-	-
Fe/C <sup>60</sup>	1.25 g/L	-	No	3	< 20%	-	-
Fe/Ni <sup>61</sup>	2 g/L	600 mg/L	50 mM	4.76	61.4%	0.022 (303K )	0.011
Fe/Ni <sup>61</sup>	2 g/L	1000 mg/L	No	4.76	30.8%	0.012 (303k )	0.006
<b>Methylene Blue (MB) removal with Amorphous alloys</b>							
FeBC <sup>33</sup>	0.5 g/L	20 mg/L	0.2 mM	3.5		0.16	0.32
FeSiB <sup>35</sup>	0.5 g/L	100 mg/L	1 mM	3	95%	0.37	0.74
FePC <sup>35</sup>	0.5 g/L	100 mg/L	1 mM	3	95%	0.56	1.12
FeB <sup>37</sup>	0.5 g/L	20 mg/L	1 mM	3	-	0.302	0.60
FeSiB <sup>37</sup>	0.5 g/L	20 mg/L	1 mM	3	-	0.111	0.22

FeSiBPNbCu <sup>31</sup>	2.4 g/L	60 mg/L	0.1 M	-	67.76%	0.018 (353K)	0.008
FeSiBPNbCuNi <sup>31</sup>	2.4 g/L	60 mg/L	0.1 M	-	99.99%	0.065 (353k)	0.027
FeBC <sup>62</sup>	0.05g/L	20 mg/L	2 mM	3	-	0.19 (298K)	3.8
FeBP <sup>62</sup>	0.05g/L	20 mg/L	2 mM	3	-	0.13 (298K)	2.6
FeSiB <sup>34</sup>	0.5g/L	20 mg/L	1 mM	3	~43% (Mineralization)	0.692	1.38
FeSiBCuNb <sup>34</sup>	0.5g/L	20 mg/L	1 mM	3	~20% (Mineralization)	0.099	0.198
FePCCu <sup>39</sup>	0.5g/L	100 mg/L	1 mM	3	-	0.34	0.608
FeCoPCCu <sup>39</sup>	0.5 g/L	100 mg/L	1 mM	3	-	0.47	0.94
FeCrNbYB <sup>32</sup>	0.5g/L	100 mg/L	2 mM	3	-	0.182 (303 K)	0.364
FeSiB <sup>36</sup>	0.05g/L	20 mg/L	1 mM	3	-	0.9	18
<b>Tetracycline (TC), oxytetracycline (OT) and chlortetracycline (CTC) removal</b>							
Fe/Au*	0.015 g/L	TC 17.7 mg/L	No	7	72.3%	0.081	5.4
Fe*	0.014 g/L	TC 17.7 mg/L	No	7	33.6%	0.013	0.93
Fe/Cu <sup>63</sup>	1.2 g/L	TC 8 µg/L	2g/L	7	85.1%	-	
Fe/Cu/C <sup>64</sup>	0.5 g/L	CTC 50 mg/L	No	3.6	70.7%	0.294	0.59

Fe/Cu <sup>65</sup>	5 g/L	TC 50 mg/L	50 mM	3	97%	1.122	0.22
Fe/Pd/rGox <sup>48</sup>	0.1 g/L	OT 100 mg/L	No	5	96.5%	0.056	0.56
Fe/Pt <sup>47</sup>	0.5 g/L	OT 100 mg/L	No	5	99.2%	-	-
Fe/Cu <sup>41</sup>	0.2 g/L	OT 100 mg/L	No	5-6	71.4%	-	-
Fe/Ni <sup>41</sup>	0.2 g/L	OT 100 mg/L	No	5-6	62.3%	-	-

\*This work

## 4.4 Conclusions

In summary, galvanic Fe/Au nanoreactors, fabricated using a simple and scalable method, present excellent degradation performance at pH 7 for persistent organic pollutants using Fenton-like reactions without additives or external energy sources. One of the key advantages of the Fe/Au nanoreactors is the *in-situ* formation of H<sub>2</sub>O<sub>2</sub>, which was detected using a novel adaptation of an H<sub>2</sub>O<sub>2</sub>-mediated enzymatic system typically used in biological samples and with a limit of detection even below the micromolar range. In addition, the high reducing capabilities of Au provided by the galvanic reactor enhance the Fe<sup>2+</sup>/Fe<sup>3+</sup> regeneration in the Fenton catalytic loop, minimizing competing and undesirable side reactions that could lead to fast passivation of the catalyst. The results of the ROS scavenging experiments confirmed hydroxyl radicals as the main reactive oxygen species for pollutant degradation. Compared to other reported systems, the self-powered galvanic nanoreactor described here shows enhanced performance for analyte degradation, being highly active with a very small amount of catalyst, showing excellent catalytic activity against MB and TC (degradation efficiencies of 94 % and 72.6 %, respectively) at neutral pH without the need for any additives or external power sources.

In addition, the system has a high potential for tuning its reactivity. Since it is composed of plasmonic and magnetic materials, the ROS reaction could be further enhanced by locally increasing the temperature through the activation of plasmons using NIR light or by applying alternating magnetic fields<sup>66,67</sup>. In turn, the mass transport of reagents and products could be facilitated by magnetic stirring<sup>68</sup>.

The operational conditions of this system, including the pH, endogenous production of H<sub>2</sub>O<sub>2</sub>, and the use of a very small amount of catalyst to initiate the process, as well as its magnetoplasmonic capabilities, make it very promising for biomedical applications such as cancer treatment through ROS therapy. The

nanoreactors can also be surface engineered to control the ROS reaction by using protective coatings, enabling the reaction to be activated at the desired time and location. For example, they could be easily coated with different smart molecules, including lipid coatings, various enzymes, or pH-responsive smart molecules, which could also be activated using magnetic/NIR light heating only within the tumor region. Therefore, the combination of the galvano-magneto-plasmonic properties of these nanoreactors could open up a wide range of potential applications.

## 4.5 Materials and methods

### 4.5.1 Synthesis of large pore silica nanoparticles

The large pore silica particles (LPSNPs) with pore size around 35 nm and diameters ranging from 200 nm to 250 nm were synthesized by the Stöber method. Firstly, a cetyltrimethylammonium bromide (CTAB) (1.02 mg) and water (340 mL) mixture were prepared in an Erlenmeyer flask under vigorous stirring. Subsequently, ethanol (120 mL), 30 %  $\text{NH}_3$ , (1.5 mL), 1-3-5, Trimethylbenzene (TMB) (1.5 mL), and water (340 mL) were added to the mixture, maintaining the solution temperature at 35 °C. Finally, the solution was heated to 80 °C before adding tetraethyl orthosilicate (TEOS) (1 mL) dropwise. After 2 h, the particles were recovered by centrifugation (10000 rpm, 5 min), cleaned with an  $\text{NH}_4\text{NO}_3$ /ethanol solution, and redispersed in ethanol.

### 4.5.2 Fabrication of Fe/Au and Fe nanoreactors.

The Fe/Au and Fe nanoreactors were fabricated by combining colloidal self-assembly and physical vapor deposition techniques as shown schematically in a Silicon wafers (Siegert Wafer GmbH) were used as substrates for the colloidal self-assembly of the porous silica nanoparticles. Initially, the substrate was thoroughly cleaned several times with acetone and isopropanol, then rinsed with Milli-Q water and dried with a nitrogen gun. The silicon wafer was immersed inside a water filler container and the aqueous suspension of colloidal LPSNPs was initially deposited at a liquid/air interface over the silicon wafer. Once a close-packed, monolayer array of LPSNPs was formed at the air/water interface, the water was drained, thereby depositing the LPSNPs array on the silicon wafer. Then, the Si substrate with the array of LPSNP was cleaned with oxygen plasma (400 W,  $\text{O}_2$  - 60 sccm) for five minutes (PS210, PVA Tepla America, Inc.) to fully remove any leftover surfactants. This process avoids the need for calcination and leaves a highly hydrophilic silica surface. Finally, the 60 nm Fe film was then deposited on the array of nanoporous  $\text{SiO}_2$  beads using electron beam evaporation (UNIVEX 450, Leybold). Following this step, the 20 nm layer of Au was deposited on top of the Fe layer to obtain the galvanic Fe/Au nanoreactors.

### 4.5.3 Characterization of the nanoreactors.

The fabricated Fe and Fe/Au nanoreactors were analyzed by different characterization techniques. The size and morphology of the nanoreactors were characterized by scanning electron microscopy (FEI Magellan 400L XHRSEM). The EDX elemental mappings of nanoreactors were also monitored with the same microscope, which is equipped with an Oxford Instruments Ultim Extreme EDX detector system (Supplementary Information).

### 4.5.4 Detection of the produced H<sub>2</sub>O<sub>2</sub>

The combination of Amplex Red (10-acetyl-3,7-dihydroxyphenoxazine) and horseradish peroxidase (HRP) has been used as an ultrasensitive assay to detect hydrogen peroxide (H<sub>2</sub>O<sub>2</sub>), with a detection limit of around 50 nM. In the presence of HRP, the Amplex Red reagent reacts with H<sub>2</sub>O<sub>2</sub> in a 1:1 stoichiometry to produce the red-fluorescent oxidation product, resorufin. The concentration of H<sub>2</sub>O<sub>2</sub> is proportional to the generated resorufin. The fluorescence emission maxima of resorufin are at 587 nm upon excitation at 488 nm. The process was followed using confocal fluorescence microscopy (Leica, SP5) by focusing on the interface of the supported nanoreactors.

The procedure started with the preparation of fresh stock solutions: 10 mM Amplex Red reagent in DMSO, 1X Reaction Buffer, 10 U/mL Horseradish Peroxidase (HRP), and 20 mM H<sub>2</sub>O<sub>2</sub> in 1X buffer. The H<sub>2</sub>O<sub>2</sub> calibration curve was prepared by diluting the appropriate amount of 20 mM H<sub>2</sub>O<sub>2</sub> into 1 X buffer to produce H<sub>2</sub>O<sub>2</sub> concentrations of 0.5, 2.5, 5, 7.5, and 10 μM, including a no-H<sub>2</sub>O<sub>2</sub> control (See Figure 2A, Appendix A). Appropriate amounts of Amplex red and HRP were added to the standard solutions of H<sub>2</sub>O<sub>2</sub> in order to achieve a final concentration of 100 μM in the case of Amplex Red and 0.2 U/mL in the case of HRP. The reaction between H<sub>2</sub>O<sub>2</sub>, Amplex Red, and HRP was incubated for 30 min in order to produce resorufin as a fluorescent probe of the H<sub>2</sub>O<sub>2</sub> standard solutions. Afterward, the fluorescence emission of the resorufin was measured as a function of the concentration of the standard solutions of H<sub>2</sub>O<sub>2</sub> that underwent reaction. Then, the concentration of H<sub>2</sub>O<sub>2</sub> at the nanoreactor interface was determined by the addition of 100 μM Amplex Red and 0.2 U/mL HRP.

### 4.5.5 Catalytic activity tests

The catalytic performance of the Fe and Fe/Au nanoreactors was tested by using Methylene Blue (MB) and Tetracycline (TC), which exhibit absorption peaks at 664 and 362 nm, respectively. In these tests, the Fe and Fe/Au nanoreactors attached to the silicon substrate (size 0.7x2 cm<sup>2</sup>) were immersed in the pollutant solution with initial concentrations of 3.2 mg/mL MB or 17.7 mg/mL TC at room temperature (25 °C). The color change and decrease of the absorbance were monitored in 15 min intervals using UV-vis spectroscopy (Cary 4000, PerkinElmer) in quartz-cuvettes. The degradation percentage (D%) of the pollutants was calculated by the following expression:



$$D\% = \frac{A_0 - A_{90}}{A_0} \times 100$$

where  $A_0$  is the initial pollutant absorbance and  $A_{90}$  the pollutant absorbance at the final time point.

Total Organic Carbon Content (TOC) was used to evaluate the mineralization efficiency in order to confirm the degradation of the contaminants using TOC-VCSH equipment (Shimadzu) with a high-sensitivity column.

#### 4.5.6 Scavenger experiments.

Radical scavenging tests were carried out with the addition of scavenging agents in the MB solutions to identify the reactive oxygen species involved in the pollutant degradation. Accordingly, two different scavengers were used in presence of MB: benzoquinone (1 mM) as quencher for the superoxide radical ( $\cdot\text{O}_2^-$ ), and isopropanol (1 mM) as a quencher for the hydroxyl radical ( $\cdot\text{OH}$ ).

## 4.6 References

1. Wu J, Ning P, Gao R, et al. Programmable ROS-Mediated Cancer Therapy via Magneto-Inductions. *Adv Sci.* 2020;7(12):1-16. doi:10.1002/advs.201902933
2. Perillo B, Di Donato M, Pezone A, et al. ROS in cancer therapy: the bright side of the moon. *Exp Mol Med.* 2020;52(2):192-203. doi:10.1038/s12276-020-0384-2
3. Xu X, Wang J, Chen T, et al. Deep insight into ROS mediated direct and hydroxylated dichlorination process for efficient photocatalytic sodium pentachlorophenate mineralization. *Appl Catal B Environ.* 2021;296(February):120352. doi:10.1016/j.apcatb.2021.120352
4. Li Q, Ren J, Hao Y, et al. Insight into reactive species-dependent photocatalytic toluene mineralization and deactivation pathways via modifying hydroxyl groups and oxygen vacancies on BiOCl. *Appl Catal B Environ.* 2022;317(June). doi:10.1016/j.apcatb.2022.121761
5. Jiang B, Yao Y, Xie R, et al. Enhanced generation of reactive oxygen species for efficient pollutant elimination catalyzed by hemin based on persistent free radicals. *Appl Catal B Environ.* 2016;183:291-297. doi:10.1016/j.apcatb.2015.10.051
6. Zhou P, Zhang J, Zhang Y, et al. Activation of hydrogen peroxide during the corrosion of nanoscale zero valent copper in acidic solution. *J Mol Catal A Chem.* 2016;424:115-120. doi:10.1016/j.molcata.2016.08.022
7. Wen G, Wang SJ, Ma J, et al. Oxidative degradation of organic pollutants

- in aqueous solution using zero valent copper under aerobic atmosphere condition. *J Hazard Mater.* 2014;275:193-199. doi:10.1016/j.jhazmat.2014.05.002
8. Lien HL, Wilkin R. Reductive activation of dioxygen for degradation of methyl tert-butyl ether by bifunctional aluminum. *Environ Sci Technol.* 2002;36(20):4436-4440. doi:10.1021/es011449a
  9. Bokare AD, Choi W. Zero-valent aluminum for oxidative degradation of aqueous organic pollutants. *Environ Sci Technol.* 2009;43(18):7130-7135. doi:10.1021/es9013823
  10. Joo SH, Feitz AJ, Waite TD. Oxidative Degradation of the Carbothioate Herbicide, Molinate, Using Nanoscale Zero-Valent Iron. *Environ Sci Technol.* 2004;38(7):2242-2247. doi:10.1021/es035157g
  11. Sung HJ, Feitz AJ, Sedlak DL, Waite TD. Quantification of the oxidizing capacity of nanoparticulate zero-valent iron. *Environ Sci Technol.* 2005;39(5):1263-1268. doi:10.1021/es048983d
  12. Noubactep C. Comment on "Oxidative degradation of organic compounds using zero-valent iron in the presence of natural organic matter serving as an electron shuttle." *Environ Sci Technol.* 2009;43(10):3964-3965. doi:10.1021/es900076m
  13. Guan X, Sun Y, Qin H, et al. *The Limitations of Applying Zero-Valent Iron Technology in Contaminants Sequestration and the Corresponding Countermeasures: The Development in Zero-Valent Iron Technology in the Last Two Decades (1994-2014).* Vol 75.; 2015. doi:10.1016/j.watres.2015.02.034
  14. Phenrat T, Saleh N, Sirk K, Tilton RD, Lowry G V. Aggregation and sedimentation of aqueous nanoscale zerovalent iron dispersions. *Environ Sci Technol.* 2007;41(1):284-290. doi:10.1021/es061349a
  15. Jin Q, Kang J, Chen Q, Shen J, Guo F, Chen Z. Efficiently enhanced Fenton-like reaction via Fe complex immobilized on silica particles for catalytic hydrogen peroxide degradation of 2,4-dichlorophenol. *Appl Catal B Environ.* 2020;268(June 2019):118453. doi:10.1016/j.apcatb.2019.118453
  16. Cheng M, Lai C, Liu Y, et al. Metal-organic frameworks for highly efficient heterogeneous Fenton-like catalysis. *Coord Chem Rev.* 2018;368:80-92. doi:10.1016/j.ccr.2018.04.012
  17. Cai QQ, Lee BCY, Ong SL, Hu JY. Fluidized-bed Fenton technologies for recalcitrant industrial wastewater treatment—Recent advances, challenges and perspective. *Water Res.* 2021;190:1-4. doi:10.1016/j.watres.2020.116692

18. Stefaniuk M, Oleszczuk P, Ok YS. Review on nano zerovalent iron (nZVI): From synthesis to environmental applications. *Chem Eng J.* 2016;287:618-632. doi:10.1016/j.cej.2015.11.046
19. Qin H, Li J, Yang H, Pan B, Zhang W, Guan X. Coupled Effect of Ferrous Ion and Oxygen on the Electron Selectivity of Zerovalent Iron for Selenate Sequestration. *Environ Sci Technol.* 2017;51(9):5090-5097. doi:10.1021/acs.est.6b04832
20. Tarekegn MM, Hiruy AM, Dekebo AH. Nano zero valent iron (nZVI) particles for the removal of heavy metals (Cd<sup>2+</sup>, Cu<sup>2+</sup> and Pb<sup>2+</sup>) from aqueous solutions. *RSC Adv.* 2021;11(30):18539-18551. doi:10.1039/d1ra01427g
21. Liu Y, Zhao Y, Wang J. Fenton/Fenton-like processes with in-situ production of hydrogen peroxide/hydroxyl radical for degradation of emerging contaminants: Advances and prospects. *J Hazard Mater.* 2021;404(PB):124191. doi:10.1016/j.jhazmat.2020.124191
22. Nie X, Liu J, Yue D, Zeng X, Nie Y. Dechlorination of hexachlorobenzene using lead-iron bimetallic particles. *Chemosphere.* 2013;90(9):2403-2407. doi:10.1016/j.chemosphere.2012.10.068
23. Zhang Z, Shen Q, Cissoko N, Wo J, Xu X. Catalytic dechlorination of 2,4-dichlorophenol by Pd/Fe bimetallic nanoparticles in the presence of humic acid. *J Hazard Mater.* 2010;182(1-3):252-258. doi:10.1016/j.jhazmat.2010.06.022
24. Zhang Z, Lv X, Baig SA, Xu X. Catalytic dechlorination of 2,4-dichlorophenol by Ni/Fe nanoparticles in the presence of humic acid: Intermediate products and some experimental parameters. *J Exp Nanosci.* 2014;9(6):603-615. doi:10.1080/17458080.2012.680929
25. Liu WJ, Qian TT, Jiang H. Bimetallic Fe nanoparticles: Recent advances in synthesis and application in catalytic elimination of environmental pollutants. *Chem Eng J.* 2014;236:448-463. doi:10.1016/j.cej.2013.10.062
26. Qin X, Wang Z, Guo C, Guo R, Lv Y, Li M. Fulvic acid degradation in Fenton-like system with bimetallic magnetic carbon aerogel Cu-Fe@CS as catalyst: Response surface optimization, kinetic and mechanism. *J Environ Manage.* 2022;306(September 2021):114500. doi:10.1016/j.jenvman.2022.114500
27. Castro A, Carvalho I, Marques L, et al. Galvanic oxidation of bimetallic Zn-Fe nanoparticles for oxygen scavenging. *Appl Surf Sci.* 2021;537(May 2020):147896. doi:10.1016/j.apsusc.2020.147896
28. Luo S, Yang S, Sun C, Gu JD. Improved debromination of polybrominated

- diphenyl ethers by bimetallic iron-silver nanoparticles coupled with microwave energy. *Sci Total Environ.* 2012;429:300-308. doi:10.1016/j.scitotenv.2012.04.051
29. Xia Q, Zhang D, Yao Z, Jiang Z. Revealing the enhancing mechanisms of Fe–Cu bimetallic catalysts for the Fenton-like degradation of phenol. *Chemosphere.* 2022;289(December 2021):133195. doi:10.1016/j.chemosphere.2021.133195
  30. Zhou X, Jing G, Lv B, Zhou Z, Zhu R. Highly efficient removal of chromium(VI) by Fe/Ni bimetallic nanoparticles in an ultrasound-assisted system. *Chemosphere.* 2016;160:332-341. doi:10.1016/j.chemosphere.2016.06.103
  31. Shi J, Ni B, Zhang J, et al. Effect of Ni addition on catalytic performance of Fe<sub>87</sub>Si<sub>5</sub>B<sub>2</sub>P<sub>3</sub>Nb<sub>2</sub>Cu<sub>1</sub> amorphous alloys for degrading methylene blue dyes. *Metals (Basel).* 2019;9(3):341.
  32. Yang W, Wang Q, Li W, et al. A novel thermal-tuning Fe-based amorphous alloy for automatically recycled methylene blue degradation. *Mater Des.* 2019;161:136-146. doi:10.1016/j.matdes.2018.11.031
  33. Wei B, Li X, Sun H, Song K, Wang L. Improved degradation capability of Fe<sub>81</sub>B<sub>10</sub>C<sub>9</sub> amorphous ribbon with the nanoscale layer rich of small atoms (B, C). *J Non Cryst Solids.* 2021;564(April):120838. doi:10.1016/j.jnoncrysol.2021.120838
  34. Wang X, Zhang Q, Liang SX, et al. Fe-based metallic glasses and dyes in fenton-like processes: Understanding their intrinsic correlation. *Catalysts.* 2020;10(1):1-17. doi:10.3390/catal10010048
  35. Wang Q, Chen M, Lin P, Cui Z, Chu C, Shen B. Investigation of FePC amorphous alloys with self-renewing behaviour for highly efficient decolorization of methylene blue. *J Mater Chem A.* 2018;6(23):10686-10699. doi:10.1039/c8ta01534a
  36. Liang SX, Zhang Q, Jia Z, Zhang W, Wang W, Zhang LC. Tailoring surface morphology of heterostructured iron-based Fenton catalyst for highly improved catalytic activity. *J Colloid Interface Sci.* 2021;581:860-873. doi:10.1016/j.jcis.2020.07.138
  37. Liang SX, Jia Z, Liu YJ, et al. Compelling Rejuvenated Catalytic Performance in Metallic Glasses. *Adv Mater.* 2018;30(45):1-11. doi:10.1002/adma.201802764
  38. Jia Z, Duan X, Zhang W, et al. Ultra-sustainable Fe<sub>78</sub>Si<sub>9</sub>B<sub>13</sub> metallic glass as a catalyst for activation of persulfate on methylene blue degradation under UV-Vis light. *Sci Rep.* 2016;6(October):1-10.

- doi:10.1038/srep38520
39. Hou L, Wang Q, Fan X, Miao F, Yang W, Shen B. Effect of Co addition on catalytic activity of FePCCu amorphous alloy for methylene blue degradation. *New J Chem.* 2019;43(16):6126-6135. doi:10.1039/c9nj00369j
  40. Liu Y, Chen Z, Yang X, et al. High entropy nanoparticles of CoCrXFeNi (X=Al, Cu, Mn) loaded on activated carbon for efficient degradation of methylene blue. *J Mater Res Technol.* 2021;15:256-267. doi:10.1016/j.jmrt.2021.08.001
  41. Wu Y, Yue Q, Gao Y, Ren Z, Gao B. Performance of bimetallic nanoscale zero-valent iron particles for removal of oxytetracycline. *J Environ Sci (China).* 2018;69:173-182. doi:10.1016/j.jes.2017.10.006
  42. Duan J, Zhu H, Xu F, Zhao J. A new approach to 4-chlorophenol dechlorination on monometallic copper compared to its Cu/Fe bimetallic system. *Chem Eng J.* 2016;304:282-288. doi:10.1016/j.cej.2016.06.089
  43. Soler L, Sánchez S. Catalytic nanomotors for environmental monitoring and water remediation. *Nanoscale.* 2014;6(13):7175-7182. doi:10.1039/c4nr01321b
  44. Ruan X, Liu H, Ning X, Zhao D, Fan X. Screening for the action mechanisms of Fe and Ni in the reduction of Cr(VI) by Fe/Ni nanoparticles. *Sci Total Environ.* 2020;715(Vi):136822. doi:10.1016/j.scitotenv.2020.136822
  45. Gao JF, Wu ZL, Duan WJ, Zhang WZ. Simultaneous adsorption and degradation of triclosan by Ginkgo biloba L. stabilized Fe/Co bimetallic nanoparticles. *Sci Total Environ.* 2019;662:978-989. doi:10.1016/j.scitotenv.2019.01.194
  46. Zhang S, Wang D, Zhou L, Zhang X, Fan P, Quan X. Intensified internal electrolysis for degradation of methylene blue as model compound induced by a novel hybrid material: Multi-walled carbon nanotubes immobilized on zero-valent iron plates (Fe<sup>0</sup>-CNTs). *Chem Eng J.* 2013;217:99-107. doi:10.1016/j.cej.2012.11.103
  47. Tran ML, Nguyen CH, Tran TT Van, Juang RS. One-pot synthesis of bimetallic Pt/nZVI nanocomposites for enhanced removal of oxytetracycline: Roles of morphology changes and Pt catalysis. *J Taiwan Inst Chem Eng.* 2020;111:130-140. doi:10.1016/j.jtice.2020.05.001
  48. Nguyen CH, Tran ML, Van Tran TT, Juang RS. Efficient removal of antibiotic oxytetracycline from water by Fenton-like reactions using reduced graphene oxide-supported bimetallic Pd/nZVI nanocomposites. *J Taiwan Inst Chem Eng.* 2021;119:80-89. doi:10.1016/j.jtice.2021.02.001

49. Nogueira RFP, Oliveira MC, Paterlini WC. Simple and fast spectrophotometric determination of H<sub>2</sub>O<sub>2</sub> in photo-Fenton reactions using metavanadate. *Talanta*. 2005;66(1):86-91. doi:10.1016/j.talanta.2004.10.001
50. Nosaka Y, Nosaka AY. Generation and detection of reactive oxygen species in photocatalysis. *Chem Rev*. 2017;117(17):11302-11336.
51. Votyakova T V, Reynolds IJ.  $\Delta\Psi_m$ -Dependent and-independent production of reactive oxygen species by rat brain mitochondria. *J Neurochem*. 2001;79(2):266-277.
52. Loures CCA, Alcântara MAK, Filho HJI, et al. Advanced Oxidative Degradation Processes: Fundamentals and Applications. *Int Rev Chem Eng*. 2013;5(2):102. doi:10.15866/ireche.v5i2.6909
53. Bayat M, Nasernejad B, Falamaki C. Preparation and characterization of nano-galvanic bimetallic Fe/Sn nanoparticles deposited on talc and its enhanced performance in Cr(VI) removal. *Sci Rep*. 2021;11(1):1-17. doi:10.1038/s41598-021-87106-0
54. Khan I, Saeed K, Zekker I, et al. Review on Methylene Blue: Its Properties, Uses, Toxicity and Photodegradation. *Water (Switzerland)*. 2022;14(2). doi:10.3390/w14020242
55. Fiaz A, Zhu D, Sun J. Environmental fate of tetracycline antibiotics: degradation pathway mechanisms, challenges, and perspectives. *Environ Sci Eur*. 2021;33(1). doi:10.1186/s12302-021-00505-y
56. Xu C, Yuan Z, Kohler N, Kim J, Chung MA, Sun S. FePt nanoparticles as an Fe reservoir for controlled Fe release and tumor inhibition. *J Am Chem Soc*. 2009;131(42):15346-15351. doi:10.1021/ja905938a
57. Paquin F, Rivnay J, Salleo A, Stingelin N, Silva C. Multi-phase semicrystalline microstructures drive exciton dissociation in neat plastic semiconductors. *J Mater Chem C*. 2015;3(207890):10715-10722. doi:10.1039/b000000x
58. Li Z, Aranda-Ramos A, Güell-Grau P, et al. Magnetically amplified photothermal therapies and multimodal imaging with magneto-plasmonic nanodomains. *Appl Mater Today*. 2018;12:430-440. doi:10.1016/j.apmt.2018.07.008
59. Fluksman A, Lafuente A, Li Z, et al. Efficient Tumor Eradication at Ultralow Drug Concentration via Externally Controlled and Boosted Metallic Iron Magnetoplasmonic Nanocapsules. *ACS Nano*. Published online 2022. doi:10.1021/acsnano.2c05733

60. Lu C, Sun W, Yue T, et al. A way out of the alkaline bauxite residue: Synthesizing micro-electrolysis composite material towards the synergistic fenton degradation of high-concentration organic wastewater. *J Hazard Mater.* 2020;400(January):123210. doi:10.1016/j.jhazmat.2020.123210
61. Liu J, Du Y, Sun W, Chang Q, Peng C. Preparation of new adsorbent-supported Fe/Ni particles for the removal of crystal violet and methylene blue by a heterogeneous Fenton-like reaction. *RSC Adv.* 2019;9(39):22513-22522. doi:10.1039/c9ra04710g
62. Wei B, Li X, Sun H, Song K, Wang L. Comparative study on the corrosion and self-cleaning behavior of Fe-B-C and Fe-B-P amorphous alloys in methylene blue dye solution degradation. *J Non Cryst Solids.* 2022;575(October 2021):121212. doi:10.1016/j.jnoncrysol.2021.121212
63. Ayoub M. Degradation of tetracycline using nanoparticles of zero-valent iron and copper. *Water Pract Technol.* 2022;17(1):246-253. doi:10.2166/wpt.2021.100
64. Liu Y, Wang C, Sui Z, Zou D. Degradation of chlortetracycline using nano micro-electrolysis materials with loading copper. *Sep Purif Technol.* 2018;203:29-35. doi:10.1016/j.seppur.2018.03.064
65. Jiang Y, Sun D, Wang D, et al. Rapid degradation of tetracycline in aqueous solution by Fe/Cu catalysis enhanced by H<sub>2</sub>O<sub>2</sub> activation. *Environ Technol.* Published online 2021:1-9.
66. Tang Z, Zhao P, Wang H, Liu Y, Bu W. Biomedicine meets Fenton chemistry. *Chem Rev.* 2021;121(4):1981-2019. doi:10.1021/acs.chemrev.0c00977
67. Shi L, Wang X, Hu Y, He Y. Investigation of photocatalytic activity through photo-thermal heating enabled by Fe<sub>3</sub>O<sub>4</sub>/TiO<sub>2</sub> composite under magnetic field. *Sol Energy.* 2020;196(June 2019):505-512. doi:10.1016/j.solener.2019.12.053
68. Serrà A, Montiel M, Gómez E, Vallés E. Electrochemical synthesis of mesoporous CoPt nanowires for methanol oxidation. *Nanomaterials.* 2014;4(2):189-202. doi:10.3390/nano4020189

## **5. 2D MoS<sub>2</sub>/Cu photocatalytic nanoreactors on 3D mesoporous silica support for environmental remediation and biomedical applications.**

Transition metal dichalcogenides (TMD) have attracted great attention in the field of photocatalysts due to their remarkable optoelectronic properties. This section describes 2D MoS<sub>2</sub>/Cu photocatalytic nanoreactors on 3D mesoporous silica templates fabricated by a combination of hydrothermal synthesis (HT) and e-beam deposition methods.

The resulting hydrothermal MoS<sub>2</sub> phase consists of two different semiconductor phases with clear experimental indications to be ascribed to a combined trigonal prismatic phase 2H and the distorted trigonal phase 1T'. The deposition of copper (Cu) onto the MoS<sub>2</sub> greatly enhanced the photocatalytic activity due to the system's outstanding light absorption properties and charge separation provided by the copper heterojunction.

The MoS<sub>2</sub>/Cu nanoreactors showed excellent stability and could be applied for wastewater treatment with safe white light. Moreover, the catalytic activity of MoS<sub>2</sub>/Cu nanoreactors was tested in vitro on cancer cells with near-infrared (660 nm) light actuation, showing a large decrease in cell viability after 90 min actuation, thereby being a very promising system for biomedical applications.



## 5.1 Introduction

Water pollution is severely harming the ecosystem as a result of growing industrialization, with industrial effluent containing organic pollutants serving as a major source of contamination<sup>1,2</sup>. These highly resistant industrial pollutants not only threaten the available freshwater sources but also endangers the life of living organisms. In this context, photocatalytic materials have been developed for the degradation and mineralization of these organic pollutants.

Within the photocatalytic materials, 2D transition metal dichalcogenides and, particularly molybdenum disulphide ( $\text{MoS}_2$ ), have attracted wide attention due to their bandgap tunability, favourable bands alignment, earth abundance and cost-effectiveness<sup>3,4</sup>.

Molybdenum disulphide exhibits polyphasic nature, showing a stable hexagonal 2H phase and metastable 1T or distorted 1T' octahedral phases due to the formation of different coordination bonds between Mo and S atoms<sup>5,6</sup>. In turn, the structural coordination of the Mo metal and its d-electrons impacts on the electronic properties of the  $\text{MoS}_2$  phases. As mentioned in the introduction, the bulk 2H phase of  $\text{MoS}_2$  holds semiconducting properties with an indirect bandgap of 1.2 eV, whereas a monolayer of  $\text{MoS}_2$  exhibits a direct bandgap of 1.8 eV. The T phase is metallic while the distorted octahedral T' phase is a small bandgap semiconductor<sup>7</sup>. The thermodynamically stable 2H phase is valuable in the fields of optoelectronics, photonics etc., due to high photon absorption<sup>8,9</sup>. The unstable octahedral metallic 1T phase exhibits great potential in catalysis, batteries, superconductivity, photothermal cancer therapy, etc., due to its reduced charge transfer resistance<sup>10-12</sup>. Combinations of different  $\text{MoS}_2$  phases have recently been found to be extremely efficient catalysts, particularly for hydrogen evolution reactions and wastewater remediation<sup>13-15</sup>. The direct bandgap of  $\text{MoS}_2$ , resulting from quantum confinement in 2D, also enables highly efficient charge separation, which can be exploited in photocatalytic reactions to produce reactive oxygen species through the activation of oxygen<sup>16</sup>. The photocatalytic activity of  $\text{MoS}_2$  could be further increased by the formation of different heterojunctions. However, the recovery of  $\text{MoS}_2$  structures from solution after degradation can be complex, costly, and potentially cause secondary pollution when used as dispersed heterogeneous catalysts. Growing  $\text{MoS}_2$  on a solid support may alleviate these issues, but its 2D nature would significantly decrease the number of active sites for catalytic reactions<sup>1,17-19</sup>.

Here, with the aim to achieve highly reactive 2D MoS<sub>2</sub> supported on 3D templates, we fabricated multifunctional MoS<sub>2</sub> nanostructures on mesoporous silica nanoparticles by a cost-effective hydrothermal process. The characterization output of the supported hydrothermal MoS<sub>2</sub> suggests a combined 2H-1T' semiconducting structure. In addition, a thin Cu layer deposited on the grown MoS<sub>2</sub> favoured an efficient electron transfer to enhance the photocatalytic reactions. The optimized MoS<sub>2</sub>/Cu nanoreactor exhibited a remarkable photocatalytic performance in a wide pH range, being capable to degrade and mineralize organic pollutants and biotoxins with white light. In addition, the MoS<sub>2</sub>/Cu nanoreactor exhibited very high efficacy to kill cancer cells by illumination with near-infrared light in the first biological window (660 nm). Therefore, the MoS<sub>2</sub>/Cu heterojunction nanoreactors on the 3D mesoporous supports could be appealing for both environmental remediation and therapeutic applications.

## 5.2 Results and discussions

### 5.2.1 Fabrication

The fabrication process of hydrothermal MoS<sub>2</sub>/Cu follows four different steps. The first fabrication step follows the same procedure that is presented in Chapter 4. The other steps are ii) silanization, iii) hydrothermal growth of MoS<sub>2</sub> and iv) Cu deposition (Figure 5-1). As known, MSNPs are negatively charged. Therefore, a silanization process is needed to grow MoS<sub>2</sub> flakes on the silica surface. For this purpose, the substrate was immersed in (3-Aminopropyl) triethoxysilane (APTES (4%)) solution in toluene for 2 h at 80 °C. Then, the substrate was rinsed with toluene and immersed in DI water for 2 h to clean the excess APTES. In the third step, 0.3 mg ammonium tetrathiomolybdate (NH<sub>4</sub>)<sub>2</sub>MoS<sub>4</sub> was dissolved in 10 ml dimethylformamide (DMF) and the solution was sonicated for 30 min. Subsequently, the substrate was submerged in DMF solution, transferred to a stainless-steel autoclave, and hydrothermally treated for 18 h at 180 °C. After 18 h, the as-prepared sample was rinsed with water and dried with a nitrogen gun. Finally, 3 nm copper (Cu) was deposited onto the MoS<sub>2</sub> nanoreactors via e-beam deposition.

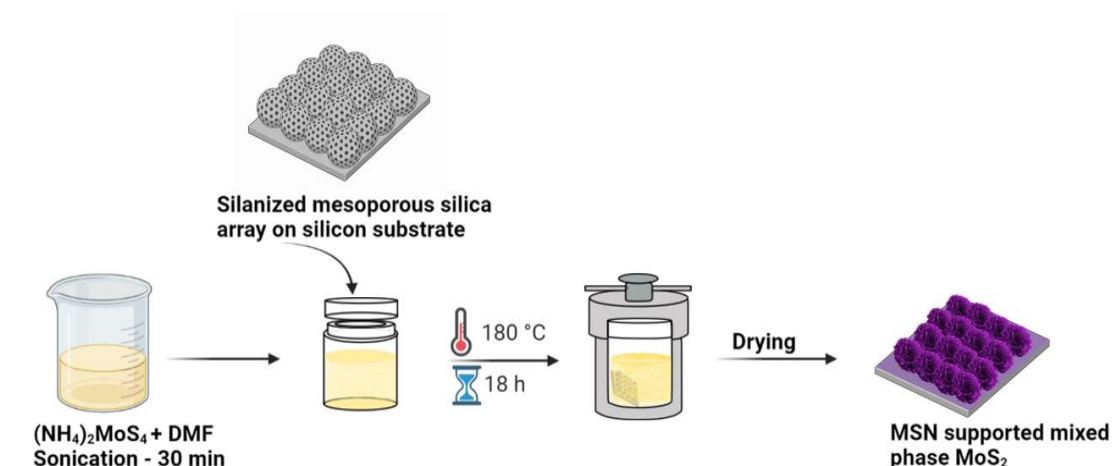


**Figure 5-1.** Schematic of the fabrication process of hydrothermal MoS<sub>2</sub>/Cu nanoreactors.

To understand better the morphology, we also fabricated monolayer MoS<sub>2</sub> flakes grown by chemical vapor deposition (CVD)<sup>20</sup>. For this purpose, an alumina boat with a precursor MoO<sub>3</sub> (5 mg) was placed in the middle of the quartz tube furnace. Then the wafer with 2x2 cm<sup>2</sup> dimensions was placed onto the alumina boat in an upside-down manner. Another alumina boat was inserted at the cold side of the quartz tube in a distance of 15 cm with sulfur as the other reagent precursor. The furnace was heated up to 750 °C at a rate of 50 °C/min under Ar 40 sccm to induce the reaction. After 25 min growth time, the furnace rapidly cooled down.

### 5.2.2 Structural characterization of 2D MoS<sub>2</sub>/Cu nanoreactors on mesoporous SiO<sub>2</sub> supports

The morphology of the hydrothermal MoS<sub>2</sub>/Cu nanostructures was observed by SEM and HRTEM. The SEM image in Figure 5-2a shows that the MoS<sub>2</sub> flakes form a high density and uniform 3D network on the mesoporous silica particles. The TEM image illustrated in Figure 5-2b shows the thin 2D MoS<sub>2</sub> flakes, and the elemental mapping (Figure 5-2c) confirmed the uniform distribution of the Cu, Mo and S elements and the absence of contaminants.

To determine the crystallographic structure, the samples were analyzed by XRD, Raman, XPS and UV-VIS spectra. To understand better the structure, the hydrothermally grown MoS<sub>2</sub> samples were compared to CVD-grown flakes of MoS<sub>2</sub> flakes which are known to be either 2H or 1H phase.

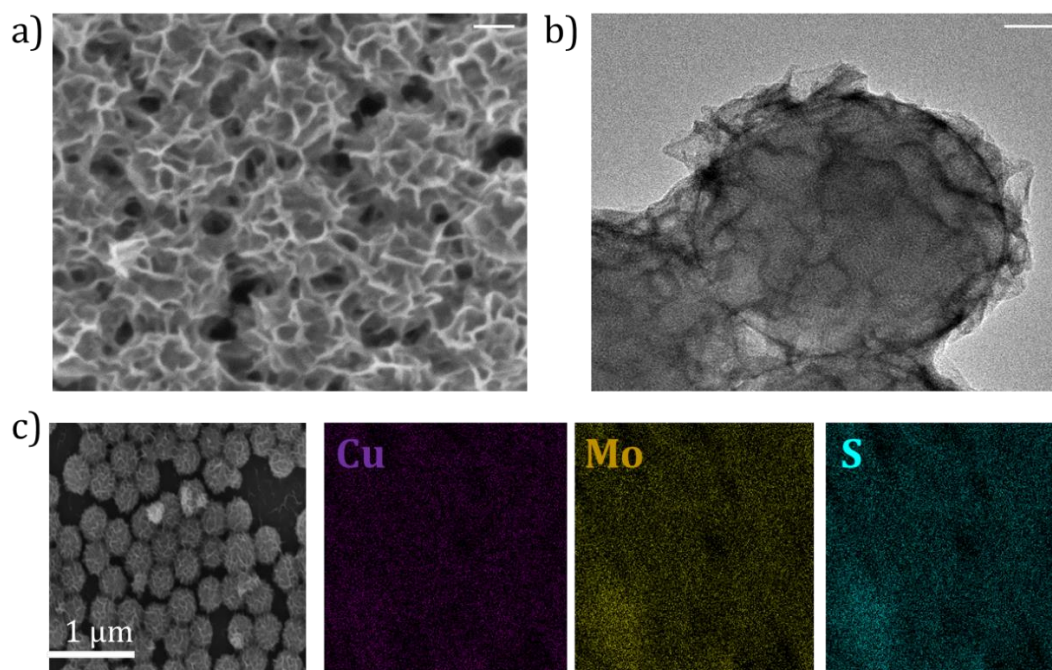


**Figure 5-2.** a) SEM image of hydrothermal MoS<sub>2</sub>/Cu, b) HRTEM image of hydrothermal MoS<sub>2</sub>/Cu, c) SEM image of hydrothermal MoS<sub>2</sub>/Cu together with elemental mappings corresponding to Cu, Mo and S maps, respectively. Scale bars a) 100 nm, b) 50 nm.

Unlike the H phase, the growth of the 1T or 1T' phase is challenging due to their high formation energy (0.84 eV for T phase and 0.55 eV for T' phase)<sup>21,22</sup>. Figure 5-3a depicts the UV-Vis spectra of hydrothermal MoS<sub>2</sub> and CVD MoS<sub>2</sub> nanoflakes. The CVD MoS<sub>2</sub> exhibited the three characteristic peaks at 614 nm, 667 nm and 440 nm, which are related to the direct band gap and quantum confinement effect. These peaks are typical for the semiconducting 2D 1H phase<sup>5,23</sup>. In contrast, no visible peaks appeared for the hydrothermal MoS<sub>2</sub>. Likewise, CVD MoS<sub>2</sub> exhibit strong photoluminescence as a result of direct band gap excitations at the K point of the Brillouin zone<sup>24,25</sup>, whereas the hydrothermal MoS<sub>2</sub> did not exhibit any photoluminescence, which could be due to the presence of phases with very small bandgap or more metallic nature (Figure 5-3b)<sup>6,7</sup>.

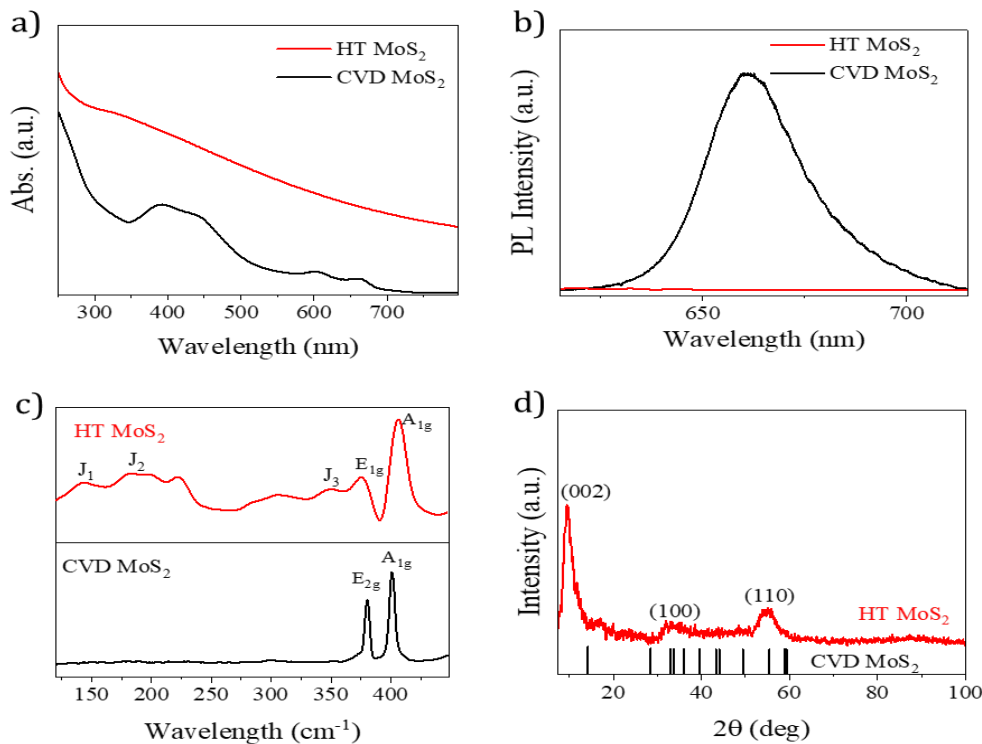


**Figure 5-3.** Characterization of MoS<sub>2</sub> samples grown by CVD and by hydrothermal processes. a) UV-Vis spectra, b) photoluminescence spectra, c) Raman spectra and d) XRD spectra.

Raman spectroscopy was also performed to characterize the differences between CVD and hydrothermal MoS<sub>2</sub>. As shown in Figure 5-3c Raman spectra, the CVD MoS<sub>2</sub> with the typical 2H phase contains only two main peaks the E<sub>2g</sub> mode at 384 cm<sup>-1</sup> and the A<sub>1g</sub> mode at 410.15 cm<sup>-1</sup><sup>26,27</sup>. However, the hydrothermal MoS<sub>2</sub> possesses several peaks: J<sub>1</sub> (143.6), J<sub>2</sub> (223.6), J<sub>3</sub>(350.6), E<sub>1g</sub> (~306.4), E<sub>2g</sub> (376.7), A<sub>1g</sub> (406.1), respectively<sup>28-30</sup>. The defect related J<sub>1</sub> (143.6 cm<sup>-1</sup>) peak illustrates the presence of a quite defective phase that could be related with a T' phase<sup>31,32</sup>. Furthermore, the two typical E<sub>2g</sub> and A<sub>1g</sub> Raman modes although slightly shifted give indications that a 2H phase would also be present in the hydrothermal sample. The J<sub>2</sub> (223.6) and J<sub>3</sub> (350.6) modes illustrate the shifting of S atoms with respect to Mo atoms.

The X-ray diffraction (XRD) patterns of the hydrothermal and CVD grown MoS<sub>2</sub> are shown in Figure 5-3d. The hydrothermal MoS<sub>2</sub> phase had poor crystallinity compared to the CVD 2H MoS<sub>2</sub> (JCPDS Card No. 37-1492), and exhibited a shifted peak located at 9.5° (002)<sup>33,34</sup>.

To get more insights into the physicochemical differences between the HT MoS<sub>2</sub> and CVD MoS<sub>2</sub> samples, X-ray Photoelectron Spectroscopy (XPS) measurements were performed. The emission of X-ray photons has been used not only to obtain information of the composition and chemical state of the elements but also to

provide hints of the electronic structure/properties of the sample. The Valence Band Maximum (VBM), which is the highest occupied energy level in a solid material, is an important parameter in the electronic structure of the material. VBM is typically determined using photoemission data that corresponds to low binding energies in the range of about 1-5 eV above the Fermi level of the system (being this latter parameter located at 0 binding energy).

To accomplish a more complete characterization of the hydrothermal samples, we have also analyzed CVD grown MoS<sub>2</sub> samples and a MoS<sub>2</sub> natural crystal (SPI supplies), with the well-known and stable 2H structure.

Figure 5-4 shows high resolution XPS spectra of the Mo3d/S2s lines (left) and of the S2p lines (right) for (a) a mechanically exfoliated MoS<sub>2</sub> natural crystal, (b) a CVD grown MoS<sub>2</sub> sample and (c) a MoS<sub>2</sub> sample prepared by hydrothermal methods. Least-squares fits of the experimental data (black lines) after a Shirley-type background subtraction (grey lines) are shown using a combination of Gaussians and Lorentzian functions. The branching ratios for the Mo3d and S2p doublets are set to 2/3 and 1/2, respectively, and the spin-orbit splitting is fixed to 3.16 and 1.19 eV, respectively. The envelopes of the fits are represented by orange lines.

In Figure 5-4(Left, a) the Mo3d doublet can be deconvoluted into two components, the main contribution (blue lines) centered at 229.5 eV (Mo3d<sub>5/2</sub>), indicated by a continuous straight line, and a minor contribution (olive line) centered at 232.6 eV, while the S2s line (also indicated by a continuous straight line) shows a single peak at 226.7 eV (magenta line). In Figure 5-4(right, a) the S2p line can be fitted with a single doublet (blue lines), with the S2p<sub>3/2</sub> line centered at 162.4 eV, indicated by a continuous straight line, and with a full width at half maximum (FWHM) of 0.7 eV, which approaches the combined X-ray source-analyzer energy resolution<sup>35</sup>. The 229.5 and 162.4 eV features are characteristic of n-type 2H MoS<sub>2</sub> (Mo<sup>4+</sup>)<sup>36,37</sup> and the 232.6 eV is assigned to MoO<sub>3</sub> (Mo<sup>6+</sup>)<sup>38</sup>, respectively. This is further evidenced by the position of the valence band maximum (VBM) that is located at 1.3 eV below the Fermi level of the system [see inset in Figure 5-4 (a)]. The VBM is obtained by a linear extrapolation (blue straight lines) of the leading edges in the valence band spectra. Such VBM value is nearly the full band gap of bulk MoS<sub>2</sub>, indicating that the Fermi level should be very close to the conduction band<sup>36</sup>.

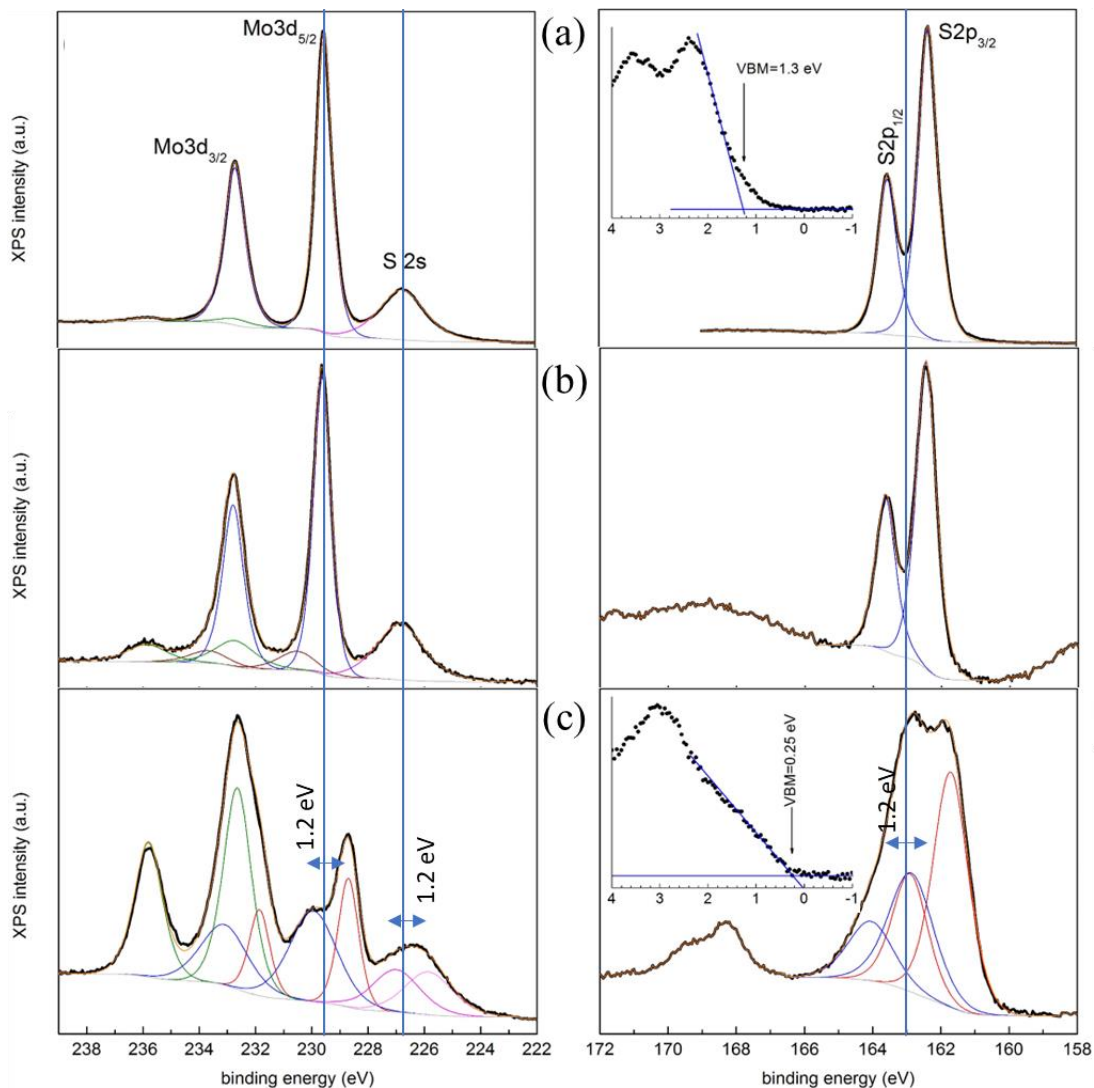


**Figure 5-4** XPS spectra of the Mo3d/S2s lines (left) and of the S2p lines (right) for (a) a mechanically exfoliated MoS<sub>2</sub> natural crystal, (b) a CVD grown MoS<sub>2</sub> sample and (c) a MoS<sub>2</sub> sample prepared by hydrothermal methods. For all samples, the binding energy of C1s is 284.5±0.1 eV, arising from graphitic carbon contamination, ruling out any charging effects. The insets of a) and b) correspond to the low photoemission binding energies where the valence band can be collected. Evaluation of the VBM is also indicated.

The deconvolution of the Mo3d, S2s and S2p lines in Figure 5-4 (left, b) and (right, b) provide a S2s singlet centered at 226.9 eV, a S2p single doublet with the S2p<sub>3/2</sub> line centered at 162.5 eV (FWHM = 0.7 eV) and three components for the Mo3d lines, the main contribution at 229.6 eV and two smaller contributions at 230.5 and 232.7 eV, respectively. Both the main and the higher binding energy contributions are assigned to n-type 2H MoS<sub>2</sub> and to MoO<sub>3</sub>, respectively, as discussed for the MoS<sub>2</sub> natural crystal. The 230.5 eV feature has been assigned to defect Mo<sup>+4</sup>, corresponding to Mo atoms close to sulfur vacancies<sup>39</sup>.

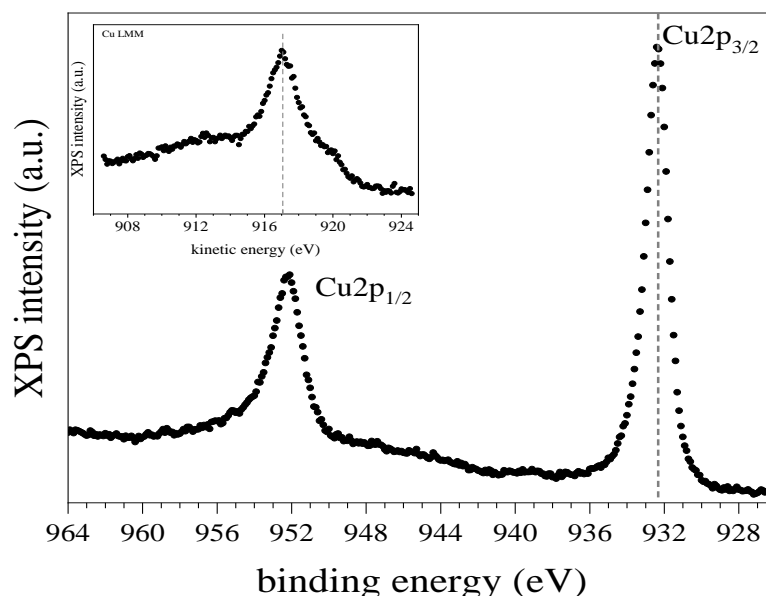
The convolution of the spectra corresponding to the hydrothermal sample is more complex. Let us start with Figure 5-4 (right, c). The region between 166 and 158 eV binding energies is satisfactorily deconvoluted with two doublets, with the S2p<sub>3/2</sub> lines centered at 161.7 (red line) and 162.9 eV (blue line), respectively, with FWHMs of 1.2 and 1.5 eV, respectively. The shift between both components is 1.2 eV. The doublet in the 170-166 eV region corresponds to contributions from sulfates<sup>40</sup>. From the deconvolution from Figure 5-4 (left, c) we obtain two S2s contributions (magenta lines) at 225.9 and 227.0 eV, respectively (1.1 eV shift) and three contributions to the Mo3d lines with the corresponding Mo3d<sub>5/2</sub> lines centered at 228.7 (red line), 229.9 (blue line) and 232.6 eV (olive line), respectively. Note that in this case the contribution from MoO<sub>3</sub> (232.6 eV) dominates and that the remaining features are shifted by 1.2 eV. In the inset we observe that for the hydrothermal samples the VBM is located at 0.25 eV.

Figure 5-4c evidence the presence of two different MoS<sub>2</sub> materials or phases in the hydrothermal samples, in addition to the MoO<sub>3</sub> component. We identify n-type 2H MoS<sub>2</sub> (blue lines), with the Mo3d<sub>5/2</sub> and S2p<sub>3/2</sub> peaks located at 229.9 and 162.9 eV, respectively, by direct comparison with the MoS<sub>2</sub> natural crystal and CVD-grown references in Figure 5-4a, b. The second material or phase exhibits binding energies (core levels and VBM) that are rigidly shifted by 1.2 eV towards lower energies, a value that approaches the full indirect band gap of MoS<sub>2</sub>. This rigid shift is due to band bending<sup>41,42</sup>. The comparison of the FWHM of the S2p line corresponding to the hydrothermal sample (above 1 eV) as compared to the natural crystal and CVD samples (0.7 eV) evidence considerable disorder in the nanocrystals due to the presence of defects, which could induce the pinning of the Fermi level and thus the band bending. All these features indicate that the second phase could be assigned to either a defective p-type 2H MoS<sub>2</sub> or to a defective small-gap octahedral phase. Coming back to the previous measurements of UV-visible absorbance we have observed that the characteristic absorption bands of 2H-MoS<sub>2</sub> have smeared out and instead a monotonic change is captured. That indicates that the spectrum is dominated by octahedral T phases, which have a more metallic character, rather than a p-type 2H MoS<sub>2</sub>. That is also supported by the lack of photoluminescence signals on the hydrothermal samples, indicating again that the overall performance is dominated by a more metallic character. However, a pure metallic phase is ruled out since the VBM does not coincide with the Fermi level of the system, depicting 0.25 eV of difference between E<sub>f</sub> and VBM. Such finding discourages the presence of the pure metallic T phase, which is also unstable due to its high energy<sup>7</sup>. These results are more consistent with the presence of the distorted T' phase, which exhibits small bandgaps and is more prone to defects, doping and lattice deformation inducing band shifting and band bending<sup>7</sup>.

Finally, our fits consider exclusively Mo<sup>+4</sup> oxidation states (apart from the Mo<sup>+6</sup> from oxides used as precursors in the hydrothermal growth). No hint of lower



oxidation states, e.g.,  $\text{Mo}^{3+}$ , is observed, although residual traces cannot be completely excluded given the complexity of the fit. Recently, a critical review on the experimental characterization of the  $\text{MoS}_2$  1T phases has pointed out the presence of  $\text{Mo}^{3+}$  species<sup>43</sup>. In the case of XPS experiments this is based on the observation of binding energies of the  $\text{Mo}3d_{5/2}$  line of about 228 eV. One has to bear in mind that when dealing with defective semiconductors, band bending can shift the binding energies with a difference up to the band gap without the relevant presence of lower oxidation states<sup>44–46</sup>.



**Figure 5-5.** The XPS fitting of Cu of hydrothermal  $\text{MoS}_2/\text{Cu}$  nanoreactors

XPS measurements have been performed on the copper deposited on the  $\text{MoS}_2$ . Figure 5-5 shows the XPS spectra of the Cu2p line (main frame) and of the Auger Cu LMM region (inset), respectively. Both the binding energy and shape of the Cu2p<sub>3/2</sub> component (932.3 eV) together with the shape of the Cu LMM line, which exhibits a prominent maximum at a kinetic energy of 917.1 eV, are indicative of an oxidation state of +1 for copper<sup>47</sup>.

## 5.2.3 Photocatalytic degradation of organic pollutants.

### 5.2.3.1 Photocatalytic removal of tetracycline.

The photocatalytic degradation ability of the hydrothermal  $\text{MoS}_2/\text{Cu}$  nanoreactors was investigated at pH 6 and 8 with Tetracycline (TC) as the target pollutant. Firstly, the photocatalytic tests were performed in the absence of the nanoreactors in the dark and under visible light irradiation to obtain the adsorption-desorption equilibrium.

The changes of the TC absorbance were acquired during 180 min of irradiation with visible light (Figure 5-6a). The TC degradation ability of HT  $\text{MoS}_2$  nanoreactors was 33.1 % and 43.9 % at pH=6 and pH=8, respectively. Interestingly, the deposition of a thin 3 nm copper (Cu) layer on the HT  $\text{MoS}_2$

significantly promoted the degradation rate of TC to 90 % and 92 % at pH=6 and pH=8, respectively, indicating its excellent catalytic performance. The photodegradation kinetics was analyzed by fitting the first-order kinetic equation (Figure 5-6c). By the addition of Cu, the rate constant of HT MoS<sub>2</sub>/Cu system increased by 5.95 and 4.05 times from 0.002 min<sup>-1</sup> to 0.013 min<sup>-1</sup> and from 0.0034 min<sup>-1</sup> to 0.013 min<sup>-1</sup> at pH=6 and pH=8, respectively. In addition, the mass-normalized kinetic constant was calculated ( $k_{norm} = k/m_{cat}$ ). According to ICP-MS results only 0.0073 g of catalyst was used in order to completely remove TC in 180 min. Thus, the corresponding  $k_{norm}$  values for TC at pH 6 and pH 8 were 1.79 min<sup>-1</sup> g<sup>-1</sup> and 1.89 min<sup>-1</sup> g<sup>-1</sup>, respectively.

The total organic carbon (TOC) was measured to assess the mineralization of TC by the HT MoS<sub>2</sub> and HT MoS<sub>2</sub>/Cu systems. Especially, the MoS<sub>2</sub>/Cu system achieved a high TOC removal rate of 74.6 % and 86.2 % at pH=6 and pH=8 respectively, which is nearly double or triple the rate obtained with the MoS<sub>2</sub> system (22.6 % at pH=6, 33.8 % at pH=8) (Figure 5-6b).

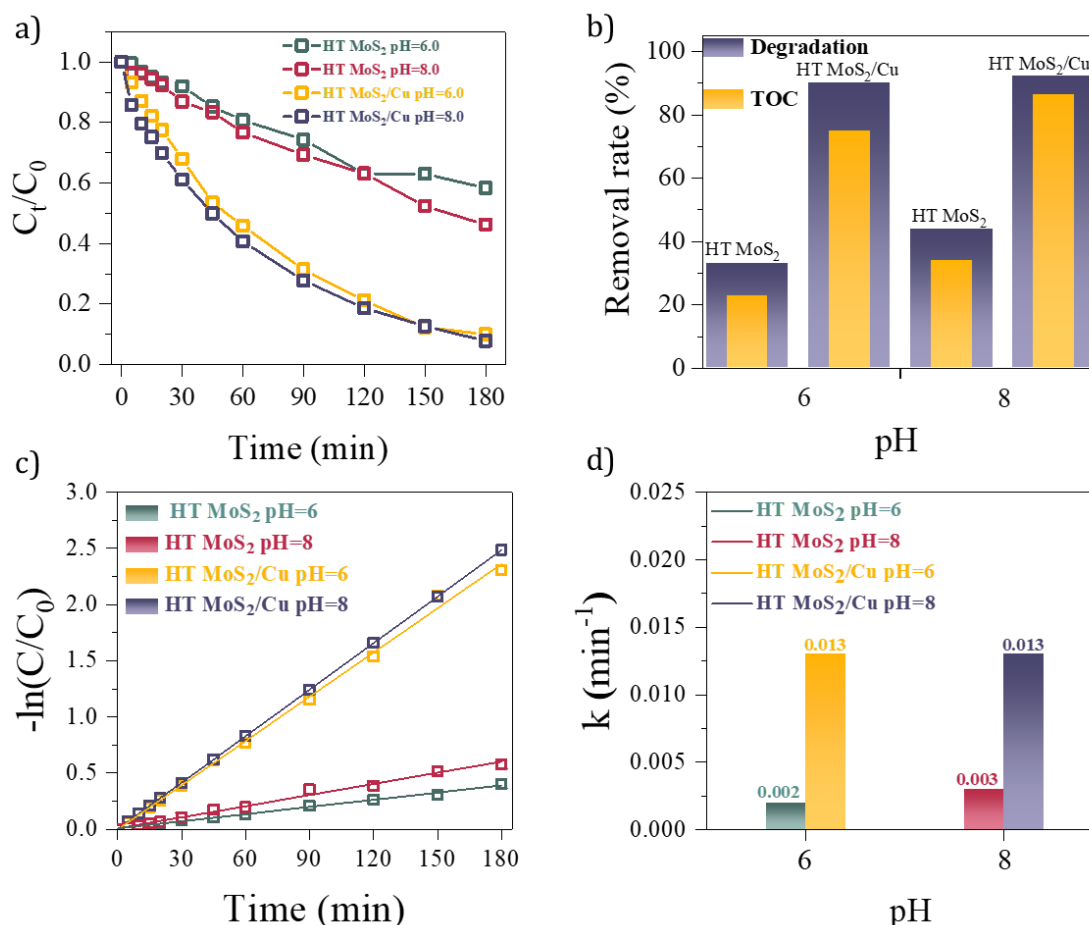


**Figure 5-6.** TC degradation in the presence of hydrothermal MoS<sub>2</sub> with/without copper at different pH. a) Variation of the TC concentration versus time. b) Degradation and TOC removal percentage. c) Reduction of the TC concentration over time in logarithmic scale, d) Obtained reaction rate ( $k$ ) values.

### 5.2.3.2 ROS quenching and reusability of the catalyst

Generally, hydroxyl radicals ( $\cdot\text{OH}$ ) and superoxide radicals ( $\text{O}_2^-$ ) are the main reactive oxygen species (ROS) for organic pollutant removal. Therefore, the ROS quenching experiments on  $\cdot\text{OH}$ ,  $\text{O}_2^-$  and  $\text{h}^+$  were performed for determining the generated active species. We used 1mM p-benzoquinone (p-BQ) as a quenching agent for  $\text{O}_2^-$ , 1mM isopropyl alcohol (IPA) as a quenching agent for  $\cdot\text{OH}$ , and 1mM triethanolamine (TEA) as a quenching agent of  $\text{h}^+$ . Figure 5-7a shows that the removal efficiency of TC was significantly affected by IPA and p-BQ after 180 min. At pH=8, only 16.3 % and 34.5 % TC was degraded in the presence of IPA and p-BQ respectively. Similarly, in the presence of IPA and p-BQ, the nanoreactors decomposed 23.1 % and 21.2 % of TC at pH=6, respectively. In contrast, when TEA was added, the removal rate was 81.5 % and 72.3 % at pH=6 and pH=8, thus suggesting that  $\cdot\text{OH}$  and  $\text{O}_2^-$  were the main active species for TC removal.

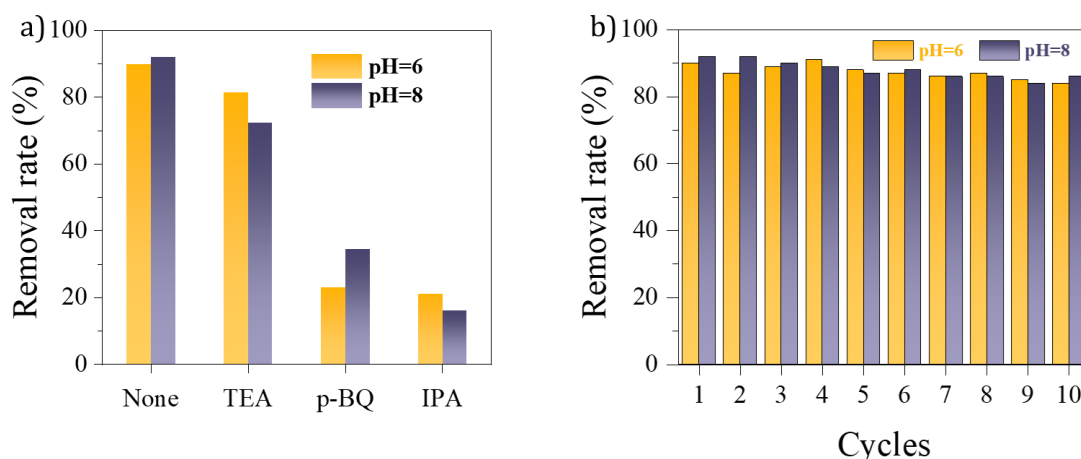


**Figure 5-7.** a) ROS quenching experiments in the presence of p-BQ, IPA and TEA, b) regeneration cycles of the catalyst.

Evaluating reusability and stability is crucial for commercial wastewater treatment. Therefore, we conducted a cyclic experiment of the TC removal at pH 6 and 8. Figure 5-7b reveals that the photocatalytic activity of  $\text{MoS}_2/\text{Cu}$  nanoreactors keeps nearly unchanged even after 10 cycles both at pH 6 and pH 8. These results confirm that the  $\text{MoS}_2/\text{Cu}$  nanoreactors could be a potential candidate for commercial wastewater treatment.

### 5.2.4.2 Anatoxin degradation catalytic tests

Cyanobacteria are aquatic, photosynthetic bacteria that use sunlight for the conversion of a carbon dioxide-rich atmosphere to an oxygen-rich atmosphere<sup>48,49</sup>. Currently, the excessive reproduction and accumulation of cyanobacteria and the toxins they produce pose a growing challenge to the water industry<sup>50,51</sup>. The cyanobacterial blooms are promoted by climate change especially, ocean warming and the high N/P ratio in wastewater which is in great

supply due to the pesticides and fertilizers in agricultural runoff and detergents from water treatment plants<sup>52</sup>.

Cyanotoxins are classified into three main groups according to their mechanism of action in tissues: hepatotoxins, dermatotoxins and neurotoxins<sup>51,53</sup>. Anatoxin-a (ATX-a) is one of the potent alkaloid neurotoxins produced by cyanobacteria globally<sup>54</sup>. It can cause death in animals via severe asphyxiation, and in humans via respiratory paralysis<sup>48</sup>.

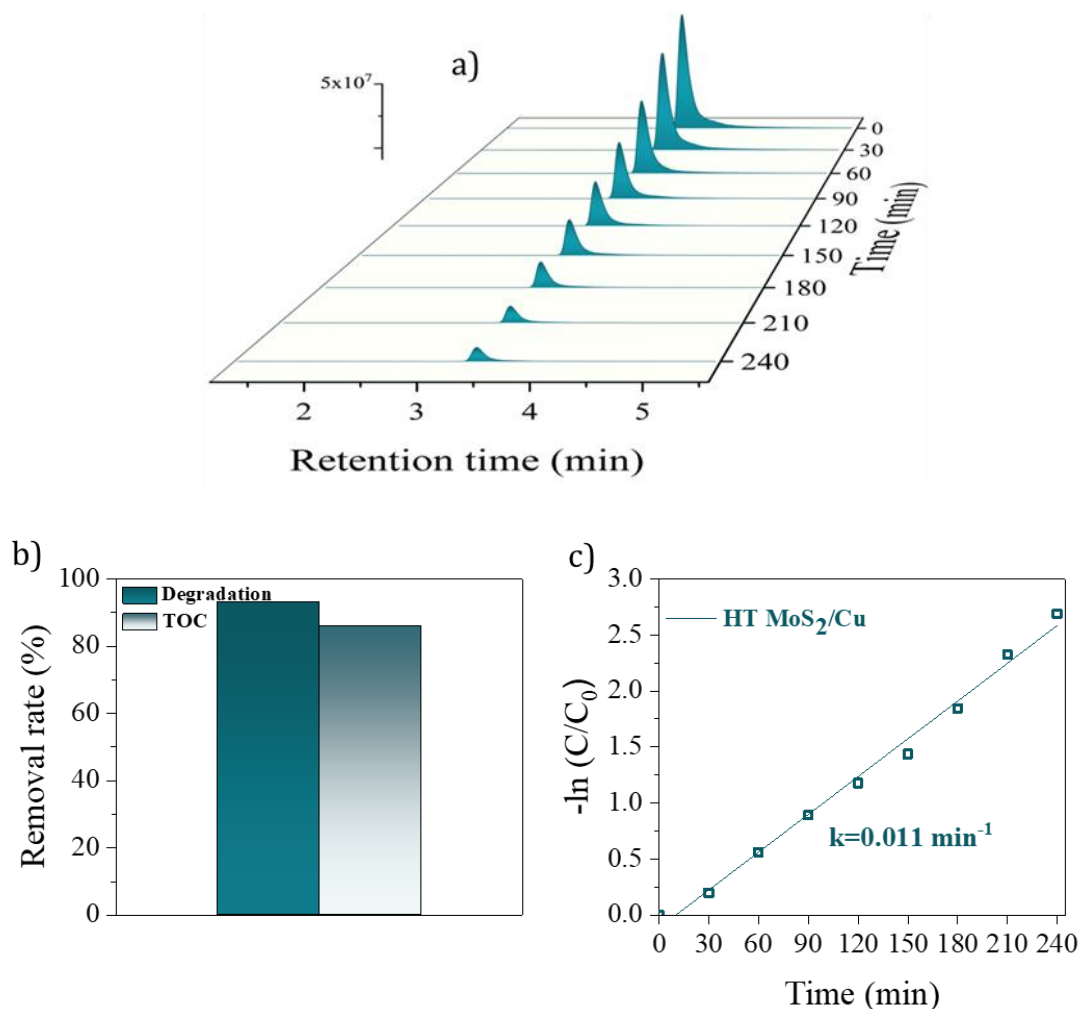


**Figure 5-8.** a) The decrease of absorbance of Anatoxin. Retention time (RT) is a measure of the time taken for a solute to pass through a chromatography column. b) The degradation and TOC, c) the linear fitting of rate constant ( $k$ ).

Although several water treatment techniques such as coagulation, flocculation, sedimentation, filtration, flotation, chlorination, ozonation, and adsorption on activated carbon have been used for the removal of cyanotoxins, for total removal a combination of different methods is required, which can be expensive<sup>54-56</sup>. Moreover, conventional treatments are unable to eliminate extracellular anatoxin-A.

To prove the potential of the MoS<sub>2</sub>/Cu nanoreactors for complex environmental applications, we analyzed the removal of anatoxin-A under white light irradiation. The nanoreactors were immersed into the anatoxin-A solution on the silicon substrate which helped the quick, time-efficient and clean recovery.

Figure 5-8a shows the anatoxin chromatograms in which the decrease in the intensity of anatoxin over time in the presence of nanoreactors can be clearly seen. Exposing the nanoreactors to artificial sunlight efficiently degraded 93.11 % of the anatoxin-A in 240 min. To validate the mineralization, the TOC measurements were conducted. The MoS<sub>2</sub>/Cu system achieved a high TOC removal rate of 86 % Figure 5-8b. In addition, the rate constant of anatoxin photodegradation was calculated according to the Langmuir-Hinshelwood model, following the pseudo-first-order kinetics. Figure 5-8c indicates that the photodegradation rate constant of anatoxin-A over the hydrothermal MoS<sub>2</sub>/Cu system was 0.011 min<sup>-1</sup> ( $k_{app}=1.54 \text{ min}^{-1} \text{ g}^{-1}$ ). These results suggest that the hydrothermal MoS<sub>2</sub>/Cu system is extremely efficient for the removal of cyanotoxins without using any noble metal co-catalyst<sup>57</sup>.

#### 5.2.4 Photocatalytic mechanism

The introduction of copper (Cu) significantly improved the photocatalytic activity of the hydrothermal MoS<sub>2</sub> system. According to the XPS results the Cu is oxidized to Cu<sup>+</sup> upon its combination with hydrothermal MoS<sub>2</sub>. The resulting Cu<sub>2</sub>O is generally a p-type semiconductor and exhibits remarkable photocatalytic properties due to its band gap (1.9~2.2 eV)<sup>58,59</sup>. Apart from the already good visible light absorption characteristics of MoS<sub>2</sub>, the presence of Cu<sub>2</sub>O promotes furthermore the efficiency of light absorption. The Cu<sub>2</sub>O heterojunction also contributes to improving the charge separation of the photocarriers. Proof of that may be attributed to the lack of photoluminescence of the overall MoS<sub>2</sub>/Cu<sub>2</sub>O system, indicating its excellent photocatalytic activity due to a lower electron-pair recombination rate<sup>60</sup>. Moreover, the presence of the additional T' phase in the hydrothermal MoS<sub>2</sub> provides more conductivity and high density of exposed active basal, edge and defect sites as compared to a pure 2H MoS<sub>2</sub> phase. These sites serve as catalytic sites for the redox processes of the analytes at the liquid interface. All these aspects greatly enhance the catalytic performance of the hybrid system. Furthermore, the ROS quenching results showed that the hydroxyl and superoxide radicals play a vital role in pollutant removal.

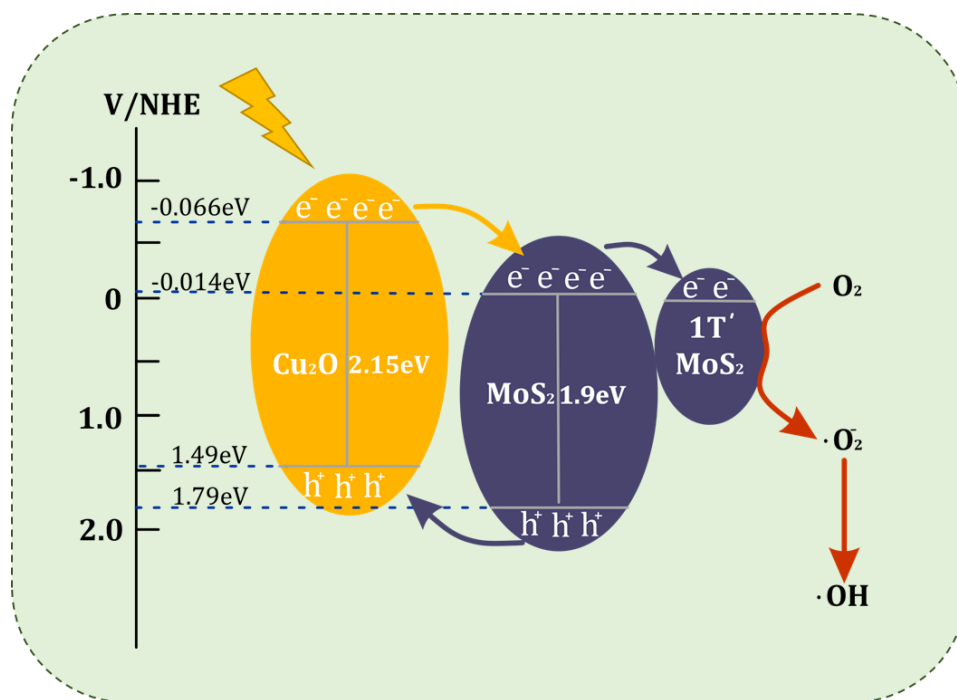
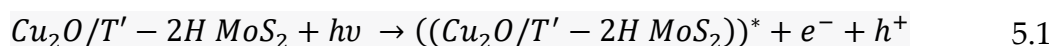


**Figure 5-9.** Schematic of photocatalytic degradation mechanism of hydrothermal MoS<sub>2</sub>/Cu.

Based on above the investigations, the proposed. The photocatalytic degradation pathway of the MoS<sub>2</sub>/Cu system is shown in Figure 5-9. Previous calculations have shown that the conduction band of Cu<sub>2</sub>O is more negative than that of MoS<sub>2</sub>, so under visible light illumination, Cu<sub>2</sub>O will guide the electron pathways. Electrons from the valence band (VB) of Cu<sub>2</sub>O will be transferred to 2H-MoS<sub>2</sub> and then to the conduction band (CB) of T' MoS<sub>2</sub>, which is an excellent electron acceptor, leaving holes behind. The excited electrons on the CB of 1T' phase will reduce oxygen to generate superoxide radicals ( $\cdot O_2^-$ ), which will then react with water to form hydroxyl radicals ( $\cdot OH$ ) (according to the chemical pathways outlined below). On the other side, the holes migrate towards the valence band of Cu<sub>2</sub>O. However, these holes may not have enough energy to oxidize water to  $\cdot OH$  radicals (requiring redox potentials of around 1.9-2.8 eV depending on the pH) because the band levels are below 1.78 eV. Some minor oxidations of analytes may still be possible through other pathways, although quenching experiments have shown that the role of the oxidizing holes is minor in analyte degradation (5.1-5.4).



### 5.2.5 Catalytic activity of MoS<sub>2</sub>/Cu nanoreactors on cancer cells.

Recently the biomedical applications of MoS<sub>2</sub> have attracted considerable attention due to its biocompatibility and good photodynamic activity. In this section, we will introduce preliminary but very encouraging findings on the use of MoS<sub>2</sub>-based nanoreactors as photodynamic agents for cancer therapies. To assess the therapeutic response *in vitro* a cell viability assay was performed in human osteoblast-like Saos-2 cell line (human osteosarcoma). The cells were plated inside a plastic well (thickness 120 μm) located in the center of the Petri dish. Then the supported MoS<sub>2</sub>/Cu photocatalyst on the silicon substrate or a bare silicon substrate without photocatalyst were placed on the top part of the plastic well, thereby forming a cavity with a separation distance of 100 μm between cells and the active nanostructures (Figure 5-1a).

Firstly, the cells were irradiated with near-infrared light (660 nm, 100 mW/cm<sup>2</sup>) for 90 min and then were incubated for 24 hours under normal conditions (37 °C, 5 % CO<sub>2</sub>). Then the live-dead assay was conducted (Figure 5-10c, d, e).

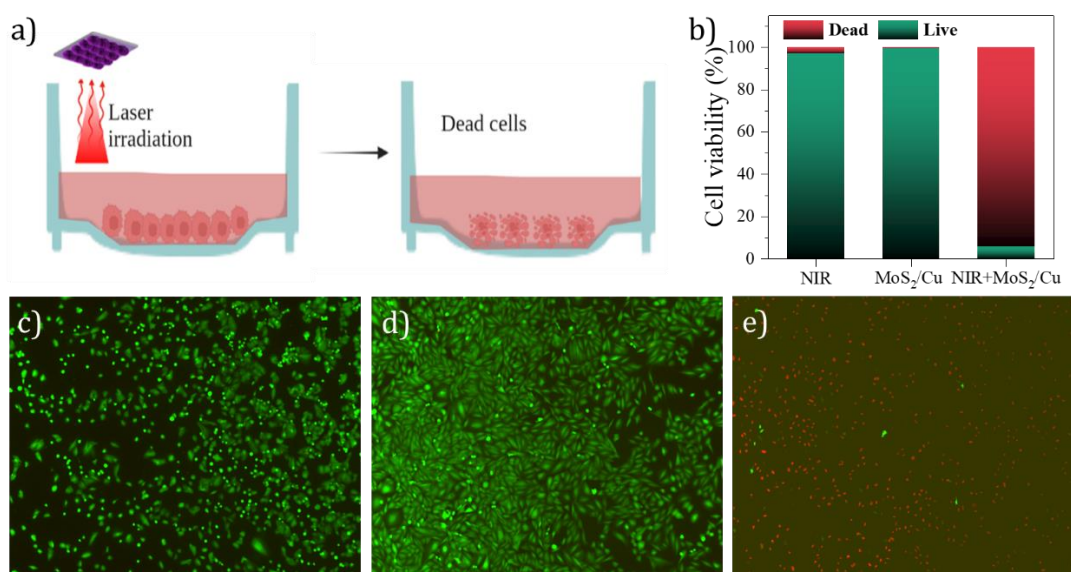


**Figure 5-10.** Live/dead staining of the Saos-2 cells after different treatments a) control, b) cells treated with hydrothermal MoS<sub>2</sub>/Cu catalyst, c) cells treated with NIR and MoS<sub>2</sub>/Cu, d) cell viability assay, e) scheme of *in vitro* analysis.

As can be seen, after red light irradiation, the viability of the cell population was 97 % (Figure 5-10b). Similarly, the incubation of cells with nanoreactors exhibited good biocompatibility and safety (viability 99.56 %). In contrast, the incubation of cancer cells with nanoreactors and NIR-light illumination led a drastic decrease on the viability (5.77% viability). This result highlights the remarkable catalytic performance of the hydrothermal MoS<sub>2</sub>-Cu system under physiological

conditions, especially considering the large separation distance between the nanoreactors and the cells. Even stronger photodynamic effects would be expected in the case of nanoreactors directly interacting with the cells, either at the cell membrane or internalized.

### 5.3 Conclusions

The 2D MoS<sub>2</sub> nanoreactors were successfully grown on the mesoporous silica nanoparticles by hydrothermal treatment. XPS measurements have provided relevant insights by comparing the hydrothermal samples with the well-known structures of CVD MoS<sub>2</sub> or natural crystals of MoS<sub>2</sub>. The joint analysis of the findings obtained with XPS and other characterization techniques such as UV-visible absorption, Raman spectroscopy and photoluminescence suggests that the most likely structure of HT MoS<sub>2</sub> is a combined 2H-1T' phase, featuring defects and chemical doping. Compared to the reactive sites of CVD 2H MoS<sub>2</sub>, the HT 2H-1T' MoS<sub>2</sub> has a higher density of catalytic sites (basal, edge defect active sites), which promote the transfer of photogenerated charges to analytes at the liquid interface. The deposition of an extremely thin layer of Cu has greatly enhanced the photocatalytic properties of the system. Cu in the form of the semiconducting Cu<sub>2</sub>O promotes light absorption and charge separation. The synergistic effect of all these features makes the photocatalytic performance of HT MoS<sub>2</sub>/Cu nanoreactors superior to that of HT MoS<sub>2</sub> towards TC and Anatoxin (A+) degradation and mineralization with white light. Moreover, the 2H-1T' MoS<sub>2</sub> nanoreactors were notably stable even after 10 cycles. In addition, the catalytic activity of the HT MoS<sub>2</sub>/Cu nanoreactors was tested on cancer cells *in vitro* under NIR light irradiation. The 2H-1T' MoS<sub>2</sub> nanoreactors showed negligible cytotoxicity and efficiently kill cancer cells under NIR light irradiation. Overall, we anticipate that the environmentally friendly, cost-efficient HT MoS<sub>2</sub>/Cu nanoreactors could be a potential catalyst not only for cost-effective environmental applications but also for biomedical applications, especially for photodynamic cancer treatment.

### 5.4 Materials and methods

#### 5.4.1 Studies on the degradation of pollutants

Firstly, the photo degradability of the photocatalysts was examined through the degrading organic pollutant of Tetracycline (TC). The experimental procedures were as follows: 5 ppm TC aqueous solution was prepared, and the solution pH was set to pH 6 and 8. Then the nanoreactors on the silicon substrate (2x3 cm<sup>2</sup>) were immersed in pollutants. Subsequently, the mixture was continuously stirred in the dark for 60 min to reach the adsorption equilibrium. Once the equilibrium was achieved, the nanoreactors were irradiated under visible light (24.2 mW/cm<sup>2</sup>).



The photocatalytic activity of HT MoS<sub>2</sub>/Cu nanoreactors against cyanotoxins was evaluated using a solution containing 20 ppm of (±)-anatoxin-A fumarate as a model cyanotoxin. Briefly, the nanoreactors were suspended in the cyanotoxin solution in the dark to establish adsorption-desorption equilibrium. A 24.2 mW LED lamp setup was used as a simulated solar light source. To determine photocatalytic activity, the pollutant solutions were exposed to irradiation. The reduction of cyanotoxin concentration was measured using ultrahigh-performance-liquid chromatography (UHPLC) system.

The reaction rate constant was calculated according to the Langmuir-Hinshelwood model, following first-order-kinetics:  $\ln \frac{[A_t]}{[A_0]} = -kt$ .

### 5.4.2 Studies of cancer cell apoptosis

A sterile Secure-Seal™ spacer of 9 mm diameter was placed in the middle of a 35 mm petri dish. Saos-2 cells were seeded inside the spacer at a density of 10,000 cells for 48 hours. Then, UV-sterilized MoS<sub>2</sub>/Cu nanoreactors on the silicon wafer were placed on top of cells with particles facing cells and kept for 90 minutes. The live/dead assay was performed after 24 hours. 0,1 μL of Calcein-AM (Green, excitation/emission spectra: 495/515 nm) and 1 μL of Ethidium homodimer-1 (Red, excitation/emission spectra: 528/617 nm) were added into 1 mL of culture media and incubated with cells for 30 minutes at RT.

### 5.4.3 Studies of XPS

XPS experiments were carried out using a SPECS PHOIBOS150 hemispherical analyser with a monochromatic X-ray source (1486.6 eV) operated at 300W. The reported binding energies have been obtained with an error of ±0.1 eV and are referred to the Fermi level (E<sub>F</sub>) of the analyser, which is periodically determined by measuring the photoelectron energies from an atomically clean reference Au (111) sample.

## 5.5 References

1. Wang L, Bahnemann DW, Bian L, Dong G, Zhao J, Wang C. Two-Dimensional Layered Zinc Silicate Nanosheets with Excellent Photocatalytic Performance for Organic Pollutant Degradation and CO<sub>2</sub> Conversion. *Angew Chemie - Int Ed.* 2019;58(24):8103-8108. doi:10.1002/anie.201903027
2. Chen X, Mao SS. Titanium dioxide nanomaterials: Synthesis, properties, modifications and applications. *Chem Rev.* 2007;107(7):2891-2959. doi:10.1021/cr0500535
3. Rehman FU, Zhao C, Jiang H, Wang X. Biomedical applications of nanotitania in theranostics and photodynamic therapy. *Biomater Sci.* 2016;4(1):40-54. doi:10.1039/c5bm00332f

4. Li H, Lu G, Yin Z, et al. Optical identification of single- and few-layer MoS<sub>2</sub> sheets. *Small*. 2012;8(5):682-686. doi:10.1002/sml.201101958
5. Voiry D, Mohite A, Chhowalla M. Phase engineering of transition metal dichalcogenides. *Chem Soc Rev*. 2015;44(9):2702-2712. doi:10.1039/c5cs00151j
6. Zhuang HL, Johannes MD, Singh AK, Hennig RG. Doping-controlled phase transitions in single-layer MoS<sub>2</sub>. *Phys Rev B*. 2017;96(16):1-8. doi:10.1103/PhysRevB.96.165305
7. Pariari D, Sarma DD. Nature and origin of unusual properties in chemically exfoliated 2D MoS<sub>2</sub>. *APL Mater*. 2020;8(4). doi:10.1063/5.0005413
8. Tran VT, Kim J, Tufa LT, Oh S, Kwon J, Lee J. Magnetoplasmonic Nanomaterials for Biosensing/Imaging and in Vitro/in Vivo Biocompatibility. *Anal Chem*. 2018;90(1):225-239. doi:10.1021/acs.analchem.7b04255
9. Mak KF, Lee C, Hone J, Shan J, Heinz TF. Atomically thin MoS<sub>2</sub>: A new direct-gap semiconductor. *Phys Rev Lett*. 2010;105(13):2-5. doi:10.1103/PhysRevLett.105.136805
10. Wang DS, Fan SK. Microfluidic surface plasmon resonance sensors: From principles to point-of-care applications. *Sensors (Switzerland)*. 2016;16(8). doi:10.3390/s16081175
11. Jin W, Pastor-Pérez L, Yu J, Odriozola JA, Gu S, Reina TR. Cost-effective routes for catalytic biomass upgrading. *Curr Opin Green Sustain Chem*. 2020;23:1-9. doi:10.1016/j.cogsc.2019.12.008
12. Acero JL, Von Gunten U. Characterization of oxidation processes: Ozonation and the AOP O<sub>3</sub>/H<sub>2</sub>O<sub>2</sub>. *J Am Water Work Assoc*. 2001;93(10):90-100. doi:10.1002/j.1551-8833.2001.tb09311.x
13. Zhu L, Ji J, Liu J, et al. Designing 3D-MoS<sub>2</sub> Sponge as Excellent Cocatalysts in Advanced Oxidation Processes for Pollutant Control. *Angew Chemie - Int Ed*. 2020;59(33):13968-13976. doi:10.1002/anie.202006059
14. Zhao N, Wang L, Zhang Z, Li Y. Activating the MoS<sub>2</sub> Basal Planes for Electrocatalytic Hydrogen Evolution by 2H/1T' Structural Interfaces. *ACS Appl Mater Interfaces*. 2019;11(45):42014-42020. doi:10.1021/acsami.9b11708
15. Li Z, Meng X, Zhang Z. Recent development on MoS<sub>2</sub>-based photocatalysis: A review. *J Photochem Photobiol C Photochem Rev*. 2018;35:39-55. doi:10.1016/j.jphotochemrev.2017.12.002
16. Yu Y, Lu L, Yang Q, Zupanic A, Xu Q, Jiang L. Using MoS<sub>2</sub> Nanomaterials to Generate or Remove Reactive Oxygen Species: A Review. *ACS Appl Nano Mater*. 2021;4(8):7523-7537. doi:10.1021/acsanm.1c00751

17. Barbosa Ferreira M, Souza FL, Muñoz-Morales M, et al. Clopyralid degradation by AOPs enhanced with zero valent iron. *J Hazard Mater.* 2020;392. doi:10.1016/j.jhazmat.2020.122282
18. Moussa H, Girot E, Mozet K, Alem H, Medjahdi G, Schneider R. ZnO rods/reduced graphene oxide composites prepared via a solvothermal reaction for efficient sunlight-driven photocatalysis. *Appl Catal B Environ.* 2016;185:11-21. doi:10.1016/j.apcatb.2015.12.007
19. Li J, Xu M, Yao G, Lai B. Enhancement of the degradation of atrazine through CoFe<sub>2</sub>O<sub>4</sub> activated peroxymonosulfate (PMS) process: Kinetic, degradation intermediates, and toxicity evaluation. *Chem Eng J.* 2018;348:1012-1024. doi:10.1016/j.cej.2018.05.032
20. Ahn JH, Parkin WM, Naylor CH, Johnson ATC, Drndić M. Ambient effects on electrical characteristics of CVD-grown monolayer MoS<sub>2</sub> field-effect transistors. *Sci Rep.* 2017;7(1):1-9. doi:10.1038/s41598-017-04350-z
21. Xu Z, Fang J, Lu J, He D, He S, Luo Y. The nature of K-induced 2H and 1T'-MoS<sub>2</sub> species and their phase transition behavior for the synthesis of methanethiol (CH<sub>3</sub>SH). *Iscience.* 2022;25(9):104999.
22. Duerloo KAN, Li Y, Reed EJ. Structural phase transitions in two-dimensional Mo- and W-dichalcogenide monolayers. *Nat Commun.* 2014;5(May). doi:10.1038/ncomms5214
23. Jiao Y, Hafez AM, Cao D, Mukhopadhyay A, Ma Y, Zhu H. Metallic MoS<sub>2</sub> for High Performance Energy Storage and Energy Conversion. *Small.* 2018;14(36):1-20. doi:10.1002/sml.201800640
24. Wang Y, Ou JZ, Balendhran S, et al. Electrochemical control of photoluminescence in two-dimensional MoS<sub>2</sub> nanoflakes. *ACS Nano.* 2013;7(11):10083-10093. doi:10.1021/nn4041987
25. Eda G, Yamaguchi H, Voiry D, Fujita T, Chen M, Chhowalla M. NI201874W.Pdf. *Nano Lett.* Published online 2011:5111-5116. doi:10.1021/nl201874w
26. Peng J, Liu Y, Luo X, et al. High Phase Purity of Large-Sized 1T'-MoS<sub>2</sub> Monolayers with 2D Superconductivity. *Adv Mater.* 2019;31(19):1-7. doi:10.1002/adma.201900568
27. Li H, Zhang Q, Yap CCR, et al. From bulk to monolayer MoS<sub>2</sub>: Evolution of Raman scattering. *Adv Funct Mater.* 2012;22(7):1385-1390. doi:10.1002/adfm.201102111
28. Xiong F, Wang H, Liu X, et al. Li Intercalation in MoS<sub>2</sub>: In Situ Observation of Its Dynamics and Tuning Optical and Electrical Properties. *Nano Lett.*

- 2015;15(10):6777-6784. doi:10.1021/acs.nanolett.5b02619
29. Er E, Hou HL, Criado A, et al. High-Yield Preparation of Exfoliated 1T-MoS<sub>2</sub> with SERS Activity. *Chem Mater.* 2019;31(15):5725-5734. doi:10.1021/acs.chemmater.9b01698
  30. Guo C, Pan J, Li H, et al. Observation of superconductivity in 1T'-MoS<sub>2</sub> nanosheets. *J Mater Chem C.* 2017;5(41):10855-10860. doi:10.1039/c7tc03749j
  31. Paris JL, Cabanas MV, Manzano M, Vallet-Regí M. Polymer-Grafted Mesoporous Silica Nanoparticles as Ultrasound-Responsive Drug Carriers. *ACS Nano.* 2015;9(11):11023-11033. doi:10.1021/acs.nano.5b04378
  32. Campos-Martin JM, Blanco-Brieva G, Fierro JLG. Hydrogen peroxide synthesis: An outlook beyond the anthraquinone process. *Angew Chemie - Int Ed.* 2006;45(42):6962-6984. doi:10.1002/anie.200503779
  33. Wu M, Zhan J, Wu K, et al. Metallic 1T MoS<sub>2</sub> nanosheet arrays vertically grown on activated carbon fiber cloth for enhanced Li-ion storage performance. *J Mater Chem A.* 2017;5(27):14061-14069.
  34. Fang Y, Pan J, He J, et al. Structure Re-determination and Superconductivity Observation of Bulk 1T MoS<sub>2</sub>. *Angew Chemie.* 2018;130(5):1246-1249. doi:10.1002/ange.201710512
  35. Fraxedas J, Schütte M, Sauthier G, et al. In situ XPS analysis of the electronic structure of silicon and titanium thin films exposed to low-pressure inductively-coupled RF plasma. *Appl Surf Sci.* 2021;542:148684. doi:10.1016/j.apsusc.2020.148684
  36. Lee SY, Kim UJ, Chung J, et al. Large Work Function Modulation of Monolayer MoS<sub>2</sub> by Ambient Gases. *ACS Nano.* 2016;10(6):6100-6107. doi:10.1021/acs.nano.6b01742
  37. Addou R, McDonnell S, Barrera D, et al. Impurities and Electronic Property Variations of Natural MoS<sub>2</sub> Crystal Surfaces. *ACS Nano.* 2015;9(9):9124-9133. doi:10.1021/acs.nano.5b03309
  38. Ganta D, Sinha S, Haasch RT. 2-D Material Molybdenum Disulfide Analyzed by XPS. *Surf Sci Spectra.* 2014;21(1):19-27. doi:10.1116/11.20140401
  39. Syari'Ati A, Kumar S, Zahid A, Ali El Yumin A, Ye J, Rudolf P. Photoemission spectroscopy study of structural defects in molybdenum disulfide (MoS<sub>2</sub>) grown by chemical vapor deposition (CVD). *Chem Commun.* 2019;55(70):10384-10387. doi:10.1039/c9cc01577a
  40. Fraxedas J, García-Gil S, Monturet S, et al. Modulation of surface charge transfer through competing long-range repulsive versus short-range

- attractive interactions. *J Phys Chem C*. 2011;115(38):18640-18648. doi:10.1021/jp2050838
41. Zhang Z, Yates JT. Band bending in semiconductors: Chemical and physical consequences at surfaces and interfaces. *Chem Rev*. 2012;112(10):5520-5551. doi:10.1021/cr3000626
  42. McDonnell S, Addou R, Buie C, Wallace RM, Hinkle CL. Defect-DOMINATED DOPING and CONTACT RESISTANCE in MoS<sub>2</sub>. *ACS Nano*. 2014;8(3):2880-2888. doi:10.1021/nn500044q
  43. Strachan J, Masters AF, Maschmeyer T. Critical review: hydrothermal synthesis of 1T-MoS<sub>2</sub>- an important route to a promising material. *J Mater Chem A*. 2021;9(15):9451-9461. doi:10.1039/d1ta01230d
  44. Justicia I, Ordejón P, Canto G, et al. Designed self-doped titanium oxide thin films for efficient visible-light photocatalysis. *Adv Mater*. 2002;14(19):1399-1402.
  45. Fraxedas J, Schütte M, Sauthier G, et al. In situ XPS analysis of the electronic structure of silicon and titanium thin films exposed to low-pressure inductively-coupled RF plasma. *Appl Surf Sci*. 2021;542:148684.
  46. Diebold U. The surface science of titanium dioxide. *Surf Sci Rep*. 2003;48(5-8):53-229.
  47. Biesinger MC. Advanced analysis of copper X-ray photoelectron spectra. *Surf Interface Anal*. 2017;49(13):1325-1334. doi:10.1002/sia.6239
  48. Christensen VG, Khan E. Freshwater neurotoxins and concerns for human, animal, and ecosystem health: A review of anatoxin-a and saxitoxin. *Sci Total Environ*. 2020;736:139515. doi:10.1016/j.scitotenv.2020.139515
  49. John N, Baker L, Ansell BRE, Newham S, Crosbie ND, Jex AR. First report of anatoxin-a producing cyanobacteria in Australia illustrates need to regularly up-date monitoring strategies in a shifting global distribution. *Sci Rep*. 2019;9(1):1-9. doi:10.1038/s41598-019-46945-8
  50. Huisman J, Codd GA, Paerl HW, Ibelings BW, Verspagen JMH, Visser PM. Cyanobacterial blooms. *Nat Rev Microbiol*. 2018;16(8):471-483. doi:10.1038/s41579-018-0040-1
  51. Merel S, Walker D, Chicana R, Snyder S, Baurès E, Thomas O. State of knowledge and concerns on cyanobacterial blooms and cyanotoxins. *Environ Int*. 2013;59:303-327. doi:10.1016/j.envint.2013.06.013
  52. Carmichael WW. Human and Ecological Risk Assessment: An International Journal Health Effects of Toxin-Producing Cyanobacteria: "The CyanoHABs "; Health Effects of Toxin-Producing

- Cyanobacteria: &quot;The CyanoHABs &quot; *Hum Ecol Risk Assess An Int J Hum Ecol Risk Assess.* 2001;7(5):1393-1407. <http://www.tandfonline.com/action/journalInformation?journalCode=bher20%5Cnhttp://dx.doi.org/10.1080/20018091095087>
53. Pantelić D, Svirčev Z, Simeunović J, Vidović M, Trajković I. Cyanotoxins: Characteristics, production and degradation routes in drinking water treatment with reference to the situation in Serbia. *Chemosphere.* 2013;91(4):421-441. doi:10.1016/j.chemosphere.2013.01.003
  54. Song J, Wang X, Ma J, Wang X, Wang J, Zhao J. Visible-light-driven in situ inactivation of *Microcystis aeruginosa* with the use of floating g-C<sub>3</sub>N<sub>4</sub> heterojunction photocatalyst: Performance, mechanisms and implications. *Appl Catal B Environ.* 2018;226:83-92. doi:10.1016/j.apcatb.2017.12.034
  55. He P, Zhao Z, Tan Y, et al. Photocatalytic degradation of deoxynivalenol using cerium doped titanium dioxide under ultraviolet light irradiation. *Toxins (Basel).* 2021;13(7). doi:10.3390/toxins13070481
  56. Serrà A, Pip P, Gómez E, Philippe L. Efficient magnetic hybrid ZnO-based photocatalysts for visible-light-driven removal of toxic cyanobacteria blooms and cyanotoxins. *Appl Catal B Environ.* 2020;268(January):118745. doi:10.1016/j.apcatb.2020.118745
  57. Tian L, Wu R, Liu HY. Synthesis of Au-nanoparticle-loaded 1T@2H-MoS<sub>2</sub> nanosheets with high photocatalytic performance. *J Mater Sci.* Published online 2019. doi:10.1007/s10853-019-03545-1
  58. Wang JC, Zhang L, Fang WX, et al. Enhanced photoreduction CO<sub>2</sub> activity over direct Z-Scheme  $\alpha$ -Fe<sub>2</sub>O<sub>3</sub>/Cu<sub>2</sub>O heterostructures under visible light irradiation. *ACS Appl Mater Interfaces.* 2015;7(16):8631-8639. doi:10.1021/acsami.5b00822
  59. He J, Shao DW, Zheng LC, et al. Construction of Z-scheme Cu<sub>2</sub>O/Cu/AgBr/Ag photocatalyst with enhanced photocatalytic activity and stability under visible light. *Appl Catal B Environ.* 2017;203:917-926. doi:10.1016/j.apcatb.2016.10.086
  60. Belmabkhout Y, Serna-guerrero R, Å AS. Amine-bearing mesoporous silica for CO<sub>2</sub> removal from dry and humid air. *Chem Eng Sci.* 2010;65(11):3695-3698. doi:10.1016/j.ces.2010.02.044

## **6. Ni/Pt nanoreactors on porous silica nanostructures as thermocatalysts**

Transition-metal-catalyzed transfer hydrogenation with an in situ hydrogen donor has received a great deal of attention as an alternative to the traditional high-pressure-hydrogen process, owing to its better efficiency, atom economy, and sustainability features. Hydrogen stored in the chemical bonds of formic acid (FA), a promising hydrogen storage compound that could be derived from biomass or reduction of CO<sub>2</sub>, can be extracted selectively, and used for diverse catalytic transformations. This Chapter describes some preliminary results of Levulinic acid conversion to gamma Valerolactone over Ni/Pt nanoreactors.

## 6.1 Introduction

Fossil fuel use, which has climbed alongside economic growth since the industrial revolution, currently supplies 80 % of the world's energy. The reliance on fossil fuels worsens air quality, causes water pollution, and significantly increases global carbon fingerprint and greenhouse gas emissions<sup>1</sup>. Recently the world has been tackling with the issue of soaring energy prices. Higher energy costs have been a major cause of excruciatingly unbearably high inflation, pushing households into poverty, forcing some firms to reduce output or even close down, and delaying economic growth to the point that several nations are on the verge of a severe recession<sup>2</sup>. On the other hand, the unprecedented energy crisis should also be seen as a turning point to speed up the world's transition to green energy.

Lignocellulosic biomass, the main renewable energy source, is derived from organic materials such as trees, plants, and agricultural and urban waste<sup>3-5</sup>. This biomass is mainly composed of cellulose, hemicellulose and lignin<sup>6,7</sup>. The sustainable production of lignocellulosic biomass can be used for heating, electricity generation, and transport fuels, effectively reducing greenhouse gas emissions<sup>8-10</sup>. Lignocellulose can be catalytically converted into numerous added-value chemicals such as alkanes<sup>11,12</sup>, acids<sup>13-15</sup>, aldehydes<sup>16,17</sup>, esters<sup>18,19</sup> etc. For example, the catalytic dehydration of glucose yields Levulinic acid (LA)<sup>20</sup>. LA is one of the most relevant chemicals produced from a variety of biomass-rich carbohydrates, including agricultural residues and food waste<sup>21-23</sup>. Hydrogenation of LA is a promising path for the conversion of biomass to value-added chemicals<sup>24</sup>. The transient state of 4-Hydroxyvaleric acid (4-HVA) is formed when the LA carbonyl group is reduced, yielding  $\gamma$ -valerolactone (GVL). GVL is an essential biomass derivative used in many areas, such as food or fuel additives, and is a safe intermediate for the production of gasoline and fine chemicals. Furthermore, GVL can be transformed into methyl tetrahydrofuran, 1-4 pentadiol and methyl tetrahydrofuran in the presence of hydrogen. Direct hydrogenation with H<sub>2</sub> gas is one of the ways to convert LA to GVL in the presence of metal catalysts such as Ru, Pd, Cu, Ir, Fe, Ni and metal phosphide catalysts<sup>25-29</sup>. However, the direct hydrogenation process requires high temperature and pressure which makes the process extremely dangerous and expensive. Catalytic transfer hydrogenation (CTH) is one of the cost-effective and safe alternatives to direct hydrogenation. The CTH process is based on hydrogen transferring from the hydrogen donor such as formic acid, various alcohols, etc., via transition metal complexes, especially Ru, Ni, Pt, Fe, Cu, Mg etc<sup>30-35</sup>.



In this Chapter, the fabrication of Ni/Pt alloy nanoreactors for the conversion of LA to GVL is first described. Large pore silica nanoparticles were used as catalyst support onto which Ni and Pt were deposited. The chapter then presents preliminary findings for the LA conversion to GVL using hydrothermal treatment in the presence of Ni/Pt nanoreactors, with formic acid (FA) used as a hydrogen donor. The results indicate that Ni/Pt alloy nanoreactors display good catalytic performance (50 % conversion) under hydrothermal treatment. The chapter also covers the first results on the capabilities of these nanoreactors as highly promising photothermal agents.

## 6.2 Materials and methods

### 6.2.1 The fabrication of Ni/Pt alloy nanoreactors

The fabrication of Ni/Pt alloy nanoreactors follows similar steps as previously described in other chapters. The fabrication scheme is shown in **Figure 6-1a**. Firstly, large pore silica nanoparticles (LPSN) were colloiddally self-assembled on a silicon wafer. Then, Ni (60 nm) and Pt (nm) layers were deposited on the LPSN array by electron beam evaporation. In order to induce a Ni/Pt alloying, the nanoreactors were then subjected to thermal treatment using a tubular furnace fed by Ar and H<sub>2</sub> gases under low pressure (**Figure 6-1b**). The silicon wafer with 2x2 cm<sup>2</sup> dimensions was placed in the quartz tube and Ar was blown into the tube to remove oxygen from the tube (Ar 40 sccm 5 min). The temperature was then set to 500 °C for 3 h in the presence of 400 sccm Ar and 200 sccm H<sub>2</sub> at vacuum. At the end of the process the quartz tube was cooled down at room temperature.

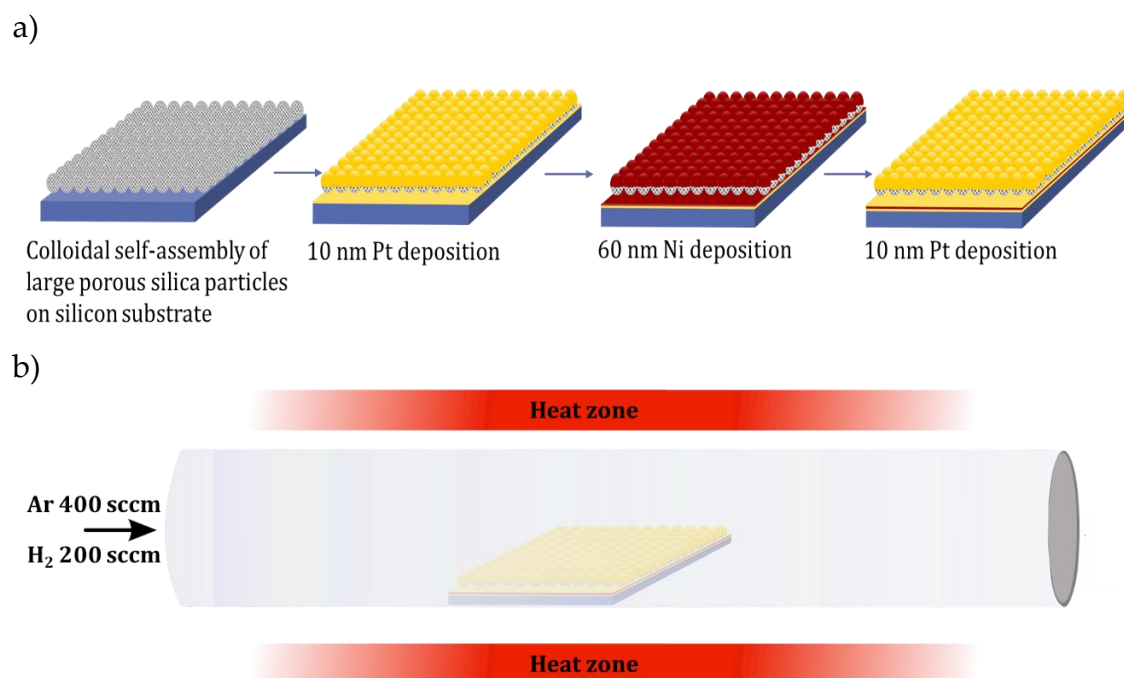


**Figure 6-1.** Schematic of fabrication of Ni/Pt alloy nanoreactor and b) the heat treatment of fabricated Ni/Pt nanoreactors.

### 6.2.2 The experimental conditions.

The catalytic transfer hydrogenation (CTH) of LA was carried out in a Teflon-lined stainless-steel autoclave (**Figure 6-1**). In a typical process, 5 mg Ni/Pt alloy nanoreactors were dispersed in 4 mL water. Then, 0.386 g Formic acid (HCOOH) and 1 g LA (C<sub>5</sub>H<sub>8</sub>O<sub>3</sub>) were added to the nanoreactor/water mixture. The sealed autoclave was placed in the furnace heated up to 180 °C for 4 h. After the CTH reaction, the autoclave was cooled down at room temperature and the nanoreactors were recovered by the magnet. The solution was analyzed using HPLC.

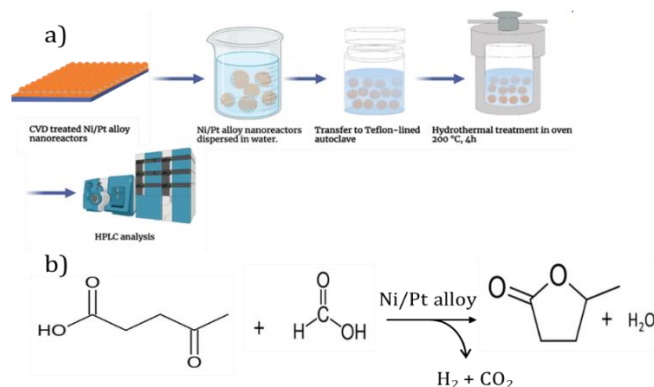


**Figure 6-2.** Schematics of the experiment of LA conversion of GVL

### 6.3 Results

In this section we will first discuss the performance of Ni/Pt nanoreactors for CTH of LA to GA under metal alloying and without alloying. As mentioned, alloying formation is promoted through thermal annealing, a process that forms alloys through solid-state mixing. During this process, the atoms of Ni and Pt diffuse together, creating a solid solution of the alloy.

The Ni/Pt alloy nanoreactors were characterized by HRSEM. **Figure 6-3a, b** shows the SEM images of Ni/Pt nanoreactors before and after thermal annealing for alloy formation. The heat-treated nanoreactors exhibit changes in their morphology as a result of the high diffusion of atoms during the thermal alloying process. The EDS result (**Figure 6-3c**) confirms the presence of the metal elements in the nanoreactors after the alloying process.

The catalytic conversion of LA was analyzed by HPLC. The As previously mentioned the product identification and conversion yield were obtained by HPLC. According to the HPLC results 50% of LA was converted to GVL when using alloyed Ni/Pt nanoreactors.

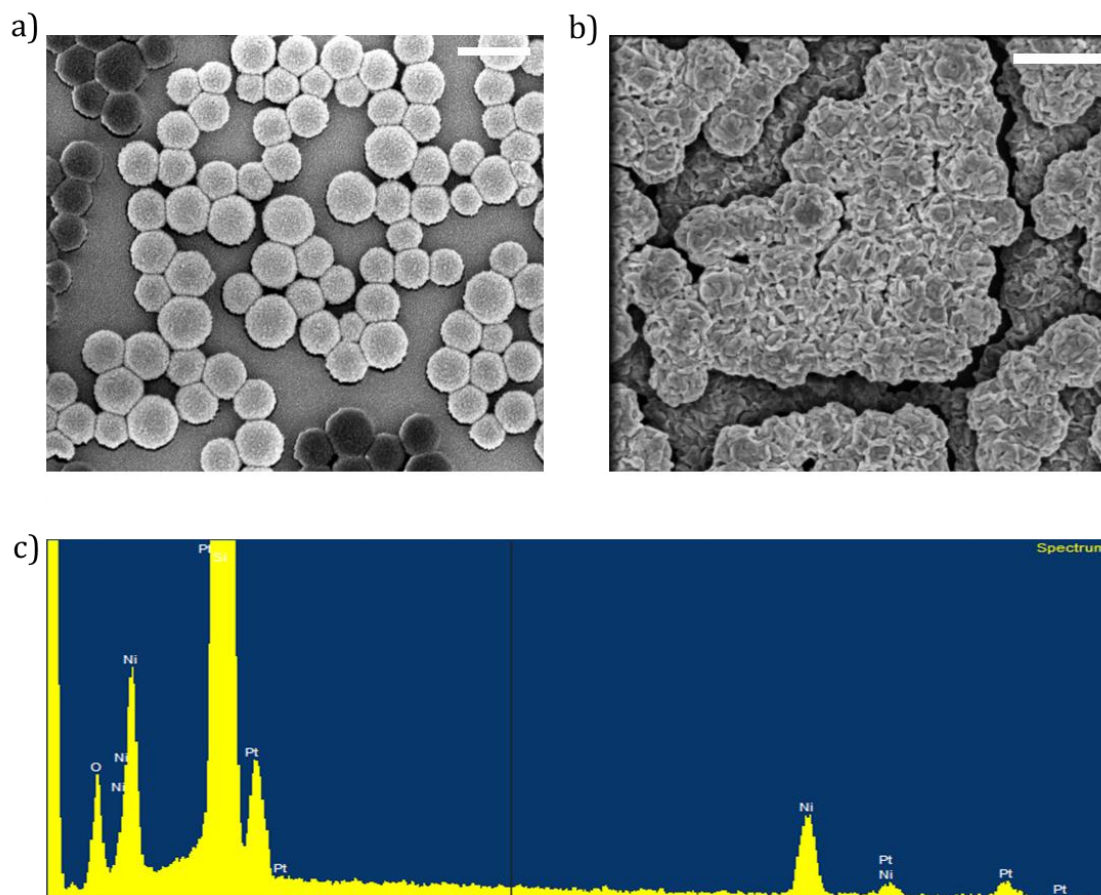


**Figure 6-3.** a) SEM image of Ni/Pt nanoreactors before the heat treatment, b) heat treated Ni/Pt alloy nanoreactors, c) the EDS of Ni/Pt alloy nanoreactors.

We have also addressed the capabilities of these Ni/Pt nanoreactors as photothermal agents by inducing heat in the reaction medium under NIR light illumination. Firstly, the light absorbance spectrum of the nanoreactors was analysed.

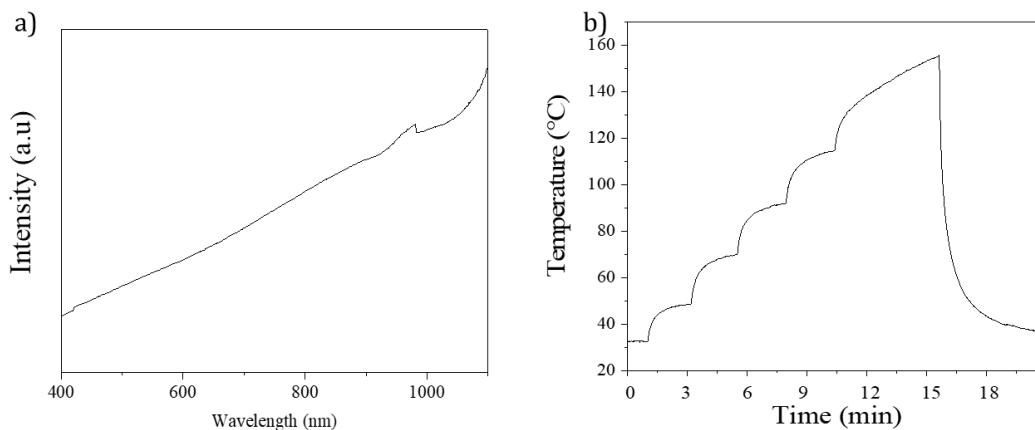


**Figure 6-4.** a) UV-Vis of Ni/Pt alloy nanoreactors, b) temperature changes of Ni/Pt alloy nanoreactors under 808 nm laser.

Figure 6-4a shows the UV-Vis spectra of the Ni/Pt alloy nanoreactors. Although no characteristic peaks could be observed, a significant absorption increase profile was captured in the NIR region with the wavelength increase. Then the photothermal effect of the nanoreactors on a thin plastic film in air was investigated upon the irradiation of 808 nm laser as shown in *Figure 6-4b*. Under non-illumination conditions, the temperature of the film was 32.7 °C, but as soon as the catalytic system is illuminated, the temperature of the film increases up to 156°C ( $T = 123.7$  °C) with a light intensity of 2.3 W/cm<sup>2</sup>. Therefore, the photothermal conversion efficiency in air was 53.7 °C cm<sup>2</sup>/W, thereby demonstrating the potential of these nanoreactors as photothermal agents.

## 6.4 Discussion

The results show the Ni/Pt alloying effect has a relevant impact on the catalytic performance of the CTH process for LA/GLV conversion compared to the unalloyed Ni/Pt where no evidence of chemical conversion was obtained.

Different reasons can be behind such findings which can be related to the interaction of the reagents with the catalytic system and competition with side reactions<sup>36-38</sup>. Specifically, in the CTH of LA, the conversion of LA and the yield of GVL are highly dependent on the ability to efficiently generate active H atoms from the hydrogen donor. The CTH process is strongly influenced by the chemical properties of the hydrogen donor. The use of FA as hydrogen donor possesses many advantages. FA has high capacity of hydrogen storage which prevents the need for high-pressure H<sub>2</sub> usage. This not only decrease the costs but also improve the sustainability and safety. Additionally, its low activation barrier for dehydrogenation leads to an accelerated CTH process. However, in

some cases, using FA can lead to an increase in competing reactions. This could be due to several factors, such as FA decomposition. Generally, FA decomposition follows two different routes, either it forms carbon dioxide (CO<sub>2</sub>) and hydrogen (6.1) or carbon monoxide (CO) and water (6.2 *Error! Reference source not found.*)<sup>39</sup>.



The CO formation is one of the reasons for low conversion of LA to GVL due to its poisoning effect on the active sites of catalyst.

In this context one of the reasons of the higher performance of the alloying Ni/Pt system can be attributed to the minimization of poisoning effects. As previously mentioned in the introductory part of this thesis, in general, the high performance of alloying catalysts is often attributed to ensemble or ligand effects upon alloying<sup>40-42</sup>. These effects have been studied in many alloying systems and have been found to result in improved catalytic performance, with superior catalytic selectivity and minimal poisoning effects. The ensemble effects refer to the specific arrangement of a finite number of active atoms required to promote catalysis, and are affected by the dilution of the more active metal (e.g., Pt) with respect to the less active one (e.g. Ni) during alloying. Very often has been observed that catalytic processes are enhanced when contiguous ensembles of the more active metal disappear to form more isolated active atoms surrounded by an area of the less active ones. The disappearance of contiguous ensembles of the more active material switches off side reactions, explaining the selectivity increase of certain reactions. The ligand effects, on the other hand, refer to changes in the electronic structure of the metals that occur as a result of heteronuclear metal-metal bond formation, involving charge transfer or orbital rehybridization between the heterometals. In turn, the metal bonds (e.g. Pt-Pt bonds) can be changed by perturbation of the metal lattice constant of the more active metal by the other metal component. The ligand effects can strongly impact on the interaction strength between adsorbates and the catalytic system.

It is quite probable that a more complete dispersion of the active material on the nanoreactor (optimum ensemble) is achieved with the alloying system as compared to non-alloying nanoreactors, thus favoring the CTH process and preventing CO adsorption. However, further studies are needed to better address the ensemble and ligand effects that typically characterize bimetallic catalyst alloys. Additionally, it should be noted that the large pore silica particles used as a support material can become easily deformed when subjected to long-

term heat treatment. This deformation can lead to the mixing of the silica with Ni/Pt, potentially forming porous alloys that may even improve the catalytic process.

Finally, the preliminary results of using Ni/Pt nanoreactors as photothermal agents are encouraging for the development of nanoreactors that can self-generate heat locally to induce reactions without the need for a furnace, thereby increasing portability, affordability, and sustainability.

## 6.5 Conclusion

In conclusion, we have developed a process to produce GVL from LA using a catalytic transfer hydrogenation (CTH) process with formic acid as the hydrogen source, and large porous silica-supported Ni/Pt alloy nanoreactors. The Ni/Pt alloy was formed through heat annealing pretreatment. The alloyed Ni/Pt catalyst displayed good catalytic performance, resulting in a good conversion (50 %) of LA to GVL compared to unalloyed nanoreactors. We believe that the alloying process optimizes the dispersion of heteroatoms, which, along with ligand effects, enhances the catalyst's activity. These are preliminary results that require further study to fully support our claims.

Moreover, we have also presented the first attempts to use the Ni/Pt nanoreactors as photothermal agents. The nanoreactors can absorb efficiently NIR light to increase temperature with a high efficiency of 326.85 K·cm<sup>2</sup>/W. Although there is a lot of room for to optimize the photothermal process, the results are encouraging and may open new routes for the generation of self-powered nanoreactors for thermally induced reactions.

## 6.6 References

1. Bilgen S. Structure and environmental impact of global energy consumption. *Renew Sustain Energy Rev.* 2014;38:890-902. doi:10.1016/j.rser.2014.07.004
2. Wang G, Liao Q, Li Z, Zhang H, Liang Y, Wei X. How does soaring natural gas prices impact renewable energy: A case study in China. *Energy.* 2022;252:123940.
3. Gong W, Chen C, Fan R, Zhang H, Wang G, Zhao H. Transfer-hydrogenation of furfural and levulinic acid over supported copper catalyst. *Fuel.* 2018;231(January):165-171. doi:10.1016/j.fuel.2018.05.075
4. Gilkey MJ, Xu B. Heterogeneous Catalytic Transfer Hydrogenation as an Effective Pathway in Biomass Upgrading. *ACS Catal.* 2016;6(3):1420-1436. doi:10.1021/acscatal.5b02171
5. Cai B, Zhou XC, Miao YC, Luo JY, Pan H, Huang YB. Enhanced catalytic

- transfer hydrogenation of ethyl levulinate to  $\gamma$ -valerolactone over a robust Cu-Ni bimetallic catalyst. *ACS Sustain Chem Eng.* 2017;5(2):1322-1331. doi:10.1021/acssuschemeng.6b01677
6. Yan L, Yao Q, Fu Y. Conversion of levulinic acid and alkyl levulinates into biofuels and high-value chemicals. *Green Chem.* 2017;19(23):5527-5547.
  7. Sun S, Chen Y, Ji P. Simultaneous Coordination of Zn(II) and Zr(IV) to d - Amino Acid Oxidase: Highly Efficient Catalytic Transfer Hydrogenation of Levulinic Acid to  $\gamma$ -Valerolactone. *ACS Sustain Chem Eng.* 2022;(11). doi:10.1021/acssuschemeng.2c00155
  8. Zhu W, Chen S. Recent Progress of Single-atom Catalysts in the Electrocatalytic Reduction of Oxygen to Hydrogen Peroxide. *Electroanalysis.* 2020;32(12):2591-2602. doi:10.1002/elan.202060334
  9. Stanford MG, Pudasaini PR, Belianinov A, et al. Focused helium-ion beam irradiation effects on electrical transport properties of few-layer WSe<sub>2</sub>: Enabling nanoscale direct write homo-junctions. *Sci Rep.* 2016;6(June):1-10. doi:10.1038/srep27276
  10. Espro C, Paone E, Mauriello F, et al. Sustainable production of pharmaceutical, nutraceutical and bioactive compounds from biomass and waste. *Chem Soc Rev.* Published online 2021.
  11. Li G, Li N, Yang J, et al. Synthesis of renewable diesel range alkanes by hydrodeoxygenation of furans over Ni/H $\beta$  under mild conditions. *Green Chem.* 2014;16(2):594-599.
  12. Huber GW, Chheda JN, Barrett CJ, Dumesic JA. Production of liquid alkanes by aqueous-phase processing of biomass-derived carbohydrates. *Science (80- ).* 2005;308(5727):1446-1450.
  13. Mei N, Liu B, Zheng J, Lv K, Tang D, Zhang Z. A novel magnetic palladium catalyst for the mild aerobic oxidation of 5-hydroxymethylfurfural into 2, 5-furandicarboxylic acid in water. *Catal Sci Technol.* 2015;5(6):3194-3202.
  14. Dutta S, Wu L, Mascall M. Efficient, metal-free production of succinic acid by oxidation of biomass-derived levulinic acid with hydrogen peroxide. *Green Chem.* 2015;17(4):2335-2338.
  15. de Souza ROMA, Miranda LSM, Luque R. Bio (chemo) technological strategies for biomass conversion into bioethanol and key carboxylic acids. *Green Chem.* 2014;16(5):2386-2405.
  16. Mariscal R, Maireles-Torres P, Ojeda M, Sádaba I, Granados ML. Furfural: a renewable and versatile platform molecule for the synthesis of chemicals and fuels. *Energy Environ Sci.* 2016;9(4):1144-1189.

17. Lange J, Van Der Heide E, van Buijtenen J, Price R. Furfural—a promising platform for lignocellulosic biofuels. *ChemSusChem*. 2012;5(1):150-166.
18. Weingarten R, Conner WC, Huber GW. Production of levulinic acid from cellulose by hydrothermal decomposition combined with aqueous phase dehydration with a solid acid catalyst. *Energy Environ Sci*. 2012;5(6):7559-7574.
19. Ding D, Xi J, Wang J, Liu X, Lu G, Wang Y. Production of methyl levulinate from cellulose: selectivity and mechanism study. *Green Chem*. 2015;17(7):4037-4044.
20. Yu Z, Meng F, Wang Y, et al. Catalytic Transfer Hydrogenation of Levulinic Acid to  $\gamma$ -Valerolactone over Ni<sub>3</sub>P-CePO<sub>4</sub> Catalysts. *Ind Eng Chem Res*. 2020;59(16):7416-7425. doi:10.1021/acs.iecr.0c00257
21. Radhakrishnan K, Gupta S, Gnanadhas DP, Ramamurthy PC, Chakravorty D, Raichur AM. Protamine-capped mesoporous silica nanoparticles for biologically triggered drug release. *Part Part Syst Charact*. 2014;31(4):449-458. doi:10.1002/ppsc.201300219
22. Leonard RH. Levulinic acid as a basic chemical raw material. *Ind Eng Chem*. 1956;48(8):1330-1341.
23. Horvat J, Klaić B, Metelko B, Šunjić V. Mechanism of levulinic acid formation. *Tetrahedron Lett*. 1985;26(17):2111-2114.
24. Huang X, Liu K, Vrijburg WL, et al. Hydrogenation of levulinic acid to  $\gamma$ -valerolactone over Fe-Re/TiO<sub>2</sub> catalysts. *Appl Catal B Environ*. 2020;278(May):119314. doi:10.1016/j.apcatb.2020.119314
25. Pariari D, Sarma DD. Nature and origin of unusual properties in chemically exfoliated 2D MoS<sub>2</sub>. *APL Mater*. 2020;8(4). doi:10.1063/5.0005413
26. Liu D, Xue C. Plasmonic Coupling Architectures for Enhanced Photocatalysis. *Adv Mater*. 2021;33(46):1-22. doi:10.1002/adma.202005738
27. Li S, Dong G, Hailili R, et al. Effective photocatalytic H<sub>2</sub>O<sub>2</sub> production under visible light irradiation at g-C<sub>3</sub>N<sub>4</sub> modulated by carbon vacancies. *Appl Catal B Environ*. 2016;190:26-35. doi:10.1016/j.apcatb.2016.03.004
28. Feng HJ, Li XC, Qian H, et al. Efficient and sustainable hydrogenation of levulinic-acid to gamma-valerolactone in aqueous solution over acid-resistant CePO<sub>4</sub>/Co<sub>2</sub>P catalysts. *Green Chem*. 2019;21(7):1743-1756.
29. Cao W, Lin L, Qi H, et al. In-situ synthesis of single-atom Ir by utilizing metal-organic frameworks: An acid-resistant catalyst for hydrogenation of levulinic acid to  $\gamma$ -valerolactone. *J Catal*. 2019;373:161-172.



30. Wang J, Nie R, Xu L, Lyu X, Lu X. Catalytic transfer hydrogenation of oleic acid to octadecanol over magnetic recoverable cobalt catalysts. *Green Chem.* 2019;21(2):314-320.
31. Wang H, Chen C, Zhang H, Wang G, Zhao H. An efficient and reusable bimetallic Ni<sub>3</sub>Fe NPs@ C catalyst for selective hydrogenation of biomass-derived levulinic acid to  $\gamma$ -valerolactone. *Chinese J Catal.* 2018;39(10):1599-1607.
32. Wang F, Planas O, Cornella J. Bi (I)-catalyzed transfer-hydrogenation with ammonia-borane. *J Am Chem Soc.* 2019;141(10):4235-4240.
33. Ma M, Liu H, Cao J, et al. A highly efficient Cu/AlOOH catalyst obtained by in situ reduction: catalytic transfer hydrogenation of ML into  $\gamma$ -GVL. *Mol Catal.* 2019;467:52-60.
34. Hengne AM, Kadu BS, Biradar NS, Chikate RC, Rode C V. Transfer hydrogenation of biomass-derived levulinic acid to  $\gamma$ -valerolactone over supported Ni catalysts. *RSC Adv.* 2016;6(64):59753-59761.
35. Bauer H, Thum K, Alonso M, Fischer C, Harder S. Alkene Transfer Hydrogenation with Alkaline-Earth Metal Catalysts. *Angew Chemie.* 2019;131(13):4292-4297.
36. Yang Y, Gao G, Zhang X, Li F. Facile fabrication of composition-tuned Ru-Ni bimetals in ordered mesoporous carbon for levulinic acid hydrogenation. *ACS Catal.* 2014;4(5):1419-1425.
37. Tang Y, Fu J, Wang Y, Guo H, Qi X. Bimetallic Ni-Zn@ OMC catalyst for selective hydrogenation of levulinic acid to  $\gamma$ -valerolactone in water. *Fuel Process Technol.* 2023;240:107559.
38. Lu K, Li Z, Hai C, Li J, Liu CL, Dong WS. One-pot selective hydroconversion of levulinic acid to 2-methyltetrahydrofuran catalyzed by Ni-based catalysts derived from phyllosilicates. *Sustain Energy Fuels.* 2022;6(14):3425-3434.
39. Hijazi A, Khalaf N, Kwapinski W, Leahy JJ. Catalytic valorisation of biomass levulinic acid into gamma valerolactone using formic acid as a H<sub>2</sub> donor: a critical review. *RSC Adv.* 2022;12(22):13673-13694. doi:10.1039/d2ra01379g
40. Zhang J, Wang F, Shenoy VB, Tang M, Lou J. Towards controlled synthesis of 2D crystals by chemical vapor deposition (CVD). *Mater Today.* 2020;40(xx):132-139. doi:10.1016/j.mattod.2020.06.012
41. Nakaya Y, Furukawa S. Catalysis of Alloys: Classification, Principles, and Design for a Variety of Materials and Reactions. *Chem Rev.* Published

online 2022.

42. Gao F, Goodman DW. Pd–Au bimetallic catalysts: understanding alloy effects from planar models and (supported) nanoparticles. *Chem Soc Rev.* 2012;41(24):8009-8020.

## 7. Conclusion

In the present thesis, various multicomponent materials supported on nanoporous silica nanostructures have been developed as catalysts for their application in environmental remediation, biomedical therapies and energy conversion. In particular, the combination of different metals and/or metal/semiconductor materials has enabled achieving enhanced physicochemical properties. The following list of conclusions for the different developed materials can be drawn up.

1. A simple, cost-effective and scalable fabrication method has been applied to develop novel Fe/Au galvanic nanoreactors. These nanoreactors are based on the anisotropic physical vapor deposition of a Fe/Au bilayer with a semi-shell fashion on mesoporous silicon oxide nanoparticles. The bimetallic coating enabled the efficient *in-situ* production of H<sub>2</sub>O<sub>2</sub> (36-fold higher than the Fe counterpart) and the release of Fe<sup>2+</sup> in water at neutral pH by exploiting the different electrochemical potentials of the metal. This triggers the Fenton chemical path for ROS production.
2. The catalytic activity of the Fe/Au nanoreactors was demonstrated by the excellent degradation of the organic dye methylene blue (MB) and antibiotic tetracycline (TC) without any external additive or energy supply at pH=7 and using a minimal amount of catalysts (ca. 15 μg/mL). The enhanced reactivity with respect to the Fe nanoreactors was highlighted by (i) the 5-fold higher MB degradation kinetic constant, (ii) the 3.2-fold higher MB mineralization efficiency after 15 min reaction, and (iii) the 2.3-fold higher TC mineralization efficiency after 90 min reaction. Therefore, the Au layer accelerated the Fe corrosion rate and increased the Fe<sup>3+</sup>/Fe<sup>2+</sup> reconversion, efficiently sustaining the redox catalytic cycle for the generation of highly reactive •OH from the decomposition of the *in-situ* produced H<sub>2</sub>O<sub>2</sub>.
3. Compared to other zero-valent iron-based catalysts, the FeAu nanoreactors exhibited unprecedented reactivity at neutral pH and without the external supply of H<sub>2</sub>O<sub>2</sub>, showing substantially higher normalized kinetic constant and promising prospects for biomedical applications.
4. The novel 2D MoS<sub>2</sub>/Cu photocatalytic nanoreactors on 3D mesoporous nanostructures could be obtained by the combination of colloidal self-assembly, hydrothermal growth and electron-beam deposition. The experimental findings suggested that the hydrothermal MoS<sub>2</sub> has a combined structure: the semiconducting trigonal prismatic 2H phase and

the distorted octahedral T' phase. The latter phase features a very small band gap. The Cu layer was oxidized upon deposition onto the MoS<sub>2</sub>, forming an ultrathin Cu<sub>2</sub>O layer. The phase transition of MoS<sub>2</sub> and oxidation of Cu favoured the formation of a highly efficient type II photocatalyst with enhanced photoabsorption, enhanced charge separation and a high density of catalytic active sites for the interfacial redox process.

5. The high photocatalytic efficiency of the MoS<sub>2</sub>/Cu nanoreactors with white light was demonstrated by the nearly complete degradation and mineralization of TC and the biotoxin anatoxin in a wide pH range after 90 min reaction. The nanoreactors exhibited excellent durability, keeping their reactivity after 10 cycles. The ROS quenching experiments suggested that ·OH and ·O<sub>2</sub> were the main active species for the degradation of the organic pollutants.
6. The MoS<sub>2</sub>/Cu nanoreactors showed negligible cytotoxicity and could efficiently kill cancer cells *in vitro* under NIR light irradiation, thereby highlighting their biomedical potential as photodynamic agents.
7. Ni/Pt alloy nanoreactors supported on porous silica nanoparticles were obtained via the simple and scalable electron beam deposition and thermal treatment under a hydrogen and argon environment. This high-temperature annealing induced a uniform distribution of Pt alongside the nanoreactor surface. The alloying process optimizes the dispersion/dilution of heteroatoms, which, along with ligand effects, enhances the catalyst's activity.
8. The preliminary results of the Ni-Pt alloy nanoreactors showed the thermo-catalytic capacity to drive the conversion of levulinic acid into gamma-valerolactone by using formic acid as the hydrogen source. Their photothermal properties could open up the GVL synthesis pathway by using light as an energy source.

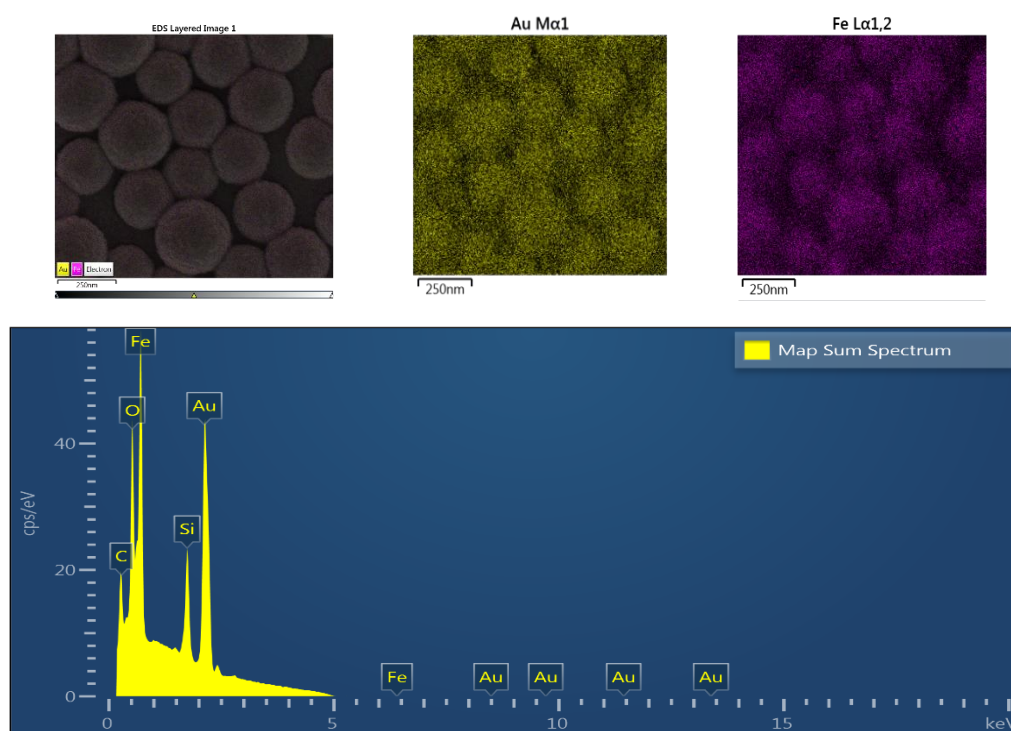
## 7.1 Future perspectives

Although the developed porous-silica-supported nanoreactors showed high catalytic efficiency, there are still many issues to be solved to enable their applications in the biomedical, environmental or energy fields.

- The reactivity of the Au/Fe should be modulated via functionalization routes. The functionalization of the Fe/Au nanoreactors can be optimized by using different lipids, cell penetration peptides or pH-sensitive smart molecules/ inorganic coatings. This will help to slow down the ROS generation, optimize the internalization pathway and activate the nanoreactors at the desired time or desired location. The bioavailability of the nanoreactors could be improved by specific ligands or polymers.
- The Fe/Au system has a high potential for tuning its reactivity due to its plasmonic and magnetic nature. Therefore, the ROS reaction can be further enhanced by locally increasing the temperature through the activation of plasmons using NIR light or by applying alternating magnetic fields. In turn, the mass transport of reagents and products could be facilitated by magnetic stirring.
- Having the unique characteristics of 2D materials and properties of semiconductors gives MoS<sub>2</sub> great application prospects in cancer therapy. Therefore, the MoS<sub>2</sub>/Cu can be further functionalized with biomolecules, lipids or polymers to improve cell internalization and biocompatibility. In addition, different nanomaterials or drugs could be integrated into the MoS<sub>2</sub>/Cu nanoreactors that could specifically respond to the tumor microenvironment, thereby increasing the antitumor efficiency.
- The stability of the MoS<sub>2</sub> can be improved by modifying the synthesis process to fine-tune the MoS<sub>2</sub> phase transitions. The monophasic MoS<sub>2</sub>/Cu nanoreactors can be developed for their application in bioimaging by exploiting their high photoluminescence. Further in vitro and in vivo experiments can be conducted to fully understand the toxicity and therapeutic potential of the nanoreactors as photodynamic agents.
- The fabrication of Ni/Pt nanoreactors needs further optimization. The alloy formation should be tested at different temperatures and better characterized by advanced surface techniques. The nanoreactors can be further employed for the levulinic acid (LA) conversion to gamma-valerolactone (GVL) via direct hydrogen transfer from water rather than hydrogen donor by using additional photocatalysts. The conversion of LA into GVL can be tested under light irradiation via photothermal processes.

## Appendix A: Supporting Information (Chapter 4)

Elemental composition of nanoreactors by EDS



Element	Atomic %
Si	17.85
Fe	51.50
Au	30.65
Total:	100.00

Figure 1A. EDS elemental mapping of Fe/Au nanoreactors

### Amplex Red / Horse Radish Peroxidase (HRP) Assay for H<sub>2</sub>O<sub>2</sub> detection: calibration curve

Amplex Red reacts with H<sub>2</sub>O<sub>2</sub> in a 1:1 stoichiometry, mediated by HRP to produce the fluorescence molecule resorufin, with emission at 586 nm. Therefore, resorufin becomes a fluorescent probe of the H<sub>2</sub>O<sub>2</sub> with detection limits in the nanomolar range. To assess the H<sub>2</sub>O<sub>2</sub> production at the Fe/Au and Fe nanoreactors, a calibration curve was performed using H<sub>2</sub>O<sub>2</sub> solutions in the presence of the reagents Amplex Red (50 μM) and HRP (0.1 U/mL). The resulting fluorescence intensity of resorufin as a function of H<sub>2</sub>O<sub>2</sub> concentration is plotted in Fig. 3. Each value is the average of three fluorescence measurements. The produced H<sub>2</sub>O<sub>2</sub> concentration was determined by fitting the linear part of the plot (dashed line).

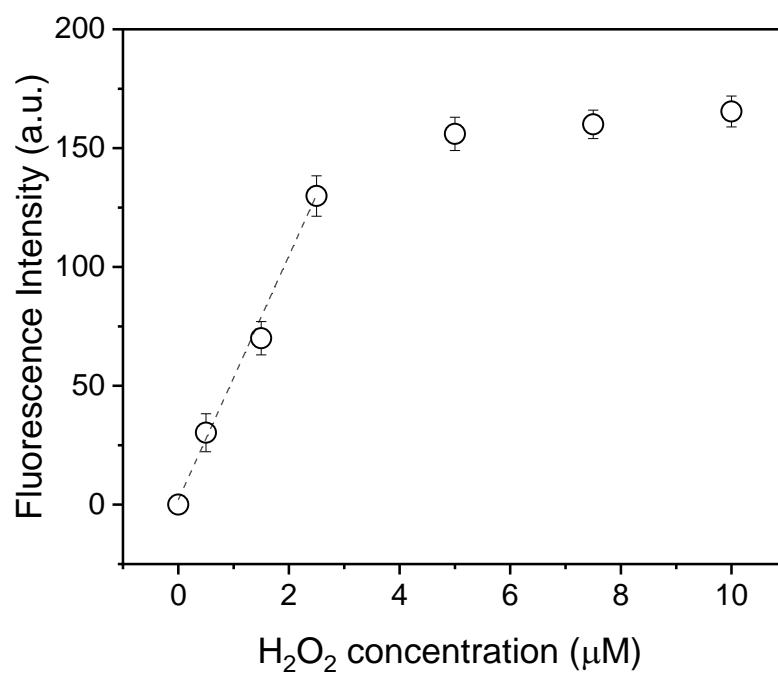


Figure 2A. The calibration curve was obtained by measuring resorufin fluorescence as a function of standard solutions of H<sub>2</sub>O<sub>2</sub>. Background fluorescence, determined for a no-H<sub>2</sub>O<sub>2</sub> control reaction, has been subtracted from each value as well as any background fluorescence from the support substrate of the Au/Fe and Fe nanoreactors.

## Appendix B: Magnetic properties

### Types of magnetic materials

The magnetic properties of the materials can be classified depending on their response to applied magnetic fields. Five main types can be found: diamagnetic, paramagnetic, ferromagnetic, ferrimagnetic and antiferromagnetic.

The atoms of **diamagnetic** materials have no unpaired electrons in their orbitals which results in zero net magnetic moment. However, the orbital motion of the electron is present and induces a weak magnetic field when applying a magnetic field but in the opposite direction, causing repulsive forces. In this case, the magnetic susceptibility ( $\chi=M/H$ ), defined as the ratio of the intensity of magnetization to the intensity(force) of the magnetizing field, is negative. Examples of these materials are Cu, Ag, Au. Diamagnetism is present in every material, but such opposing magnetic response is so weak that is usually negligible if other magnetic behaviors are possible.

Paramagnetic materials exhibit an odd number of electrons (unpaired) carrying a magnetic moment. However, the magnetic moment of the atoms is randomly orientated resulting in a null total magnetization contribution unless an external magnetic field is applied. In presence of a magnetic field, the magnetic moments of the atoms align along the direction of the applied magnetic field but getting weak magnetic moment (e.g. Al, Mg, Li, Ta). The magnetization vs. magnetic field  $H$  curve in these materials follows a linear relationship with positive magnetization,  $\chi > 0$ , unlike the diamagnetic materials. These materials do not retain magnetic moment when the magnetic field is removed.

**Ferromagnetic** materials (e.g. Fe, Ni, Co) comprise atoms with unpaired electrons which form special neighbourhoods termed domains. Each domain contains atoms whose magnetic moments are parallel producing a net magnetic moment of the domain that points in some direction. The magnetic moments of the different domains are randomly oriented with respect to each other giving a zero net magnetic moment of the material. When the ferromagnetic material is placed in a magnetic field, the magnetic moments of the domains will increasingly align along the direction of the applied magnetic field forming a large net magnetic moment. These materials keep a permanent net magnetic moment at zero fields once they are magnetized since the domains are unable to revert to a completely random orientation. This kind of material presents positive and large susceptibility and in contrast to diamagnetic and paramagnetic materials, the ferromagnetic characteristics are temperature dependent. Above a certain temperature (Curie temperature), the thermal agitation becomes so great that the material turns into paramagnetic one.



**Ferrimagnetism** is observed in compounds with complex crystal structures combining different atoms (A, B) such as magnetite  $\text{Fe}_3\text{O}_4$  and maghemite  $\gamma\text{-Fe}_2\text{O}_3$ . These materials break down into magnetic domains and possess a net magnetic moment at zero field as in the case of ferromagnetic materials. However, the exchange interactions lead to parallel alignment of atoms in some of the crystal sites (sublattice A), and anti-parallel alignment of other atoms (those in sublattice B). Magnetic dipoles lining up in one direction are stronger than those in the opposite direction which prevents the cancellation of magnetic moments with an applied magnetic field. Although they can present large magnetization and positive magnetic susceptibility, their magnetization is smaller than in the case of ferromagnetic materials. They also exhibit similar temperature dependence.

Similar to ferrimagnetic materials, **antiferromagnetic** materials are composed of distinct atom sublattices (MnO, CoO, NiO). They exhibit similar magnetic moments but with their moments antiparallel to each other. The total magnetic moment is zero at zero magnetic field. When an external magnetic field is applied, one of the groups of the dipoles can become stronger than the other inducing a kind of ferrimagnetism behavior. The magnetization susceptibility is positive but small and the magnetic response is temperature dependence. At higher temperatures can become paramagnetic.

Figure 1 a and b show in comparison, the magnetic dipole alignment and the magnetization curve starting from a demagnetized material when applied a magnetic field in one direction. The curves depict the trend of the magnetization moment (M) as a function of the applied magnetic field (H). From these curves the magnetization susceptibility (M/H) can be easily inferred.

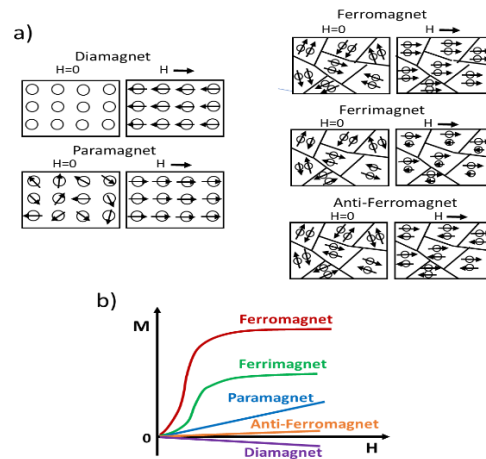


Figure 1B. a) Summary of the main relevant forms of magnetism (diamagnetic, paramagnetic, ferromagnetic, ferrimagnetic and anti-ferromagnetic materials) with the schematic representation of magnetic dipole alignment in absence and in presence of an applied magnetic field  $H$ . Just notice the domain formation in ferromagnetic, ferrimagnetic and antiferromagnetic materials. b) Variation of the magnetic moment with an applied magnetic field with positive magnetic susceptibility ( $M/H$ ) for ferromagnetic, ferrimagnetic, paramagnetic and antiferromagnetic materials and negative one for diamagnetic materials.

### Origin of the magnetic domains

The reason of the existence of magnetic domains is energy-related: the higher the number of domains, the less the internal energy of the material. The internal energy is the result of different contributions such as the exchange energy, the magnetostatic energy, the magnetocrystalline and magnetostrictive energies. The exchange energy is related with the driving force for magnetic dipole alignment, arising from the interaction of the electron spins. The magnetostatic energy is the magnetic potential energy generated by a magnetic body field and is reduced by dividing the magnetic body into domains, thus resulting in the main driving force for domain formation (Fig. 2 a, dashed field lines represent the magnetic potential energy). Magnetic materials exhibit magnetocrystalline anisotropy which refers to the crystal's property to be more easily magnetized in some directions in comparison to others. For a crystal, the axis that is easiest to magnetize is known as the easy axis, and the axis that is most difficult to magnetize is known as the hard axis. Thus, the magnetocrystalline energy is related to the excess energy required to magnetize materials in a particular direction over the one along the easy direction. The magnetostrictive energy is related to domain length changes under magnetization.

The boundaries between adjacent domains are called domain walls and their width is again determined by a balance between competing energy contributions such as the *exchange* energy (which prefers a wide wall) and the *magnetocrystalline anisotropy* energy (which prefers a narrow wall). In this wall region, the electron

spin changes gradually in going from one domain to another of different orientation. Magnetic domains are greatly affected by material miniaturization.

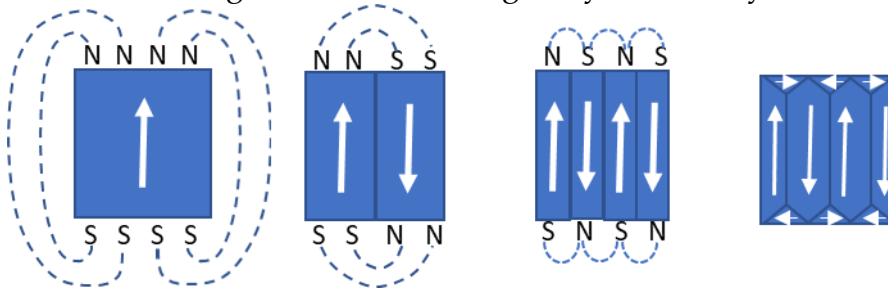


Figure 2B. Reduction of the magnetostatic energy by domain formation in a ferromagnet (Magnetostatic potential field in dashed lines)

### Magnetic vortex configuration

In a vortex configuration, the magnetic moments are curled in the plane of the structure, organized in closed circles to minimize the magnetostatic energy. Only at the centre, at the core of the vortex, the magnetic moments get out of the plane and point perpendicularly (figure 3). The figure also shows the different stages of the magnetization curve of a structure with vortex states as function of an in-plane magnetic field. At low fields, the vortex core is displaced reversibly in the plane until it reaches the structure lateral border, where it is annihilated ( $H_a$ ) and the sample becomes magnetically saturated. Reducing the magnitude of the applied field, the vortex is nucleated again ( $H_n$ ), but at a magnetic field of lower intensity than that for annihilation, and then follows back the original reversible path, corresponding to the reversible movement of the vortex core. The same trend is followed when the magnetic field is applied in the opposite direction. This causes a very peculiar hysteresis loop, with no remanence or coercive field and open lobes at high fields. The values of characteristic fields and the slope of the linear part of the hysteresis loop are strongly size-dependent.

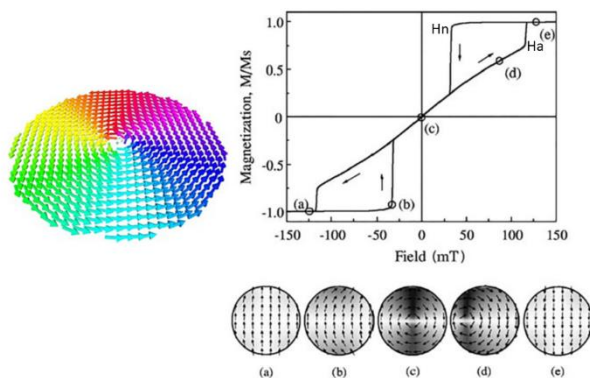


Figure 3B. Left: vortex core schematics. Right: Hysteresis loop of a magnetic vortex configuration. (Adapted from Reference Guslienko et al., Phys. Rev. B, 65, 244141–2441410 (2002)).